Measurements of charge and CP asymmetries in b-hadron decays using top-quark events collected by the ATLAS detector in pp collisions at $\sqrt{s} = 8$ TeV

Jacob Kempster

Department of Physics

Royal Holloway, University of London

A thesis submitted to the University of London for the

Degree of Doctor of Philosophy

September 12, 2017

DECLARATION

I confirm that the work presented in this thesis is my own. Where information has been derived from other sources, I confirm that this has been indicated in the document.

Jacob Kempster

Abstract

Same- and opposite-sign charge asymmetries are measured in lepton+jets $t\bar{t}$ events in which a b-hadron decays semileptonically to a soft muon, using data corresponding to an integrated luminosity of 20.3 fb^{-1} from proton-proton collisions at a centre-of-mass energy of $\sqrt{s} = 8$ TeV collected with the ATLAS detector at the Large Hadron Collider at CERN. The charge asymmetries are based on the charge of the lepton from the top-quark decay and the charge of the soft muon from the semileptonic decay of a b-hadron and are measured in a fiducial region corresponding to the experimental acceptance. Four CP asymmetries (one mixing and three direct) are measured and are found to be compatible with zero and consistent with the Standard Model.

Acknowledgements

I would like to thank my supervisor Dr. Veronique Boisvert for over eight years of teaching and support, and for getting me from the point of undergraduate beginner to the submission of this thesis at the end of this PhD. I would also like to thank Dr. John Morris for his tireless work in our two-man team, Professor Lucio Cerrito for his supervision, and Dr. Francesco Spanò for more than a few useful and lengthy discussions at times of the day others would have thought instrusive. I would like to thank the students who inspired me to take a PhD at Royal Holloway, Rob Cantrill and Tim Brooks, and to Ian Connelly for his impressive insight and to the numerous students who have come and gone in and helped me in so many ways. To James 'WetBoy' Bright and Tom 'Magma Maus' Banham, thank you for being my pseudo-brothers for many years, for giving me that escape when I needed it and somewhere to sleep on almost any occasion. I would like to thank Faye Cheung for giving me endless support, from near and from far, we keep eachother going. I would also like to thank and send the very best of luck to my sister Katrina and her husband Steve, in raising their first child Luca born on 01/03/2017. Most of all, I give my endless gratitude to my parents for 27 years of support, guidance and love, for raising me to work my hardest and reach for every goal, and for teaching me to never give up even in the face of adversity, I love you very much.

I'll do my best.

Preface

This thesis describes the measurement of charge and CP asymmetries in b-hadron decays using top quark events collected by the ATLAS detector in proton-proton collisions at a centre of mass energy of $\sqrt{s} = 8$ TeV. The analysis is based on the prescription outlined in a paper entitled *Top B Physics at the LHC*, published in Physical Review Letter **110**, and is the first to exploit the relationship between CP violation (CPV) and the relative charge of two leptons in $t\bar{t}$ ℓ+jets decays. The identification of soft muons from semileptonic b-hadron decays is required to perform this analysis, and is achieved using a method known as *soft muon tagging* (SMT). The soft muon tagger relies on the fractional difference in momentum between reconstructed tracks in the inner detector and the muon spectrometer (extrapolated back to the primary vertex) of the ATLAS detector (known as the *momentum imbalance* (MI)), to separate true soft muons from heavy-flavour decays from fakes of other sources. The calibration of the tagger is described herein. Chapter 1 includes a brief introduction to the Large Hadron Collider and top-quark physics. Chapter 2 includes an overview of the Standard Model (SM) of particle physics, with specific focus on CPV which leads into the more detailed discussion of CPV in the B-physics sector in Section 2.6. Chapter 3 includes an overview of top-quark physics, including details on the primary production and decay mechanisms at $\sqrt{s} = 8$ TeV, as well as updates in the most recent experimental developments. Chapter 4 gives an outline of the analysis motivation and technique, with definitions of the charge and CP asymmetries measured. Chapter 5 describes the Large Hadron Collider (LHC), the ATLAS experiment and each of the subsystems relevant to top-quark measurements. Chapter 6 includes an introduction to the reconstruction of physics objects following particle collisions and utilising the physics signatures in the aforementioned detector systems, it also includes some discussion of collisions simulations used to test data against the SM or beyond the Standard Model (BSM) theories. Chapter 7 describes the calibration of the soft muon tagger using a tag and probe analysis. Tag and probe analyses are widely utilised in the ATLAS

collaboration as calibration techniques, Chapter 7 is built upon a calibration code written by a previous Royal Holloway (RHUL) student, using a χ^2 track fit as the discriminating variable instead of momentum imbalance (as defined later). The MC and data samples derived from selected triggers were already implemented, and my involvement was to update the calibration to discriminate between real and fake soft muons using MI, to provide code maintenance and bug-fixing, to retrieve the data/MC scale factors as binned by angular information and transverse momentum and to take the results through the internal ATLAS approval procedure. All results and plots presented are updated versions of those previously derived for the χ^2 calibration. Chapter 8 describes the event selection utilised for the charge and CP asymmetry analysis, it is based upon a standard selection used to identify $t\bar{t}$ events as prescribed by the ATLAS top quark group. Alterations to this selection are derived following joint studies between myself and a colleague at Queen Mary, University of London (QMUL). A more detailed description of the W+jets data-driven estimation is provided as I was involved in the early implementation of this background estimation, however the final code used to complete the estimation and retrieve the relevant scale factors is not my own. Chapter 9 includes descriptions of the sources of experimental and modelling uncertainties considered to be relevant to the charge and CP asymmetry analysis. Chapter 10 describes the implementation and optimisation of a Kinematic Likelihood Fitter (KLFitter) which contributes information paramount to the measurement. I was in charge of the implementation and optimisation of the KLFitter. Chapter 11 describes the unfolding procedure used to correct the reconstructed charge asymmetries to the particle level in a fiducial volume, I was in charge of the implementation and optimisation of the unfolding. Chapter 12 presents the results of the culmination of work by the joint RHUL-QMUL analysis team, and my contribution of an interpretation of the measured charge and CP asymmetries. Chapter 13 provides a summary of the analysis and the individual studies performed in the prior chapters, as well as my contribution of quantified estimations of future performance for a repeat of the analysis with more statistics and utilising my ideas for reductions in the systematic uncertainties. Much work in this thesis is similar in tone to my contributions to the published paper:

J Kempster et al. *Measurements of charge and CP asymmetries in b-hadron decays using top-quark events collected by the ATLAS detector in pp collisions at* $\sqrt{s} = 8$ *TeV*, J. High Energ. Phys. (2017) 2017:71.

Contents

1 Introduction **24**

2 The Standard Model of particles physics **26**
2.1 Elementary particles . . . 27
2.2 Fundamental forces . . . 27
2.3 Quantum electrodynamics . . . 29
2.4 Quantum chromodynamics . . . 29
2.5 Weak interactions . . . 30
2.5.1 The CKM matrix . . . 32
2.5.2 Charge and parity operators . . . 33
2.5.3 *CP* violation and neutral meson-mixing . . . 36
2.6 *B*-physics and *CP* violation with time-integrated analyses . . . 40
2.6.1 *CP* violation in decays . . . 41
2.6.2 *CP* violation in mixing . . . 42
2.6.3 *CP* violation in the interference between decays with and without mixing 42
2.6.4 Relation to the CKM matrix . . . 43
2.6.5 New Physics . . . 43
2.6.6 *CP* violation in the SM . . . 45
2.7 The Higgs Mechanism and electroweak unification . . . 46
2.7.1 Gauge invariance . . . 46
2.7.2 Spontaneous symmetry breaking . . . 47
2.7.3 Top quark . . . 48

3 Top-quark physics **50**
3.1 Top-quark production . . . 51
3.2 Top quark decay modes . . . 53
3.3 Top quark properties . . . 55

4 Analysis outline **60**
4.1 *CP* violation in heavy flavours with top-quark events at ATLAS . . . 60
4.1.1 Charge asymmetries . . . 61
4.1.2 *CP* asymmetries . . . 63
4.2 The D0 like-sign dimuon asymmetry . . . 65

5 The LHC and ATLAS Detector **68**
5.1 Large hadron collider . . . 68
5.2 ATLAS . . . 72
5.2.1 Inner Detector . . . 74
5.2.2 Calorimetry . . . 77
5.2.3 Muon Spectrometer . . . 80
5.2.4 Magnet system . . . 81
5.2.5 Triggers and Data Acquisition . . . 82

6 Data simulation and object selection **84**
6.1 Monte Carlo simulation . . . 84
6.1.1 Event generation . . . 84
6.1.2 Detector simulation . . . 86
6.2 Object reconstruction . . . 87
6.2.1 Vertices and Tracks . . . 87
6.2.2 Electron reconstruction . . . 88
6.2.3 Muon reconstruction . . . 89
6.2.4 Jet reconstruction . . . 91
6.2.5 b-Tagging techniques . . . 94
6.2.6 Missing momentum reconstruction . . . 97

7 Calibration of the Soft Muon Tagger **99**
7.1 Tag and Probe . . . 100
7.1.1 Collision data and Monte Carlo samples . . . 101
7.1.2 Selection . . . 101
7.2 Invariant mass fitting and background subtraction . . . 103
7.2.1 Uncertainty measurement . . . 104
7.3 Efficiencies . . . 106
7.3.1 $Z \to \mu\mu$ . . . 107
7.4 Fake rate . . . 112

8 Event selection **118**
8.1 Collision data and simulated samples . . . 118
8.2 Object identification and event selection . . . 121
8.2.1 Trigger selection . . . 121
8.2.2 Offline selection . . . 121
8.2.3 Event selection . . . 124
8.2.4 Optimisation . . . 125
8.2.5 Fiducial selection . . . 126
8.3 Background estimation . . . 128
8.4 W+jets data-driven estimation . . . 133
8.4.1 *b*-Tagging combinations . . . 136
8.4.2 Extrapolation of flavour fractions to 4-jet inclusive region . . . 136
8.4.3 Charge asymmetry in the 4-jet inclusive region . . . 137
8.4.4 Final combined scale factors . . . 138
8.5 Multijet data-driven estimation . . . 138
8.6 Control plots . . . 139

9 Systematic Uncertainties **143**
9.1 Experimental uncertainties . . . 143
9.1.1 Lepton reconstruction, identification and trigger . . . 144
9.1.2 Lepton energy scale and resolution . . . 144
9.1.3 Lepton charge misidentification . . . 145
9.1.4 Jet energy scale (JES) . . . 146
9.1.5 Jet energy resolution (JER) . . . 147
9.1.6 Jet reconstruction efficiency . . . 149
9.1.7 Jet vertex fraction (JVF) . . . 149
9.1.8 Flavour tagging uncertainty . . . 149
9.1.9 SMT uncertainty . . . 151
9.1.10 Background uncertainties . . . 151
9.1.11 Luminosity . . . 151
9.1.12 Beam energy . . . 151
9.2 Modelling uncertainties . . . 151
9.2.1 b-hadron production . . . 152
9.2.2 Hadron-to-muon branching ratios . . . 152
9.2.3 Asymmetry of single-top production . . . 152
9.2.4 Next-to-leading order (NLO) generator . . . 153
9.2.5 Parton shower and hadronisation . . . 153
9.2.6 Additional radiation . . . 154
9.2.7 Parton distribution function . . . 154

10 Kinematic Fitting **155**
10.1 Kinematic Likelihood Fitter . . . 155
10.1.1 Kinematic fitting . . . 156
10.1.2 The likelihood function . . . 158
10.2 KLFitter optimisation . . . 160
10.2.1 Truth matching and performance . . . 160
10.2.2 Nominal setup . . . 164
10.2.3 Semileptonic corrections . . . 164
10.2.4 Configuration optimisation . . . 169
10.2.5 Likelihood interpretation . . . 188
10.2.6 Likelihood manipulation . . . 191
10.2.7 KLFitter performance . . . 193

11 Unfolding techniques **195**
11.1 Unfolding formulation . . . 196
11.2 Combination of e+jets and μ+jets channels . . . 197
11.3 Fiducial volume . . . 197
11.4 Acceptance . . . 198
11.5 Response matrix . . . 200
11.6 Particle-level corrections . . . 201
11.7 Matrix inversion and regularisation . . . 202
11.7.1 Unregularised matrix inversion . . . 204
11.7.2 Iterative Bayesian matrix inversion . . . 204
11.8 Statistical uncertainty and bias . . . 204

11.8.1 Closure test 204
11.8.2 Stress tests 205
11.8.3 Statistical Uncertainty 207

12 Results **212**
12.1 Measurement of $t\bar{t}$ cross-section 212
12.2 Measurement of charge asymmetries 214
12.3 Measurement of CP asymmetries 218
12.3.1 Decay chain fractions 218
12.3.2 CP asymmetry extraction 219
12.4 Interpretation of results 220
12.4.1 The D0 anomalous dimuon asymmetry 222

13 Conclusions **225**
13.1 Future improvements 226

A Charge and CP asymmetry relations **230**

B Decay chain fractions and CP asymmetries with normalisations **234**
B.1 Performing the substitution 234

C Electron identification criteria **236**

List of Figures

2.1 The elementary particles of the SM as classified by their properties and quantum numbers, labelled with the charge and mass of each. Also shown are the mediators of the fundamental forces, and the most recently discovered Higgs boson. . . . 28
2.2 The primary vertex for QED showing the interaction between a photon and two fermions. Rotation of this vertex and replacement of the generic fermions f with appropriate particles describes all possible QED processes. . . . 29
2.3 The primary vertices for QCD showing the interaction between a gluon and two quarks, as well as the three- and four-gluon self-interaction vertices. . . . 30
2.4 The primary vertices for the weak interaction. (a) Z boson coupling to fermions, (b) W boson coupling with a lepton and a neutrino and (c) W coupling with two differently-charged quarks. . . . 31
2.5 The LQS vertices for the weak interaction. (a,b) pair the W boson with the first generation quarks, (c,d) pair the W boson with the second generation quarks. . 33
2.6 Neutral meson mixing in the SM via the weak interaction. (a) converts between the neutral K^0 and $\bar{K}^0$ states, (b) converts between the neutral B_d^0 and $\bar{B}_d^0$ states. 36
2.7 Constraints following a global CKM fit in the $(\bar{\rho},\bar{\eta})$ plane for all modern experimental inputs. . . . 44
2.8 The potential $V(\eta) = \mu^2(\eta^*\eta) + \lambda(\eta^*\eta)^2$, for a complex scalar field with $\mu^2 < 0$ and $\lambda > 0$. . . . 48
2.9 Lowest order Feynman diagrams for Higgs production via gluon fusion and a top-quark loop, and Higgs decay to two photons via a top-quark loop. . . . 49
2.10 Predictions for the Higgs boson mass, as a function of the t and W masses. . . . 49

3.1 Feynman diagrams showing top-quark pair production via (a) gluon fusion and (b) quark-antiquark annihilation. . . . 52
3.2 NLO predictions for parton distribution functions with the proton as a function momentum fraction. . . . 52
3.3 Feynman diagrams showing single top-quark production via (a) the s-channel, (b) the Wt-channel, (c) the t-channel in association with a sea b-quark from the proton, and (d) the t-channel in association with a b-quark from a gluon. . . . 53
3.4 Top-quark pair branching fractions. . . . 54
3.5 Summary of ATLAS direct top-quark mass measurements, compared to the overall ATLAS, Tevatron, and Tevatron+LHC combinations. . . . 56

3.6 Summary of the top-quark pair production cross-section measurements on ATLAS and CMS at 8 TeV in the ℓ+jets and dilepton channels, compared with an NNLO QCD calculation. 57
3.7 Feynman diagrams for the (a) Born and (b) Box diagrams which interfere to produce forward-backward and charge asymmetries. Additional diagrams with (c) initial and (d) final state radiation which contribute a similar but reduced effect. 58
3.8 Rapidity distributions of top and anti-top quarks at (a) the Tevatron showing a forward-backward asymmetry, and (b) the LHC showing a charge-asymmetry. . 59
3.9 Summary of the charge asymmetry measurements on ATLAS and CMS at 8 TeV 59

4.1 The $t\bar{t}$ ℓ+jets decay channel, highlighting the W-boson lepton and a soft muon from a semileptonic B-meson decay. 61
4.2 Overview of measurements of $a^d_{\rm sl}$ and $a^s_{\rm sl}$ (flavour-dependent CP violation asymmetries in neutral B-meson mixing). The black dot represents the SM expectation value, the yellow ellipse represents interpretation of the D0 dimuon observation, and the green bands represent naive averages of previous measurements. 66
4.3 Interpretation of the D0 dimuon (A) and single muon (a) observations, detailing the magnitude of direct CP violation in b and c decays required to produce them assuming SM-like neutral B mixing. 66

5.1 A diagrammatic layout of the CERN complex, including the LHC, major experiments and preparatory accelerators prior to the primary ring. 69
5.2 Beam squeezing prior to collision at the ATLAS experiment. 71
5.3 Performance related parameters of the 2012 protons beams compared with the overall LHC design specifications. 72
5.4 Pile-up conditions in the ATLAS detector during the 7 and 8 TeV data taking. . 73
5.5 A cut-away diagram of the overall construction of the ATLAS detector, labelling the individual components. 74
5.6 Design goals for the precision of the components of the ATLAS detector. The units for E ad p_T are GeV. 75
5.7 A cut-away diagram of the overall construction of the ATLAS inner detector, labelling the individual components. 75
5.8 A cut-away diagram of the overall construction of the ATLAS inner detector, with detailed structure of the Pixels, SCT and TRT. 76

6.1 Diagrammatic representation of proton-proton collisions as segmented by event-generators. 85
6.2 A representation of a collinear safe algorithm (left) for which the number of jets is not modified due to the soft gluon emissions in (a) and (b). A collinear unsafe algorithm is also represented (right) for which the number of jets reconstructed is altered by the same emissions, between (c) and (d). The verticle lines represent partons with the height of each line proportional to their transverse momentum, the horizontal axis indicates rapidity. 91
6.3 A representation of two jets (a) which remain as two jets when reconstructed with an infrared safe algorithm (b), but converge to a single jet when reconstructed using an infrared unsafe algorithm (c). 92

6.4 Four examples of jet reconstruction on a parton-level event generated with $\sim 10^4$ random soft particles. The k_T and C/A algorithms show dependency on the distribution of the soft particles. The anti-k_T algorithm is less influenced by soft radiation and produces uniformly shaped jets. 93
6.5 A curve to show the light-flavour rejection rate for given b-jet efficiencies of the MV1 b-tagging algorithm, measured on 8 TeV MC simulated top-quark pair events. 96
6.6 The momentum imbalance distribution of 'signal' soft muons, and 'fakes' from the decay of non-b-hadrons comprised of u-, d- or s-quarks ('UDS'), using $t\bar{t}$ MC. The area under each distribution has been normalised to unity. 97

7.1 The momentum imbalance distribution of all MuonProbe candidates in both 2012 Data and MC12 Monte Carlo simulation. The integral of the Monte Carlo distribution has been normalised to that of the data. 103
7.2 Illustration of the fitting procedure. Note the composite fit function made of a Gaussian plus a 2nd-order polynomial (blue), the background fit and the respective maximum and minimum variation (dashed lines) and the implied signal Gaussian (red). The integration window shown for the nominal 3σ range (pink) and the wider 5σ range for uncertainty (bright green). The lines drawn are for illustration purposes only. 105
7.3 Tag and Probe invariant mass, showing the fitted composite function (blue), the background fit, with maximum and minimum (dashed), the 3σ and 5σ ranges (magenta and green respectively), and an approximation of the signal distribution (red). Shown here are invariant mass distributions for all of the 2012 data, for probe muons with 4 GeV $< p_{\mathrm{T}} <$ 5 GeV, in the barrel region of the detector. 108
7.4 MI efficiencies and Data/Monte Carlo scale factor with respect to various isolation variables, for positively charged probes. 109
7.5 MI efficiencies and Data/Monte Carlo scale factor with respect to various isolation variables, for negatively charged probes. 110
7.6 MI efficiencies and Data/Monte Carlo scale factors with respect to the η and ϕ of the positively charged probe. 110
7.7 MI efficiencies and Data/Monte Carlo scale factors with respect to the η and ϕ of the negatively charged probe. 112
7.8 MI efficiencies with respect to the p_{T} of the positively charged probe, for the five positive $|\eta|$ regions using all 2012 data. 113
7.9 MI efficiencies with respect to the p_{T} of the negatively charged probe, for the five positive $|\eta|$ regions using all 2012 data. 114
7.10 MI efficiencies with respect to the p_{T} of the positively charged probe, for the five negative $|\eta|$ regions using all 2012 data. 115
7.11 MI efficiencies with respect to the p_{T} of the negatively charged probe, for the five negative $|\eta|$ regions using all 2012 data. 116
7.12 The SMT efficiencies with respect to the p_{T} of the Probe, for the barrel region with $J/\psi \to \mu\mu$ and $Z \to \mu\mu$ combined 117
7.13 Coarsely-binned scale factors for the mistag rate between data and MC simulation. The purple line is an all-data derived SF of $0.87^{+0.18}_{-0.38}$. 117

8.1 Example Feynman diagrams for each of the main backgrounds to a ℓ+jets $t\bar{t}$ signal. Labels indicate the production charge (a)symmetries in terms of the charge of the charged-lepton (from the W-boson decay), and correlations between the charges of the charged-lepton (from the W-boson decay) and the soft-muon. . . 132
8.2 Jet multiplicity distributions. 140
8.3 b-tagged jet multiplicity. 140
8.4 b-tagged jet p_T distributions. 140
8.5 Lepton p_T distributions. 141
8.6 Lepton η distributions. 141
8.7 SMT p_T distributions. 141
8.8 SMT η distributions. 142
8.9 SMT *MI* distributions. 142

9.1 Measured combined reconstruction and identification efficiencies as a function of E_T and η for different cut-based selections in data, compared to MC simulations. The lower panel shows the Data/MC SFs. 145
9.2 Muon reconstruction efficiency as a function of η for different muon reconstruction techniques, CB = Combined, ST = Segment-Tagged. The lower panel shows the Data/MC SFs. 145
9.3 Charge misidentification probability in data as a function of η for different reconstruction criteria, compared to MC simulations. The lower panel shows the Data/MC SFs. 147
9.4 The fractional systematic uncertainty components as a function of p_T on the JES for jets with $|\eta|= 0.0$. The total uncertainty (all components summed in quadrature) is shown as a filled blue region topped by a solid black line. 148
9.5 The fractional systematic uncertainty components as a function of η on the JES for jets with $p_T = 40$ GeV. The total uncertainty (all components summed in quadrature) is shown as a filled blue region topped by a solid black line. 148

10.1 e+jets background composition. This is a stacked histogram showing the relative contributions in simulation to the total event yield from the signal $t\bar{t}$, the $t\bar{t}$ backgrounds which consist of fake SMT muons within $t\bar{t}$ events, and the non-$t\bar{t}$ backgrounds (in green) which consist of the other channels such as W+jets and single top decays. 170
10.2 μ+jets background composition. This is a stacked histogram showing the relative contributions in simulation to the total event yield from the signal $t\bar{t}$, the $t\bar{t}$ backgroundswhich consist of fake SMT muonswithin $t\bar{t}$ events, and the non-$t\bar{t}$ backgrounds (in green) which consist of the other channels such as W+jets and single top decays. 171
10.3 SMT p_T distributions broken down by b-quark decay chain in the e+jets channel. The μ+jets distribution is analogous 172
10.4 Magnitude of the difference between reconstructed jet p_T and the matching MC parton b-quark p_T in the e+jets channel. The μ+jets distribution is analogous . . 172
10.5 KLFitter performance as a function of the magnitude of the difference between reconstructed jet p_T and the matching MC parton b-quark p_T. Shown in in the e+jets channel. the μ+jets distribution is analogous 173

10.6 Magnitude of the difference between reconstructed jet p_T (with SLC correction) and the matching MC parton b-quark p_T in the e+jets channel. The μ+jets distribution is analogous 173
10.7 Difference between reconstructed jet p_T (with and without SLC correction) and fitted jet p_T returned by the KLFitter. The shift of the mean towards zero in the SLC corrections indicates a less strenuous fit performed, and leads to a higher permutation likelihood. Shown in the e+jets channel, the μ+jets distribution is analogous 174
10.8 Log likelihood distributions for the best permutation in each event as decided by the KLFitter, overlayed for events before and after the jet SLC corrections, for the PRL2 and PRL5 decay channels. The improvement in likelihood leads to a better performance of the KLFitter. Shown in the e+jets channel, the μ+jets distribution is analogous 174
10.9 KLFitter top-quark mass reconstruction with removal of fixed top-quark mass constraint, for $t\bar{t}$ MC with $t\bar{t}$ backgrounds removed, and W+jets background estimation, in the e+jets channel 187
10.10 KLFitter likelihood distributions for signal and background events in the e+jets channel. The μ+jets distribution is analogous 192
10.11 KLFitter likelihood distributions for $t\bar{t}$ MC signal (with $t\bar{t}$ backgrounds removed) separated by correct or incorrect KLFitter decision, in the e+jets channel. The μ+jets distribution is analogous 193

11.1 The statistical uncertainty on A^{ss} as measured in the nominal $t\bar{t}$ MC scaled to an integrated luminosity of 20.3 fb^{-1}, when using the UMI, IB4 and IB8 unfolding techniques. The uncertainty is found to be stable and similar for each. 209
11.2 The statistical uncertainty on A^{os} as measuredin the nominal $t\bar{t}$ MC scaled to an integrated luminosityof 20.3 fb^{-1}, when using the UMI, IB4 and IB8 unfolding techniques. The uncertainty is found to be stable and similar for each. 210
11.3 The statistical uncertainty on A^{ss} as measured in the nominal $t\bar{t}$ MC scaled to an integrated luminosity of 20.3 fb^{-1}, when using the UMI, IB4 and IB8 unfolding techniques. The uncertainty is found as a function of the KLFitter purity ρ_{KL}. All three unfolding techniques converge in statistical uncertainty around $\rho_{\mathrm{KL}} = 80\%$. 210
11.4 The statistical uncertainty on A^{os} as measured in the nominal $t\bar{t}$ MC scaled to an integrated luminosity of 20.3 fb^{-1}, when using the UMI, IB4 and IB8 unfolding techniques. The uncertainty is found as a function of the KLFitter purityρ_{KL}. All three unfolding techniques converge in statistical uncertainty around $\rho_{\mathrm{KL}} = 80\%$. 211

12.1 Same-top-like charge-pairings distributions. The hashed area represents all experimental systematic uncertainties as well as the b-hadron production and hadron-to-muon branching ratio uncertainties. The lower panel of the distributions show the ratio of the data divided by the simulation. (a) shows the e+jets channel while (b) shows the μ+ jets channel. 223

12.2 Different-top-like charge-pairings distributions. The hashed area represents all experimental systematic uncertainties as well as the b-hadron production and hadron-to-muon branching ratio uncertainties. The lower panel of the distributions show the ratio of the data divided by the simulation. (a) shows the e+jets channel while (b) shows the μ+jets channel. 224

C.1 The variables used in the different selections of the electron identification menu 236

List of Tables

2.1 Relative strengths of the fundamental forces of nature as considered for two particles at a distance of 10^{-15} m. Included for reference is the theoretical boson responsible for meditation of the gravitational force. 28

3.1 The measured branching ratios of the W-boson decay channels. 54

5.1 Design event rates and processing times compared to the 8 TeV rates for the ATLAS detector. 83

6.1 Summary of MC simulation tools used in this analysis and their key features. . 86
6.2 Working Points for the MV1(c) tagger as calibrated at ATLAS for Run 1 collisions at $\sqrt{s} = 8$ TeV. 95
6.3 Performance of the SMT and MV1 b-tagging algorithms, including their combination, using the 85% MV1 working point. Performance measured on $t\bar{t}$ MC for $\sqrt{s} = 8$ TeV, for events which pass the pretag selection discussed in Section 8 98

7.1 List of the η ranges used in binning the scale factor and their respective names. 107
7.2 Data/Monte Carlo Scale Factors for 2012 Data in all five regions of the detector as a function of p_{T}, separated by probe charge. The uncertainties include systematic and statistical components 111
7.3 Summary of SMT mistag rate and Data/MC scale factors 117

8.1 Production fractions for b-hadrons as observed in the PYTHIA6 and HERWIG++ MC generators, compared to the RPP reference values. 120
8.2 Branching ratios for $b \to \mu$ decays as observed in the PYTHIA6 and HERWIG++ MC generators, compared to the RPP reference values. 120
8.3 Event optimisation table for events in which at least one jet is tagged by the SMT algorithm. Shown with and without E_T^{miss} and m_T^W criteria applied. No uncertainties are shown and no weights are applied to the W+jets. Yields are scaled to an integrated luminosity of 20.3 fb^{-1}. 126
8.4 Event yields in which at least one jet is tagged by the SMT algorithm combined with the MV1@70% algorithm. Shown with and without E_T^{miss} and m_T^W criteria applied. No uncertainties are shown and no weights are applied to the W+jets. Yields are scaled to an integrated luminosity of 20.3 fb^{-1}. 127

8.5 Event yields in which at least one jet is tagged by the SMT algorithm combined with the MV1@80% algorithm. Shown with and without E_T^{miss} and m_T^W criteria applied. No uncertainties are shown and no weights are applied to the W+jets. Yields are scaled to an integrated luminosity of 20.3 fb^{-1}. 128
8.6 Event yields in which at least one jet is tagged by the SMT algorithm combined with the MV1@85% algorithm. Shown with and without E_T^{miss} and m_T^W criteria applied. No uncertainties are shown and no weights are applied to the W+jets. Yields are scaled to an integrated luminosity of 20.3 fb^{-1}. 129
8.7 Event yields in which at least one jet is tagged by the SMT algorithm combined with the MV1c@70% algorithm. Shown with and without E_T^{miss} and m_T^W criteria applied. No uncertainties are shown and no weights are applied to the W+jets. Yields are scaled to an integrated luminosity of 20.3 fb^{-1}. 130
8.8 Event yields in which at least one jet is tagged by the SMT algorithm combined with the MV1c@80% algorithm. Shown with and without E_T^{miss} and m_T^W criteria applied. No uncertainties are shown and no weights are applied to the W+jets. Yields are scaled to an integrated luminosity of 20.3 fb^{-1}. 131
8.9 Event optimisation summary table for all event selections considered. The magnitude of the uncertainty on values of the signal significance in the first column is $\sigma_{\text{signif}} \sim 0.5$, the uncertainty on the values of the background fraction in the second column is $\sigma_{\text{bkgFrac}} \sim 0.002$, the uncertainty on the values of the proxy for the statistical uncertainty in the third column is $\sigma_{\text{statProxy}} \sim 10^{-5}$. 131
8.10 Relative percentage of charged lepton production in MC for each W+jets background following a l+jets selection in the e+jets channel. Separated by N-jet bins. 134
8.11 Relative percentage of charged lepton production in MC for each W+jets background following a l+jets selection in the μ+jets channel. Separated by N-jet bins. 135
8.12 Scale factors K_i for each b-tagging option for the 2-jet exclusive region 136
8.13 Flavour fractions f_i for each b-tagging option for the 4-jet inclusive region . . . 137
8.14 Flavour fractions f_i for each b-tagging option for the 4-jet inclusive region . . . 138
8.15 Scale factors K_i for each b-tagging option for the 2-jet exclusive region 138

9.1 Theoretical cross sections for single-top at $\sqrt{s} = 8$TeV at the LHC. The numbers in parentheses detail the expected relative amount of t and $\bar{t}$ predicted for each single top channel. 153
9.2 Single-top t-channel production asymmetry systematic variations, with relative top and anti-top cross-sections determined in MC. 153
9.3 Single-top s-channel production asymmetry systematic variations, with relative top and anti-top cross-sections determined in MC. 153

10.1 $t\bar{t}$ background composition of e+jets same-top like events, rounded to the nearest integer. The percentage MC statistical uncertainty is given in parentheses. Where a percentage of zero appears in the dilepton channel, this is due to a very small number of weighted events which round to zero for one significant digit. . 162
10.2 $t\bar{t}$ background composition of e+jets different-top like events, rounded to the nearest integer. The percentage MC statistical uncertainty is given in parentheses. 162

10.3 $t\bar{t}$ background composition of μ+jets same-top like events, rounded to the nearest integer. The percentage MC statistical uncertainty is given in parentheses. Where a percentage of zero appears in the dilepton channel, this is due to a very small number of weighted events which round to zero for one significant digit. . 163
10.4 $t\bar{t}$ background composition of μ+jets different-top like events, rounded to the nearest integer. The percentage MC statistical uncertainty is given in parentheses. Where a percentage of zero appears in the dilepton channel, this is due to a very small number of weighted events which round to zero for one significant digit 163
10.5 Overview of the nominal KLFitter configuration. 164
10.6 Performance of the KLFitter using the nominal configuration, in the e+jets channel. The MC statistical uncertainty is ~ 0.002. 165
10.7 Performance of the KLFitter using the nominal configuration, with the combined e+jets and μ+jets channels, with ST and DT also combined. The MC statistical uncertainty is ~ 0.001 165
10.8 Purity of the KLFitter selection broken down by true decay chain in the e+jets channel 166
10.9 Yields broken down by true decay chain, in the e+jets channel 166
10.10 Purity of the KLFitter selection broken down by decay chain in the e+jets channel, after applying semileptonic corrections to the SMT tagged jets 168
10.11 Performance of the KLFitter using the nominal configuration with semileptonic jet corrections in the e+jets channel. The MC statistical uncertainty is ~ 0.002 . 168
10.12 Performance of the KLFitter using the nominal configuration with semileptonic jet corrections, with the combined e+jets and μ+jets channels, with ST and DT also combined. The MC statistical uncertainty is ~ 0.001 168
10.13 Performance of the KLFitter using the nominal configuration with SMT tagging only, in the e+jets channel. The MC statistical uncertainty is ~ 0.002 175
10.14 Performance of the KLFitter using the nominal configuration with SMT tagging only, with the combined e+jets and μ+jets channels, with ST and DT also combined. The MC statistical uncertainty is ~ 0.001 175
10.15 Performance of the KLFitter using the nominal configuration with SMT and MV1@70% tagging, in the e+jets channel. The MC statistical uncertainty is ~ 0.002 175
10.16 Performance of the KLFitter using the nominal configuration with SMT and MV1@70% tagging, with the combined e+jets and μ+jets channels, with ST and DT also combined. The MC statistical uncertainty is ~ 0.001 176
10.17 Performance of the KLFitter using the nominal configuration with SMT and MV1@80% tagging, in the e+jets channel. The MC statistical uncertainty is ~ 0.002 176
10.18 Performance of the KLFitter using the nominal configuration with SMT and MV1@80% tagging, with the combined e+jets and μ+jets channels, with ST and DT also combined. The MC statistical uncertainty is ~ 0.001 176
10.19 Performance of the KLFitter using the nominal configuration with SMT and MV1c@70% tagging, in the e+jets channel. The MC statistical uncertainty is ~ 0.002 176
10.20 Performance of the KLFitter using the nominal configuration with SMT and MV1c@70% tagging, with the combined e+jets and μ+jets channels, with ST and DT also combined. The MC statistical uncertainty is ~ 0.001 177

10.21 Performance of the KLFitter using the nominal configuration with SMT and MV1c@80% tagging, in the e+jets channel. The MC statistical uncertainty is ~ 0.002 177
10.22 Performance of the KLFitter using the nominal configuration with SMT and MV1c@80% tagging, with the combined e+jets and μ+jets channels, with ST and DT also combined. The MC statistical uncertainty is ~ 0.001 177
10.23 Summary of performance of the KLFitter for different b-tagging combinations . 177
10.24 Performance of the KLFitter using the nominal configuration permutations of the five highest p_T jets, in the e+jets channel. The MC statistical uncertainty is ~ 0.002 178
10.25 Performance of the KLFitter using the nominal configuration with permutations of the five highest p_T jets, with the combined e+jets and μ+jets channels, with ST and DT also combined. The MC statistical uncertainty is ~ 0.001 178
10.26 Performance of the KLFitter using the nominal configuration with permutations of the six highest p_T jets, in the e+jets channel. The MC statistical uncertainty is ~ 0.002 179
10.27 Performance of the KLFitter using the nominal configuration with permutations of the six highest p_T jets, with the combined e+jets and μ+jets channels, with ST and DT also combined. The MC statistical uncertainty is ~ 0.001 179
10.28 Performance of the KLFitter using the nominal configuration with permutations of the seven highest p_T jets, in the e+jets channel. The MC statistical uncertainty is ~ 0.002 179
10.29 Performance of the KLFitter using the nominal configuration with permutations of the seven highest p_T jets, with the combined e+jets and μ+jets channels, with ST and DT also combined. The MC statistical uncertainty is ~ 0.001 179
10.30 Performance of the KLFitter using the nominal configuration with permutations of the eight highest p_T jets, in the e+jets channel. The MC statistical uncertainty is ~ 0.002 180
10.31 Performance of the KLFitter using the nominal configuration with permutations of the eight highest p_T jets, with the combined e+jets and μ+jets channels, with ST and DT also combined. The MC statistical uncertainty is ~ 0.001 180
10.32 Summary of performance of the KLFitter for different jet multiplicity permutations 180
10.33 Performance of the KLFitter using the nominal configuration with jet priority set to PtPAdv, in the e+jets channel. The MC statistical uncertainty is ~ 0.002 . 182
10.34 Performance of the KLFitter using the nominal configuration with jet priority set to PtPAdv, with the combined e+jets and μ+jets channels, with ST and DT also combined. The MC statistical uncertainty is ~ 0.001 182
10.35 Performance of the KLFitter using the nominal configuration with jet priority set to bTagP, in the e+jets channel. The MC statistical uncertainty is ~ 0.002 . 182
10.36 Performance of the KLFitter using the nominal configuration with jet priority set to bTagP, with the combined e+jets and μ+jets channels, with ST and DT also combined. The MC statistical uncertainty is ~ 0.001 182
10.37 Performance of the KLFitter using the nominal configuration with jet priority set to bTagPAdv, in the e+jets channel. The MC statistical uncertainty is ~ 0.002 183
10.38 Performance of the KLFitter using the nominal configuration with jet priority set to bTagPAdv, with the combined e+jets and μ+jets channels, with ST and DT also combined. The MC statistical uncertainty is ~ 0.001 183

10.39 Performance of the KLFitter using the nominal configuration with permutations of up to five jets and jet priority set to PtPAdv, in the e+jets channel. The MC statistical uncertainty is ~ 0.002 . . . 183
10.40 Performance of the KLFitter using the nominal configuration with permutations of up to five jets and jet priority set to PtPAdv, with the combined e+jets and μ+jets channels, with ST and DT also combined. The MC statistical uncertainty is ~ 0.001 . . . 183
10.41 Performance of the KLFitter using the nominal configuration with permutations of up to five jets and jet priority set to bTagP, in the e+jets channel. The MC statistical uncertainty is ~ 0.002 . . . 184
10.42 Performance of the KLFitter using the nominal configuration with permutations of up to five jets and jet priority set to bTagP, with the combined e+jets and μ+jets channels, with ST and DT also combined. The MC statistical uncertainty is ~ 0.001 . . . 184
10.43 Performance of the KLFitter using the nominal configuration with permutations of up to five jets and jet priority set to bTagPAdv, in the e+jets channel. The MC statistical uncertainty is ~ 0.002 . . . 184
10.44 Performance of the KLFitter using the nominal configuration with permutations of up to five jets and jet priority set to bTagPAdv, with the combined e+jets and μ+jets channels, with ST and DT also combined. The MC statistical uncertainty is ~ 0.001 . . . 184
10.45 Performance of the KLFitter using the nominal configuration with removal of the fixed top-quark mass constraint, in the e+jets channel. The MC statistical uncertainty is ~ 0.002 . . . 186
10.46 Performance of the KLFitter using the nominal configuration with removal of the fixed top-quark mass constraint, with the combined e+jets and μ+jets channels, with ST and DT also combined. The MC statistical uncertainty is ~ 0.001 . . . 187
10.47 Performance of the KLFitter using the nominal configuration with the angular likelihood in the e+jets channel. The MC statistical uncertainty is ~ 0.002 . . . 187
10.48 Performance of the KLFitter using the nominal configuration with the angular likelihood, with the combined e+jets and μ+jets channels, with ST and DT also combined. The MC statistical uncertainty is ~ 0.001 . . . 188
10.49 Performance of the KLFitter using the optimised configuration, with averaged likelihood calculations, in the e+jets channel. The MC statistical uncertainty is ~ 0.002 . . . 189
10.50 Performance of the KLFitter using the optimised configuration, with averaged likelihood calculations, with the combined e+jets and μ+jets channels, with ST and DT also combined. The MC statistical uncertainty is ~ 0.001 . . . 189
10.51 Performance of the KLFitter using the optimised configuration, with dominant likelihood selection, in the e+jets channel. The MC statistical uncertainty is ~ 0.002 . . . 190
10.52 Performance of the KLFitter using the optimised configuration, with dominant likelihood selection, with the combined e+jets and μ+jets channels, with ST and DT also combined. The MC statistical uncertainty is ~ 0.001 . . . 190
10.53 Performance of the KLFitter using the optimised configuration, with rejection of the lowest likelihood decision, in the e+jets channel. The MC statistical uncertainty is ~ 0.002 . . . 191

10.54 Performance of the KLFitter using the optimised configuration, with rejection of the lowest likelihood decision, with the combined e+jets and μ+jets channels, with ST and DT also combined. The MC statistical uncertainty is ~ 0.001 . . . 191
10.55 Overview of the optimised KLFitter configuration 194
10.56 Performance of the KLFitter using the optimised configuration, in the e+jets channel. The MC statistical uncertainty is ~ 0.002 194
10.57 Performance of the KLFitter using the optimised configuration, with the combined e+jets and μ+jets channels, with ST and DT also combined. The MC statistical uncertainty is ~ 0.001 194

11.1 Data / MC scale factor for the e/μ ratio, $\varepsilon_{e/\mu}$ 198
11.2 Acceptance for the combination of the e+jets and μ+jets channels, with ST and DT combined also. Uncertainties are given as a percentage of the nominal value. 200
11.3 Response matrix for the combined e+Jets and μ+Jets channels, with ST and DT also combined. The MC statistical uncertainty is ~ 0.001 201
11.4 Efficiency for the combination of the e+jets and μ+jets channels, with ST and DT combined also. Uncertainties are given as a percentage of the nominal value. 203
11.5 Bias of the response matrix on the truth-level charge asymmetry A^{ss} (prior to efficiency factors), for the unregularised matrix inversion (UMI) and interative bayes algorithms (IB4, IB8 with four and eight iterations respectively) for MC samples reweighted to have different fiducial truth-level same-sign charge asymmetries A^{ss}. The first value in each column is the raw bias, the value in parentheses is the bias as a percentage of the truth-level A^{ss}. Note, the leftmost column gives the fiducial charge asymmetries for the whole sample, without the reduction of events by the efficiency factors, which will change the observed asymmetry. The percentages in parentheses are percentages of the observed charge asymmetry when the efficiency factors are applied to the whole sample (not shown). 206
11.6 Bias of the response matrix on the truth-level charge asymmetry A^{os} (prior to efficiency factors), for the unregularised matrix inversion (UMI) and interative bayes algorithms (IB4, IB8 with four and eight iterations respectively) for MC samples reweighted to have different fiducial truth-level opposite-sign charge asymmetries A^{os}. The first value in each column is the raw bias, the value in parenthesesis the bias as a percentage of the truth-level A^{os}. Note, the leftmost column gives the fiducial charge asymmetries for the whole sample, without the reduction of events by the efficiency factors, which will change the observed asymmetry. The percentages in parentheses are percentages of the observed charge asymmetry when the efficiency factors are applied to the whole sample (not shown). 207
11.7 Bias of the response matrix on the fiducial truth-level charge asymmetry A^{ss} (after efficiency factors), for the unregularised matrix inversion (UMI) and interative bayes algorithms (IB4, IB8 with four and eight iterations respectively) for MC samples reweighted to have different fiducial truth-level same-sign charge asymmetries A^{ss}. The first value in each column is the raw bias, the value in parenthesesis the bias as a percentage of the fiducial truth-level A^{ss}. 207

11.8 Bias of the response matrix on the fiducial truth-level charge asymmetry A^{os} (after efficiency factors), for the unregularised matrix inversion (UMI) and interative bayes algorithms (IB4, IB8 with four and eight iterations respectively) for MC samples reweighted to have different fiducial truth-level opposite-sign charge asymmetries A^{os}. The first value in each column is the raw bias, the value in parenthesesis the bias as a percentage of the fiducial truth-level A^{ss}. 208
11.9 Pulls on the charge asymmetrys calculated after 5000 MC toys, for three different matrix inversion techniques. 209

12.1 Measurements of $\sigma_{t\bar{t}}$ for the e+jets, μ+jets and combined ℓ+jets channels, with systematic uncertainties in percentage. 214
12.2 Summary of all $\sqrt{s} = 8$TeV $\sigma_{t\bar{t}}$ measurements and the theoretical prediction. . . 215
12.3 Measurements A^{ss} and A^{os}, in units of 10^{-2}, and breakdown of absolute uncertainties. 216
12.4 The diagonal components of response matrices generated by the nominal and systematically altered MC samples. The numbers in brackets are the raw differences between the nominal values and the systematic values in each bin. 217
12.5 The diagonal components of the nominal response matrix with a measure of the total systematic uncertainty. The subsequent rows show the contributions (to be added in quadrature across all systematics) of individual systematic uncertainties. The largest uncertainties on the response matrix (the largest modifiers to the KLFitter performance) align with the largest uncertainties on the measured charge and CP asymmetries. 217
12.6 Decay-chain fractions obtained from MC simulation at the particle level. Uncertainties are in percent. 219
12.7 Measurements of A^{b}_{mix}, $A^{b\ell}_{\mathrm{dir}}$, $A^{c\ell}_{\mathrm{dir}}$ and A^{bc}_{dir}, in units of 10^{-2}, and breakdown of absolute uncertainties. 221
12.8 Comparison of measurements of charge asymmetries and constraints on CP asymmetries, with MC simulation (detailed in the text), existing experimental limits and SM predictions. 222

13.1 Predictions for the uncertainties on a repeated analysis using 100 fb^{-1} of Run 2 LHC data at a collision energy of $\sqrt{s} = 13$ TeV. 227
13.2 Decay chain fractions as determined using the nominal $t\bar{t}$ MC for different fiducial volumes, varied by selection on transverse momenta of the soft muon and of the jets. 228

C.1 Definitions of the electron discriminating variables 237

Do. Or do not. There is no try

Yoda

Chapter 1

Introduction

This thesis describes an analysis based on data from proton-proton collisions at the ATLAS experiment [1] general purpose detector, based on the Large Hadronic Collider (LHC) [2] ring at the European Centre Nuclear Research (CERN) [3] in Geneva, Switzerland. The LHC is a high energy circular particle accelerator designed to collide protons in the centre of four detector points on the ring, for study and analysis. High energy physics analyses probe parameters of the Standard Model (SM) [4] of particle physics, to search for discrepancies in experimental observations from our present understanding of the universe. Analyses may also constrain measurements of known processes with ever-increasing precision, and search for signals of new processes, to find or constrain models of new physics.

Studies of top-quark physics are considered to be fertile ground in the search for new physics. The top quark is the most massive of all known fundamental particles and may couple to as of yet undiscovered higher energy particles and processes. The top quark is also unable to hadronise, and its decay products provide a unique opportunity to study the properties of a 'bare' quark. Properties on the top quark, such as its mass, are crucial parameters which can provide stringent tests of the SM.

Top quarks are produced in large numbers at the LHC as the centre-of-mass energy of collisions is enough to produce on-shell top quarks. The most common mechanism at the LHC is the production of top-quark pairs from gluon splitting, $g \to t\bar{t}$, which then each decay with an almost 100% branching ratio to a W-boson and a b-quark. The final state searched for in physics analyses depends on the subsequent decay of the W-boson, into a lepton and neutrino pair, or into two quarks which form hadrons. For all final states the b-quark will also hadro-

nise, leading to a collimated chain of decays forming a detectable signal called a jet. Jets which originate from b-quarks specifically are known as b-jets and their identification is crucial to the measurements of many processes. Algorithms used to identify b-jets are known as b-taggers. A particular technique, known as *soft muon tagging* (SMT) relies on the observations of a muon aligned with the b-jet, which originates from a 21% branching ratio of $b \to \mu$ process. The SMT tagger is described in detail in Section 7, where it is calibrated on $J/\psi \to \mu\mu$ decays.

In this thesis, the SMT tagger is utilised to identify soft muons in b+jets from $t\bar{t}$ decays in the lepton+jets channel. In this channel, the W-boson from one top-quark decays to a lepton and a neutrino, and the W-boson from the other top quark produces a pair of jets. In this event topology, the measurement of the charged lepton from the W-boson decay provides information about the charge of the b-quark from the same top-quark decay. This information can be combined with the charge of a soft muon produced in the subsequent decay of the b-hadron to build asymmetries sensitive to charge-parity (CP) violating effects in the heavy-flavour sector. *CP* violation implies that physical laws for matter and antimatter are different, and understanding the source and magnitude of this difference may be key to understanding the observed matter-antimatter asymmetry in the universe [5]. Existing measurements in the heavy-flavour sectors [6–16] continue to be insufficient to explain the observed cosmological asymmetry, and precision measurements of potential CP violating processes are required to search for discrepancies from the SM.

A lot of people have tried to kill me, and I'm still here

Logan

Chapter 2

The Standard Model of particles physics

The Standard Model of Particle Physics (SM) [4] is the culmination of knowledge regarding the fundamental constituents of our universe and its interactions. Its development has proceeded through both theoretical and experimental exploration and is considered to describe all known particles and three of the discovered fundamental forces. The SM has stood up to rigorous examination and is able to make precise predictions about our universe.The SM however is however incomplete, and this drives the field of particle physics research to continue to search for answers. In the context of this thesis, the most notable deficiency in the SM is the prediction for the relative yields of matter and antimatter in our universe (see Section 2.5.2). A naïve study of the Big Bang would suggest that matter and antimatter should have been produced and destroyed in equal numbers, which would continue to be the case in the modern universe. However, an asymmetry of the order 10^{-9} is actually observed [5]. Charge-parity (*CP*) violating processes (along with other effects) can go some way towards an explanation, but current measurements of *CP* violation known to be allowed within the SM are insufficient by several orders of magnitude to produce the required effect, this is discussed further in Section 2.6.6. Experiments continue make precise measurements of *CP* violating decays to find discrepancies which might lead help develop new theories to go beyond the standard model (BSM). The work in this chapter is based on the documentation in [4], [17] and [18].

2.1 Elementary particles

The SM describes the existence of 12 spin-half particles (plus their antiparticles) and their interactions via unitary-spin particles. These particles are summarised in Figure 2.1 [19] below. Each particle is uniquely defined by its properties and quantum numbers, such as its mass m, charge q and spin S. Spin-half particles (e.g. $S = \frac{1}{2}, \frac{3}{2}, ...$) are called *fermions*, and 12 exist within the current framework. The first six are *leptons*, three of which carry unitary electric charge (electron e, muon μ and tau τ), and 3 of which carry zero electric charge (electron-neutrino ν_e, muon-neutrino ν_μ, tau-neutrino ν_τ). These 6 leptons are separated into doublets by the increasing mass of those with unitary charge, they therefore exist as three generations of leptons. The second 6 fermions are known as *quarks*. Quarks are analogously separated by mass into three generations. The first generation doublet consists of the up (u) and down (d) quarks, the second of the charm (c) and strange (s) quarks, and the third of the heaviest top (t) and bottom (b) quarks. In each generation, the quarks (in order) have charge of $Q_{u,c,t} = +\frac{2}{3}$ and $Q_{d,s,b} = -\frac{1}{3}$, and are hitherto known as *up-type* and *down-type* quarks respectively. The quark names are referred to as *flavours* and as such their study is often called the study of *flavour physics* (as opposed to lepton 'flavours', e,μ and τ). All fermions above are described as they exist in matter. Antimatter partners for each exist for which the electric charge, colour and weak hypercharge are reversed. This makes for a total of 24 fundamental fermions described by the SM.

2.2 Fundamental forces

The fermions described above are only known to interaction via three fundamental forces; the electromagnetic, weak (or unified electroweak, see Section 2.7), and strong, with the latter most reserved to interactions in the quark sector only. In the SM each of these forces is described as being carried (or mediated by) unitary spin particles known as *bosons*, which are also shown in Figure 2.1. Missing from this figure is the theoretical boson responsible for mediation of the gravitational force, the true mechanism for which has yet to be discovered and is not incorporated in the SM. Electromagnetic interactions proceed via the exchange of a massless photon γ, described in Section 2.3. Strong interactions proceed via the exchange of massless gluons g, described in Section 2.4. Most relevant for this thesis, the weak interaction proceeds by a neutral massive boson Z, and two charged massive bosons $W^\pm$, described in Section 2.5. Just

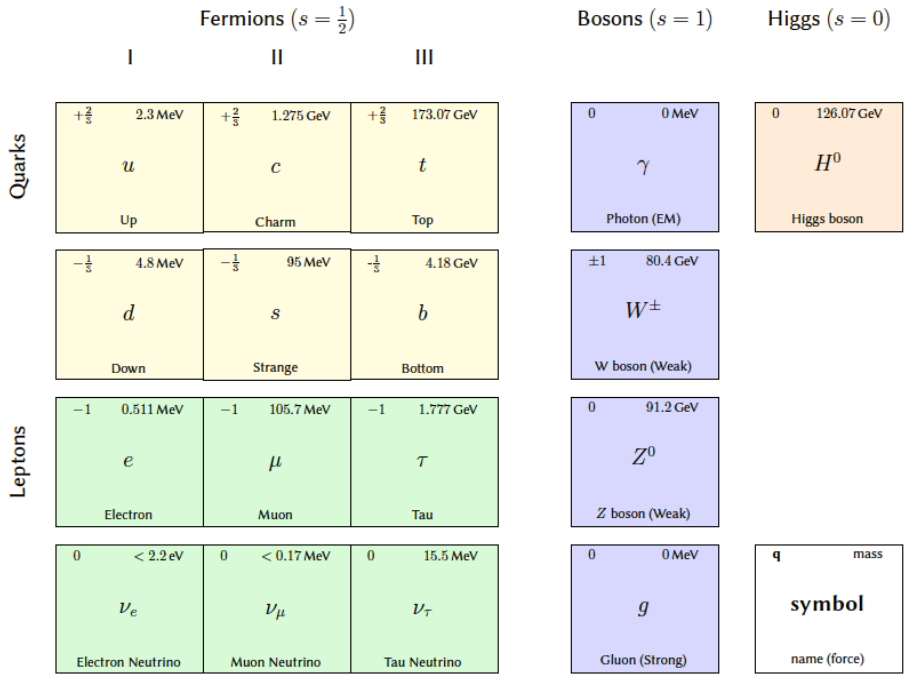

Figure 2.1: The elementary particles of the SM as classified by their properties and quantum numbers, labelled with the charge and mass of each. Also shown are the mediators of the fundamental forces, and the most recently discovered Higgs boson.

as in the case of the fermions, bosons also have antiparticle forms. The W^+ antiparticle is the W^-, the other bosons are their own antiparticles. The relative strengths of the forces are shown in Table 2.1.

Force	Strength	Boson		Spin	Mass/GeV
Strong	1	Gluon	g	1	0
Electromagnetism	10^{-3}	Photon	γ	1	0
Weak	10^{-8}	W boson	$W^{\pm}$	1	80.4
		Z boson	Z^0	1	91.2
Gravity	10^{-37}	Graviton	G	2	0

Table 2.1: Relative strengths of the fundamental forces of nature as considered for two particles at a distance of 10^{-15} m. Included for reference is the theoretical boson responsible for meditation of the gravitational force.

2.3 Quantum electrodynamics

Quantum electrodynamics (QED) describes the electromagnetic force mediated by the γ boson. This force acts upon all charged fermions, via the vertex of Figure 2.2 [19]. Conservation of electric charge is a fundamental symmetry of the SM and the electromagnetic force interacts with a coupling strength proportional to the electronic charge $g_{QED} = qe$, where q is the electric charge of the interacting particle in units of e.

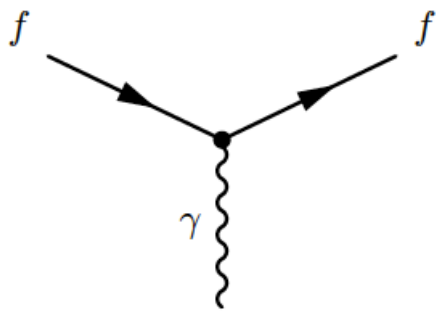

Figure 2.2: The primary vertex for QED showing the interaction between a photon and two fermions. Rotation of this vertex and replacement of the generic fermions f with appropriate particles describes all possible QED processes.

2.4 Quantum chromodynamics

Quantum chromodynamics (QCD) describes the strong force mediated by the gluon, with coupling strength g_s. This force acts upon all particles which carry a quantum *colour*, namely those in the quark sector. Colour is conserved at all strong interaction vertices and is represented by three orthogonal states:

$$\text{red}\,(r) = \begin{pmatrix} 1 \\ 0 \\ 0 \end{pmatrix}, \quad \text{green}\,(g) = \begin{pmatrix} 0 \\ 1 \\ 0 \end{pmatrix}, \quad \text{blue}\,(b) = \begin{pmatrix} 0 \\ 0 \\ 1 \end{pmatrix}. \tag{2.1}$$

Quarks are defined to carry colours (r, g, b) and anti-quarks carry anti-colours $\left(\bar{r}, \bar{g}, \bar{b}\right)$. Gluons also carry colour and are therefore capable of self-interaction. Through the conservation of colour at gluon-quark vertices, it is necessary for each gluon to carry a combination of colour and anti-colour, and therefore the gluon in SU(3) exists in a colour octet, with assignments:

$$r\bar{g},\ g\bar{r},\ r\bar{b},\ b\bar{r},\ g\bar{b},\ b\bar{g},\ \frac{1}{\sqrt{2}}\left(r\bar{r}-g\bar{g}\right) \quad \text{and} \quad \frac{1}{\sqrt{6}}\left(r\bar{r}+g\bar{g}-2b\bar{b}\right) \tag{2.2}$$

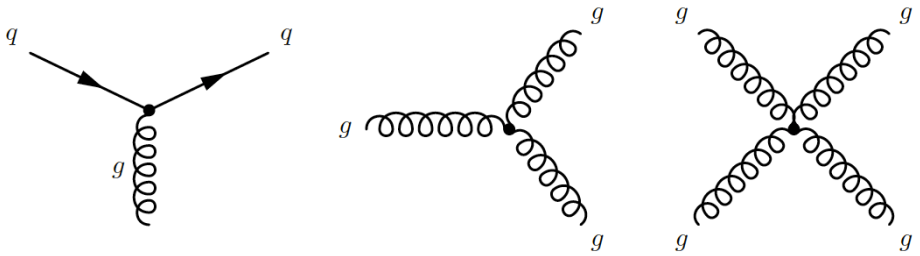

(a) Quark-gluon vertex **(b)** Three-gluon vertex **(c)** Four-gluon vertex

Figure 2.3: The primary vertices for QCD showing the interaction between a gluon and two quarks, as well as the three- and four-gluon self-interaction vertices.

Naively nine gluons would be expected from simple combinations of colour-anti-colour pairs, however this would lead to a colourless gluon which could not interact strongly. The vertices for the strong interaction are shown in Figure 2.3 [19]. The strong interaction is responsible for the binding of quarks into heavier particles known as hadrons, which are categorised as mesons ($q\bar{q}$ states) and baryons (three-quark states). More recently, experimental evidence also exists for tetraquarks (four-quark states) and pentaquarks (five-quark states) [20, 21]. Hadrons are colourless objects held together by strong interactions, which must notably be stronger than QED by several orders of magnitude to overcome the electromagnetic repulsion between similarly charged quarks. Mesons consist of a quark q and an anti-quark $\bar{q}$ as a single states $q\bar{q}$, whilst baryons can be any combination of three quarks so long as the final state remains colourless. Protons and neutrons fall into the category of some of the most well known baryons, consisting of uud and udd quark combinations respectively. Prominent examples of mesons produced at hadron colliders include the neutral pions $\pi^0\left(u\bar{u}/d\bar{d}\right)$, kaons $K^0\left(d\bar{s}/s\bar{d}\right)$ and B-mesons $B^0\left(d\bar{b}/b\bar{d}\right)$, as well as their charged alternatives.

2.5 Weak interactions

The weak interaction is mediated by three massive bosons, the neutral Z and the charged $W^{\pm}$, with coupling strength g_Z and g_W respectively. The weak force is responsible most famously for nuclear β-decay ($n \to pe^-\bar{\nu}_e$), and has considerably different behaviour in the SM compared with QED and QCD, which will be discussed in detail in this chapter. It is for example the only

known source of processes in the SM which violate the conservation of parity.

The Z boson is similar in concept to a massive γ, with the exception that it can couple to neutral fermions such as neutrinos. This allows for processes such as elastic $\nu_\mu e^-$ scattering. The other boson for the weak interaction is the W-boson. The W has unit charge and therefore must couple to fermions which are separated in charge also by one unit. This provides a mechanism for interactions between leptons and their respective neutrinos, between quarks with charges $q = \pm\frac{1}{3}$ and $q = \mp\frac{2}{3}$ respectively, between Z and W bosons themselves, and also between the γ and the W. The first three vertices are shown in Figure 2.4 [19].

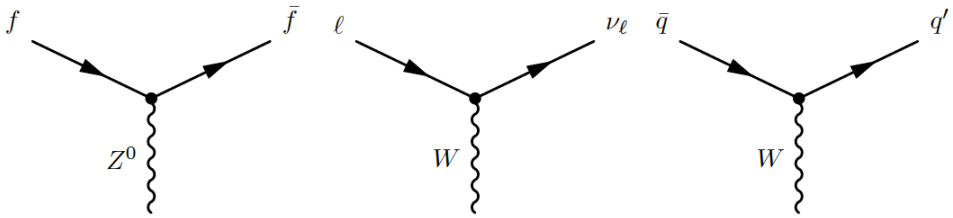

(a) Neutral vertex **(b)** Charged vertex (leptons) **(c)** Charged vertex (quarks)

Figure 2.4: The primary vertices for the weak interaction. (a) Z boson coupling to fermions, (b) W boson coupling with a lepton and a neutrino and (c) W coupling with two differently-charged quarks.

Experimental data for weak interactions with leptons is consistent with the theory of *lepton universality*, which states that after accounting for phase-space differences according to the lepton mass, the strength of the weak interaction is identical for all lepton flavours. The vertex of $e\nu_e W$ has identical form factors to $\mu\nu_\mu W$. The qW vertices are described as *flavour-changing* currents, as they have the potential to connect (or convert between) up-type and down-type quarks. Historically it was this feature which led to a long string of discoveries in flavour physics, including the prediction of the b, c and t quarks and the phenomena of neutral-meson mixing.

In order to explore the weak interactions of quarks, it is initially useful to reduce to a two-generation system. The concept of *lepton-quark symmetry (LQS)* is extremely important and drives the SM formulation which follows. LQS draws a symmetry between the lepton doublets and the quark doublets in the weak interaction, via the replacements $\nu_e \to u$, $e^- \to d$, $\nu_\mu \to c$, $\mu^- \to s$, with a weak coupling constant in all cases $g_{ud} = g_{cs} = g_W$:

$$\begin{pmatrix} \nu_e \\ e^- \end{pmatrix}, \quad \begin{pmatrix} \nu_\mu \\ \mu^- \end{pmatrix} \quad \Rightarrow \begin{pmatrix} u \\ d \end{pmatrix}, \quad \begin{pmatrix} c \\ s \end{pmatrix} \tag{2.3}$$

LQS leads to the vertices in Figure 2.5 [4]. The downfall of the basic theory of LQS came from the observation of generation-crossing interactions involving for example *usW* vertices, such as kaon decay. It was these observations which led (even before the discovery of the charm quark) to Cabibbo's hypothesis of *quark mixing*, whereby inter-generation interactions of the quark families would be permitted via a mixing angle θ_C. Otherwise forbidden vertices could then be permitted with coupling strengths modified by this angle:

$$g_{ud} = g_{cs} = g_W \cos\theta_C \tag{2.4}$$

$$g_{us} = -g_{cd} = g_W \sin\theta_C \tag{2.5}$$

Rather than interacting as mass eigenstates, the d and s are theorised to propagate instead as mass eigenstates and interact as weak eigenstates $\left(d^{'}, s^{'}\right)$, where:

$$d^{'} = d\cos\theta_C + s\sin\theta_C, \tag{2.6}$$

$$s^{'} = -d\sin\theta_C + s\cos\theta_C \tag{2.7}$$

or in matrix form:

$$\begin{pmatrix} d^{'} \\ s^{'} \end{pmatrix} = \begin{pmatrix} \cos\theta_C & \sin\theta_C \\ -\sin\theta_C & \cos\theta_C \end{pmatrix} = \begin{pmatrix} d \\ s \end{pmatrix} \tag{2.8}$$

The Cabibbo angle is a free parameter of the SM which must be measured experimentally, and was determined from the measurement of various hadronic decays to be approximately $\theta_C = 13^\circ$.

Extension to a third generation of quarks is less trivial, and described in Section 2.5.1.

2.5.1 The CKM matrix

In order to account for quark mixing in three generations, the formulation of Equation 2.8 must be extended into what has become known as the *Cabibbo-Kobayashi-Maskawa (CKM)* matrix:

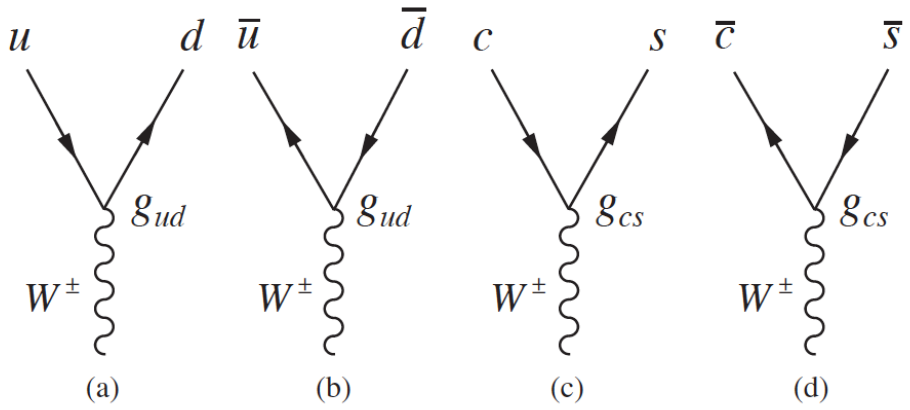

Figure 2.5: The LQS vertices for the weak interaction. (a,b) pair the W boson with the first generation quarks, (c,d) pair the W boson with the second generation quarks.

$$\begin{pmatrix} d' \\ s' \\ b' \end{pmatrix} = \begin{pmatrix} V_{ud} & V_{us} & V_{ub} \\ V_{cd} & V_{cs} & V_{cb} \\ V_{td} & V_{ts} & V_{tb} \end{pmatrix} \begin{pmatrix} d \\ s \\ b \end{pmatrix}, \tag{2.9}$$

where all required coupling constants then take the form $g_{ij} = g_W V_{ij}$, and where the entries to the CKM matrix must be determined from experiment. The probability for quark interactions is proportional to $|V_{ij}|^2$, and the near-diagonality of Equation 2.10 shows reduced likelihood for inter-generation vertices. These are referred to as being *suppressed* vertices.

$$\text{CKM} = \begin{pmatrix} 0.97425 \pm 0.00022 & 0.2253 \pm 0.0008 & 0.00413 \pm 0.00049 \\ 0.225 \pm 0.008 & 0.986 \pm 0.016 & 0.0411 \pm 0.0013 \\ 0.0084 \pm 0.0006 & 0.040 \pm 0.0027 & 1.021 \pm 0.032 \end{pmatrix} \tag{2.10}$$

2.5.2 Charge and parity operators

This section explores the phenomena of charge and parity violation in the weak interactions as part of the SM.

Charge operator

Application of a charge operator $\hat{C}$ to a quantum state takes the effect of swapping all particles q for antiparticles $\bar{q}$, i.e. their charge conjugates. Eigenstates of the charge conjugation operator

are those for which the system remains unchanged. QED and QCD interactions are invariant under charge conjugation, however the weak interaction has the potential to violate this symmetry. Consider a particle wavefunction Ψ for a neutral particle α under charge conjugation in the following notation:

$$\hat{C}\,|\alpha\Psi\rangle = C_\alpha\,|\alpha\Psi\rangle \tag{2.11}$$

Charged particles have well defined anti-particles, however neutral particles with nonzero magnetic moments such as the neutron must be carefully considered. The phase factor $\hat{C}_\alpha$ eigenvalue can be determined using the conservation of charge if the operator is applied twice, $\hat{C}_\alpha^2 = 1$. Therefore the eigenvalue must be:

$$\hat{C}_\alpha = \pm 1 \tag{2.12}$$

which is referred to as a particle's intrinsic *C-parity*. C-parities may be determined as above through the principle of charge conservation.

Two-particle states with particle-antiparticle pairs $(a, \bar{a})$ can also form eigenstates of the $\hat{C}$ operator.

$$\hat{C}\,|a\Psi_1, \bar{a}\Psi_2\rangle = |\bar{a}\Psi_1, a\Psi_2\rangle = \pm\,|a\Psi_1, \bar{a}\Psi_2\rangle \tag{2.13}$$

With proper treatment, the orbital angular momentum (L) of the pair of particles must be considered during charge conjugation, as interchanging particle with antiparticle will reverse their relative positions, and this is true for hadrons and fermions alike. Furthermore, when accounting for the interchanging of particles in the spin (S) wave functions, the eigenvalues for a charge conjugated two-particle state are:

$$\hat{C}\,|a\bar{a}; J, L, S\rangle = (-1)^{L+S}\,|a\bar{a}; J, L, S\rangle \tag{2.14}$$

Parity operator

Analogous to the concept of charge conjugation which swaps particles and their antiparticles, the Parity operator $\hat{P}$ reverse all space-like dimensions of a system:

$$\mathbf{r}_i \rightarrow \mathbf{r}_i^{'} = -\mathbf{r}_i \tag{2.15}$$

Parity is conserved by QED and QCD, but is maximally violated by the weak interaction, discussed in Section 2.5.3.

Consider a single particle wavefunction $\psi(\mathbf{r},t)$, the parity operator has the effect:

$$\hat{P}\psi(\mathbf{r},t) = P_a\psi(-\mathbf{r},t) \tag{2.16}$$

$$\hat{P}^2\psi(\mathbf{r},t) = P_a^2\psi(\mathbf{r},t) \tag{2.17}$$

$$P_a = \pm 1 \tag{2.18}$$

For particles at rest, the eigenvalue P_a is known as the *intrinsic parity*, and again must be equal to ± 1 in order to return a system to its nominal state after two successive parity operations. Electron scattering experiments are able to determine the product $P_{e^+}P_{e^-} = -1$, however in electromagnetic interactions electrons are never produced or destroyed by themselves, this means that cancellations between parity factors always occur and so the unique parity P_{e^-} cannot be determined. A convention is taken to define all fermion parities as positive unity, and all antifermion parities as negative unity:

$$P_f = P_q = 1 \tag{2.19}$$

$$P_{\bar{f}} = P_{\bar{q}} = -1 \tag{2.20}$$

Moving to two-particle states, and taking into account orbital angular momentum again (which has direction and is affected by parity conjugation), the intrinsic parity of a meson $M = a\bar{b}$ is then:

$$\hat{P}\left|a\bar{b}\right\rangle = P_a P_{\bar{b}} (-1)^L \left|a\bar{b}\right\rangle = P_M \left|a\bar{b}\right\rangle \tag{2.21}$$

$$P_M = P_a P_{\bar{b}} (-1)^L = (-1)^{L+1} \tag{2.22}$$

2.5.3 *CP* violation and neutral meson-mixing

CP violation in the SM comes about as a result of the structure of the weak interaction, which is outside the scope of this thesis. In short however, five forms of interaction are possible within the SM to represent the bosons whilst maintaining Lorentz-invariance, these are *scalar*, *pseudoscalar*, *vector*, *axial vector* and *tensor*, named to reflect their individual ranks and intrinsic parities. To explain parity violation in particular, the weak interaction propagates as a linear combination of the vector and axial vector type currents, to form the so called $V-A$ structure. As the vector and axial vector currents are of the same rank but have opposing intrinsic parities, application of $\hat{P}$ on weak interactions is able to violate parity conservation. The violation of combined *CP* invariance was first discovered in the decays of neutral kaons. Neutral mesons such as the K^0 and B^0 have the freedom to *mix* with their antiparticles due to the weak interactions permitted by the CKM matrix. This means that as a neutral meson propagates, it will oscillate between its particle and antiparticle state via Feynman diagrams such as that in Figure 2.6 [4].

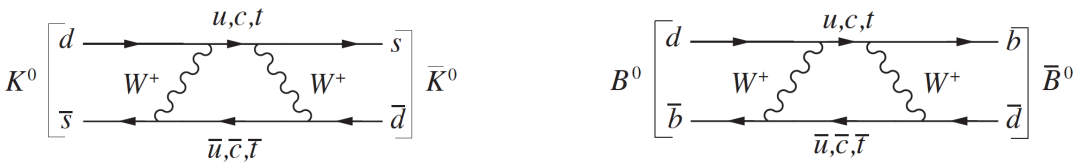

Figure 2.6: Neutral meson mixing in the SM via the weak interaction. (a) converts between the neutral K^0 and $\bar{K}^0$ states, (b) converts between the neutral B_d^0 and $\bar{B}_d^0$ states.

Neutral kaon mixing

Historically, neutral meson mixing was first observed in the kaon system. As this particle-antiparticle oscillation is possible, it means that the kaon must be considered to propagate as *CP* eigenstates in the form of a superposition of its mass eigenstates:

$$K_1 = \frac{1}{\sqrt{2}}\left(K^0 + \bar{K}^0\right), \tag{2.23}$$

$$K_2 = \frac{1}{\sqrt{2}}\left(K^0 - \bar{K}^0\right). \tag{2.24}$$

Since experimentally two kaons are observed with separate lifetimes, the K-short (K_S) and the K-long (K_L), and as kaons decay almost exclusively to either two- or three-pion states, comparing the intrinsic charge-parities arguments below initially led to the belief that $K_1 = K_S$ and $K_2 = K_L$, as the two-pion states and the K_1 stay have positive instrinsic CP and the three-ption states and the K_2 have negative instrinsic parity.

$$\hat{C}\hat{P}|K_1\rangle = +|K_1\rangle \quad \text{and} \quad \hat{C}\hat{P}|K_2\rangle = -|K_2\rangle \tag{2.25}$$

$$\hat{C}\hat{P}\left|\pi^0\pi^0\right\rangle = +\left|\pi^0\pi^0\right\rangle \quad \text{and} \quad \hat{C}\hat{P}\left|\pi^+\pi^-\right\rangle = +\left|\pi^+\pi^-\right\rangle \tag{2.26}$$

$$\hat{C}\hat{P}\left|\pi^0\pi^0\pi^0\right\rangle = -\left|\pi^0\pi^0\pi^0\right\rangle \quad \text{and} \quad \hat{C}\hat{P}\left|\pi^+\pi^-\pi^0\right\rangle = -\left|\pi^+\pi^-\pi^0\right\rangle \tag{2.27}$$

Assuming CP invariance the K_S should be responsible for the two-pion final states (and forbidden from producing three-pions) and the K_L should be responsible for the three-pion final states (and forbidden from producing two-pions). However, an experiment to study the decays of a pure K_L beam found two-pion contributions, which violate the CP symmetry, albeit by a very small amount [22]. This leads to the reformulation of the kaon system to instead describe the $K_{S,L}$ as linear combinations of $K_{1,2}$, with a small complex parameter ε introduced to allow for CP violating effects:

$$|K_S\rangle = \frac{1}{\sqrt{1+|\varepsilon|^2}}\left(|K_1\rangle + \varepsilon|K_2\rangle\right), \tag{2.28}$$

$$|K_L\rangle = \frac{1}{\{\sqrt{1+|\varepsilon|^2}}\left(|K_2\rangle + \varepsilon|K_1\rangle\right). \tag{2.29}$$

CP violation is then incorporated in two ways, in the context of the pure K_L beam experiment:

1. *Mixing*; The K_L interacts via its *CP*-forbidden component K_1 which then decays in a *CP*-conserving manner. $\left(\Gamma\left(A \to \bar{A} \to \bar{X}\right) \neq \Gamma\left(\bar{A} \to A \to X\right)\right)$.

2. *Direct*; The K_L interacts via its *CP*-conserving component K_2 which then decays in a *CP*-violating manner. $\left(\Gamma\left(A \to X\right) \neq \Gamma\left(\bar{A} \to \bar{X}\right)\right)$.

The relative strength of the direct CP violation may be parameterised by $\varepsilon' = \Gamma\left(K_2 \to \pi\pi\right)/\Gamma\left(K_2 \to \pi\pi\pi\right)$, which has been measured at NA48, CERN [23] to be

$$\mathrm{Re}\left(\frac{\varepsilon'}{\varepsilon}\right) = (1.47 \pm 2.2) \times 10^{-3} \quad . \tag{2.30}$$

As neutral kaons are able to mix the time evolution of a neutral kaon state is

$$\left|K\left(t\right)\right\rangle = a\left(t\right)\left|K^0\right\rangle + b\left(t\right)\left|\bar{K}^0\right\rangle, \tag{2.31}$$

where $a\left(t\right)$ and $b\left(t\right)$ are the amplitudes and phases of the K^0 and $\bar{K}^0$ components. These give the coupled time evolution equations and effective Hamiltonion

$$\begin{pmatrix} M_{11} - \frac{i}{2}\Gamma_{11} & M_{12} - \frac{i}{2}\Gamma_{12} \\ M_{21} - \frac{i}{2}\Gamma_{21} & M_{22} - \frac{i}{2}\Gamma_{22} \end{pmatrix} = \begin{pmatrix} a\left(t\right)\left|K^0\right\rangle \\ b\left(t\right)\left|\bar{K}^0\right\rangle \end{pmatrix} = i\frac{\partial}{\partial t}\begin{pmatrix} a\left(t\right)\left|K^0\right\rangle \\ b\left(t\right)\left|\bar{K}^0\right\rangle \end{pmatrix}, \tag{2.32}$$

$$\mathcal{H} = \mathbf{M} - \frac{i}{2}\Gamma = \begin{pmatrix} M & M_{12} \\ M_{12}^* & M \end{pmatrix} - \frac{i}{2}\begin{pmatrix} \Gamma & \Gamma_{12} & \Gamma_{12}^* & \Gamma \end{pmatrix} \tag{2.33}$$

where from the CPT theorem $M = M_{11} = M_{22}$, $\Gamma = \Gamma_{11} = \Gamma_{22}$.
The solutions for $a\left(t\right)$ and $b\left(t\right)$ are typically found by solving the eigenvalue equation of the form

$$\begin{pmatrix} M - \frac{i}{2}\Gamma & M_{12} - \frac{i}{2}\Gamma_{12} \\ M_{12}^* - \frac{i}{2}\Gamma_{21}^* & M - \frac{i}{2}\Gamma \end{pmatrix}\begin{pmatrix} p \\ q \end{pmatrix} = \lambda\begin{pmatrix} p \\ q \end{pmatrix}. \tag{2.34}$$

This yields solutions

$$\frac{q}{p} = \pm\xi = \pm\left(\frac{M_{12}^{*} - \frac{i}{2}\Gamma_{12}^{*}}{M_{12} - \frac{i}{2}\Gamma_{12}}\right)^{\frac{1}{2}}, \tag{2.35}$$

where ξ is eventually found to be a measure of the CP-violating effects, $|\xi| = \frac{1-\varepsilon}{1+\varepsilon}$.
The final time-dependent equations for the physiccal K_S and K_L states are

$$|K_S(t)\rangle = \frac{1}{\sqrt{2(1+|\varepsilon|^2)}}\left[(1+\varepsilon)\left|K^0\right\rangle + (1-\varepsilon)\left|\bar{K}^0\right\rangle\right] e^{-i\lambda_S t}, \tag{2.36}$$

$$|K_L(t)\rangle = \frac{1}{\sqrt{2(1+|\varepsilon|^2)}}\left[(1+\varepsilon)\left|K^0\right\rangle + (1-\varepsilon)\left|\bar{K}^0\right\rangle\right] e^{-i\lambda_L t} \tag{2.37}$$

where $\lambda_{S,L} = m_{S,L} - \frac{i/2}{\Gamma}_{S,L}$, and $m_{S,L}, \Gamma_{S,L}$ are eigenvalues related to the difference in mass and width between the two physical states, and equivalently

$$|K_S(t)\rangle = \frac{1}{\sqrt{1+|\varepsilon|^2}}\left[|K_1\rangle + \varepsilon|K_2\rangle\right] e^{-i\lambda_S t}, \tag{2.38}$$

$$|K_L(t)\rangle = \frac{1}{\sqrt{1+|\varepsilon|^2}}\left[|K_2\rangle + \varepsilon|K_1\rangle\right] e^{-i\lambda_S t} \tag{2.39}$$

Neutral B mixing

Analogous to neutral kaon mixing, CP violation is also been observed in the oscillations for heavy neutral mesons such as the B^0 and D^0, which are most relevant to this thesis. The B-mesons are categorised by the subsequent partner quark to the b, which affects the CKM matrix elements involved in the oscillation diagrams. Neutral B mesons with a down-component are labelled $B_d^0\left(\bar{b}d\right)$, and with a strange-component are labelled $B_s^0\left(b\bar{s}\right)$. For the remainder of this section, the label B^0 shall be used to refer to both inclusively. Instead of the short- and long-lived particles of the kaon system, the B-system is described by a light- and heavy-mesons, B_L^0 and B_H^0 respectively, which have comparable lifetimes and a very small difference in mass Δm_d which provides a useful variable in the determination of factors in the CKM matrix.

Like the kaon system, the B-meson decays are sensitive to a third type of CP violation due to interference between decays which share a common final state, where one B-decay requires

mixing and the other does not, $B^0 \to X$ vs. $B^0 \to \bar{B}^0 \to X$.

Experimentally, CP violation in B-mesons is accessible by construction of CP-sensitive asymmetries. Using the notation above a CP violation sensitive asymmetry can be defined for direct $B \to X$ decays:

$$A^b_{\text{dir}} = \frac{\mathbf{P}\left(B^0 \to X\right) - \mathbf{P}\left(\bar{B}^0 \to \bar{X}\right)}{\mathbf{P}\left(B^0 \to X\right) + \mathbf{P}\left(\bar{B}^0 \to \bar{X}\right)} \tag{2.40}$$

where $\mathbf{P}\left(B^0 \to X\right)$ denotes the inclusive probability of a B^0 meson decaying to a final state X, and is most commonly assessed via the decay width $\Gamma\left(B^0 \to X\right)$. It is with this sort of asymmetry that this thesis is concerned.

2.6 B-physics and CP violation with time-integrated analyses

In the B-meson system the mass and flavour eigenstates are distinct, and are not equivalent to CP eigenstates (although the CP and mass eigenstates are nearly identical in the neutral B-meson system). The neutral flavour eigenstates, which are most useful for describing particle production and decay are $B^0_d = \bar{b}d$ and $\bar{B}^0_d = \bar{d}b$ (with an equivalent B^0_s definition). Each particle propagates as a mass eigenstate (either a heavy B_H or light B_L) governed by a time-dependent Schrödinger equation:

$$|B_L\rangle = p\left|B^0\right\rangle + q\left|\bar{B}^0\right\rangle, \qquad |B_H\rangle = p\left|B^0\right\rangle - q\left|\bar{B}^0\right\rangle, \tag{2.41}$$

$$i\frac{d}{dt}\begin{pmatrix} p \\ q \end{pmatrix} = \left(M - \frac{i}{2}\Gamma\right)\begin{pmatrix} p \\ q \end{pmatrix}. \tag{2.42}$$

where p and q are complex coefficients, and B_H and B_L are seen to have a mass difference Δm_B and width difference $\Delta\Gamma$ and where it is expected that $\Delta\Gamma \ll \Delta m_B$. During the lifetime of a neutral B-meson, the particle wavefunction oscillates between the B^0 and $\bar{B}^0$, via the box diagram in Figure 2.6. The complex coefficients have phases which are unique to the weak sector in the SM, appearing only in the CKM matrix. These are referred to as *weak phases*, and open the possibility for CP violation. Other phases, which do not violate CP, are also present and these are referred to as *strong phases*. In each case, only phase differences between multiple terms within a decay amplitude are important, not the phase of any individual term itself as

this is convention-dependent. For a particle decay amplitude (such as A_f for $B^0 \to f$, or its CP conjugate) it is possible to write down three parts; the magnitude A_i, the weak phase $e^{i\phi_i}$ and the strong phase $e^{i\delta_i}$, such that for multiple contributing terms

$$A_f = \sum_i A_i e^{i(\delta_i+\phi_i)}, \tag{2.43}$$

$$\bar{A}_{\bar{f}} = e^{2i\left(\zeta_f-\zeta_B\right)} \sum_i A_i e^{i(\delta_i-\phi_i)}, \tag{2.44}$$

where ζ_B and ζ_f are arbitrary phases related to the flavour content of the initial- and final-states.

2.6.1 *CP* violation in decays

A meaningful quantity for the study of direct CP violation in decays is the ratio of the CP conjugate amplitudes

$$\left|\frac{\bar{A}_{\bar{f}}}{A_f}\right| = \left|\frac{\sum_i A_i e^{i(\delta_i-\phi_i)}}{\sum_i A_i e^{i(\delta_i+\phi_i)}}\right|, \tag{2.45}$$

which exhibit CP violation if $\left|\frac{\bar{A}_{\bar{f}}}{A_f}\right| \neq 1$. This can only occur if multiple contributing terms to the amplitudes have both different weak and different strong phases ($\Delta\phi = (\phi_i - \phi_j) \neq 0$, $\Delta\delta = (\delta_i - \delta_j) \neq 0$), since

$$|A|^2 - \left|\bar{A}\right|^2 = -2\sum_{i,j} A_i A_j \sin\Delta\phi \sin\Delta\delta. \tag{2.46}$$

A CP asymmetry may then be defined as the magnitude of this difference in amplitudes

$$a_f = \frac{1-\left|\bar{A}/A\right|^2}{1+\left|\bar{A}/A\right|^2} = \frac{|A|^2-\left|\bar{A}\right|^2}{|A|^2+\left|\bar{A}\right|^2}. \tag{2.47}$$

As the width of a process is proportional to the square of its amplitude, experiments can detect direct CP violating effects by studying asymmetries of differences in rates, such as

$$a_f = \frac{\Gamma(B^+ \to f) - \Gamma\left(B^- \to \bar{f}\right)}{\Gamma(B^+ \to f) + \Gamma\left(B^- \to \bar{f}\right)}. \tag{2.48}$$

The direct CP asymmetries measured in this analysis are of this format.

2.6.2 *CP* violation in mixing

The meaningful quantity for the study of CP violation in mixing is the ratio of the complex coefficients in the propagation of the mass eigenstates. CP violation in mixing occurs if $\left|\frac{q}{p}\right| \neq 1$. A relevant asymmetry may be defined (using semileptonic decays as an example) as

$$a_{\rm sl} = \frac{1-|q/p|^4}{1+|q/p|^4} = \frac{|p|^4-|q|^4}{|p|^4+|q|^4}, \tag{2.49}$$

which leads to

$$a_{\rm sl} = \frac{\Gamma\left(\bar{B}^0_{\rm phys}(t) \to \ell^+\nu X\right) - \Gamma\left(B^0_{\rm phys}(t) \to \ell^-\nu X\right)}{\Gamma\left(\bar{B}^0_{\rm phys}(t) \to \ell^+\nu X\right) + \Gamma\left(B^0_{\rm phys}(t) \to \ell^-\nu X\right)}, \tag{2.50}$$

following from the time evolution of an initial pure $\bar{B}^0_{\rm phys}$ or $B^0_{\rm phys}$. The mixing CP asymmetries measured in the this analysis are of this format. The asymmetry formula may be re-arranged to measure $|q/p|$

$$|q/p| = \left(\frac{1-a_{\rm sl}}{1+a_{\rm sl}}\right). \tag{2.51}$$

However the approximation that $a_{\rm sl} = {\rm Im}\left(\frac{\Gamma_{12}}{M_{12}}\right)$ does not allow access to Γ_{12} or M_{12} without input of a separate measurements.

2.6.3 *CP* violation in the interference between decays with and without mixing

A meaningful quantity to measure CP violation in the interference between decays with and without mixing is a combination of the important variables for mixing and decay themselves

$$\lambda_f = \frac{q}{p}\frac{\bar{A}_f}{A_f}. \tag{2.52}$$

In this case, the relevant asymmetries have to be measured in a time-dependent way and provide sensitivity to the mass difference Δm_B

$$a_f = \frac{\Gamma\left(B^0_{\text{phys}}(t) \to f\right) - \Gamma\left(\bar{B}^0_{\text{phys}}(t) \to f\right)}{\Gamma\left(B^0_{\text{phys}}(t) \to f\right) + \Gamma\left(\bar{B}^0_{\text{phys}}(t) \to f\right)}, \tag{2.53}$$

$$a_f = \frac{\left(1 - \left|\lambda_f\right|^2\right)\cos\Delta m_b t - 2\,\text{Im}\left(\lambda_f\right)\sin\Delta m_B t}{1 + \left|\lambda_f\right|^2}. \tag{2.54}$$

However as this analyis is time-integrated it is not sensitive to these effects. Time-dependent analyses are employed to probe additional variables of interest such as Δm_B, and provide sensitivty to parameters of the CKM matrix. It is not the goal of this analysis to measure those parameters, but rather to probe for the presence of new physics in an inclusive B-meson decay system.

2.6.4 Relation to the CKM matrix

Semileptonic decays of B-mesons involve either the $b \to u\mu\nu$ process, sensitive to V_{ub}, or $b \to c\mu\nu$ which is sensitive to V_{cb}, although neither may be inferred seperately when measuring inclusive decays [24]. Through these parameters, measurements of direct CP asymmetries in B-meson decays can provide inputs to probe angles of the CKM matrix such as $\gamma = \arg\left(\frac{-V_{ud}V^*_{ub}}{V_{cd}V^*_{cb}}\right)$. The green ring in Figure 2.7 requires the input of $|V_{ub}|$ (it is labelled thus because it is the least accurately measured of the three elements required $\sqrt{\rho^2+\eta^2} = |V_{ub}/V_{us}V_{cb}|$). Following the vertices in Figure 2.6, neutral B-meson mixing is sensitive to $V_{tb}V^*_{td}$ and $V_{tb}V^*_{ts}$, these are used determine the yellow and orange rings in Figure 2.7 [25] which further constrain the CKM angles.

2.6.5 New Physics

There are numerous models describing BSM physics which could contribute to measurements of CP violation in mixing and direct decays. New physics may result in asymmetries which are expected to be very small in SM model instead being found to be much larger than predicted. These changes would derive from new interactions in tree-level B-decays or from the presence of new phases in virtual contributions to loop-processes such as neutral B-meson mixing. For example CP violation in a minimal supersymmetric (SUSY) standard model (MSSM) may affect B_s meson mixing [26, 27]. Other possibilites include:

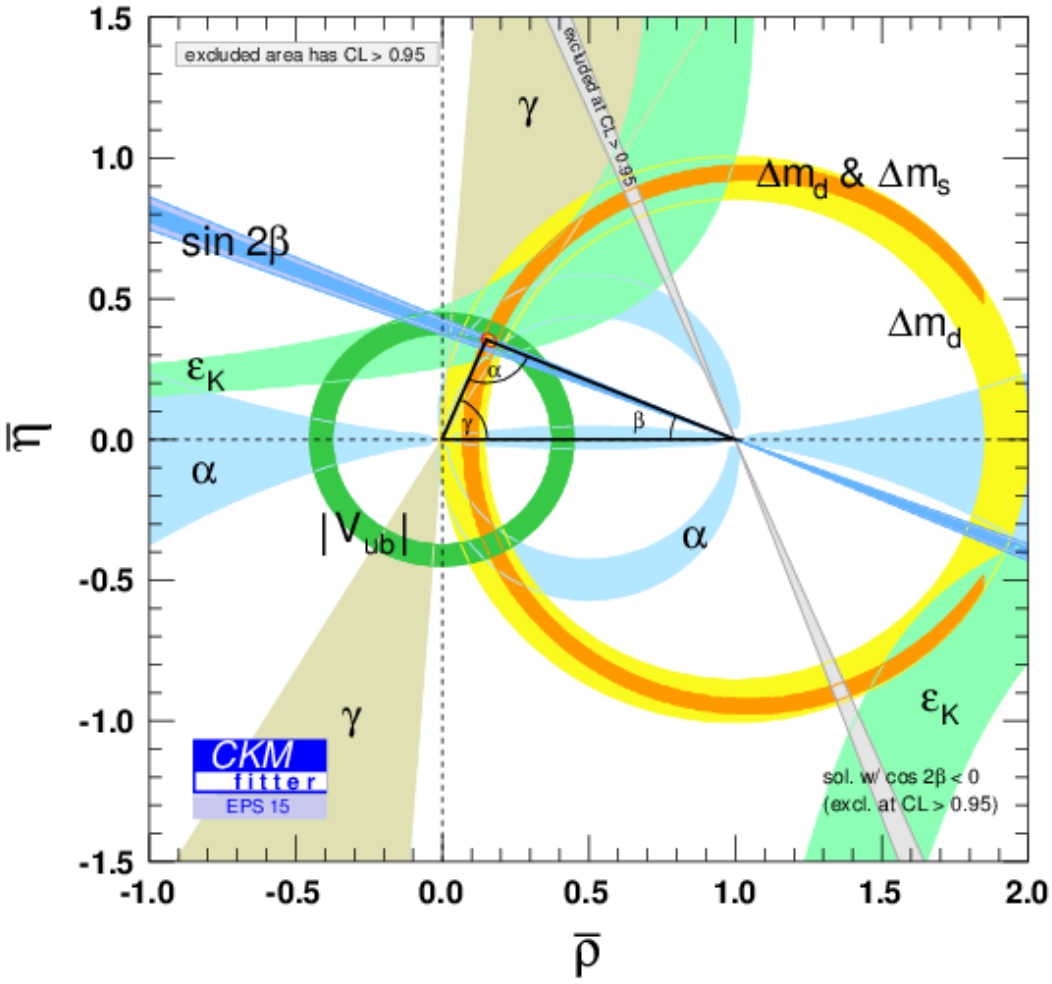

Figure 2.7: Constraints following a global CKM fit in the $(\bar{\rho}, \bar{\eta})$ plane for all modern experimental inputs.

- Effective supersymmetry [28]
- Supersymmetry without R-parity [28]
- Enhanced chromomagnetic dipole operators [28, 29]
- Models with additional quarks [30]

2.6.6 *CP* violation in the SM

CP violation as described by the SM is fundamental to our understanding of the universe, and believed to be the key to the mystery of big bang baryogenesis, the process due to which it is hypothesised that we live in a matter-dominated universe.

Big bang baryogenesis

It is considered that in the early universe shortly after the big bang there would have been equal numbers of baryons (n_B) and antibaryons $(n_{\bar{B}})$. In thermal equilibrium (using protons as an example) with the thermal energy $k_B T$ far greater than the masses of the hadrons, the reversible process for photon production and combination would have occurred

$$p + \bar{p} \rightleftharpoons \gamma + \gamma. \tag{2.55}$$

On expansion the universe cooled and eventually the production of baryons would have ceased and the low-density of the baryon pairs would have also made the forward reaction unlikely. It is expected at that point that the (n_B) and $(n_{\bar{B}})$ would be equal and follow the relation

$$n_B = n_{\bar{B}} \sim 10^{-18} n_\gamma. \tag{2.56}$$

However, the observations of the numbers of baryons and antibaryons in our universe suggest that this relation is far from true, with a measured baryonic asymmetry of the order

$$\frac{n_B - n_{\bar{B}}}{n_\gamma} \sim 10^{-9}, \tag{2.57}$$

a naïve estimate is clearly insufficient. In 1967, Sakharov formulated three conditions which must be met in order to produce any baryonic asymmetry in the early universe:

1. *Baryon number violating interactions*; Processes must exist which allow for the production or destruction of baryons and antibaryons in unequal numbers.

2. *CP violation*; A baryon number violating process is not enough to produce an asymmetry if the *CP* conjugate generates the exact opposite process, as this would re-balance the total number of baryons and antibaryons present.

3. *Departure from thermal equilibrium*; In thermal equilibrium, even with the first two conditions satisfied every process would occur at an equal rate to its inverse process and again the baryon numbers would be balanced.

CP violation then opens the possibility to explain the matter-antimatter asymmetry in the universe. However to date all experimental observations of *CP* violation in the quark sector have been insufficient to explain the magnitude observed in Equation 2.57. It is this question which drives precision measurements of *CP* violation in the SM, particularly in the *B* sector which is expected to yield the largest effect. At present, it is believed that a BSM source of *CP* violation must be responsible to explain the matter-antimatter asymmetry and therefore results which are in tension with the SM predictions could be fertile ground for the discovery of new physics (*NP*). If a *CP*-violating BSM source couples to the *B* sector, it will show up in precision measurements.

2.7 The Higgs Mechanism and electroweak unification

The Higgs mechanism is responsible for allowing fermions and bosons in the SM to have non-zero mass (prior to this theory, inserting mass terms by-hand would break gauge-symmetries, see below). Theories of electroweak unification prescribe that the observed fundamental electromagnetic and weak forces represent low-energy manifestations of a single force. The clearest difference in their manifestation is the difference in the masses of the gauge bosons, with the massless γ compared to the heavy W, Z bosons. Electroweak symmetry breaking, which makes use of the Higgs mechanism, provides a solution to this disparity.

2.7.1 Gauge invariance

Gauge theories represent fundamental symmetries in the SM in the form of local and global phase transformations, under which the Lagrangian is required to be invariant. As an example, the basic free-particle Lagrangian for a free Dirac field

$$\mathcal{L} = i\bar{\psi}\gamma^{\mu}\partial_{\mu}\psi - m\bar{\psi}\psi, \tag{2.58}$$

transforms with a global gauge invariance

$$\psi \rightarrow \psi' = e^{i\theta}\psi, \tag{2.59}$$

where θ is an arbitrary non-complex phase, which allows each term $\bar{\psi}'\psi'$ to exactly equal $\bar{\psi}\psi$. This Lagrangian however is not invariant under a local gauge transformation where the phase has some space-time dependence, $\theta(x)$. Modifying the basic Lagrangian with substitutions including a new field A_μ

$$\partial_\mu \rightarrow D_\mu = \partial_\mu + iqA_\mu, \tag{2.60}$$

leads to a new Lagrangian:

$$\mathcal{L} = \bar{\psi}\left(i\gamma^\mu\partial_\mu - m\right)\psi - q\bar{\psi}A_\mu\psi, \tag{2.61}$$

which is both globally and locally gauge-invariant, if A_μ transforms as $A_\mu \rightarrow A_\mu^{'} = A_\mu - \partial_\mu\chi$. The A_μ can be identified as the photon.

In the Standard Model, the local gauge invariance of the Lagrangian is broken by terms corresponding to particle masses. A massive photon for example would introduce the term $\frac{1}{2}m_\gamma^2 A_\mu A^\mu$ which does not cancel under the gauge transformations. In this case the gauge symmetries may only be satisfied for particles which are massless. This is accurate for the photon and gluon, however it is in direct conflict with experimental results showing massive W and Z-bosons.

2.7.2 Spontaneous symmetry breaking

The Higgs mechanism attests the existence of a complex scalar field able to provide the fermions and weak interaction bosons with mass terms without affecting the massless photon and gluon. The scalar field is constructed to have a so-called sombrero-style potential, with degenerate vacuum energy states as shown in Figure 2.8 [4], and a *vacuum expectation energy* ν. This figure represents the potential $V(\eta)$ for a complex scalar field η which can be written in terms of two real fields η_1 and η_2.

With similar substitutions to the above, a complex scalar field doublet (the Higgs field, $\eta = \frac{1}{\sqrt{2}}\begin{pmatrix} \eta_a + i\eta_b \\ \eta_c + i\eta_d \end{pmatrix}$) can be designed to exhibit gauge-invariance. The derivation is beyond the scope of this thesis, however is it important to note that this Higgs field leads to the generation of an additional scalar particle (the Higgs boson). A phenomenon called *spontaneous symmetry breaking* occurs when a choice of the physical vacuum state is made from the infinite degeneracy. The result is that the manipulation of the doublet is seen to permit a massless photon and 3

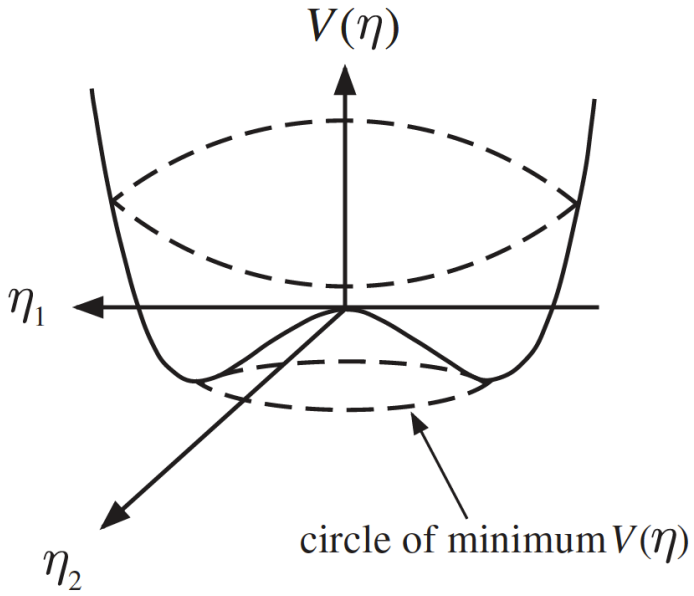

Figure 2.8: The potential $V(\eta) = \mu^2(\eta^*\eta) + \lambda(\eta^*\eta)^2$, for a complex scalar field with $\mu^2 < 0$ and $\lambda > 0$.

massive weak bosons as different manifestations of the same interaction. The masses of the bosons are directly related to the vacuum expectation energy, for example for the W

$$m_W = \frac{1}{2} g_W \nu \quad . \tag{2.62}$$

The γ and Z can then be shown to be eigenvectors of a single process, but for which only the Z obtains a mass via the Higgs mechanism. Furthermore, it is derived that the coupling strength of fermions with the Higgs field run as a function of their attained mass, such that the heaviest observed particles will feel the largest coupling with the Higgs field. As the most massive of all known fermions, the top quark is an obvious candidate for additional study of the Higgs.

2.7.3 Top quark

The top quark is described in further detail in Section 3, the top-quark mass is of particular importance in both the search for new physics and, prior to its discovery, the search for and understanding of the Higgs boson. As mentioned previously, the coupling with the Higgs boson uniquely scales as a function of the mass of the particles with which it is interacting, $g_H(m_i)$. This means that the Higgs boson couples most strongly to the top quark and the W boson.

Important production (and decay) mechanisms for the Higgs boson involve radiative corrections from top loops and W loops (such as in Figure 2.9 [31]), this means that predictions for the Higgs boson mass were made using precision measurements of the top and W masses. These are now comparable with the measurement of the Higgs mass itself and provide a rigorous consistency check for the SM, as in Figure 2.10 [32]. More detailed theory, experimental techniques and results for measurements of the top-quark properties are described further in Section 3.

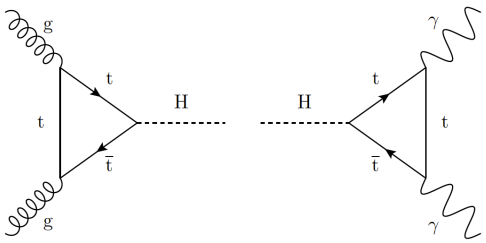

Figure 2.9: Lowest order Feynman diagrams for Higgs production via gluon fusion and a top-quark loop, and Higgs decay to two photons via a top-quark loop.

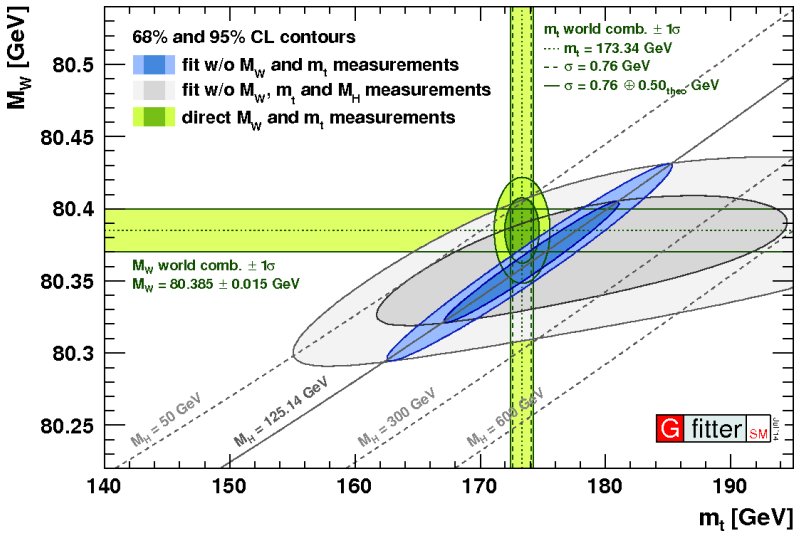

Figure 2.10: Predictions for the Higgs boson mass, as a function of the t and W masses.

Do you know who I am?... I am destined to be the worlds number one... come and get me!

Ash Ketchum

Chapter 3

Top-quark physics

The top quark is by far the most massive of all known fundamental particles, with $m_t \sim 173$ GeV. Discovered at Fermilab in 1995 [33], it was originally postulated to exist alongside the lighter b-quark as a third quark generation to solve the problem of CP violation observations in kaon decays [22]. Although the b-quark was discovered in 1977 [34], it took 23 years for particle accelerators to reach the centre-of-mass energy required to detect top quarks via on-shell production. The mass window prior to its discovery had already been constrained to approximately $m_t = 170 \pm 30$ GeV at the Large Electron-Positron collider (LEP) [35] through measurements of the cross-section $\sigma\left(e^+e^- \to b\bar{b}\right)$ in which a virtual top quark appears in an intermediate loop, with two W-bosons.

Top-quark studies at high-energy colliders have a high potential for sensitivity to NP. The large mass implies it may be the most likely particle to couple to NP at the TeV level and is crucial to the electroweak symmetry breaking mechanism. It may also appear as a background to potential searches for BSM physics.

The top quark also has an extremely short lifetime τ_t due to its large mass, which means that unlike other quarks it cannot hadronise as there is not sufficient time for a strong interaction to take place. This is shown in Equation 3.2, where G_F is the usual Fermi constant and the near-unity branching ratio of $t \to Wb$, provided by the CKM element $|V_{tb}|^2$, is used to justify the approximation of the partial decay rate $\Gamma(t \to Wb)$ as equivalent to the total decay rate Γ_t. Preservation of properties such as spin through the weak interaction provide the opportunity for the study of the 'bare' top quark through analysis of its decay products.

$$\Gamma(t \to Wb) = \frac{G_F m_t^3}{8\pi\sqrt{(2)}} |V_{tb}^2| \sim 1.74 \text{ GeV}, \tag{3.1}$$

$$\tau_t = \frac{1}{\Gamma_t} \sim 3.8 \times 10^{-25} \text{ s} \tag{3.2}$$

Precision studies of top-quark properties form a stringent test of the SM, and at the ATLAS experiment require the entire detector to be utilised, as the most common decay channels for the top quark include charged leptons (detected using the inner detector, electromagnetic calorimeter and muon spectrometer), jets (detected using the inner detector, electromagnetic calorimeter and hadronic calorimeter) and missing energy (reconstructed via momentum conservation using many detector parts, see Section 6.2.6).

3.1 Top-quark production

The primary production mechanism for top quarks at the LHC is in $t\bar{t}$ production through gluon fusion, as in Figure 3.1a [36]. This is in contrast to the primary production mechanism at the Tevatron which was quark-antiquark annihilation interactions, as in Figure 3.1b [36]. The difference stems from the centre-of-mass energy at which the collisions occur and the different initial colliding hadrons (pp at the LHC and $p\bar{p}$ at the Tevatron). For the Tevatron at $\sqrt{s} = 1.96$ TeV the valence quarks in the $p\bar{p}$ collisions carried the largest momentum fractions x_i of all of the partons. At LHC energies of 8 TeV and 13 TeV the gluon interactions dominate. At the Tevatron the quark to gluon production mechanism ratios were about 9:1, at the LHC the ratios are 1:4 and 1:9 at 8 TeV and 13 TeV respectively [37]. Figure 3.2 [38] shows the predicted parton interactions at next-to-leading order (NLO) as a function of x_i. The theoretical cross-section at next-to-next-to-leading-order (NNLO) for top-quark pair production at the LHC at 8 TeV is $\sigma_{t\bar{t}} = 252.0 \pm 11.7^{+6.4}_{-8.6}$pb [39].

In addition to $t\bar{t}$ pairs it is also possible to produce single top quarks through several mechanisms: $q\bar{q}^{'} \to \bar{b}t$ via a virtual W-boson Wtb vertex (s-channel), $bg \to tW^-$ via a virtual b or t (Wt-channel), and $qb \to q^{'}t$ or $\bar{q}b \to \bar{q}^{'}t$ also via a virtual W-boson (t-channel). These are shown in Figure 3.3a- 3.3d [36], with predicted cross-sections at 8 TeV [40]:

- $\sigma_t^{s-\text{channel}} = 3.79 \pm 0.07 \pm 0.13$ pb

(a) (b)

Figure 3.1: Feynman diagrams showing top-quark pair production via (a) gluon fusion and (b) quark-antiquark annihilation.

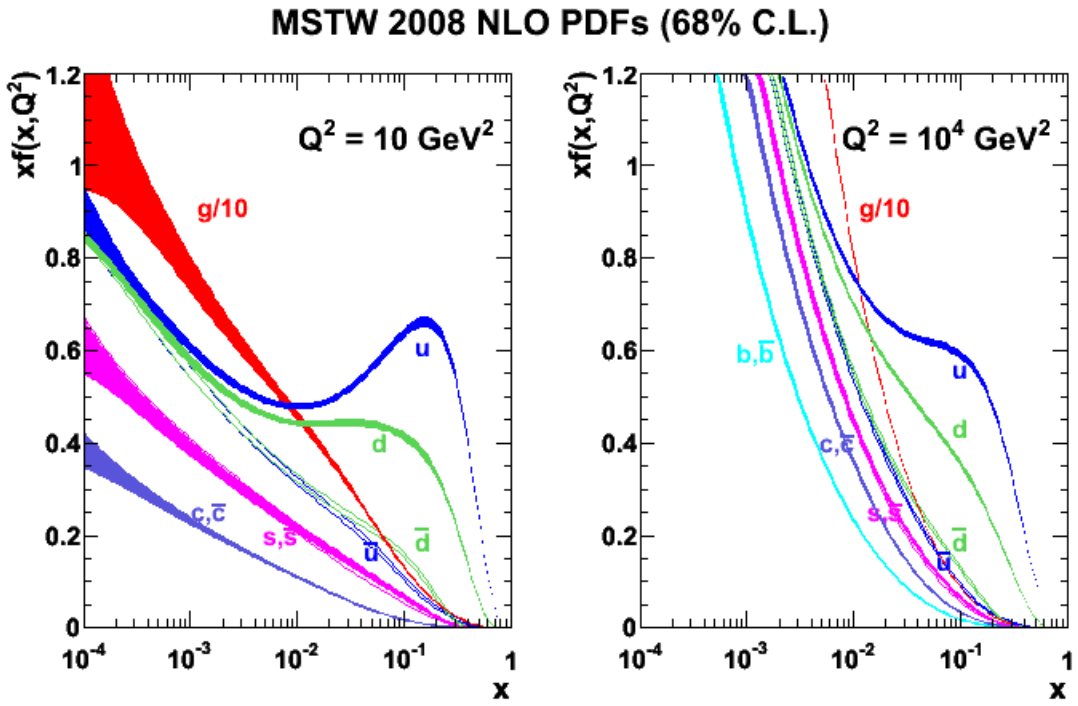

Figure 3.2: NLO predictions for parton distribution functions with the proton as a function momentum fraction.

.

- $\sigma_{\bar{t}}^{s-\text{channel}} = 1.76 \pm 0.01 \pm 0.08$ pb
- $\sigma_{t}^{t-\text{channel}} = 56.4^{+2.1}_{-0.3} \pm 1.1$ pb
- $\sigma_{\bar{t}}^{t-\text{channel}} = 30.7 \pm 0.7^{+0.9}_{-1.1}$ pb
- $\sigma_{t}^{Wt-\text{channel}} = 11.1 \pm 0.3 \pm 0.7$ pb

The cross-sections for these processes are significantly smaller than for the top-quark pair

production, as they proceed via the weak force rather than the strong force. The top-quark cross-sections for the t- and s-channels are larger than the anti-top-quark cross-sections due to available valence quarks in proton-proton collisions. The proton valence quarks are able to produce more W^+-bosons than W^--bosons in each case, resulting in more $W^+ \to tb$ vertices than the charge conjugate.

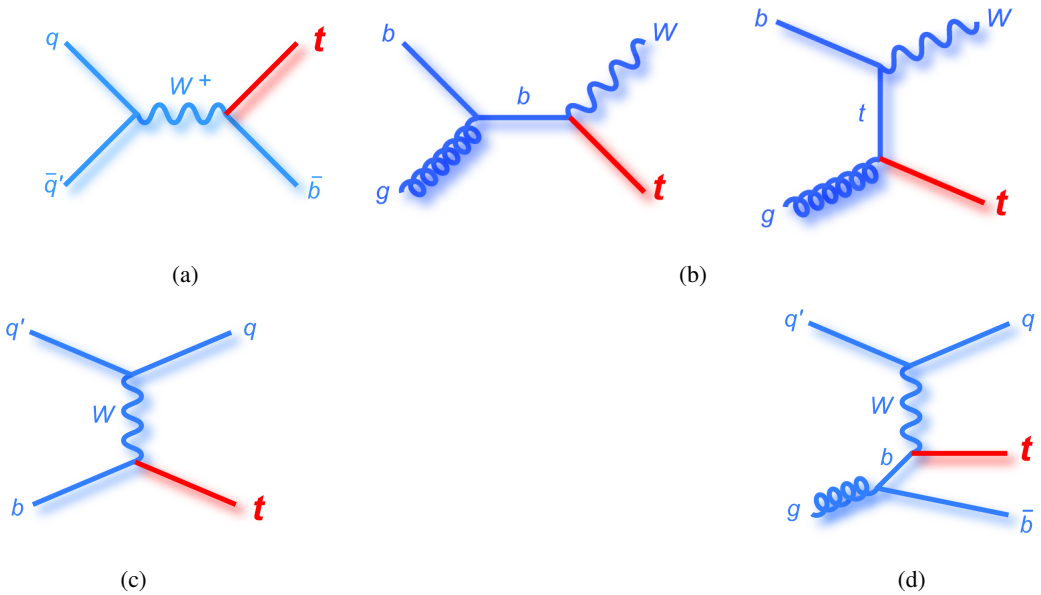

Figure 3.3: Feynman diagrams showing single top-quark production via (a) the s-channel, (b) the Wt-channel, (c) the t-channel in association with a sea b-quark from the proton, and (d) the t-channel in association with a b-quark from a gluon.

3.2 Top quark decay modes

Due to the near-unity value of the V_{tb} coupling constant the branching ratio for top-quark decays to Wb is almost 100%. Top-quark pairs produced at the LHC then follow down the major decay channels detailed in Figure 3.4 [36].

The dominant decay channels (not including τ's), dependent on the branching ratios of the W-boson decays (Table 3.1 [41]), are:

- ℓ+jets : $t\bar{t} \to Wb\,Wb \to b\ell\nu\; bq\bar{q}' \sim 5\%$
- Dilepton : $t\bar{t} \to Wb\,Wb \to b\ell\nu\; b\ell\nu \sim 30\%$
- Fully hadronic : $t\bar{t} \to Wb\,Wb \to bq\bar{q}'\; bq\bar{q}' \sim 45\%$

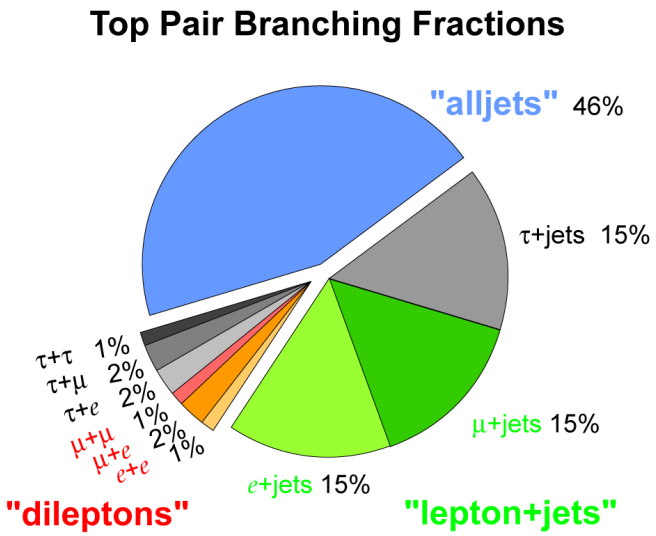

Figure 3.4: Top-quark pair branching fractions.

W decay channel	Branching ratio (%)
$e\nu$	10.75 ± 0.13
$\mu\nu$	10.57 ± 0.15
$\tau\nu$	11.25 ± 0.20
Hadronic	67.60 ± 0.27

Table 3.1: The measured branching ratios of the W-boson decay channels.

These three categories of top-quark pair decay channel are often studied separately, as the final states are significantly different. As such they have different analytical challenges. Each channel will also have considerably different background processes and require different techniques to identify. Fully-hadronic events suffer from extremely large multijet backgrounds due to the number of expected jets (8) to be reconstructed in the final state, but benefit from the largest branching ratio. Fully-hadronic analysis typically suffer from large jet-calibration related systematics. Dilepton events in contrast have the smallest branching ratio, but also the cleanest signature requiring a trigger on two oppositely-charge leptons. However the missing energy from two neutrinos may cause issues when trying to reconstruct the top-quark four-momenta. The ℓ+jets can be considered as a balance between the other scenarios, both in terms of cross-section and reconstruction. The complication in the ℓ+jets channel comes from τ+jets events.

The τ's may decay leptonically or hadronically, and the leptonic decays may fall within the acceptance of e+jets and μ+jets channels. Due to the complex nature of the τ particle, often ℓ+jets analyses focus on e and μ only and τ-type analyses are performed separately.

3.3 Top quark properties

Precision measurements of many different properties of the top quark act as stringent tests of the SM and may yield the first signs of evidence of BSM physics.

Mass

The top quark is the heaviest known fundamental particle and a crucial parameter of the SM and electroweak symmetry breaking, which must be accommodated for in BSM theories. Due to this it has the largest coupling to the Higgs boson and is predicted to have large couplings to many BSM models. Knowledge of the top-quark mass also plays a role in predicting the vacuum stability of the universe [42]. Therefore precision measurements of the top-quark mass may provide powerful constraints on many different SM and BSM scenarios. Many Run 2 top-quark mass measurements are expected to kick off shortly at both ATLAS and CMS. The ATLAS results at 8 TeV are summarised in Figure 3.5.

Width

The top-quark width is dominated by $t \to Wb$ decays, however there are some suggestions of tension between the a previous measurement of the ratio of the top-quark widths and the expectations for those values from the CKM matrix ($|V_{tb}|^2 = 1.021 \pm 0.032$). The measured branching ratio at D0 is $\Gamma(t \to Wb)/\Gamma(t \to Wq) = 0.9 \pm 0.04$ [41], however a more recent measurement at CMS is in better agreement with $|V_{tb}|^2$ with $\Gamma(t \to Wb)/\Gamma(t \to Wq) = 1.014 \pm 0.03$ [41]. Deviations from the predicted top-quark width could indicate the possibility for top quark to be decaying to other final states or BSM particles which escape detection. It would also open the possibility for a fourth generation of quarks to exist which are not currently accounted for.

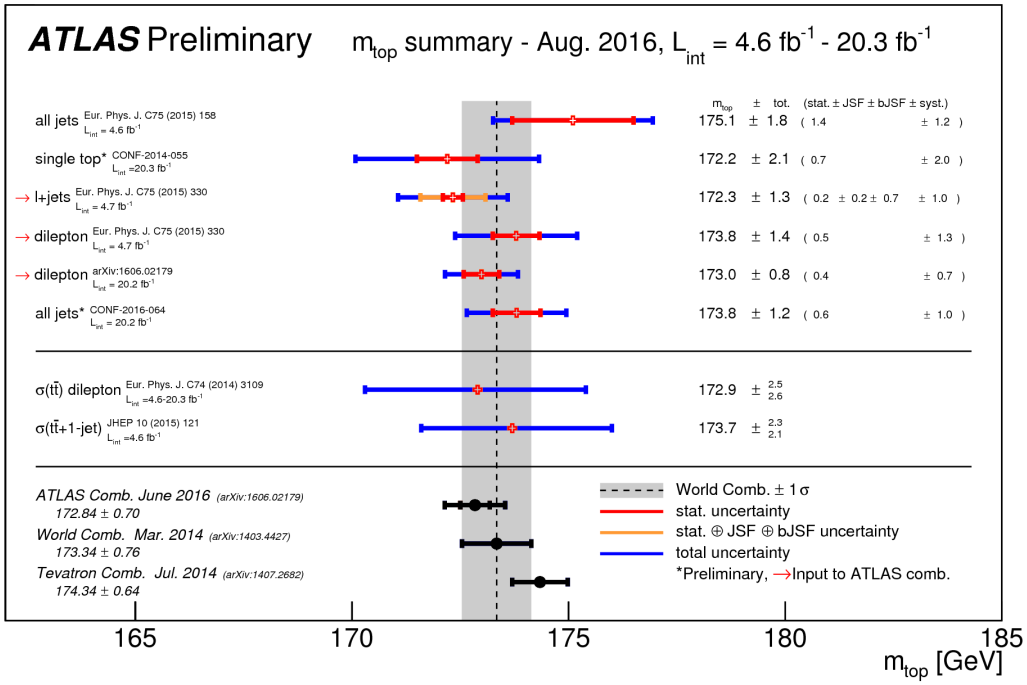

Figure 3.5: Summary of ATLAS direct top-quark mass measurements, compared to the overall ATLAS, Tevatron, and Tevatron+LHC combinations.

.

Cross-section

Deviations of the measure cross-section for the production or decay of top quarks could indicate the presence of couplings to NP. An excess in the cross-section would imply the possibility of heavy BSM particles being produced at the LHC and decaying via top quarks. Additionally, precision knowledge of the top-quark cross-section is important as it appears as a large background to other physics analyses such as Higgs-boson measurements. Differential cross-section measurements also have the potential to be sensitive to more subtle signals from NP. Top-quark pair decay cross-section measurements are made in all channels by both ATLAS and CMS, and contribute to combinations to tighten the overall results. Figures 3.6 details the results at 8 TeV and 13 TeV, with no significant deviations from the SM expectations.

Spin-correlation

As the top quark does not hadronise its spin information is preserved and affects the kinematic properties of its decay products. While the spin of either top quark in a $t\bar{t}$ decay individually

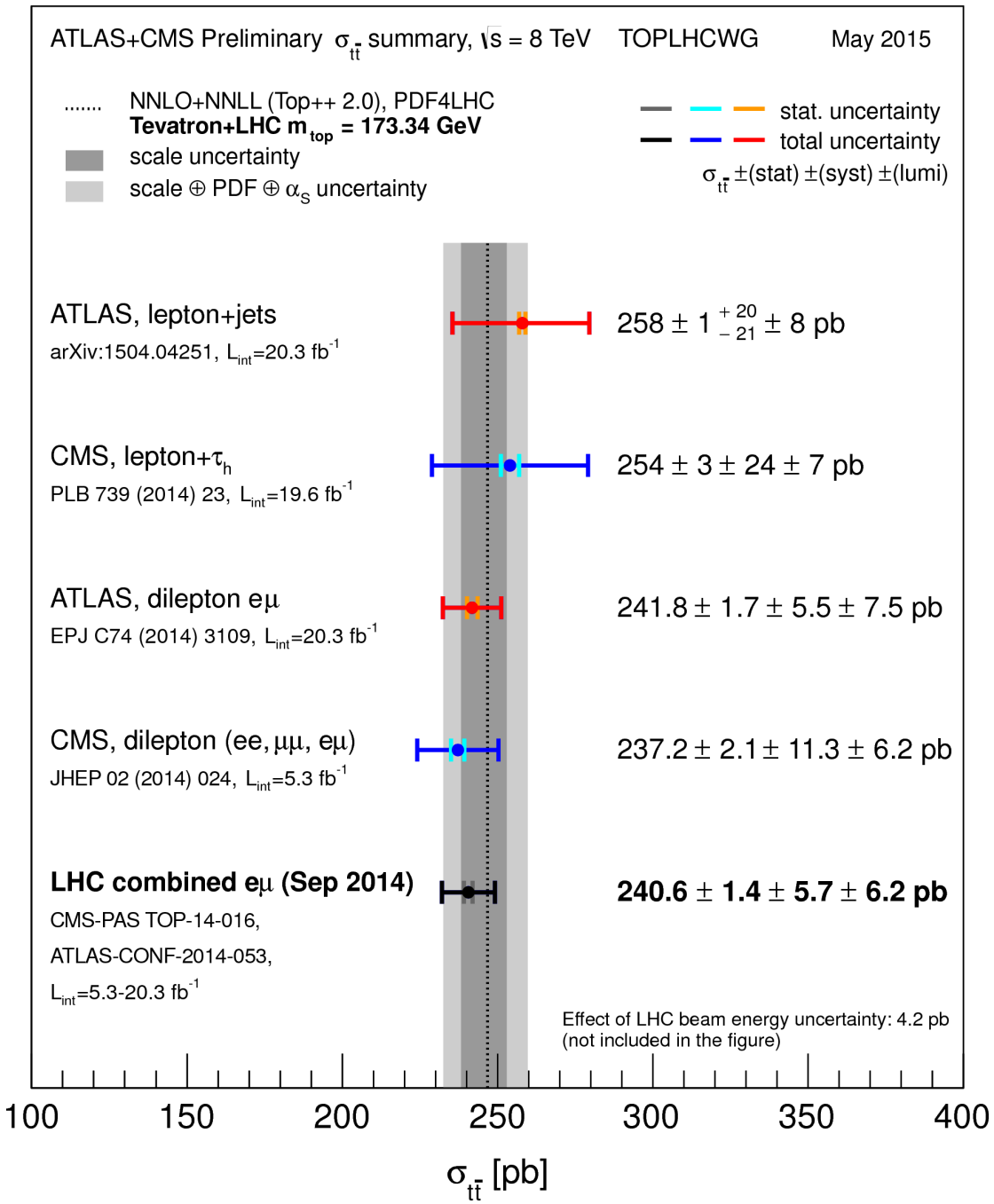

Figure 3.6: Summary of the top-quark pair production cross-section measurements on ATLAS and CMS at 8 TeV in the ℓ+jets and dilepton channels, compared with an NNLO QCD calculation.

.

may not be measured, there are SM predictions for the correlation between their spins, which yields observables in the angular properties of the leptons in the dilepton decay channel. BSM scenarios (such as supersymmetric stop-quark decays) may give predictions for different spin

correlations [43] which could be detected by precision measurements of those angular properties.

Charge asymmetry

At leading order (LO) the rapidity distributions of top and anti-top quark are expected to be symmetric. However at next-to-leading-order (NLO), interference between the Born and Box feynman diagrams, and diagrams with initial and final state radiation, in the quark annihilation production processes yields asymmetries (Figure 3.7 [44]). At the Tevatron, as the collisions were between protons and anti-protons, this interference manifests itself as a forward-backward asymmetry in the top quarks, however at the LHC as the pp collisions are initially symmetric the effect is instead to create a difference in the width of the rapidity distributions, shown in Figure 3.8 [45]. BSM models may enhance or reduce the expected charge asymmetry. Charge asymmetry measurements have been made by ATLAS and CMS at 8 TeV, the results show no significant deviations from SM expectations and are shown in Figures 3.9.

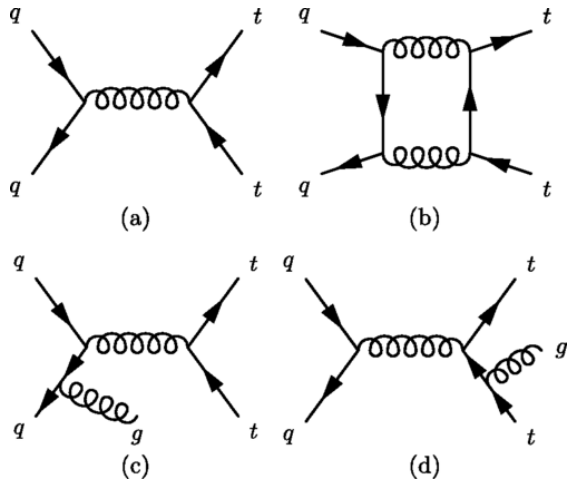

Figure 3.7: Feynman diagrams for the (a) Born and (b) Box diagrams which interfere to produce forward-backward and charge asymmetries. Additional diagrams with (c) initial and (d) final state radiation which contribute a similar but reduced effect.

.

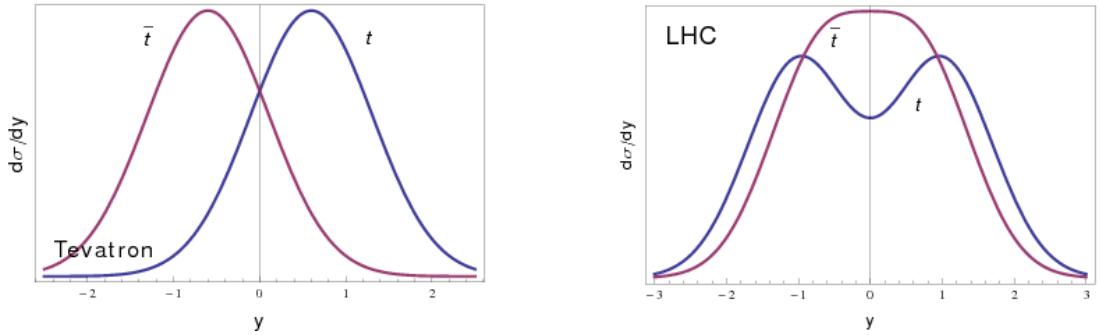

(a) (a) (b) (b)

Figure 3.8: Rapidity distributions of top and anti-top quarks at (a) the Tevatron showing a forward-backward asymmetry, and (b) the LHC showing a charge-asymmetry.

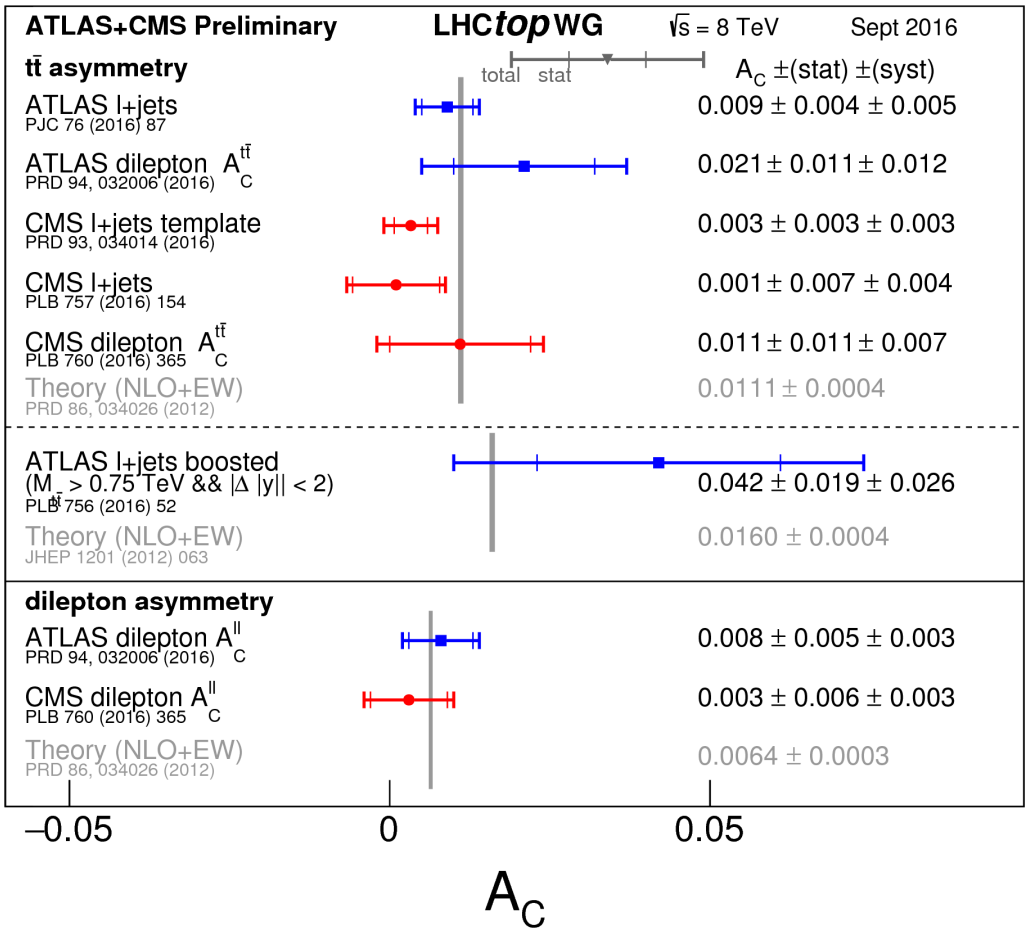

Figure 3.9: Summary of the charge asymmetry measurements on ATLAS and CMS at 8 TeV

.

We've got a plan, and we're going to stick to it

Tony Stark

Chapter 4

Analysis outline

As discussed in Section 2.6.6, *CP* violation implies that physical laws for matter and antimatter are different, and that understanding the source and magnitude of this difference may be key to understanding the matter-antimatter asymmetry in the universe. Existing measurements in the heavy-flavour sector [6–16] continue to be insufficient to explain the observed asymmetry, and all are in good agreement with SM predictions. There are however hints at the potential for new physics following an inclusive like-sign dimuon charge asymmetry measurement reported by the D0 experiment [46], which observed an excess of approximately 3σ from the SM, but has not been confirmed by similar analyses at LHCb [47, 48] and BaBar [49]. This is discussed at the end of this chapter.

4.1 *CP* violation in heavy flavours with top-quark events at ATLAS

The abundance of top quarks produced at the LHC, with the near-unity $t \to Wb$ branching ratio, may be exploited as a high statistics source of b-quarks. This production mechanism, differing from the coherent $b\bar{b}$ production at B-factory experiments, opens the possibility to utilise new techniques in measuring *CP* asymmetries. As each b-quark is produced with a partner W-boson, in cases where the W-boson decays to a leptonic final state the charged lepton will be correlated precisely to the charge of the associated b-quark. The b-quark will hadronise, and in the events where the hadron follows a semileptonic decay path, the charge of the resultant soft lepton will determine unambiguously the charge of the b-quark at decay. Soft electrons from jets in the ATLAS detector are extremely difficult to detect as they are buried in the electromagnetic

components of the jet absorbed in the ECAL. Soft muons however leave a signal in the muon spectrometer aligned with a jet, and analyses may exploit a soft muon heavy-flavour tagging algorithm (described in Section 7) to detect them. Knowledge of the charge of a b-quark at the point of production and the point of decay provides information relevant to potentially *CP*-violating processes.

4.1.1 Charge asymmetries

Using the ℓ+jets channel, there are three decay chains in a $t\bar{t}$ system (Figure 4.1) which would produce a W-boson lepton and a soft muon with the same charge (*same-sign*) (SS) and three which would produce a pair of leptons with opposite charge (*opposite-sign*) (OS). These are described by Equations (4.1)–(4.3) and Equations (4.4)–(4.6) respectively,

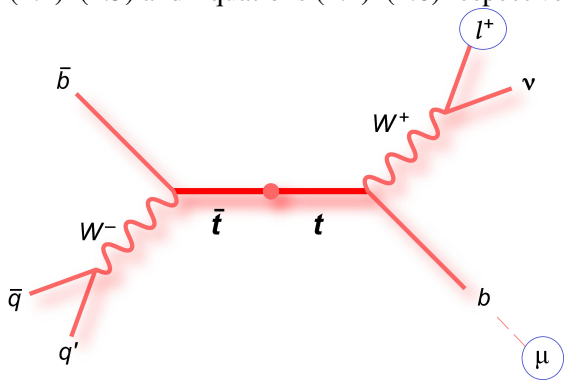

Figure 4.1: The $t\bar{t}$ ℓ+jets decay channel, highlighting the W-boson lepton and a soft muon from a semileptonic B-meson decay.

$$N_{r_b} = N\left[t \to \ell^+\nu\left(b \to \bar{b}\right) \to \ell^+\ell^+X\right], \tag{4.1}$$

$$N_{r_c} = N\left[t \to \ell^+\nu\left(b \to c\right) \to \ell^+\ell^+X\right], \tag{4.2}$$

$$N_{r_{c\bar{c}}} = N\left[t \to \ell^+\nu\left(b \to \bar{b} \to c\bar{c}\right) \to \ell^+\ell^+X\right], \tag{4.3}$$

$$N_{\tilde{r}_b} = N\left[t \to \ell^+\nu b \to \ell^+\ell^-X\right], \tag{4.4}$$

$$N_{\tilde{r}_c} = N\left[t \to \ell^+\nu\left(b \to \bar{b} \to \bar{c}\right) \to \ell^+\ell^-X\right], \tag{4.5}$$

$$N_{\tilde{r}_{c\bar{c}}} = N\left[t \to \ell^+\nu\left(b \to c\bar{c}\right) \to \ell^+\ell^-X\right], \tag{4.6}$$

where $N_{\tilde{r}_i}$ represents the number of soft muons in a well-defined fiducial region, described in Section 8.2.5. The equations which include $J/\Psi\left(c\bar{c}\right)$ decays provide CP violating information in

the semileptonic decay of an individual quark [50] (a very small effect), or dilution in the decay of $J/\Psi \to \ell\ell$. Let $N^{\alpha\beta}$ represent the number of soft muons with charge β which are paired with W-boson leptons of charge α. The charge of the W-boson lepton is correlated to the initial charge of the b-quark. It is usual to measure the magnitude of *CP* violation in SM processes by building asymmetries from *CP* conjugate decays. Following [50], SS and OS *charge asymmetries* (CA) are defined as

$$A^{\text{ss}} = \frac{(N^{++} - N^{--})}{(N^{++} + N^{--})}, \tag{4.7}$$

$$A^{\text{os}} = \frac{(N^{+-} - N^{-+})}{(N^{+-} + N^{-+})}. \tag{4.8}$$

However there are experimental issues which have been neglected in this definition and must be accounted for. Alterations to the expressions for the CAs are necessary to normalise the observables to account for detector-related and other effects which could introduce unrelated asymmetries into the measurement.The sources of other asymmetries include:

- $t\bar{t}$ **pair production charge asymmetry.** In next-to-leading order (NLO) calculations for pp collisions at the LHC experiment, interferences between the born- and box-diagrams for $q\bar{q} \to t\bar{t}$ production results in different rapidity distributions for the top and the anti-top quarks. As the detector has a finite acceptance and analyses introduce selection requirements on pseudorapidity η, the sampled data will contain more anti-top quarks than top quarks, and therefore more initial negatively charged W-boson leptons than positively charged. This is a small effect as the LHC production of $t\bar{t}$ pairs is dominated by gluon fusion, and has been measured at ATLAS to be $A_C = (0.9 \pm 0.5)\,\%$ [51].

- **Lepton reconstruction.** Any charge-dependency in the reconstruction of leptons at the ATLAS detector would lead to a different initial number of positive and negative W-boson leptons. However at ATLAS no such dependence is known to exist.

- b**-jet reconstruction.** Any charge-dependency in the reconstruction of b-jets at the ATLAS detector would enter into an event selection at the same level as the lepton reconstruction, and lead to a different initial number of positive and negative W-boson leptons.

It should be noted that a charge-dependency in the soft muon tagging algorithm will not

be resolved by normalising the observables as described below. The performance of the tagger must therefore be studied as a function of charge explicitly, which is done in Section 7.

Redefining the CAs to normalise for these experimental issues (using the substitution $N^{\alpha\beta} \rightarrow \frac{N^{\alpha\beta}}{N^{\alpha}}$) gives

$$A^{\text{ss}} = \frac{\left(\frac{N^{++}}{N^{+}} - \frac{N^{--}}{N^{-}}\right)}{\left(\frac{N^{++}}{N^{+}} + \frac{N^{--}}{N^{-}}\right)}, \qquad A^{\text{os}} = \frac{\left(\frac{N^{+-}}{N^{+}} - \frac{N^{-+}}{N^{-}}\right)}{\left(\frac{N^{+-}}{N^{+}} + \frac{N^{-+}}{N^{-}}\right)}, \tag{4.9}$$

where $N^{\alpha} = N^{\alpha+} + N^{\alpha-}$, and is the total number of W-boson leptons with charge α. These may be considered as asymmetries of four probabilities

$$A^{\text{ss}} = \frac{P(b \rightarrow \ell^{+}) - P\left(\overline{b} \rightarrow \ell^{-}\right)}{P(b \rightarrow \ell^{+}) + P\left(\overline{b} \rightarrow \ell^{-}\right)}, \qquad A^{\text{os}} = \frac{P(b \rightarrow \ell^{-}) - P\left(\overline{b} \rightarrow \ell^{+}\right)}{P(b \rightarrow \ell^{-}) + P\left(\overline{b} \rightarrow \ell^{+}\right)}, \tag{4.10}$$

where

$$P\left(b \rightarrow \ell^{+}\right) = \frac{N(b \rightarrow \ell^{+})}{N(b \rightarrow \ell^{-}) + N(b \rightarrow \ell^{+})} = \frac{N^{++}}{N^{+-} + N^{++}} = \frac{N^{++}}{N^{+}}, \tag{4.11}$$

$$P\left(\overline{b} \rightarrow \ell^{-}\right) = \frac{N\left(\overline{b} \rightarrow \ell^{-}\right)}{N\left(\overline{b} \rightarrow \ell^{-}\right) + N\left(\overline{b} \rightarrow \ell^{+}\right)} = \frac{N^{--}}{N^{--} + N^{-+}} = \frac{N^{--}}{N^{-}}, \tag{4.12}$$

$$P\left(b \rightarrow \ell^{-}\right) = \frac{N(b \rightarrow \ell^{-})}{N(b \rightarrow \ell^{-}) + N(b \rightarrow \ell^{+})} = \frac{N^{+-}}{N^{+-} + N^{++}} = \frac{N^{+-}}{N^{+}}, \tag{4.13}$$

$$P\left(\overline{b} \rightarrow \ell^{+}\right) = \frac{N\left(\overline{b} \rightarrow \ell^{+}\right)}{N\left(\overline{b} \rightarrow \ell^{-}\right) + N\left(\overline{b} \rightarrow \ell^{+}\right)} = \frac{N^{-+}}{N^{--} + N^{-+}} = \frac{N^{-+}}{N^{-}}. \tag{4.14}$$

4.1.2 *CP* asymmetries

As described by Equations 4.1- 4.6, the CAs are built from events following multiple possible decay channels. The CAs are combinations of multiple individual CP asymmetries (CPA), defined as

$$A_{\text{mix}}^{b\ell} = \frac{\Gamma\left(b \to \overline{b} \to \ell^+ X\right) - \Gamma\left(\overline{b} \to b \to \ell^- X\right)}{\Gamma\left(b \to \overline{b} \to \ell^+ X\right) + \Gamma\left(\overline{b} \to b \to \ell^- X\right)}, \tag{4.15}$$

$$A_{\text{mix}}^{bc} = \frac{\Gamma\left(b \to \overline{b} \to \overline{c} X\right) - \Gamma\left(\overline{b} \to b \to c X\right)}{\Gamma\left(b \to \overline{b} \to \overline{c} X\right) + \Gamma\left(\overline{b} \to b \to c X\right)}, \tag{4.16}$$

$$A_{\text{dir}}^{b\ell} = \frac{\Gamma\left(b \to \ell^- X\right) - \Gamma\left(\overline{b} \to \ell^+ X\right)}{\Gamma\left(b \to \ell^- X\right) + \Gamma\left(\overline{b} \to \ell^+ X\right)}, \tag{4.17}$$

$$A_{\text{dir}}^{c\ell} = \frac{\Gamma\left(\overline{c} \to \ell^- X_L\right) - \Gamma\left(c \to \ell^+ X_L\right)}{\Gamma\left(\overline{c} \to \ell^- X_L\right) + \Gamma\left(c \to \ell^+ X_L\right)}, \tag{4.18}$$

$$A_{\text{dir}}^{bc} = \frac{\Gamma\left(b \to c X_L\right) - \Gamma\left(\overline{b} \to \overline{c} X_L\right)}{\Gamma\left(b \to c X_L\right) + \Gamma\left(\overline{b} \to \overline{c} X_L\right)}, \tag{4.19}$$

where $X\,(X_L)$ denotes an inclusive hadronic final state with no leptons, and with both light and charm quarks (or with light quarks only). The CP asymmetries are related to B-meson mixing and direct CP-violating b- and c-decays (additional negligible contributions from cham mixing are omitted [50]). The decay-chain fractions, r_i and $\widetilde{r}_i$, represent the relative rates of each channel. The decay-chain fractions are dependent on the fiducial region chosen and are calculated in MC as:

$$r_b = \frac{N_{r_b}}{N_{r_b} + N_{r_c} + N_{r_{c\overline{c}}}}, \qquad \widetilde{r}_b = \frac{N_{\widetilde{r}_b}}{N_{\widetilde{r}_b} + N_{\widetilde{r}_c} + N_{\widetilde{r}_{c\overline{c}}}}, \tag{4.20}$$

$$r_c = \frac{N_{r_c}}{N_{r_b} + N_{r_c} + N_{r_{c\overline{c}}}}, \qquad \widetilde{r}_c = \frac{N_{\widetilde{r}_c}}{N_{\widetilde{r}_b} + N_{\widetilde{r}_c} + N_{\widetilde{r}_{c\overline{c}}}}, \tag{4.21}$$

$$r_{c\overline{c}} = \frac{N_{r_{c\overline{c}}}}{N_{r_b} + N_{r_c} + N_{r_{c\overline{c}}}}, \qquad \widetilde{r}_{c\overline{c}} = \frac{N_{\widetilde{r}_{c\overline{c}}}}{N_{\widetilde{r}_b} + N_{\widetilde{r}_c} + N_{\widetilde{r}_{c\overline{c}}}}. \tag{4.22}$$

The relations between the CAs and CPAs are given by [50] as

$$A^{\text{ss}} = r_b A_{\text{mix}}^{b\ell} + r_c \left(A_{\text{dir}}^{bc} - A_{\text{dir}}^{c\ell}\right) + r_{c\overline{c}} \left(A_{\text{mix}}^{bc} - A_{\text{dir}}^{c\ell}\right), \tag{4.23}$$

$$A^{\text{os}} = \widetilde{r}_b A_{\text{dir}}^{b\ell} + \widetilde{r}_c \left(A_{\text{mix}}^{bc} + A_{\text{dir}}^{c\ell}\right) + \widetilde{r}_{c\overline{c}} A_{\text{dir}}^{c\ell}, \tag{4.24}$$

which are justified term-by-term in Appendix A. The decay chain fractions and CP asymmetries

are unaffected by the previous substitution of $N^{\alpha\beta} \to \frac{N^{\alpha\beta}}{N^{\alpha}}$, shown in Appendix B.

4.2 The D0 like-sign dimuon asymmetry

The D0 measurement has been published several times with increasingly large data sets, but the most recent utilised 10.4 fb^{-1} of $p\bar{p}$ collisions at the Tevatron collider at Fermilab, Chicago. The analysis is an inclusive counting experiment using both single muons (approximately 2×10^9 events) and like-sign dimuon signals (approximately 6×10^6 events) as inputs to asymmetries of the form

$$\text{Single muon asymmetry}: \quad a = \frac{(N^+ - N^-)}{(N^+ + N^-)}, \tag{4.25}$$

$$\text{Dimuon asymmetry}: \quad A = \frac{(N^{++} - N^{--})}{(N^{++} + N^{--})}, \tag{4.26}$$

where in the single muon case N^{α} represents the number of events with a single muon of charge α, and in the dimuon case $N^{\beta\beta}$ represents the number of events with two muons of charge β. As this is an inclusive measurement the muons may come from many different sources, after accounting for background and detector-related processes the measurement assumes that the only source of non-zero charge asymmetries to which it is sensitive come from *CP* violation in *B* decays.The single muon asymmetry is found to be consistent with zero, however *A* is found to differ from the SM expectation by approximately 3σ, when interpreted as *CP* violation in the mixing of neutral *B*-mesons (Figure 4.2 [48]), and also when interpreted as the result of *CP* violation in the direct decays of *B* and *D* mesons (Figure 4.3 [52]).

In Figures 4.2 the flavour-specific asymmetries are defined as

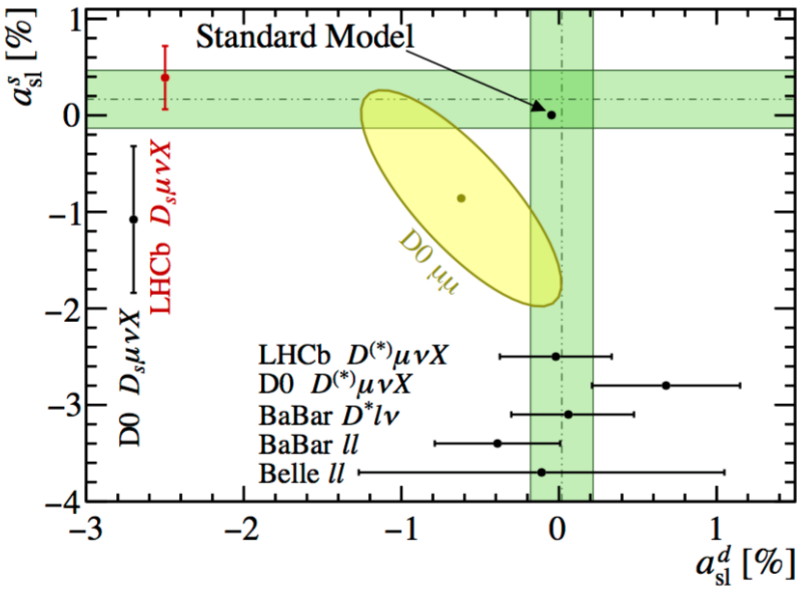

Figure 4.2: Overview of measurements of $a^d_{\rm sl}$ and $a^s_{\rm sl}$ (flavour-dependent *CP* violation asymmetries in neutral *B*-meson mixing). The black dot represents the SM expectation value, the yellow ellipse represents interpretation of the D0 dimuon observation, and the green bands represent naive averages of previous measurements.

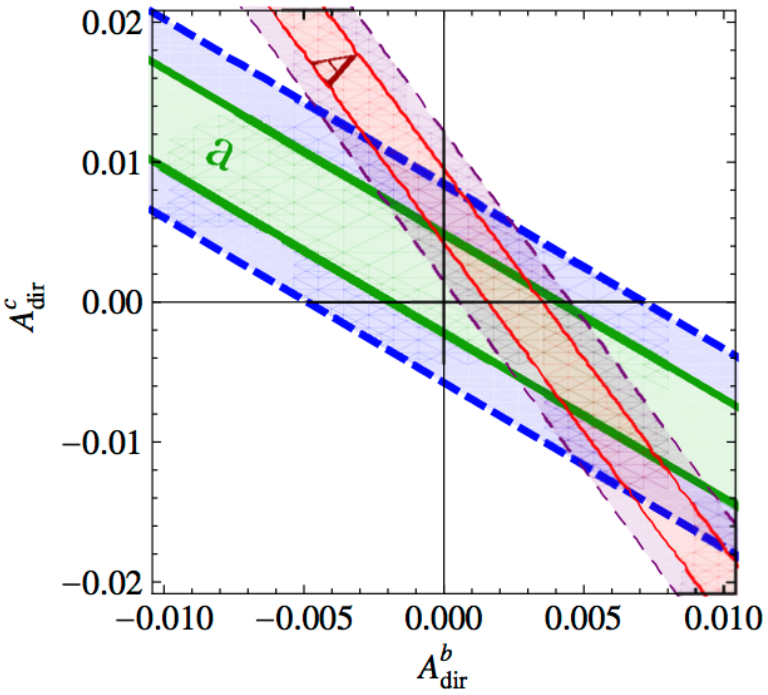

Figure 4.3: Interpretation of the D0 dimuon (*A*) and single muon (*a*) observations, detailing the magnitude of direct *CP* violation in *b* and *c* decays required to produce them assuming SM-like neutral *B* mixing.

$$a_{\mathrm{sl}}^{q} = \frac{\Gamma\left(\bar{B}_q^0 \to B_q^0 \to f\right) - \Gamma\left(B_q^0 \to \bar{B}_q^0 \to \bar{f}\right)}{\Gamma\left(\bar{B}_q^0 \to B_q^0 \to f\right) + \Gamma\left(B_q^0 \to \bar{B}_q^0 \to \bar{f}\right)}, \tag{4.27}$$

$$a_{\mathrm{dir}}^{q} = \frac{\Gamma\left(b \to \mu^- X\right) - \Gamma\left(\bar{b} \to \mu^+ X\right)}{\Gamma\left(b \to \mu^- X\right) + \Gamma\left(\bar{b} \to \mu^+ X\right)}, \tag{4.28}$$

where X is an inclusive final state, and the full asymmetry for neutral B-meson mixing is given by $a_{\mathrm{sl}}^{b} = f_s a_{\mathrm{sl}}^{s} + f_d a_{\mathrm{sl}}^{d}$ and f_q are the fragmentation functions for B_s^0 and B_d^0 production respectively.

I don't care if you're a million times stronger than me,

I'm not going to let them down

Goku

Chapter 5

The LHC and ATLAS Detector

This chapter describes the structure of the Large Hadron Collider and the ATLAS experiment, as relevant for the 2012 data taking conditions at a centre-of-mass energy of $\sqrt{s} = 8$ TeV.

5.1 Large hadron collider

The Large Hadron Collider (LHC) is the world's largest and highest energy particle collision experiment. Based at the Centre for European Nuclear Research (CERN) just outside of Geneva, Switzerland, the LHC consists of a 27 km pseudo-circular ring about which two beams of protons are accelerated in opposite directions, 100 m underground. The beams are designed to cross and collide at four *interaction points* (IP), each of which hosts a major detection experiment as shown in Figure 5.1 [3]; *ATLAS* [1], *CMS* [53], *LHCb* [54] and *ALICE* [54], as well as numerous other 'on-ring' experiments such as *TOTEM* [55] and *LHCf* [56] which focus on 'forward-physics', and 'off-ring' experiments such as *NA62* [57] which studies rare kaon decays, and *ISOLDE* [58] which studies properties of atomic nuclei.

The process of proton acceleration begins at a hydrogen bottle source at LINAC 2. An electric field is applied to strip the hydrogen of electrons, before being accelerated (as protons) through the radiofrequency (RF) cavities of the LINAC. Protons are extracted from the hydrogen in pulses at a rate of up to 100 microseconds per pulse until a high enough yield has been produced, and are held in a tight beam during acceleration by quadrupole magnets. At the end of LINAC 2, the protons have reached an energy of 50 MeV and are passed into the Proton Synchrotron (PS) Booster (labelled in Figure 5.1 as 'booster') to begin the second stage of

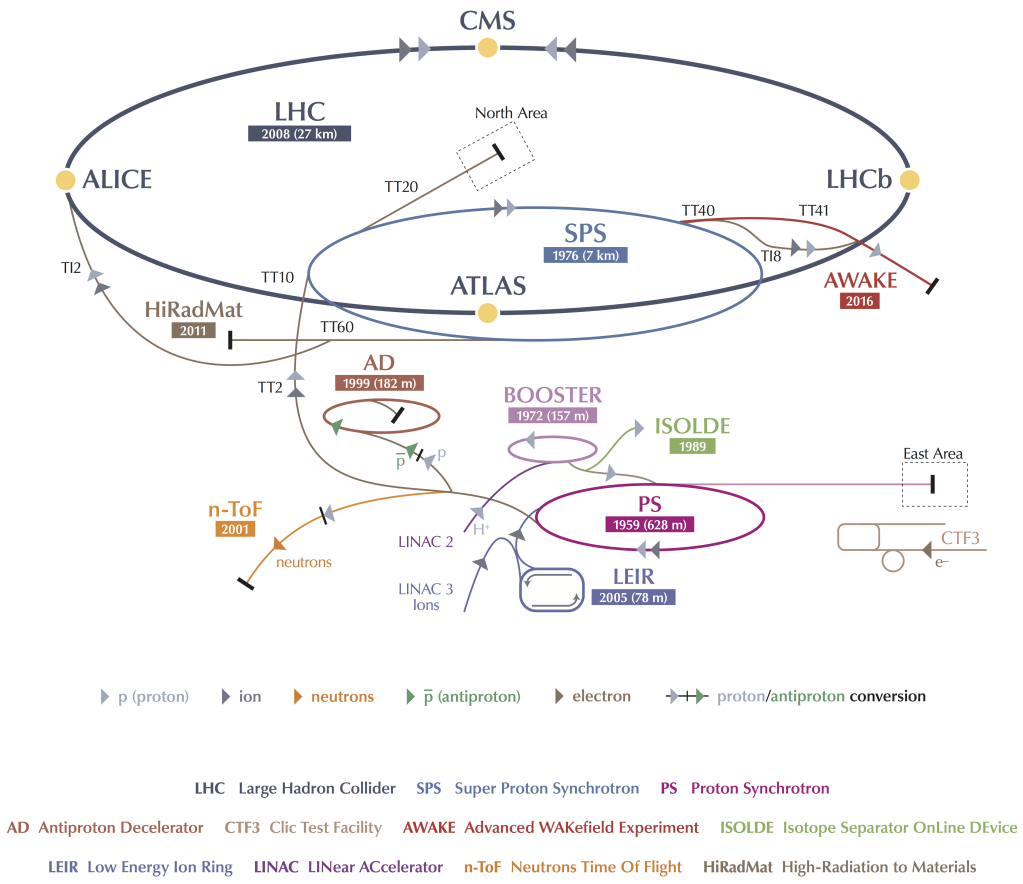

Figure 5.1: A diagrammatic layout of the CERN complex, including the LHC, major experiments and preparatory accelerators prior to the primary ring.

acceleration.

The booster uses several synchrotron rings to increase the energy of the protons to 1.4 GeV, before handing over to the PS itself. The PS is a much larger synchrotron, with a 628 m circumference and 277 electromagnets. This allows for the acceleration of the protons up to 25 GeV. Once a year outside of proton collision data taking, the PS is also used to accelerate lead-ions passed to it by the low energy ion ring (LEIR) for the heavy-ion physics experiment ALICE.

After the PS, protons are passed to the super proton-synchrotron (SPS) which has a circumference of 7 km. The SPS accelerates the proton beam to 450 GeV. Historically the SPS was used as a proton-antiproton collider prior to the LHC commission, during which time it led to the discovery of the W- and Z-bosons. As the last stage of acceleration before the primary ring, the SPS passes the protons into the LHC in two beams of opposite direction. The injection itself

takes the form of proton *bunches*. A bunch is an individual packet of protons containing of the order 10^{11} particles. This technique is used to control the collision rate of beams in the LHC. The bunches form *trains* with deliberate spacing. The number of bunches and the distance between each bunch is adjusted to increase or decrease the time between collisions according to the data recording capabilities of the detectors. Early in Run-1 a bunch spacing of 50 ns was used to test beam stability and allow for low luminosity sanity analyses. The design bunch spacing for the LHC is 25 ns, this increases the luminosity (and therefore the data yield) substantially, however additional problems are introduced related to the speed at which data can be recorded and the amount of activity in the collisions produced, which will be discussed later in Section 5.2.5.

The LHC ring is another synchrotron accelerator, but with 1232 dipole magnets (for bending), 392 quadrupole magnets (for focusing) and 16 RF cavities (8 per beam), the LHC is capable of accelerating protons up to extremely high energies. During Run-1, the nominal beam energy was 3.5 TeV to create a collision centre of mass energy $\sqrt{s} = 7$ TeV. In 2012 this was increased to 8 TeV collisions for approximately one year of data taking, it is with this data that this thesis is concerned. After the completion of Run-1, the LHC entered into a long shutdown (LS1) for repairs and upgrades to move towards design energy. Run-2 started in 2015 operating at $\sqrt{s} = 13$ TeV, with the goal being 14 TeV for the highest energy collisions. The process of accelerating protons from the hydrogen bottle up to collision energies can take several hours. The 2012 data in particular added up to just over 20 fb^{-1}, where an inverse *barn* is the standard unit for time-integrated luminosity and is equivalent to $1\text{b}^{-1} = 10^{-28}\text{m}^{-2}$. Instantaneous luminosity is a normalised measurement of particle flux, for beam collisions this is expressed as

$$\mathcal{L} = f k_b \gamma \frac{N_1 N_2}{4\pi\varepsilon_n \beta^*}, \tag{5.1}$$

where f is the revolution frequency of the two beams, k_b is the number of proton-bunches per beam, γ is the usual relativistic factor and N_i represents the average number of protons per particle bunch in each beam. The denominator is the beam cross-section (a measure of the probability for collision between two particles, with units of area) built from the normalised emittance ε_n (a measure of beam quality in terms of particle spacing, where smaller values infer denser collisions) and the amplitude function at the IP β^*. The amplitude function can be controlled by *squeezing* the beam using quadrupole magnets shortly before the IP, as shown in Figure 5.2 [59]. Higher luminosity collisions come from producing numerous, dense bunches

with minimal bunch spacing, low emittance and with low amplitude functions at the IP. After accounting for inefficiencies in data taking (due to detector down-time) the total 2012 data taken is

$$\int \mathcal{L}dt = 23.1\text{fb}^{-1}. \tag{5.2}$$

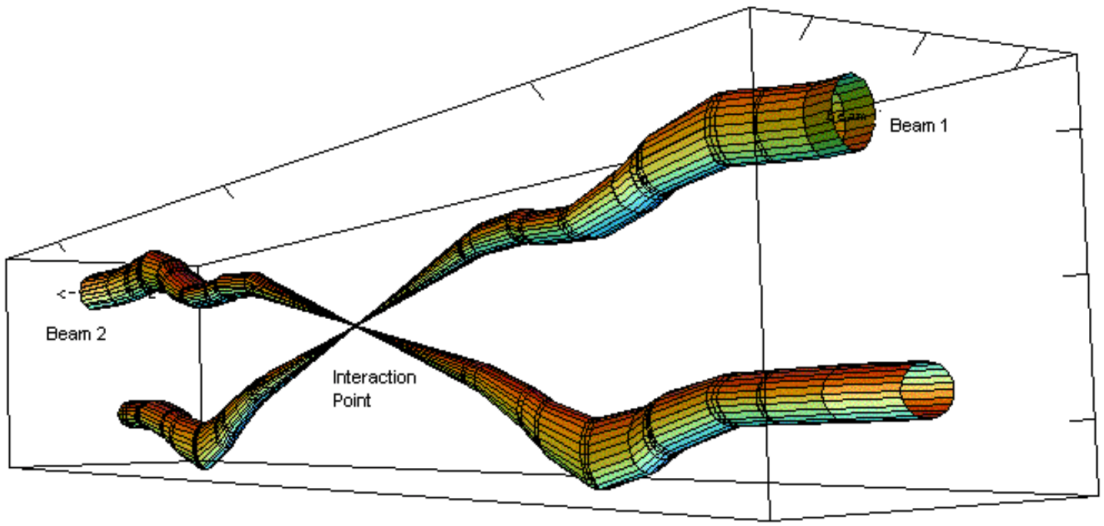

Figure 5.2: Beam squeezing prior to collision at the ATLAS experiment.

For specific physics studies however only a subset of the data will be relevant, according to the rate at which the process of interest occurs. For a given process j, the total number of recorded events (ignoring trigger efficiencies and expressed as a subset of the total number of events) can be described as a function of the process cross-section σ_j and the total integrated luminosity. For a total number of events, N, the relation is

$$N = \sum N_j = \left(\sum \sigma_j\right) \int \mathcal{L}dt \quad . \tag{5.3}$$

The design luminosity, bunch spacing, and other parameters are compared to those achieved in the 2012 8 TeV data run in Figure 5.3 [60].

As instantaneous luminosity is increased *pile-up* becomes an important problem. Pile-up describes the overlap of many proton collisions occurring concurrently, which introduces difficulties in separating and recording individual events. Pile-up can be separated into two categories, *in-time* and *out-of-time*. In-time pileup occurs when multiple proton pairs collide during

Parameter	Value in 2012	Design value
Beam energy [TeV]	4	7
β^* in IP 1,2,5,8 [m]	0.6,3.0,0.6,3.0	0.55
Bunch spacing [ns]	50	25
Number of bunches	1374	2808
Average bunch intensity [protons per bunch]	1.6 - 1.7×10^{11}	1.15×10^{11}
Normalized emittance at start of fill [mm.mrad]	2.5	3.75
Peak luminosity [$cm^{-2}s^{-1}$]	7.7×10^{33}	1×10^{34}
Max. mean number of events per bunch crossing	≈40	19
Stored beam energy [MJ]	≈140	362

Figure 5.3: Performance related parameters of the 2012 protons beams compared with the overall LHC design specifications.

the same bunch crossing and produce multiple primary vertices (PV) at the IP, which must be distinguished algorithmically. Out-of-time pile-up occurs from separate bunch crossings, but when the bunch spacing is too small or collision rate is too high for the read-out electronics to keep up with. If more data enters the system before the existing event has been fully recorded then this may cause out-of-time pile-up. This is discussed further in Section 5.2.5. Pile-up can be described by the average number of interactions per bunch crossing μ, and the distribution for pile-up during 2012 data taking is shown in Figure 5.4 [61] where it is shown that $<\mu>=20.7$. This is in contrast with the lower instantaneous luminosity during the previous 7 TeV run where the average pile-up was closer to 10 interactions per bunch crossing.

5.2 ATLAS

ATLAS (A Large Toroidal LHC Apparatus) is a forward-backward symmetric general purpose detector and one of the four major experiments based on the LHC ring. It is the largest single detector in the world, at a length of 44 m and a height of 50 m, and weighs over 7000 t. The detector is cylindrical in shape and follows an onion-skin design, whereby successive layers of different materials and technologies are used to detect, identify and measure the particles created by collisions at its centre, where the IP is. A cylindrical coordinate system is adopted (whereby the standard x, y and z coordinates can be translated into angular information). At the ATLAS

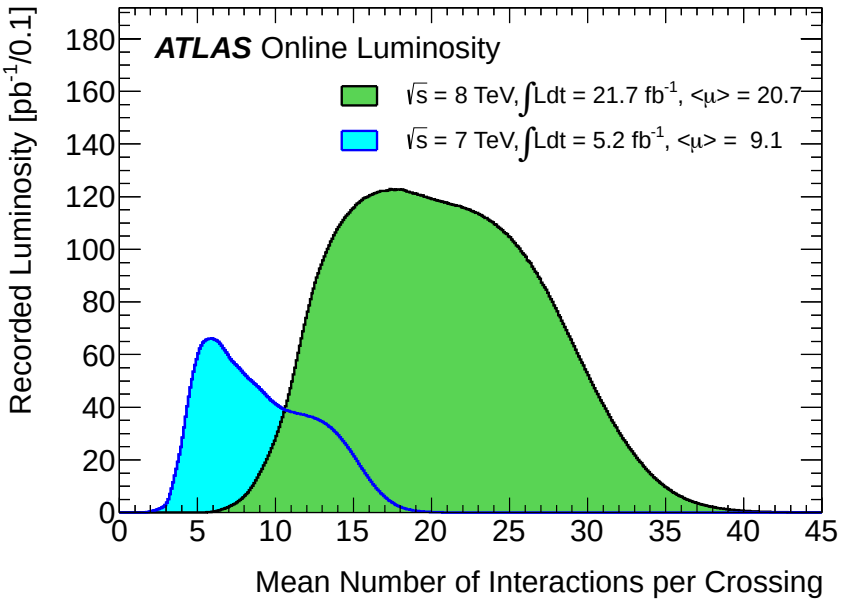

Figure 5.4: Pile-up conditions in the ATLAS detector during the 7 and 8 TeV data taking.

detector, the positive x-direction is defined as pointing radially inwards from the IP to the middle of the LHC ring, the positive y-direction is defined as pointing away from the ground, and the positive z direction is defined as pointing parallel to the beam axis in the anti-clockwise direction following the layout of Figure 5.1. The positive-z side ($z > 0$) is then labelled as Side A, as the negative-z side ($z < 0$) is labelled as Side C. Due to the geometry of the landscape, the z-axis itself actually has a 1.25% incline following the shape of the LHC ring in that region [1]. Converting to the cylindrical system, a polar angle θ is defined as the angle (starting on Side A) between 0 and π in the $z-y$ plane, an azimuthal angle ϕ spans from $-\pi$ to π in the $x-y$ plane, and the radial distance between the origin and the point of interest is labelled r. In practice a substitute angular variable η is used called the pseudorapidity, defined as $\eta = -\ln\tan\frac{\theta}{2}$. This substitution is made as at relativistic energies the pseudorapidity acts as an approximation for the rapidity of a decay, which is useful as differences in rapidity are lorentz invariant. The polar angle θ is susceptible to lorentz contractions in the z-direction. Total distance between two points is then given by $\Delta R = \sqrt{\Delta\eta^2 + \Delta\phi^2}$ and overall positions are described in (η, ϕ) space. The transverse direction is also defined as coinciding with the $x-y$ plane and is useful for describing components of variables such as the transverse momentum p_T and transverse missing energy E_T^{miss} which are conserved in particle collisions and decays (alongside the full momentum infor-

mation) which can be used in calculations when information is missing about the momentum in the z-direction of the system. The momentum in the z-direction is unknown due to missing information on a collision-to-collision basis about the parton momentum-fractions for the colliding constituents of the protons. The standard ATLAS detector diagram is shown in Figure 5.5 [1].

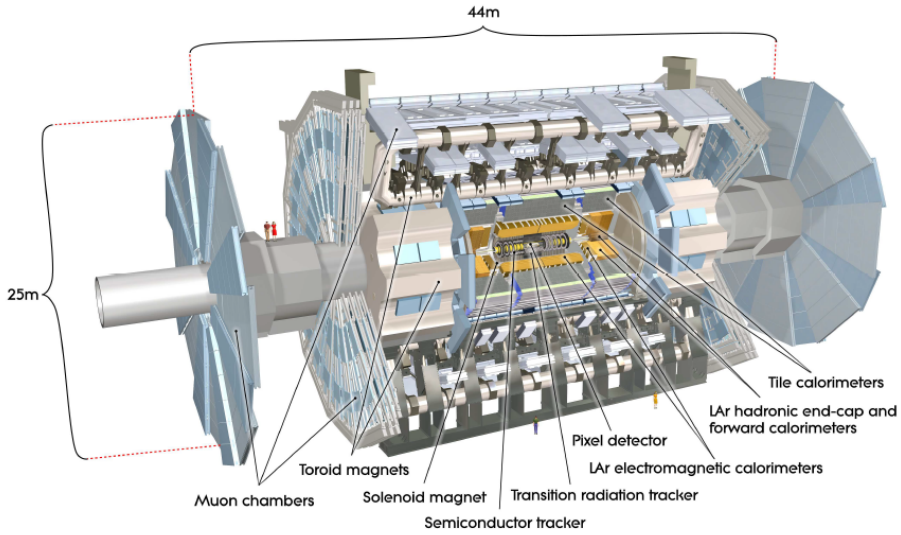

Figure 5.5: A cut-away diagram of the overall construction of the ATLAS detector, labelling the individual components.

The ATLAS detector consists of concentric sections each with a different focus. The innermost layer measures charged-particle tracks and is called the *inner detector* (ID), outside of that is the *electromagnetic calorimeter* (ECAL) which measures the energy of photons and electrons. The *hadronic calorimeter* (HCAL) then detects hadronic activity from hadrons, and finally the outermost layer detects the presence of muons and is called the *muon spectrometer* (MS). The design specifications for the intended precision of all sections is shown in Figure 5.6 [1].

5.2.1 Inner Detector

The purpose of the inner detector is to identify and distinguish tracks of charged particles in the region immediately surrounding the beam pipe and IP. It must have extremely high resolution in order to accurately locate the PV and any secondary vertices (SV) among the large track density following each pp collision. To achieve the required granularity three technologies are combined; pixel detectors, silicon micro-strip (semi-conductor) trackers (SCT) and a transition radiation tracker (TRT). The layout of these sections is shown in Figures 5.7 [1] and 5.8 [1].

Detector component	Required resolution	η coverage	
		Measurement	Trigger
Tracking	$\sigma_{p_T}/p_T = 0.05\%\ p_T \oplus 1\%$	± 2.5	
EM calorimetry	$\sigma_E/E = 10\%/\sqrt{E} \oplus 0.7\%$	± 3.2	± 2.5
Hadronic calorimetry (jets)			
barrel and end-cap	$\sigma_E/E = 50\%/\sqrt{E} \oplus 3\%$	± 3.2	± 3.2
forward	$\sigma_E/E = 100\%/\sqrt{E} \oplus 10\%$	$3.1 < \lvert\eta\rvert < 4.9$	$3.1 < \lvert\eta\rvert < 4.9$
Muon spectrometer	σ_{p_T}/p_T=10% at p_T = 1 TeV	± 2.7	± 2.4

Figure 5.6: Design goals for the precision of the components of the ATLAS detector. The units for E ad p_T are GeV.

After pattern recognition using hits throughout the ID, the PV is identified as the vertex with which the largest momentum can be associated. SVs are most usually related to the decays of b-hadrons (important to this thesis) and τ's.

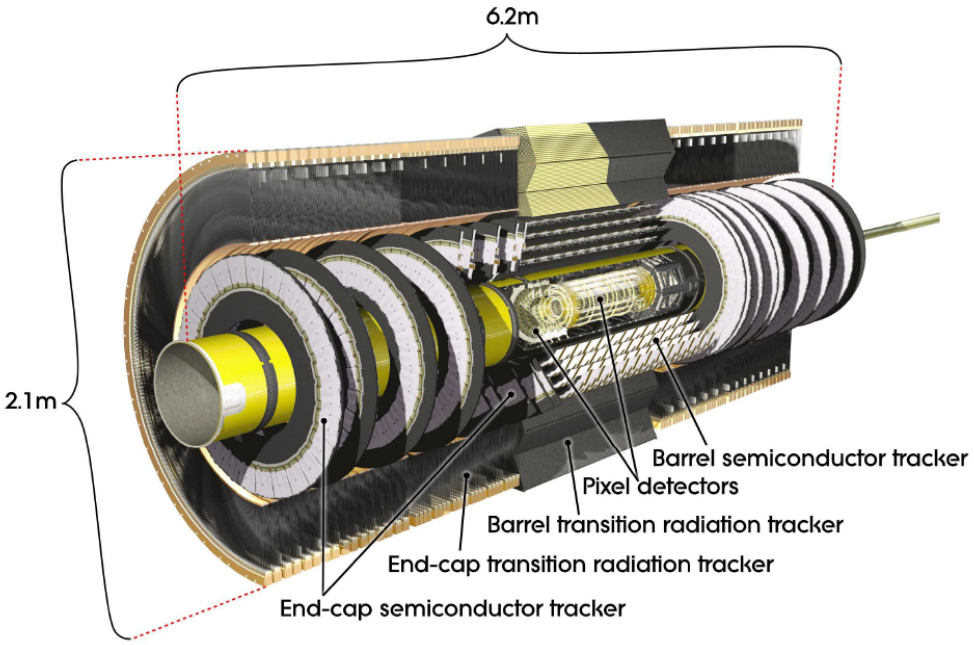

Figure 5.7: A cut-away diagram of the overall construction of the ATLAS inner detector, labelling the individual components.

The inner detector functions within a 2 tesla (T) magnetic field provided by an encasing solenoid magnet. The purpose of this field is to bend the paths of charged particles, introducing curvature to their tracks. This curvature assists in particle identification and momentum measurements. The material choice for the ID segments is also extremely important, due to the high-radiation environment in which is it required to operate, the materials must be radiation-

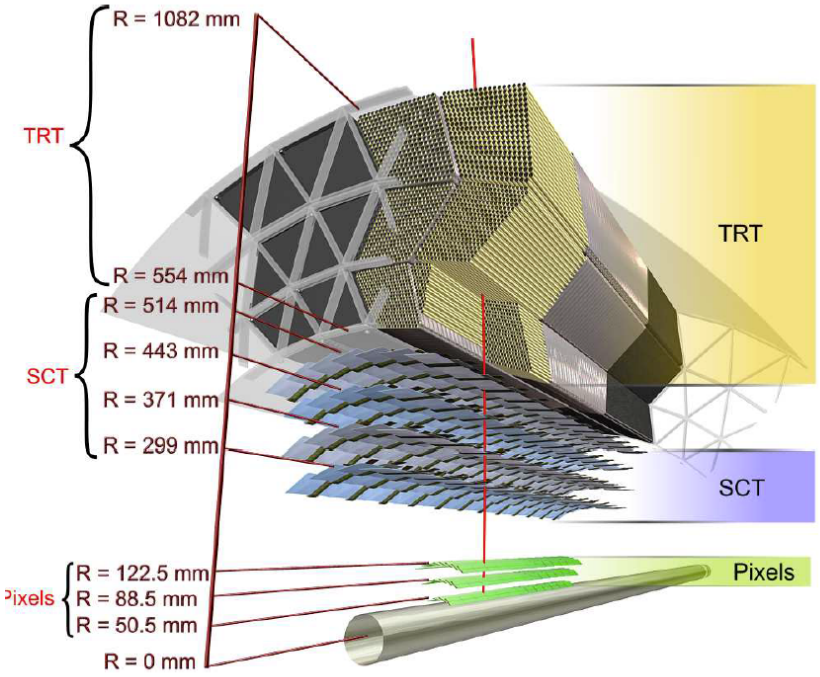

Figure 5.8: A cut-away diagram of the overall construction of the ATLAS inner detector, with detailed structure of the Pixels, SCT and TRT.

tolerant. At the centre of the ID is the beam pipe, which at the intended collision point in the ATLAS experiment is 0.8 mm thick, with an internal radius of 29 mm and made from beryllium due to it's high-transparency to particles.

The Pixel Detector wraps around the beam pipe and consists of three layers of oxygen-doped silicon wafers. The silicon is an n-type extrinsic semiconductor, which generates electron-hole pairs as charged particles pass through. It is treated with oxygen impurities in order to reduce total radiation damage from charged hadrons. After ionisation from charged particles, the electron-hole pairs drift in opposite directions under a potential difference ranging from 150 V-600 V (depending on pixel ageing), and upon reaching the ends of the pixel are detected as *hits*. There are 1744 sensors, each with 47232 pixels of approximate size $50\times400\,\mu m^2$, are arranged in concentric layers combined with three end-cap plates to cover a total pseudorapidity range of $|\eta|< 2.5$ with an intrinsic track position resolution of 10 µm in the $R-\phi$ plane and 115 µm in the z-plane [1]. The innermost pixel layer is commonly referred to as the B-layer due to its importance in identifying the presence of secondary vertices due to b-hadron decays. However it should be noted that for Run-2 an additional layer has been introduced in the form of

an instrumented beam-pipe known as the *insertable B-layer* (IBL), bringing the total number of pixel layers to 4. The IBL was introduced to improve the resolution on track parameters, in the face of higher pile-up for precision measurements such as for the Higgs boson ($H \rightarrow bb$ being an important decay channel), and to recover lost performance due to pixel failures from radiation intensity in the existing *B*-layer.

The Semi-Conductor Tracker is built from silicon strips rather than squares but has a similar purpose. Four layers of double-sided micro-strip sensors are placed at increasing radii, complemented by 9 SCT plates in the end-cap. Each strip provides 2 hits for precise tracking, and a total intrinsic resolution of 17 μm in the $R-\phi$ plane and 1580 μm in the z-plane [1].

The Transition Radiation Tracker uses substantially different technology to cover the outermost region of the ID. Transition radiation occurs when charged particles move between volumes of material with different dielectric constants, related to the difference in electric fields in each medium. The amount of radiation produced is dependent on the traversing particle's Lorentz Factor $\gamma = \frac{E}{m}$ and therefore lighter particles emit more radiation this way. The intensity of the radiation is proportional to the particle energy E. Combining the two effects provides some information for particle identification. The TRT consists of proportional drift tubes filled with a mixture of xenon (70%), carbon dioxide (27%) and oxygen (3%) gas. The drift tubes each contain four *straws*; cylindrical negatively charged cathodes around singular (31 μm diameter) anode wires. Inside each drift tube polypropylene foil is placed between the straws in order to provide the material-transitions required for the generation of transition radiation. As a particle passes through the drift tube, the transition radiation ionises the gas mixtures and the ionised electrons move towards the central anodes before being read out as electrical signals. Multiple signals are then recombined to determine a particle's trajectory. Although 52544 straws are present in the barrel, and 122880 are radially aligned in the end-caps, an average particle will only produce 35-40 hits.

5.2.2 Calorimetry

In particle physics detection, particle energies can be determined by placing absorption materials in the path of the decay products of a pp collision, by then counting the number of photons which are produced. The ATLAS experiment employs *sampling calorimeters*, these are systems which alternate between layers of absorption material (to induce particle interactions) and detection

material, known as an *active medium* (AM). Homogeneous calorimeters use the same material for absorbing and collecting particle energy. As sampling calorimeters cannot ensure that 100% of the measurable energy is deposited in the AM, the total energy contained follows the relation for the sampling fraction

$$f_{\text{samp}} = \frac{E_{\text{dep}}^{\text{AM}}}{E_{\text{dep}}^{\text{cal}}}, \tag{5.4}$$

where $E_{\text{dep}}^{\text{AM}}$ is the energy deposited into the AM, and $E_{\text{dep}}^{\text{cal}}$ is the total energy deposited into the calorimeter. The sampling fraction will depend on the materials chosen for the AM (for which also the calorimeter response, i.e. the efficiency of the AM in collecting energy, must be considered) and their relative thickness with respect to the absorption layers. This requires a scaling factor to be applied to determine the true particle energy, and the calibration is usually performed using minimally ionising particles of well known initial energy.

Electrons and photons may be detected by the ATLAS electromagnetic calorimter (ECAL). On traversing an absorber, an electron has some probability to interact and produce a single photon via bremsstrahlung (braking-radiation). Photons may also pair produce into electron-positron pairs. This creates what is known as an EM *shower* in the material. For EM interactions this is described by the *radiation length* X_0 of a material. The radiation length is the distance in a material through which an electron would have to travel to be reduced in energy to a factor of $\frac{1}{e}$ of its initial energy E_0

$$E = E_0 e^{\frac{-x}{X_0}}, \tag{5.5}$$

where (E,x) describe the energy and position of the particle at time of measurement.

Hadrons may be detected by the HCAL. On traversing the absorber the hadrons will experience nuclear interactions and create more hadrons of lower energy, this process repeats until the initial particle energy has been fully absorbed. The structure created by the decay chains of the hadrons is much larger and often travels much further than an EM shower, it is instead called a *jet*. About 30% of activity within a jet is EM showers from $\pi^0 \to \gamma\gamma$ decays. The relevant material property for nuclear interactions is the *interaction length* λ_0.

The calorimeters need to be long enough to cover enough X_0 or λ_0 lengths to contain all of the energy of EM showers and hadronic jets. Failure to contain the energy from a particle

decay is known as *punch-through* and leads to issues of fake signals in subsequent detector layers. Punch-through from the HCAL may leave a signal in the muon spectrometer and fake the signature of a muon.

Electromagnetic Calorimeter

The ECAL is made of lead absorption plates layered with liquid argon as the active medium for energy deposition. Lead is a high density material to minimise the X_0, and has a total thickness of $\sim 24X_0$ in the barrel and $\sim 26X_0$ in the end-caps. Liquid argon (LAr) is chosen as the active medium due to its intrinsic radiation hardness. The barrel region of the ECAL covers a pseudo-rapidity range of $|\eta|< 1.475$ and the two end-caps extend this range to $1.375 < |\eta|< 3.2$. There is however a *crack* region excluded from measurements, $1.37 < |\eta|< 1.52$, so-called because there is too much non-detector material (such as cabling) which makes calorimetry unreliable. The barrel sections of the ECAL follow an accordion geometry in order to be fully hermetic in the ϕ space, and are split into 16 modules of $\Delta\phi = 22.5^\circ$ each. The end-cap sections are built from two wheels behind an additional LAr presampler. Each wheel is divided into an inner and outer wheel, consisting of eight segments to again fully cover the required ϕ geometry.

Hadronic Calorimeter

The HCAL consists of both a barrel and an end-cap. The barrel section uses different materials to the rest of the detectors in order to provide the high-density environment required to minimise the interaction length λ_0 and minimise the overall size (and cost) of the detector. For the region of $|\eta|< 1.7$ it uses steel absorption layers alternated with scintillating tiles. The scintillating tiles induce production of ultraviolet scintillation photons as ionising particles pass through. These photons are collected, shifted to lower-wavelengths by doped fibres, and are directed towards photomultiplier tubes for measurement of the total energy. The total thickness corresponds to 9.7 λ_0. The end-caps of the HCAL however again use LAr, as greater radiation-hardness is required for the more forward region, combined with copper absorbers due to its slightly smaller nuclear interaction length. The end-caps consist of two wheels at each end, each split into 32 segments, and covers the range of $1.5 < |\eta|< 3.2$.

Forward Calorimeter

The forward calorimeter (FCAL) system is included to extend the range in η of ATLAS's calorimetry capabilities. Positioned inside the ECAL and HCAL end-caps close to the beam pipe, the FCAL again employs LAr active layers, interspersed with copper (for EM) and tungsten (for hadronic) absorbers to cover a pseudorapidity region of $3.1 < |\eta| < 4.9$. This is extremely high-radiation region includes only the most forward-physics, as such data from this section of the detector is not commonly found in physics analyses.

5.2.3 Muon Spectrometer

The MS is of paramount importance to the analysis presented in this thesis as it provides the basis for detection of muons, used (along with the ID) for jet *b*-tagging by the soft muon tagger (Section 7). Whilst interacting electromagnetically, muons do not get absorbed by the ECAL as their large mass minimises the energy loss through bremsstrahlung, which is proportional to $\frac{E}{m^2}$. Energy loss due to ionisation is inversely proportional to the energy of a particle also, and so at collision energies used by the LHC the resultant muons are able to escape the detector - although still leaving detectable hits in the ID and MS as they travel. Muons are also not absorbed by the HCAL again due to minimal energy loss through bremsstrahlung, and as unlike hadrons they do not undergo strong nuclear interactions. The MS has three purposes; to distinguish muon tracks in the ID from other charged particles (by combining the tracks in the ID with tracks in the MS), to provide high resolution muon momentum measurements using a combined ID-MS track under ATLAS's magnetic fields, and to provide fast muon-trigger information (see Section 5.2.5) for data taking. The MS is subject to the second magnetic field in the ATLAS detector, generated by toroids and explained in detail in Section 5.2.4. The MS is designed to have a resolution of $\sigma_{p_T} \sim 10\%$ for 1 TeV tracks, and $\sigma_{p_T} \sim 4\%$ for muons in the momentum range relevant to this anaysis. The MS, consists of both barrel and end-cap regions, with a total coverage of $|\eta| < 2.7$. For tracking, the majority of the barrel and end-cap sections used monitored drift tubes (MDT), except for the innermost end-cap for which cathode-strip chambers (CSC) are used, due to the improved capabilities in the higher-radiation region of $2 < |\eta| < 2.7$ which impacts upon the quality of pattern recognition and muon reconstruction efficiency. For triggering, the inner ($|\eta| < 1.05$) barrel region uses three concentric layers of resistive plate chambers (RPC) whilst the outer ($1.05 < |\eta| < 2.4$) region uses thin gap chambers (TGC) to deal with the high-particle-

intensity.

Tracking

Monitored drift tubes are pressurised with a mixture of argon (93%) and carbon dioxide (7%) gas, with a central tungsten-rhenium wire under a potential difference of 3080 V. With similar functionality to straws, ionising particles passing through the gas will drift towards the central point and register as a signal. This requires an average drift time of $\sim$ 700 ns and provides an average resolution of $\sim$ 80 µm per tube. Multiple tubes are then stacked together for each chamber to improve the total resolution to about 35 µm.

Cathode-strip chambers are radially-oriented multi-wire proportional chambers with several layers to resolve multi-track ambiguities. The wires act as the anodes above the orthogonally-oriented cathode strips. The total precision achieved by the CSCs is on the order of 60 µm per plane, for a total of about 40 µm in r and 4 mm in ϕ.

Triggering

Resistive plate chambers are 2 mm-separated charged plates between which an ionisable gas and a large potential difference is applied (the electric field is of the order 4.9 kV mm^{-1}). Passing charged particles will ionise and produce electron avalanches. As there are three layers, the potential for up to six measurements in η and ϕ is provided. The RPCs provide a low-p_T trigger for (three out of four) hits in two layers, and a high-p_T trigger for at least one hit in each of three layers, with a signal width in the region of 5 ns.

Thin gap chambers are similar in functionality to CSCs, as they are multi-wire proportional chambers. In this case however instead of precision tracking, the TGCs are used to provide a trigger signal within 25 ns of a particle passing combined with a lower resolution position coordinate.

5.2.4 Magnet system

The ATLAS detector uses multiple superconducting magnets (three toroids and one solenoid) to achieve the large fields used for bending charged particles to measure their momenta. The magnets are large and as such dominate multiple areas of the detector, which must be considered when calculating total X_0 and λ_0 lengths for event reconstruction and detector simulations.

The central solenoid (CS) surrounds the ID and creates a 2 T axial magnetic field to bend the paths of charged tracks. It is designed to introduce minimal radiation lengths into the detector mass and shares a vacuum vessel with the inner ECAL calorimeter.

The barrel toroid (BT) consists of eight air-core racetrack-shaped coils, which generate a total magnetic field of (up to 3.9 T but averaging) 0.5 T for the MS system.

The end-cap toroids (ECT) also consist of eight coils, offset by 22.5° to the BT, and generate a total of (up to 4.1 T but on average) 1 T for the MS in the higher pseudorapidity region.

5.2.5 Triggers and Data Acquisition

The trigger and data acquisition (TDAQ) system at the ATLAS detector is responsible for reacting to and recording events of interest. It has been changed substantially during LS1, but the description given is here as appropriate for Run-1 data taking. ATLAS employs a three-stage system. At design performance, the raw data output from the ATLAS detector if taken in full would be overwhelming with a rate of about 50 TBs^{-1}. This is prohibitively large, given a realistic data storage rate closer to 300 MBs^{-1}, and is due to the design bunch crossing rate of 40 MHz. Even during the 8 TeV run, a rate of 20 MHz was used. The vast majority of bunch collisions do not yield "interesting" physics. Low energy processes with large cross-sections dominate the output stream, and whilst these are useful for calibration and re-determination/rediscovery of known physics phenomena, the vast yield effectively gets in the way of new physics searches and measurements. The task of the three-stage system therefore is to reduce the output of known "uninteresting" physics to an acceptable level, allowing for efficient usage of the limited storage and recording speed, this is sometimes referred to as *online selection* and requires the definition of *prescales* to reduce recording rates by predetermined factors. It is a system which must be carefully managed, to minimise bias and prevent the accidental removal of new physics processes which could be missed.

The level 1 trigger (L1) is a hardware-based solution which acts first for each pp collision. The L1 uses physical signatures of electrons/photons in ECAL, jets/τ's in the HCAL, high-p_T muons in the MS, or large missing momentum to decide whether an event should be recorded. Only low-granularity information is required, coming from the MS RPC and TGC and the calorimeter subsystems (the ID is not required due to the more complex readout). The decision is only based on the multiplicity of signals. During 8 TeV data taking, the L1 trigger was

required to make this decision within about 2.5 µs and reduce the output rate to 70 kHz, with the back flow of collision information held in a buffer known as the read-out system (ROS). If the L1 trigger decides an event should be recorded, it defines a *region-of-interest* (RoI) to be used as a seed in the next stage of the triggering system. An RoI defines the physical region of each detector segment which led to an L1-acceptance and in which there is likely to be interesting physics signals.

The level 2 trigger (L2) occurs on a processing farm and uses information within the RoIs handed to it by the L1 and ROS to perform basic event reconstruction. An RoI only contains coordinates, energies and types of signatures to minimise the data transfer, although the L2 does have access to the full granularity of the detectors within the RoI, as well as tracking information from the ID. L2 selections then follow preset criteria and can process many bunch-crossings in parallel. During 8 TeV data taking, the L2 was required to make a decision within about 75 ms and reduce the output rate to 6.5 kHz. Decision parameters include shower shapes, matches between tracks and clusters, and missing momentum thresholds.

The event-builder (EB) acts after the L2 but before the final stage of the triggering system. It collects together all available information from a given event which has passed an L2 decision and assembles a single formatted data structure for further use. An average event might produce a file of approximately 1.3 MBs.

The event filter (EF) is the final stage of the online selection process. The EF has the advantage of having the fully reconstructed event and running in parallel over large computing farms. At 8 TeV it was only required to make a decision on each event within 1 s. The decisions for the EF are largely based on specific physics criteria, and the events are separated into various physics *streams* for offline analysis, where a single event may appear in multiple streams.

The L2, EB and EF are commonly referred to as the *high-level trigger* (HLT).

The design event rates and processing times for the ATLAS detector, alongside those achieved during the 8 TeV run, are shown in Table 5.1 [31].

	Collisions	L1	L2	EF
8 TeV	20 MHz	70 kHz (2.5 µs)	6.5 kHz (75 ms)	1 kHz (1 s)
Design	40 MHz	75 kHz (2.5 µs)	4.0 kHz (40 ms)	300 Hz (4 s)

Table 5.1: Design event rates and processing times compared to the 8 TeV rates for the ATLAS detector.

So get some more guys and it'll be a fair fight

James Tiberius Kirk

Chapter 6

Data simulation and object selection

6.1 Monte Carlo simulation

Monte Carlo (MC) is the name given to simulations of collision events at particle colliders. At the LHC it is required to model the propagation of physics processes resulting from pp collisions all the way to final state particles which may be detected by the instrumentation, in order to make predictions for the expected event signals for each decay process of interest in analyses. The simulations include the initial hard-scattering interactions, the underlying parton interactions, the parton shower (PS), hadronisation, the decay of the resultant hadrons and gluonic and photonic radiation throughout the whole process. It also includes the mapping of the aforementioned processes onto the detector instruments and the production of simulated output signals utilising the same reconstruction algorithms as are applied to data.

6.1.1 Event generation

Event generators for the LHC start from the point of pp (shown as incoming objects in green on both sides of Figure 6.1 [62]) collisions producing hard-scattering interactions. Matrix element information (describing partonic interactions) is combined with parton density functions (PDFs) to calculate the cross-section for different hard-scattering processes, where the PDFs describe the probability of a particular parton (quark or gluon, shown in blue) with a particular momentum fraction of the total proton momentum being present to partake in the interaction (central red circle). Once a hard-scattering interaction is modelled for a particular collision, the output particles from the interaction (shown in red) undergo parton showering. Parton showering de-

scribes the propagation of coloured objects (quarks, gluons) including the emission of gluons from quarks, and the production of quarks from gluon splitting. The remaining objects are then recombined via hadronisation (shown in pale green) into colourless hadrons, which may continue to decay (dark green). Interactions of objects not involved in the hard-scattering process (including proton remnants) are referred to as the underlying event (shown in purple), this constitutes multiple QCD processes with their own decays otherwise known as pile-up. The yellow parts of the diagram represent electromagnetic emissions.

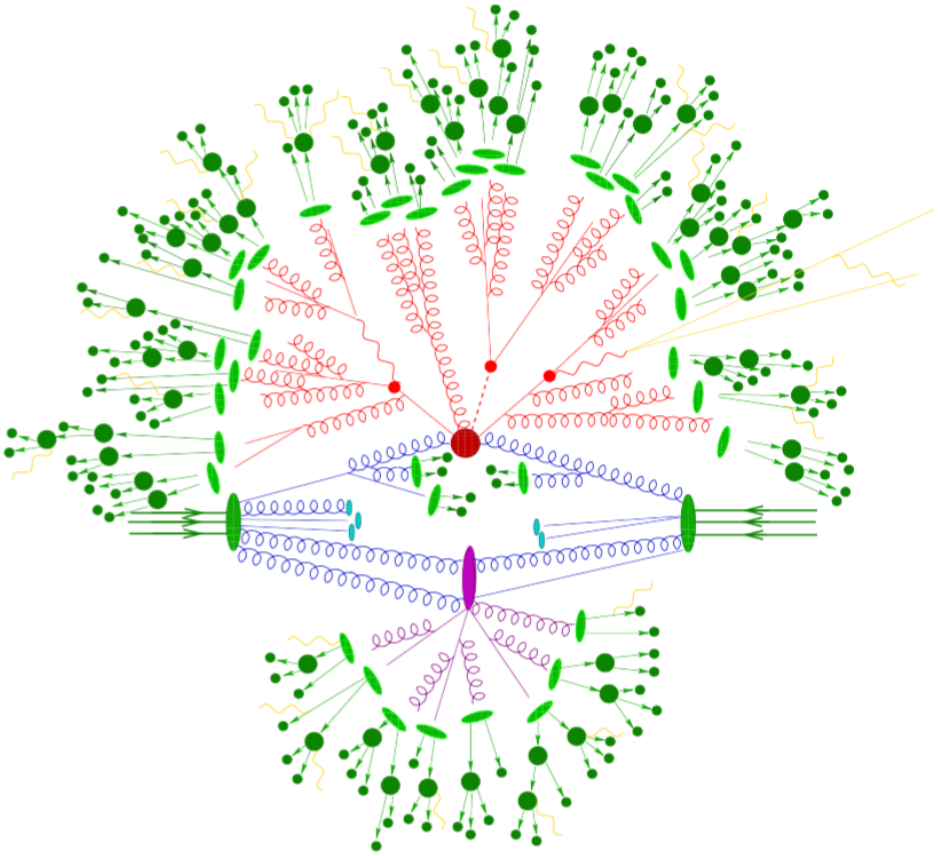

Figure 6.1: Diagrammatic representation of proton-proton collisions as segmented by event-generators.

A summary of the MC simulation tools used in this analysis and their main features is given in Table 6.1 [63]. Often separate generators and parton shower models are combined to improve the precision of event simulation. This requires 'matching' [64] to be performed to connect the 'short-distance' matrix element calculations from generators to the 'long-distance' descriptions for parton showering, without double-counting initial- and final-state radiation.

Name	Type	Key Features
POWHEG [65]	Generator	Generates heavy-quark pair production at NLO accuracy using matrix elements. Able to decay top quarks including spin correlations. May be interfaced to HERWIG or PYTHIA to perform parton showering.
MC@NLO [66]	Generator	Generates heavy-quark pair production at NLO accuracy using matrix elements. Allows for reweighting to different parton distribution functions. May be interfaced to HERWIG or PYTHIA to perform parton showering.
HERWIG++ [67]	Generator Parton Shower	Simulates hard lepton-lepton, lepton-hadron and hadron-hadron scattering, and soft-hadron-hadron collisions at LO. LO simulations using hard-coded matrix elements, or $2 \rightarrow 2$ matrix element calculations. Detailed simulation of QCD parton showers. Initial- and final-state radiation at NLO uses POWHEG formulism. Hadronisation based on colour-confinement cluster model [63].
PYTHIA6 [68]	Generator Parton Shower	Simulates hadron-hadron hard scattering, or lepton-lepton hard scattering between same-generation leptons at LO. Parton showering for initial- and final-state radiation is based on colour-dipoles stretched between two final state partons. Hadronisation is based on the Lund string model [69, 70].
ALPGEN [71]	Generator	Matrix element calculations at LO for parton-level QCD and electroweak interactions. Specialises in W+jets and Z+jets hard processes. Requires parton showering processes to be performed by HERWIG or PYTHIA.

Table 6.1: Summary of MC simulation tools used in this analysis and their key features.

6.1.2 Detector simulation

A tool-kit known as GEANT4 [72] contains all available information regarding the material construct of the ATLAS detector. This includes the functionality and alignment of each component, detailed descriptions of the wiring and support structures, and maps of the magnetic fields. The generated events are passed through GEANT4 in order to simulate the interactions of the particles with the detector mass, and the modelling of further particle decays due to these interactions, such as the formation of electromagnetic showers in the ECAL. Following modelling of particle decays with the detector, the response of the instrumentation is simulated and output signals from each section (ID, ECAL, HCAL, MS) are propagated to the same reconstruction algorithms (Sections 6.2- 6.2.6) as used for data. This results in the production of the simulated event output known as MC which may be directly compared to the measurements made during

data taking. A secondary technique for detector simulation, which is an order of magnitude faster, is 'ATLFASTII (AFII)' [73–75]. Whilst GEANT4 utilises the full detector information, AFII fully models the ID and MS but parameterises the response of the calorimeters as a function of the active material in the detector. AFII is use to simulate some of the systematic MC samples in this analysis.

6.2 Object reconstruction

The algorithms which utilise output signals from the detector and predict the particle (and their properties) which caused them, perform a task known as *object reconstruction*. The reconstruction of objects relevant to $t\bar{t}$ ℓ+jets decays requires numerous algorithms.

6.2.1 Vertices and Tracks

As described in Section 5.2.1 the ID is designed to provide a series of spacepoints following the transitions of charged particles through its layers. The first few spacepoints are used to define track *seeds* which are then extended to further layers to form track *candidates*. Each candidate track, from different combinations of the spacepoint hits within the ID, is provided a weight by comparing to a large selection of pre-simulated potential combinations of all spacepoints in the ID with the magnetic field taken into account. This procedure is an implementation of the Kalman Filter, in which each new material layer represents an opportunity to for the track to take a number of different paths, and fitting each different 'fork' provides the relevant weights. Tracks candidates below a particular weight are removed and in cases where ambiguities appear between multiple tracks (the same spacepoints are utilised in multiple separate track candidates), the tracks with the largest weights are kept. Quality conditions are then enforced (for example no track may miss a certain number of detector hits in its path) and the selections are refitted using the full ID information. The primary vertex (PV) for an event is decided by selecting the reconstructed vertex (feeding the spacepoints backwards to the beam pipe) which has the largest associated momentum.

6.2.2 Electron reconstruction

Electron reconstruction at ATLAS relies on the combination of ID and ECAL information. Association is required between reconstructed tracks and energy deposits (*clusters*) in the ECAL. Clusters are reconstructed using seed energy deposits with a transverse energy of at least 2.5 GeV [76], using MC $W \to e\nu$ and $Z \to e\bar{e}$ decays and the expected efficiency for high energy electrons ($E_T > 20$ GeV) nears 100%. Tracks with $p_T > 0.5$ GeV are extrapolated out of the ID and into the ECAL to be compared to the cluster seed position in (η, ϕ), and are considered matched if $|\Delta\eta| < 0.05$ and $|\Delta\phi| < 0.1|$, where the larger $\Delta\phi$ criterion is required to account for the effect of bremsstrahlung. Multiple track matches with ECAL clusters are distinguished by selecting the track with the most spacepoints and the smallest ΔR to the cluster seed. In the absence of matching tracks, ECAL clusters are considered to be photon candidates instead. Hard-scatter electrons are separated from those originating from pair production from photons by checking for multiple tracks which match the ECAL cluster but share a displaced vertex. The matching of a cluster with a track forms an electron candidate. Electron candidates then undergo cluster size optimisation. This process determines the measured energy of the electron candidate by varying the window in the ECAL for which deposited energy is to be associated with the candidate. It must take into account several factors; the energy loss of the electron in the ID, the energy deposited in the ECAL cluster, the correction required as part of the sampling calorimeter technique, energy deposited outside of the cluster and energy which may leak beyond the length of the ECAL. These are mostly estimated using MC simulations as functions of η and ϕ. Confirmation of electron candidates as real electrons requires the criteria to be met for the properties of the cluster and track variables. Electrons may be classified as *loose, medium* or *tight* in accordance with the strictness of the selection criteria applied. These are discussed in detail in [76] and in Appendix C. Muultiple criteria are provided in order to allow optimisation of object selection on an analysis-to-analysis basis, by providing different levels of background-rejection countered by different levels of electron identification efficiency.

An additional selection of *tight++* uses isolation requirements to further separate electron candidates from other activity such as jets, although these requirements may optimised in accordance to the needs of each analysis. Isolation requirements may take several forms [77]:

- **Calorimeter-based isolation**. The sum of transverse energy deposited in the calorimeter

cells in a cone of size ΔR around the electron is given the label $E_T^{\text{cone}\Delta\text{R}}$. The standard cone sizes for ATLAS analysis are $\Delta R = 0.2, 0.30.4$. The contribution to $E_T^{\text{cone}\Delta\text{R}}$ within $\Delta\eta \times \Delta\phi = 0.125 \times 0.175$ of the electron cluster barycentre is removed, and the total is corrected for energly leakage from the electron shower into the isolation cone. A correction is also applied to account for pileup as a function of the number of reconstructed vertices.

- **Momentum-based isolation**. The scalar sum of the transverse momentum of the tracks with $p_T > 0.4$ GeV in a cone of size ΔR around the electron is given the label $p_T^{\text{cone}\Delta\text{R}}$. The electron track itself is excluded, and all other tracks must originate from the same primary vertex, must have at least nine silicon hits and must have a hit on the innermost pixel layer (for quality control).

- **Track-based isolation**. The number of tracks within a cone around the electron, satisfying the same criteria as the momentum-based isolation, is labelled $N_{\text{trk}}^{\text{cone}\Delta\text{R}}$.

6.2.3 Muon reconstruction

Muon reconstruction at ATLAS may rely on information from the MS only, or on the combination of ID and MS information [78] as described below. In the context of this analysis, hard-muons from W-boson decays are reconstructed using the MUID [79] algorithm, whilst soft-muons from semileptonic b-decays are reconstructed using the STACO [80] algorithm.

- Standalone reconstruction: This technique utilises hits in the MS only. Pattern recognition (on each MS chamber individually) is applied to the MS hit spacepoints and straight line fits are applied, these fits are referred to as *segments*. Segments from all three MS chambers are then combined to perform a full track fit including the magnetic field effects, and extrapolation back to the primary vertex is performed accounting for expected energy loss for the muon through the detector material. Standalone reconstruction is a prerequisite to both the MUID and STACO algorithms, although the exact method differs. For MUID the standalone reconstruction employs the 'Moore' algorithm [79] which looks for hit patterns using a Hough transformation. For STACO the standalone reconstruction employs the 'Muonboy' algorithm, which builds tracks radially inwards starting from the outermost muon station.

- Tagging ID tracks: This technique tags ID tracks using additional information from the MS or calorimeters, and it is utilised to recover muons in areas with limited MS coverage. ID tracks extrapolated to the MS and associable with at least one MS segment track are labelled as *segment-tagged*. ID tracks extrapolated to the ECAL and associable with an energy deposit compatible with a minimum ionising particle are labelled as *calo-tagged*. Both techniques may be utilised to complement the MUID and STACO algorithms.

- Combined reconstruction: This technique requires explicit combination of ID and MS information. Standalone MS tracks may be extrapolated using different methods back to the ID, and matched with existing ID tracks to create a single muon track candidate. The power of this technique is in improvement in the resolution of spacial and kinematic muon measurements using all available information. The MUID combination technique performs a full track refit using all of the spacepoints in the ID and MS, whereas the STACO combination performs a statistical combination (using a χ^2 fit) of ID and MS track parameters; $\eta, \phi, p_T, d_0, z_0$. Ambiguous ID-MS track combinations are resolved by choosing the track-pair with the best χ^2.

All muons for use in analyses need to satisfy a set of requirements recommended by the Muon Combined Performance (MCP) [81] group to ensure quality criteria are met as in the points below, where TRT outliers describe either straw tubes with a signal which are not crossed by the track, or TRT track hits which failed to form a smooth trajectory with the pixel and SCT. The MCP cuts are used to reduce contamination from fake tracks and punch-through.

- MCP Cuts:
  - N(Pixel hits) + N(crossed dead pixel sensors) > 0
  - N(SCT hits) + N(crossed dead SCT sensors) < 4
  - N(Pixels holes) + N(SCT holes) < 3
  - Track extension into the TRT:
    - If $0.1 < |\eta| < 1.9$: N(TRT hits) + N(TRT outliers) > 5 and N(TRT outliers) ≤ 0.9(N(TRT hits) + N(TRT outliers))
    - if $|\eta| \geq 0.1$ or $|\eta| \leq 1.9$: If N(TRT hits) + N(TRT outliers) > 5 then require N(TRT outliers) ≤ 0.9(N(TRT hits) + N(TRT outliers))

For this analysis, hard muons are required to fulfil the MUID criteria as per the default selection for ATLAS top-quark analyses. The soft muons from semileptonic b-decays are required to fulfil the STACO selection because of historical reasons; the previous iteration of the soft muon tagger utilised a χ^2 match between ID and MS tracks, which is more in-line with the construction of a STACO muon. MUID is considered to be a slightly higher efficiency algorithm (good for identifying muons coming from the W-boson decay), whilst STACO has better fake rejection (good for improving the purity of the SMT tags).

6.2.4 Jet reconstruction

The hadronisation and subsequent decay of quarks and gluons as they traverse the detector results in the formation of cones of particles known as jets. Jets comprise of chains of hadronic decays producing increasingly soft hadrons until the full energy of the decay is absorbed by the hadronic calorimeter. Jets also contain electromagnetic components primarily from $\pi^0 \to \gamma\gamma$ decays. Jet reconstruction algorithms attempt to rebuild the original parton interaction from the combination of all reconstructed particles in the jet, by clustering together the energy deposits in the calorimeters into a single object. Some constraints must be considered in the reconstruction of jets, such as infrared and collinear safety. Infrared safety describes the requirement for the number of reconstructed jets to be independent from the effects of soft gluon emissions, such as in Figure 6.2 [82]. Collinear safety describes the requirement for the number of reconstructed jets to be independent from the effects of collinear splittings, such as in Figure 6.3 [82]. The ATLAS default reconstruction algorithm is called anti-k_T and is described below.

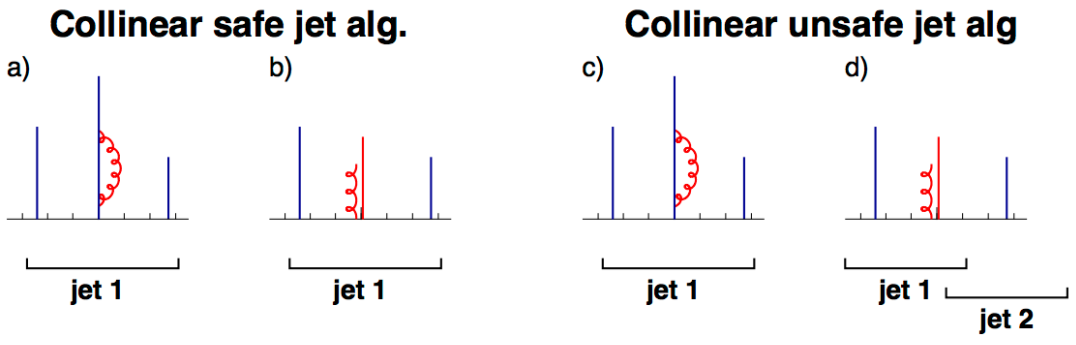

Figure 6.2: A representation of a collinear safe algorithm (left) for which the number of jets is not modified due to the soft gluon emissions in (a) and (b). A collinear unsafe algorithm is also represented (right) for which the number of jets reconstructed is altered by the same emissions, between (c) and (d). The verticle lines represent partons with the height of each line proportional to their transverse momentum, the horizontal axis indicates rapidity.

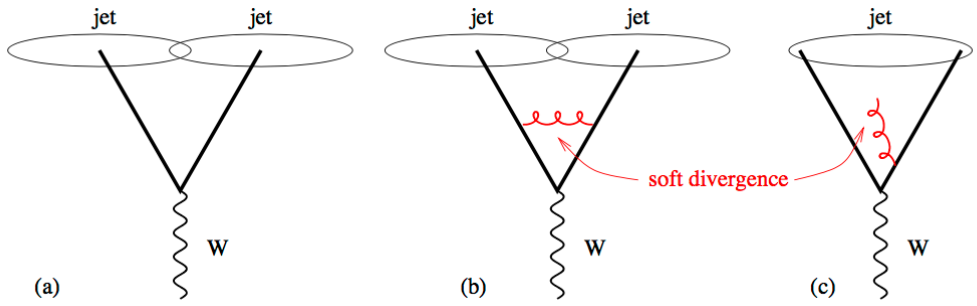

Figure 6.3: A representation of two jets (a) which remain as two jets when reconstructed with an infrared safe algorithm (b), but converge to a single jet when reconstructed using an infrared unsafe algorithm (c).

Anti-k_T algorithm

Sequential recombination algorithms such as the anti-k_T algorithm [83] work by building jets by iteratively considering particle combinations until certain conditions are met. Two variables may be defined; $d_{i,j}$ as the distance between two calorimeter cells with energy deposits, and $d_{i,B}$ as the distance between calorimeter cell i and the beam axis

$$d_{ij} = \min\left(k_{ti}^{2p}, k_{tj}^{2p}\right)\frac{\Delta_{ij}^2}{R^2}, \tag{6.1}$$

$$d_{iB} = k_{ti}^{2p}, \tag{6.2}$$

where $\Delta_{ij}^2 = (\Delta y_{ij})^2 + (\Delta\phi_{ij})^2$, k_{ti} is the transverse momentum of particle i, y_i is the rapidity, and ϕ is the azimuthal angle. The parameter R defines the intended radius for a jet, and the parameter p varies to specify the type of sequential recombination algorithm invoked; $p = 1$ is the inclusive k_T algorithm, $p = 0$ is the Cambridge/Aachen (C/A) algorithm, and $p = -1$ is the anti-k_T algorithm.

The anti-k_T algorithm considers all pairs of calorimeter cells i, j and calculates in each case d_{ij} and d_{iB}, if $d_{ij} > d_{iB}$ then the energy deposits in the two cells are combined to form the prototype of a jet, and the process continues until $d_{iB} > d_{ij}$ when the jet is considered fully constructed, and any remaining objects may begin to form the prototype for a second jet. This method is infrared and collinear safe as soft emissions are inclined to combine with hard jet prototypes before combining with one another. The radius parameter R is set to 0.4 as default in

ATLAS analyses, and objects at a distance of $2R$ or greater apart will form separate jets.

The behaviour of recombination algorithms using variables of this form depend greatly on the choice of the parameter$p$. The differences in behaviour are shown in Figure 6.4 [83], which represents the reconstruction a parton-level event surrounded by $\sim 10^4$ random soft particles. The k_T and C/A algorithms reproduce jets with jagged edges and considerable dependence on the soft particles. An additional algorithm, SISCone [84] produces more desirably circular shapes, however fails to sensible reconstruct a boundary between the hard (light green) jet and the soft (purple) jet next to it. The anti-k_T algorithm however creates uniformly shaped jets with sensible boundaries dependent on the relative p_T of nearby objects.

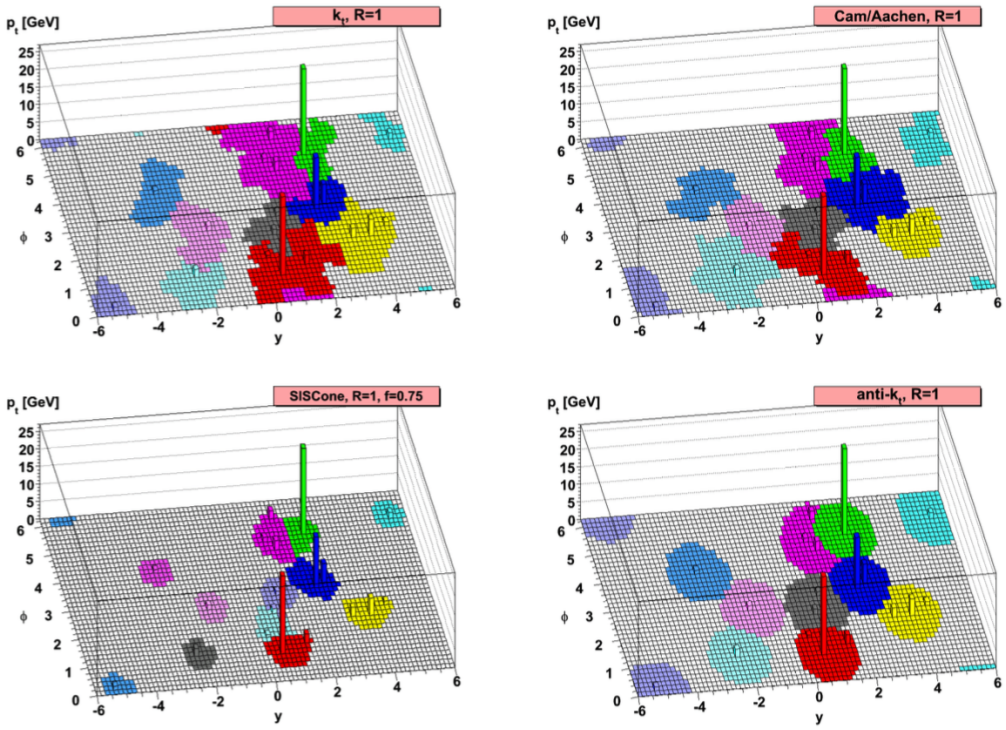

Figure 6.4: Four examples of jet reconstruction on a parton-level event generated with $\sim 10^4$ random soft particles. The k_T and C/A algorithms show dependency on the distribution of the soft particles. The anti-k_T algorithm is less influenced by soft radiation and produces uniformly shaped jets.

Jet calibration

The ATLAS HCAL has a different response for the electromagnetic and hadronic components of jets. Jets must have their measured energy corrected for this effect, and for other issues which

could lead to the incorrect determination of the energy of the initial partons, such as pile-up, PV alignment and non-instrumented areas of the detector. Groups of clusters of energy deposits in the calorimeter are known as *topo-clusters*, shower shape variables are used to determine if the clusters should be reconstructed at the electromagnetic scale (EM scale) as EM components tend to be shorter, or at the hadronic scale (called *local cluster weighting*, or the 'LCW' scale), as hadronic jets tend to penetrate further into the calorimeter due to the relative size of the hadronic and electromagnetic interaction lengths. The energy calibrations for the EM and LCW scales are derived from MC simulations. After a scale has been set, the remaining aforementioned corrections are applied to produce either the EM+JES or LCW+JES scales, where JES is the *jet energy scale*. The resulting jet energies measured in simulation should then match those from data.

6.2.5 b-Tagging techniques

The identification of jets from the decay of heavy flavour b- or c-quarks is critical to many physics analyses, from CP violation studies such as described in this thesis, to $H \to b\bar{b}$ cross-section measurements. The identification b-jet decays is known as b-tagging and there are numerous strategies for performing this task. A few techniques are described below:

- **Secondary vertex tagging (SV0, SV1):** b-hadrons are relatively long-lived particles which travel a greater distance in the ATLAS detector than other hadrons. Their decays then result in track vertices which are separated from the IP by a measurable distance, and can be reconstructed to identify the jet as a b-jet.

  A long-lived b-hadron will travel a distance of the order $d = \beta\gamma c\tau$, where $\beta = \frac{v^2}{c^2}$, $\gamma = \frac{E}{m}$ is the Lorentz factor, c is the speed of light, and τ is the average lifetime of the particle ($\tau \sim 10^{-12}$s for B-hadrons). Using $\beta\gamma = \frac{p}{m} = \frac{\sqrt{E^2 - m^2}}{m}$, a neutral b-hadron with an energy $E = 50$ GeV may travel a distance of approximately $d \sim 5$ mm.

  Secondary vertex taggers utilise the distance d as the discriminating variable for b-tagging jets, and must apply appropriate requirements on this length to define the tagging efficiency at different working points (a looser requirement will result in a high efficiency but a low purity from the large number of fakes). This is the technique of the SV0 algorithm.

  The SV1 algorithm extends the technique by considering additional variables such as the

ratio of energy assigned to the tracks in a jet to the energy assigned to tracks associated with the primary vertex. The additional parameters are combined into a likelihood fit to increase the performance of the tagger.

- **Multivariate tagging (MV1):** Multivariate taggers intake numerous jet variables such as secondary and tertiary vertex positions, topological information, track invariant mass reconstruction, and output from other taggers, and pass them through multivariate algorithms such as boosted decision trees and neural networks. The MV1 tagger is a neural network calibrated by ATLAS to separate b-jet decays from light-flavour (LF) jets, the performance for which is shown in Figure 6.5 [85] for a collision energy of $\sqrt{s} = 8$ TeV. The MV1 tagger uses as its input, the output discriminants of several other taggers:
  - SV1: As described above, a vertex based tagger.
  - IP3D: A tagger based on the transverse and longitudinal track parameters d_0, z_0.
  - JetFitter: A topology based tagger, which discriminates on the basis of the number of vertices with at least two tracks, the total number of tracks at each vertex, the number of additional single track vertices, the mass attributed to each vertex, the energy of the particles associated with each vertex as a fraction of the total energy associated to the jet, and the flight length significance (L/σ_L for each vertex).

  Alternate versions of the MV1 tagger exist, labelled MV1c, which are trained to provide extra rejection against c-jets [85]. The working points calibrated at $\sqrt{s} = 8$ TeV for the MV1 tagger discussed later in this thesis are shown in Table 6.2 [86].

Tagger	b-jet efficiency (%)	Purity (%)	c-jet rejection factor	LF-jet rejection factor
MV1	70	92.28	4.97	136.66
MV1	80	85.41	3.08	25.18
MV1	85	76.86	2.38	9.66
MV1c	70	92.52	5.32	122.87
MV1c	80	85.92	3.04	27.30

Table 6.2: Working Points for the MV1(c) tagger as calibrated at ATLAS for Run 1 collisions at $\sqrt{s} =$ 8 TeV.

- **Soft lepton tagging:** Soft lepton taggers, such as the soft muon tagger described in detail in Section 7 identify jets from heavy-flavour (HF) decays by exploiting the $\sim 21\%$ $b \rightarrow$

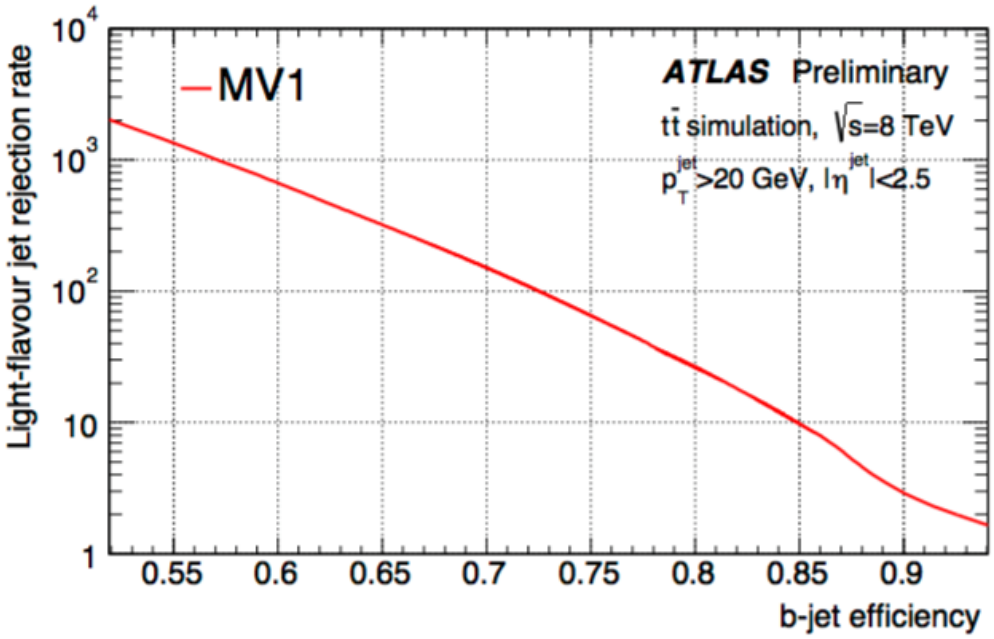

Figure 6.5: A curve to show the light-flavour rejection rate for given b-jet efficiencies of the MV1 b-tagging algorithm, measured on 8 TeV MC simulated top-quark pair events.

$(c) \rightarrow \mu$ semileptonic branching ratio. Semileptonic HF decays within jets result in a collinear electron or muon within the jet, usually with a low p_T distribution. Soft electron tagging is very challenging and not utilised at ATLAS, it would require the reconstruction of a low energy EM shower aligned with a jet. The jet itself would have EM components in the ECAL and the two would likely be indistinguishable. Soft muon tagging on the other hand is viable, as the MS is the outermost layer of ATLAS and the jet energy is usually fully absorbed by the detector prior to this region. Collinear muons from the decay of HF hadrons within jets may still be identified as hits in the MS aligned with the jet axis. Sources of fakes for soft muon taggers includes the decay-in-flight of other hadrons such as pions or kaons, and punch-through of highly energetic jets into the MS. A soft muon tagger may be calibrated using variables related to the muon to reject fakes. The soft muon tagger calibrated in this thesis utilises the fractional difference in momentum between a track candidate as measured in the ID, and as measured in the MS when extrapolated back to the ID, this is known as the Momentum Imbalance (MI):

$$\mathrm{MI} = \frac{p^{\mathrm{ID}} - p^{\mathrm{ME}}}{p^{\mathrm{ID}}} \tag{6.3}$$

As muons are minimally ionising particles, a soft muon produced from a semileptonic b-decay will lose only a small amount of energy as it traverses the detector and the fractional difference in momentum will be very small. Tracks in the MS aligned with ID tracks associated to charged hadrons and their decays, or punch-through hits in the MS associated with any ID tracks, will show a larger fractional difference in momentum and a larger value of MI, as shown in Figure 6.6.

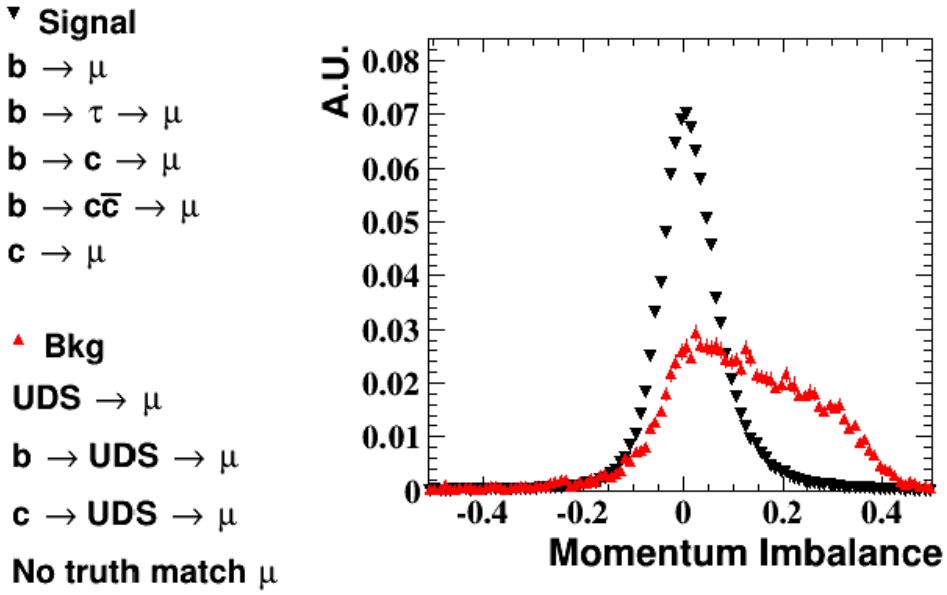

Figure 6.6: The momentum imbalance distribution of 'signal' soft muons, and 'fakes' from the decay of non-b-hadrons comprised of u-, d- or s-quarks ('UDS'), using $t\bar{t}$ MC. The area under each distribution has been normalised to unity.

Table 6.3 gives the performance of the soft muon and MV1 b-tagging algorithms, as well as they combined (justified in Section 8) when applied to the 8 TeV $t\bar{t}$ MC simulation used in this analysis.

6.2.6 Missing momentum reconstruction

Due to the unknown momentum fractions carried by colliding partons in any single event, the total initial momentum of colliding objects in the z-direction cannot be determined. However

Tagger	b-jet efficiency (%)	c-jet rejection factor	LF-jet rejection factor	Purity (%)
SMT	10.35	21.41	206.08	84.96
MV1@%85	85.19	2.36	11.18	78.77
SMT+MV1@85%	9.16	43.18	1546.55	94.43

Table 6.3: Performance of the SMT and MV1 b-tagging algorithms, including their combination, using the 85% MV1 working point. Performance measured on $t\bar{t}$ MC for $\sqrt{s} = 8$ TeV, for events which pass the pretag selection discussed in Section 8

.

as the colliding partons to good approximation will have zero momentum in the x- and $y-$ directions, it can be assumed that the total initial (and therefore final) momentum for those components (the transverse momentum) should sum to zero. In events for which the sum of transverse momentum does not equal zero, it must be assumed that an undetected particle (e.g. a neutrino) has escaped undetected, the imbalance in transverse momentum is called missing energy E_T^{miss}. The ATLAS strategy for the reconstruction of missing energy is described in detail in [87]. The missing transverse energy is defined as the quadratic sum of the x- and y-components

$$E_T^{\text{miss}} = \sqrt{\left(E_x^{\text{miss}}\right)^2 + \left(E_y^{\text{miss}}\right)^2}. \tag{6.4}$$

Each section of the detector must be taken into account when calculating the missing energy,

$$E_{x(y)}^{\text{miss}} = E_{x(y)}^{\text{miss,calo}} + E_{x(y)}^{\text{miss,MS}}, \tag{6.5}$$

where $E_{x(y)}^{\text{miss,calo}}$ represents the contribution from the calorimeters, where each contribution has been associated with an identified object type ($e/\gamma, \mu$, jets), and $E_{x(y)}^{\text{miss,MS}}$ represents the contribution from the muon spectrometer. Both are assisted by tracking information in the ID, to assist in the inclusion of low-p_T objects which fail to reach the calorimeters, and to improve the removal of fake MS hits from punch-through by only using combined ID-MS tracks.

That which does not kill us makes us stronger

Friedrich Nietzsche

Chapter 7

Calibration of the Soft Muon Tagger

Determination of jet flavour is critical to many physics analysis at ATLAS. Precision measurements of the SM (such as top quark and Higgs boson production cross-sections) and searches for new physics (NP) often rely on the identification of heavy-flavour (HF) jets. The most commonly used tools include vertex taggers, which exploit the relatively long-lifetimes of b- and c- hadrons which result in secondary particle production vertices identified in the ATLAS inner detector (ID). The soft muon heavy-flavour tagging algorithm (SMT) is designed to identify reconstructed jets from the decays of B-hadrons by exploiting the $\sim 21\%$ branching ratio for semileptonic $b \to (c) \to \mu$ decays. This branching ratio results in a tagger with an overall lower efficiency than vertex based tagging algorithms, however on the subset of events for which a soft muon exists a working point may be calibrated with is very efficient and has a good light-jet rejection. The SMT is a complementary tool which does not use vertex information. It focuses on the subset of events with semileptonic b- and c- decays and is sensitive to alternate systematic uncertainties. The calibration of a tagger is required to account for differences in performance when applied to data and to MC, and results in a set of scale factors (SF) to account for such differences. The calibration of the SMT is based on the momentum imbalance (MI) between a muon track found in the inner ID and a track in the muon spectrometer (MS) extrapolated back to the ID (ME). Selecting jets to tag based on this parameter allows for good light-jet rejection. As the SMT depends only on the quality of agreements between muon tracks as measured in the ID and MS, the calibration of the tagger does not require the presence of a jet. The calibration may be performed using isolated $J/\psi \to \mu\mu$ low-p_T muons and $Z \to \mu\mu$ high-p_T muons. This chapter will describe the calibration of the tagger for the ATLAS 8 TeV data set. I updated the

calibration code for the tagger at 8 TeV to use the momentum imbalance parameter, from the previous iteration of a track-based χ^2 technique [19], within the existing infrastructure.

7.1 Tag and Probe

Tag and probe is a well-defined technique for obtaining data-driven performance estimates. The technique attempts to utilise a 'pure' selection of events in data on which to calibrate algorithms, as the closest equivalent to a MC study where the truth information is always known. A data sample is obtained (following the selection requirements in Section 7.1.2) containing $J/\psi \to \mu\mu$ events. Each event is expected to contain two muon tracks; one is required to satisfy stringent criteria to ensure (as best as possible) that it is a muon track from a J/ψ, this track is the 'Tag' and requires the combination of an MS and ID track. A pool of secondary tracks (the 'Probes') satisfy less stringent criteria and are ID tracks only. The Tag is then paired with any Probe tracks which generate the correct invariant mass (within a window) when combined with the Tag. For the purpose of this tagger calibration a subset of Probes known as the 'MuonProbes' are defined, where a MuonProbe is a Probe track in the ID able to be combined with a track in the MS. The fraction of Tag and MuonProbe pairs out of the total number of Tag and Probe pairs is defined to be the combined muon reconstruction efficiency ($\varepsilon_{\text{reco}}$), as in Equation 7.1. On this subset the performance of the SMT tagger may then determined. The fraction of Tag and MuonProbe pairs for which the MuonProbe satisfies the SMT requirements, out of all Tag and MuonProbe pairs, is defined to be the efficiency of the SMT MI (ε_{MI}), as in Equation 7.2. The aforementioned Data/MC scale factors are defined as the ratio between the measurement efficiencies, in each relevant region of phase space, as in Equation 7.3.

$$\varepsilon_{\text{reco}} = \frac{J/\psi \text{ reconstructed from Tag and MuonProbe pair}}{J/\psi \text{ reconstructed from Tag and Probe pair}} \tag{7.1}$$

$$\varepsilon_{\text{MI}} = \frac{J/\psi \text{ reconstructed from Tag and MuonProbe pair, MuonProbe passes SMT cuts}}{J/\psi \text{ reconstructed from Tag and MuonProbe pair}} \tag{7.2}$$

$$\text{SF} = \frac{\varepsilon_{\text{MI}}^{\text{data}}}{\varepsilon_{\text{MI}}^{\text{MC}}} \tag{7.3}$$

7.1.1 Collision data and Monte Carlo samples

The data included in the calibration of the SMT represents 20.3 fb^{-1} of LHC Run 1 collisions. This included events which passed a numerous triggers, but the largest fraction are provided by the EF_mu6_Trk_JPsi_loose trigger. This trigger selects events which have at least one muon with a momentum greater than 6 GeV and an ID track which combines with the muon to produce an invariant mass in the window of 2.6 GeV $< m_{\text{inv}} <$ 3.6 GeV, around the J/ψ mass. Two MC $J/\psi \to \mu\mu$ samples are used with generator-level criteria to require that the two relevant muons had total momentum greater than 2.5 GeV and 4.0 GeV respectively.

7.1.2 Selection

The Tag and Probe selections are listed in this section. The criteria are divided into sections for each object type. Kinematic requirements are always applied on measurements made in the ID as it has better resolution than the MS, and all tracks must initially satisfy a set of requirements recommended by the Muon Combined Performance (MCP) [81] group to ensure quality criteria are met, as described in Section 6.2.3.

The Tag selection is detailed in the points below. The first four requirements focus on signal selection, whilst the remaining two are to reduce the contamination from pile-up and decay-in-flight hadrons. The last two requirements are selections on the impact parameters and their resolutions, where d_0 is the distance in the $x-y$ plane between the primary vertex and the start of the track, and z_0 is the equivalent shift along the z-axis. The Probe and MuonProbe selections are then detailed, before the criteria required to pair a Tag and a Probe muon. The pairing requirements are designed to identify objects which could come from a J/ψ decay, however overlap requirements are enforced to reduce the possibility of the same track pairing with itself due to misreconstruction. To improve the reconstruction efficiency, each Tag is permitted to pair with several Probe tracks. This introduces more combinatoric pairings than allowing only the nearest Probe in z_0, however these are removed along with other backgrounds by fitting within an invariant mass window, as will be described in Section 7.2. This technique retains higher statistics of correct Tag and Probe pairs than could otherwise be achieved. Finally, the SMT requirements are detailed at the end. These SMT requirements are the tagger specific criteria as used in an analysis setting, however as the calibration is performed on isolated muons any

requirements associating a muon with a jet are not utilised for this study.

- Tag selection:
  - STACO collection
  - Combined muon
  - $p_T > 4$ GeV
  - $|\eta| < 2.5$
  - $|d_0| < 0.3$ mm and $|z_0| < 1.5$ mm
  - $\left|\frac{d_0}{\sigma_{d_0}}\right| < 3$ and $\left|\frac{z_0}{\sigma_{z_0}}\right| < 3$
- (Muon)Probe selection:
  - ID Track
  - $p_T > 4$ GeV
  - $|\eta| < 2.5$
  - MuonProbe only: $\Delta R\,(\text{Probe track}, \text{Combined muon}) < 0.01$
- Tag and Probe pairing selection:
  - $0.2 < \Delta R\,(\text{Tag}, \text{Probe}) < 3.5$
  - Tag and Probe have opposite charge
  - $\Delta z_0 < 0.2$ mm
  - 2 GeV $\leq m_{(\text{Tag,Probe})} \leq 4$ GeV
- SMT selection:
  - $\Delta R_{\mu}^{\text{jet}} < 0.5$ (not for calibration with isolated muons)
  - $|\eta| < 2.5$
  - $p_T > 4$ GeV
  - $|d_0| < 3$ mm
  - $|z_0 \cdot \sin\theta| < 3$ mm
  - MI < 0.1

The momentum imbalance requirement in the SMT selection is defined as the difference in the total momentum of a track measured in the ID (p^{ID}), and a track measured in the MS extrapolated back to the ID (p^{ME}), as a fraction of the total momentum of the track measured in the ID. This is shown in Equation 7.4, and the calibration working point is chosen to be MI < 0.1.

$$\mathrm{MI} = \frac{p^{\mathrm{ID}} - p^{\mathrm{ME}}}{p^{\mathrm{ID}}} \tag{7.4}$$

The MI distributions for all Probe candidates in data and MC which pass the selections are shown in Figure 7.1.

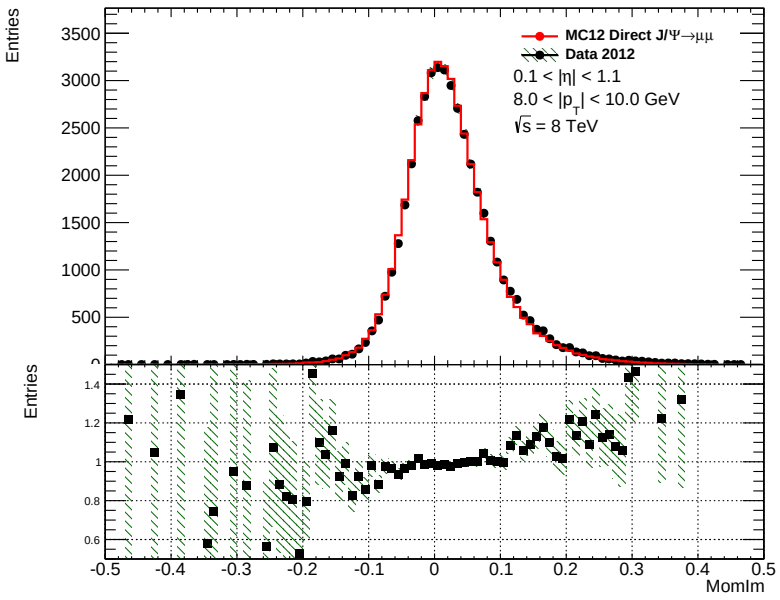

Figure 7.1: The momentum imbalance distribution of all MuonProbe candidates in both 2012 Data and MC12 Monte Carlo simulation. The integral of the Monte Carlo distribution has been normalised to that of the data.

7.2 Invariant mass fitting and background subtraction

It is possible for non-J/ψ pairs of muons or other tracks to satisfy the selection and enter into the calibration sample. This includes a combinatoric background of wrong Tag and Probe pairings, and also a continuous Drell-Yan ($q\bar{q} \to \gamma/Z \to \ell^+\ell^-$ distribution. It is important to remove these contributions to measure the efficiency of the tagger correctly. The distribution of

the invariant mass of Tag and Probe pairs shows a peak around the invariant mass of the J/ψ, $m_{J/\psi} = 3.097$ GeV, with shoulders either side indicating the distribution of the background and combinatoric pairings. A sideband fit may be performed for the underlying background distribution and also a fit for the combined background+signal. This allows for the extraction of the number of background pairings and their subsequent subtraction. The background distribution is fit with a quadratic polynomial, and the integral under the fit is subtracted from the total of the binned data. This remaining data is used as the signal, rather than relying on an accurate fit of the signal peak. However, to extract the width of the signal peak, used in the determination of the overall uncertainties described in Section 7.2.1, a Gaussian fit is applied in tandem to the signal peak region in order to extract the width of the function. An illustrative example is given in Figure 7.2, and the real fit is performed automatically for every bin in the (η, p_T) range considered, an example of which is shown in Figure 7.3 and the full results of which are shown in Figure 7.4- 7.11. The invariant mass range between $2.7 - 3.5$ GeV is utilised, and for each fit the mean is not constrained although it is expected to be close to $m_{J/\psi}$. The actual background subtraction is applied in the region of 3σ around the mean. For the Tag and Probe pairs, the remaining events after subtraction are used as the denominator of Equation 7.1. For Tag and MuonProbe pairs, the remaining events after subtraction are used the numerator of Equation 7.1 and the denominator of Equation 7.2.

7.2.1 Uncertainty measurement

The uncertainty assigned to the measured efficiencies consists of multiple components. The total is the quadratic combination of a binomial statistical uncertainty, $\sigma_{\text{stat.}}$, and two systematic uncertainties based on the fit; the first is the difference in efficiency as measured for a 3σ and 5σ range around the distribution mean σ_{sig}, the second is the difference between maximal and minimal background estimations from variation of the fit polynomial σ_{bkg}.

The statistical uncertainty is the binomial error, for efficiency ε out of total pairings N.

$$\sigma_{\text{stat.}} = \sqrt{\frac{\varepsilon(1-\varepsilon)}{N}}. \tag{7.5}$$

The first systematic uncertainty relating to the fit is obtained by comparing the measured efficiencies according to the 3σ and 5σ windows around the mean, labelled $\varepsilon_{3\sigma}$ and $\varepsilon_{5\sigma}$. The mean and widths are determined by the Gaussian fit to the signal peak. The central value used

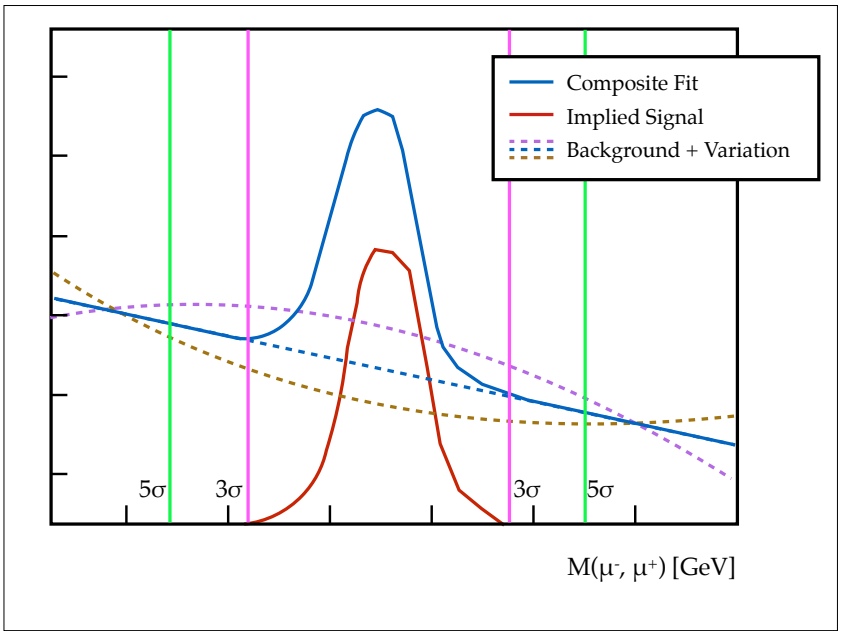

Figure 7.2: Illustration of the fitting procedure. Note the composite fit function made of a Gaussian plus a 2nd-order polynomial (blue), the background fit and the respective maximum and minimum variation (dashed lines) and the implied signal Gaussian (red). The integration window shown for the nominal 3σ range (pink) and the wider 5σ range for uncertainty (bright green). The lines drawn are for illustration purposes only.

for the efficiency calculation is the 3σ value.

$$\sigma_{\text{sig}} = |\varepsilon_{5\sigma} - \varepsilon_{3\sigma}| \tag{7.6}$$

The second systematic uncertainty relating to the fit is obtained by varying the polynomial function used in the background estimation. The nominal function takes the form

$$f(x) = ax^2 + bx + c\ . \tag{7.7}$$

Alternate 'maximal' and 'minimal' functions are created by varying each parameter away from their central values by the uncertainties determined by the fit. This produces the upper and lower variations as shown in Figure 7.2 following the functions

$$f^{\text{up}}(x) = a_{\text{min}}x^2 + b_{\text{max}}x + c_{\text{min}}, \tag{7.8}$$

$$f^{\text{down}}(x) = a_{\text{max}}x^2 + b_{\text{min}}x + c_{\text{max}}. \tag{7.9}$$

The uncertainty is defined as the average difference between the efficiencies obtained using these shifts and the nominal, where

$$\varepsilon_{\text{nominal}} = \frac{N^{\text{nominal}}_{\text{numerator}}}{N^{\text{nominal}}_{\text{denominator}}}, \tag{7.10}$$

$$\varepsilon_{\text{up}} = \frac{N^{\text{up}}_{\text{numerator}}}{N^{\text{down}}_{\text{denominator}}}, \tag{7.11}$$

$$\varepsilon_{\text{down}} = \frac{N^{\text{down}}_{\text{numerator}}}{N^{\text{up}}_{\text{denominator}}}. \tag{7.12}$$

The final uncertainty is given by

$$\sigma_{\text{bkg}} = \frac{1}{2}\left(\left|\varepsilon_{\text{up}} - \varepsilon_{\text{nominal}}\right| + \left|\varepsilon_{\text{down}} - \varepsilon_{\text{nominal}}\right|\right). \tag{7.13}$$

The total combination of all uncertainties on the efficiencies is then the quadratic sum of each effect, as given by Equation 7.14.

$$\sigma_{\varepsilon} = \sqrt{\left(\sigma_{\text{stat.}}\right)^2 + \left(\sigma_{\text{sig}}\right)^2 + \left(\sigma_{\text{bkg}}\right)^2} \tag{7.14}$$

This uncertainty is calculated separately for data and MC and propagated through to the final SFs.

7.3 Efficiencies

The Data/MC SFs for the SMT efficiencies are dependent on kinematic and spatial variables. A key factor is the behaviour of the SFs as a function of isolation of the muons. If an isolation dependency exists then it would indicate that the calibration technique is unsuitable for a tagger required to function correctly in a jet environment. Dependency on the η and the p_T of the tracks is found, as in Figures 7.10 and 7.11. No overall asymmetry is observed with regards to the positive and negative pseudorapidity regions of the detector however there is a small deviation in the efficiency as a function of the Probe muon charge. The scale factors are therefore determined separately for positive and negative muons. An example in data of the invariant mass construction and fitting distributions is shown in Figure 7.3, the sharp shoulders on the

Region Name	Range
Crack	$0.00 < \|\eta\| < 0.10$
Barrel	$0.10 < \|\eta\| < 1.10$
Transition	$1.10 < \|\eta\| < 1.30$
End-cap	$1.30 < \|\eta\| < 2.00$
Forward	$2.00 < \|\eta\| < 2.50$

Table 7.1: List of the η ranges used in binning the scale factor and their respective names.

edge of these distributions are due to the triggers. Figures 7.6 and 7.11 show the dependency of the SFs on kinematic and spatial variables, and are presented as a function of p_{T} for all five detector regions (detailed in Table 7.1) in both sides A and C, separated by probe charge. Figures 7.4 and 7.5 indicate that the tagger is not sensitive to the isolation of the muons and therefore is suitable for use in a jet environment. The first isolation variable, $E_T^{\mathrm{cone}\Delta R}$ (*etcone*) describes the sum of the transverse energy deposited in the calorimeter cells around the fitted muon track, within a cone of size ΔR. The second variable, $p_T^{\mathrm{cone}\Delta R}$ (*ptcone*) describes the sum of the transverse momentum of the tracks around the muon track within a cone of size ΔR and the third variable $N_{\mathrm{trk}}^{\mathrm{cone}\Delta R}$ (*nucone*) describes the number of tracks around the muon track with within a cone of size ΔR. All isolation variables refer to the level of activity surrounding the muon. The SFs resulting from this study are all extremely close to 1.0 with uncertainties ranging from 0.5% to 15% depending on the p_T and η bin, although the vast majority are not larger than 2%. This shows good agreement between the performance of the SMT tagger on data and on MC and that the soft muons are well modelled. The largest uncertainties in the SFs appear in the crack, transition and forward regions. In the crack and transition regions the reconstruction of tracks is hindered due to the lack of instrumentation, and the uncertainties tend to increase towards high p_T (for all η-regions) due to the lack of available statistics. Lack of statistics is also the cause of the larger uncertainties in the forward region. The bulk of the data used in an 8 TeV analysis is in the barrel and endcap regions, with a peak in the p_T spectrum of the soft muon around $5-10$ GeV, this is the region in which the data/MC agreement is the strongest.
The SFs resulting from this study are detailed in Tables 7.2a- 7.2d.

7.3.1 $Z \to \mu\mu$

The J/ψ analysis is performed to calibrate the tagger for low-p_T muons. However to calibrate in the medium- and high-p_T regions more statistics may be gained from using $Z \to \mu\mu$ events. The

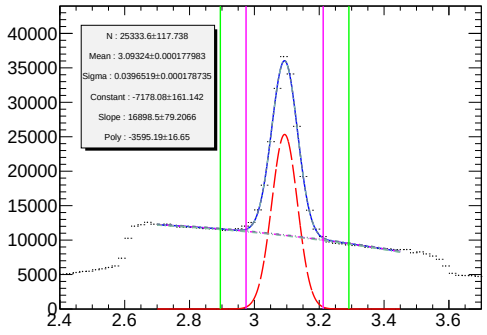

(a) Tag and Probe Invariant Mass.

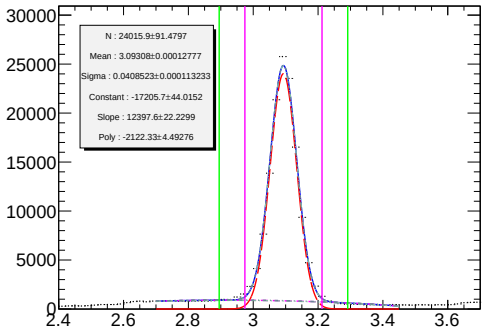

(b) Tag and MuonProbe Invariant Mass.

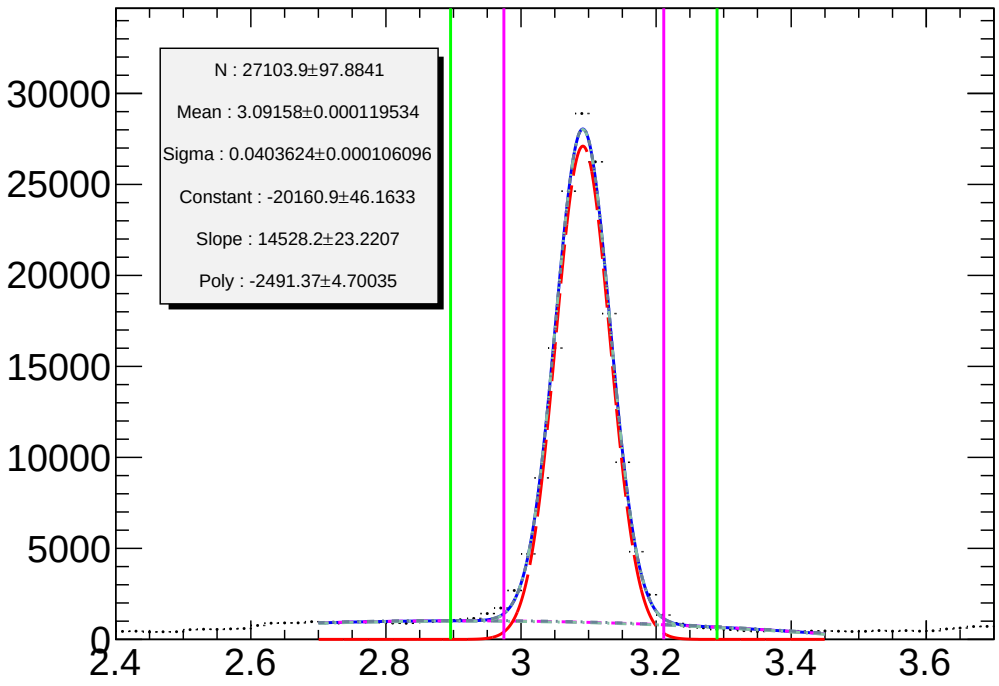

(c) Tag and Probe Invariant Mass, Probe passed SMT requirements.

Figure 7.3: Tag and Probe invariant mass, showing the fitted composite function (blue), the background fit, with maximum and minimum (dashed), the 3σ and 5σ ranges (magenta and green respectively), and an approximation of the signal distribution (red). Shown here are invariant mass distributions for all of the 2012 data, for probe muons with 4 GeV $< p_{\mathrm{T}} <$ 5 GeV, in the barrel region of the detector.

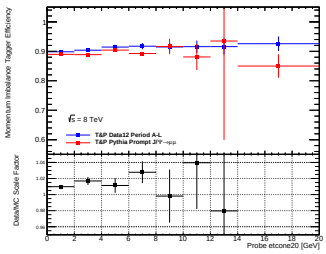

(a) MI efficiencies and Scale Factor against etcone20.

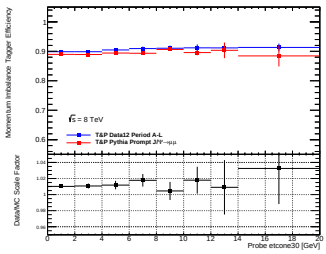

(b) MI efficiencies and Scale Factor against etcone30.

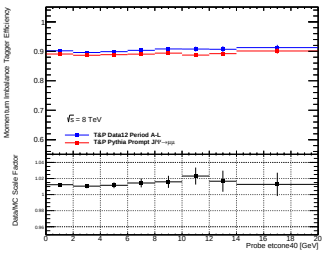

(c) MI efficiencies and Scale Factor against etcone40.

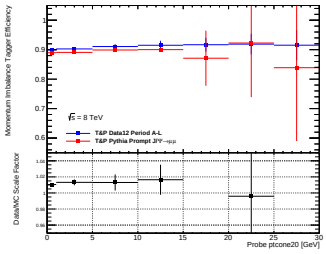

(d) MI efficiencies and Scale Factor against ptcone20.

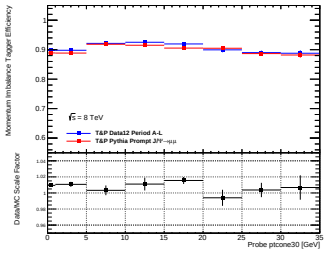

(e) MI efficiencies and Scale Factor against ptcone30.

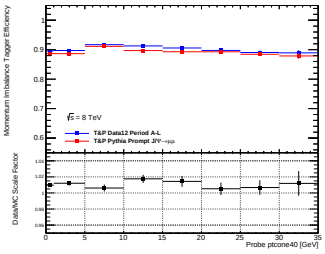

(f) MI efficiencies and Scale Factor against ptcone40.

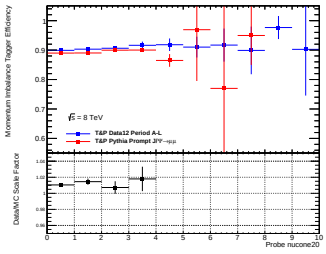

(g) MI efficiencies and Scale Factor against nucone20.

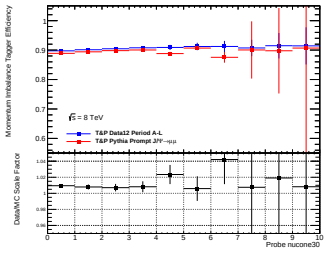

(h) MI efficiencies and Scale Factor against nucone30.

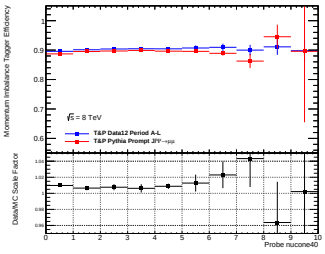

(i) MI efficiencies and Scale Factor against nucone40.

Figure 7.4: MI efficiencies and Data/Monte Carlo scale factor with respect to various isolation variables, for positively charged probes.

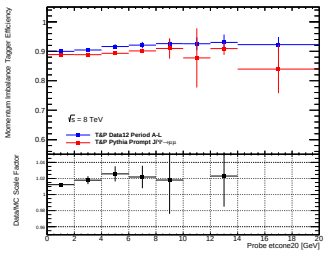

(a) MI efficiencies and Scale Factor against etcone20.

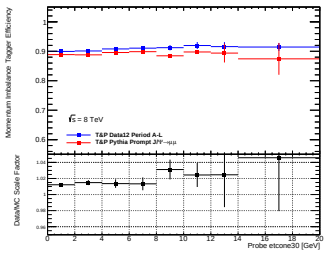

(b) MI efficiencies and Scale Factor against etcone30.

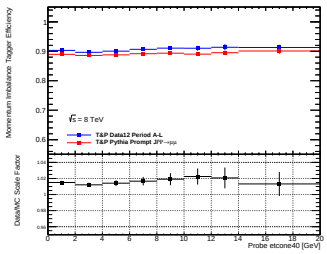

(c) MI efficiencies and Scale Factor against etcone40.

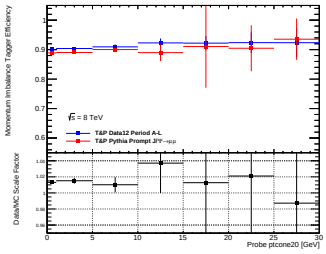

(d) MI efficiencies and Scale Factor against ptcone20.

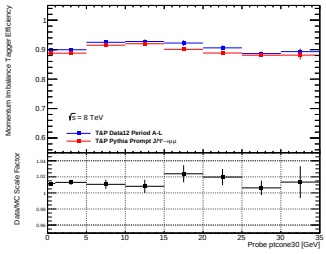

(e) MI efficiencies and Scale Factor against ptcone30.

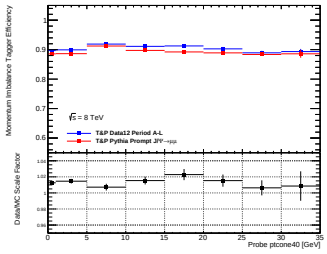

(f) MI efficiencies and Scale Factor against ptcone40.

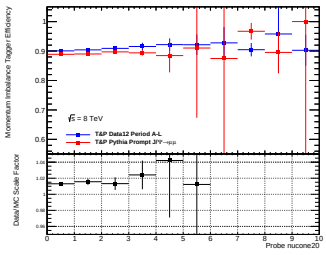

(g) MI efficiencies and Scale Factor against nucone20.

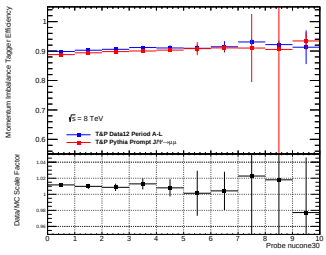

(h) MI efficiencies and Scale Factor against nucone30.

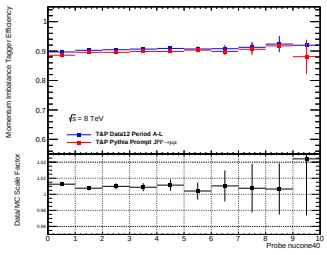

(i) MI efficiencies and Scale Factor against nucone40.

Figure 7.5: MI efficiencies and Data/Monte Carlo scale factor with respect to various isolation variables, for negatively charged probes.

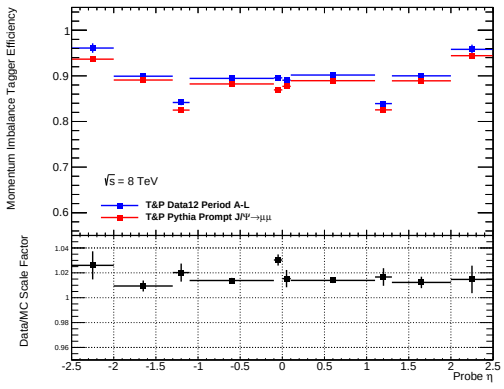

(a) MI efficiencies and Scale Factor with respect to the η of the positively charged probe.

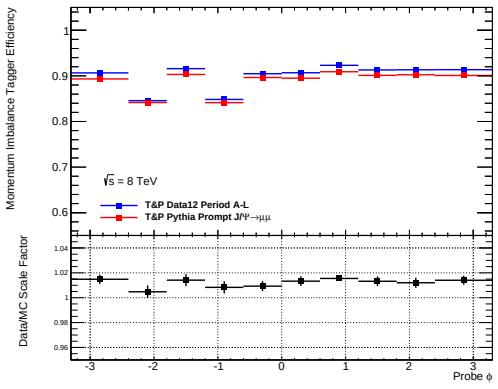

(b) MI efficiencies and Scale Factor with respect to the ϕ of the positively charged robe.

Figure 7.6: MI efficiencies and Data/Monte Carlo scale factors with respect to the η and ϕ of the positively charged probe.

Table 7.2: Data/Monte Carlo Scale Factors for 2012 Data in all five regions of the detector as a function of p_{T}, separated by probe charge. The uncertainties include systematic and statistical components

p_{T} range	Crack A	Barrel A	Transition A	End-cap A	Forward A
4-5 GeV	1.012 ± 0.006	1.011 ± 0.005	1.009 ± 0.018	1.005 ± 0.011	0.996 ± 0.024
5-6 GeV	0.998 ± 0.016	1.004 ± 0.005	1.016 ± 0.018	1.015 ± 0.012	1.026 ± 0.027
6-7 GeV	1.027 ± 0.016	1.010 ± 0.005	1.026 ± 0.015	1.018 ± 0.010	1.026 ± 0.024
7-8 GeV	1.018 ± 0.010	0.999 ± 0.006	0.999 ± 0.017	1.006 ± 0.012	1.017 ± 0.028
8-10 GeV	1.002 ± 0.009	0.998 ± 0.006	0.998 ± 0.018	1.003 ± 0.012	1.016 ± 0.030
10-12 GeV	0.990 ± 0.016	1.002 ± 0.004	1.021 ± 0.028	1.014 ± 0.021	1.000 ± 0.017
12-15 GeV	0.999 ± 0.039	1.009 ± 0.005	1.012 ± 0.039	1.001 ± 0.025	1.077 ± 0.058
15-20 GeV	0.977 ± 0.078	1.016 ± 0.006	1.004 ± 0.049	1.016 ± 0.031	1.022 ± 0.080

(a) For the positive η regions, with positively charged probes.

p_T range	Crack C	Barrel C	Transition C	End-cap C	Forward C
4-5 GeV	1.033 ± 0.019	1.011 ± 0.002	0.987 ± 0.017	1.002 ± 0.010	1.003 ± 0.022
5-6 GeV	1.011 ± 0.022	1.003 ± 0.002	1.015 ± 0.008	1.006 ± 0.011	1.026 ± 0.027
6-7 GeV	1.034 ± 0.011	1.004 ± 0.005	1.014 ± 0.017	1.012 ± 0.010	1.040 ± 0.024
7-8 GeV	1.025 ± 0.028	0.993 ± 0.006	1.007 ± 0.019	1.005 ± 0.011	1.041 ± 0.030
8-10 GeV	1.019 ± 0.015	0.997 ± 0.002	1.002 ± 0.018	1.006 ± 0.012	1.030 ± 0.030
10-12 GeV	1.015 ± 0.015	0.999 ± 0.004	1.011 ± 0.028	1.008 ± 0.019	1.06 ± 0.052
12-15 GeV	0.990 ± 0.024	1.000 ± 0.011	1.002 ± 0.015	0.997 ± 0.025	0.920 ± 0.057
15-20 GeV	1.031 ± 0.150	1.012 ± 0.014	1.023 ± 0.047	1.023 ± 0.029	1.089 ± 0.087

(b) For the negative η regions, with positively charged probes.

p_{T} range	Crack A	Barrel A	Transition A	End-cap A	Forward A
4-5 GeV	1.006 ± 0.019	1.000 ± 0.005	1.001 ± 0.008	1.006 ± 0.010	1.004 ± 0.022
5-6 GeV	1.009 ± 0.023	1.000 ± 0.005	1.013 ± 0.020	1.015 ± 0.012	1.027 ± 0.026
6-7 GeV	1.035 ± 0.011	1.004 ± 0.002	1.041 ± 0.009	1.024 ± 0.010	1.040 ± 0.025
7-8 GeV	1.027 ± 0.023	0.992 ± 0.006	1.043 ± 0.021	1.011 ± 0.012	1.043 ± 0.029
8-10 GeV	1.007 ± 0.012	0.991 ± 0.005	1.026 ± 0.019	1.016 ± 0.012	1.023 ± 0.031
10-12 GeV	0.994 ± 0.036	0.995 ± 0.009	1.028 ± 0.013	1.017 ± 0.019	1.027 ± 0.046
12-15 GeV	0.991 ± 0.050	0.995 ± 0.011	1.043 ± 0.037	1.014 ± 0.025	1.064 ± 0.071
15-20 GeV	1.007 ± 0.140	1.005 ± 0.014	1.074 ± 0.046	1.020 ± 0.031	1.090 ± 0.076

(c) For the positive η regions, with negatively charged probes.

p_T range	Crack C	Barrel C	Transition C	End-cap C	Forward C
4-5 GeV	1.041 ± 0.007	1.016 ± 0.005	1.014 ± 0.007	1.004 ± 0.011	1.022 ± 0.024
5-6 GeV	1.017 ± 0.017	1.010 ± 0.005	1.018 ± 0.017	1.016 ± 0.011	1.037 ± 0.026
6-7 GeV	1.030 ± 0.017	1.013 ± 0.005	1.014 ± 0.015	1.025 ± 0.010	1.043 ± 0.024
7-8 GeV	1.013 ± 0.020	1.000 ± 0.006	0.994 ± 0.016	1.019 ± 0.012	1.023 ± 0.030
8-10 GeV	0.995 ± 0.011	1.001 ± 0.005	0.993 ± 0.016	1.011 ± 0.011	1.017 ± 0.029
10-12 GeV	0.998 ± 0.029	1.003 ± 0.009	0.995 ± 0.024	1.016 ± 0.019	1.011 ± 0.046
12-15 GeV	0.993 ± 0.022	1.006 ± 0.011	1.011 ± 0.013	1.021 ± 0.026	1.058 ± 0.063
15-20 GeV	1.005 ± 0.133	1.012 ± 0.015	0.990 ± 0.026	1.031 ± 0.030	1.040 ± 0.093

(d) For the negative η regions, with negatively charged probes.

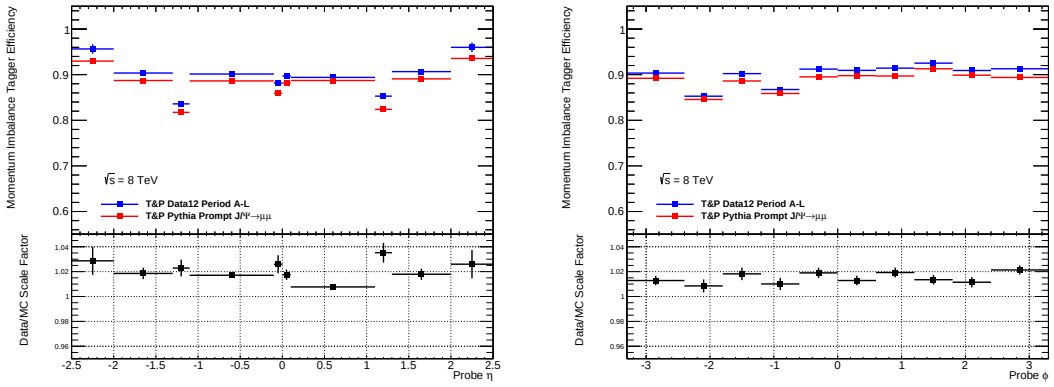

(a) MI efficiencies and Scale Factor with respect to the η of the negatively charged probe.

(b) MI efficiencies and Scale Factor with respect to the ϕ of the negatively charged robe.

Figure 7.7: MI efficiencies and Data/Monte Carlo scale factors with respect to the η and ϕ of the negatively charged probe.

procedure for obtaining the SMT efficiency and SFs is identical to the J/ψ analysis, however this is carried out by another student and therefore will not be looked at in detail in this thesis. The important feature, shown in Figure 7.13 is that the two calibration methods agree within uncertainties for the SFs derived in the overlapping p_T region. In the $15-20$ GeV region the SFs from the $Z \to \mu\mu$ method are to be used for analyses as these have the smaller overall uncertainty.

7.4 Fake rate

The fake (or mistag) rate is defined as the fraction of light-flavour (LF) jets be tagged by the SMT. Mistags occur when LF jets mimic the signals of HF jets, in the case of the SMT this can include the decay-in-flight of LF hadrons such as πs, *K*s and J/ψs which produce signal-like muons. It can also include instrumental effects such as *punch-through* of hadrons into the MS, and nuclear interactions of hard jets with the calorimeter material which can produce high-p_T muon tracks. The mistag rate is measured by another student and will not be discussed in detail here. It is studied as a function of jet p_T, pile-up, and spatial variables, and the data/MC SFs are found to be consistent within uncertainties. A low-p_T method is devised using a W+jets estimation, and a high-p_T method used dijet samples.The W+jets method is required in order to make up for low-statistics in the dijet method at low-p_T. The results, binned bt p_T, are shown in Table 7.3.

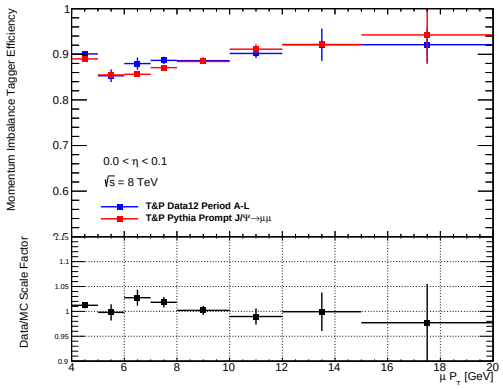

(a) Crack $|\eta|$ region.

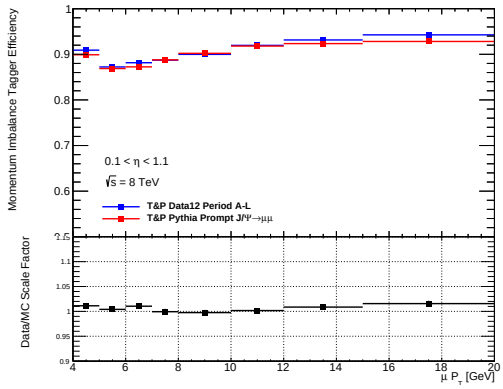

(b) Barrel $|\eta|$ region.

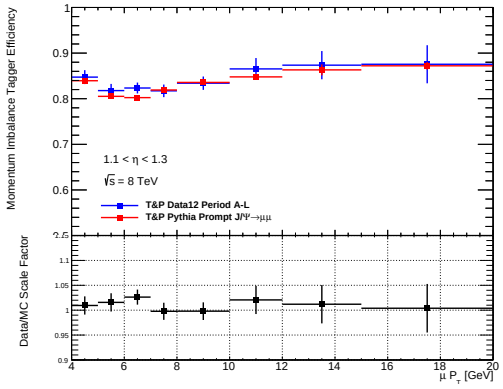

(c) Transition $|\eta|$ region.

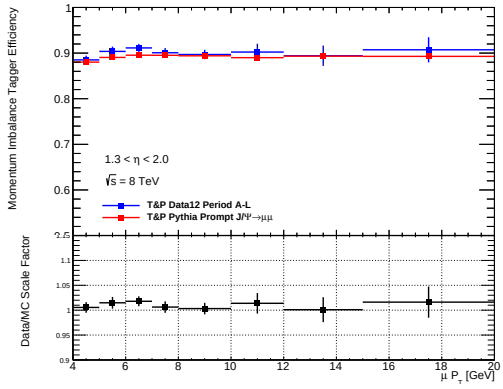

(d) End-cap $|\eta|$ region.

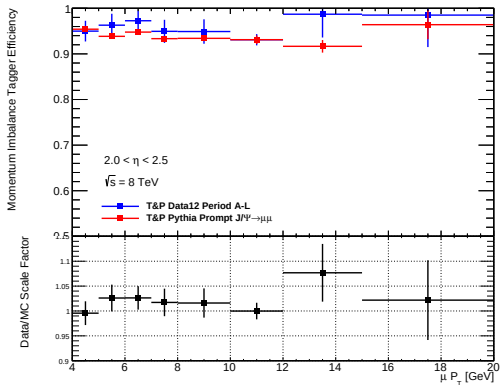

(e) Forward $|\eta|$ region.

Figure 7.8: MI efficiencies with respect to the p_{T} of the positively charged probe, for the five positive $|\eta|$ regions using all 2012 data.

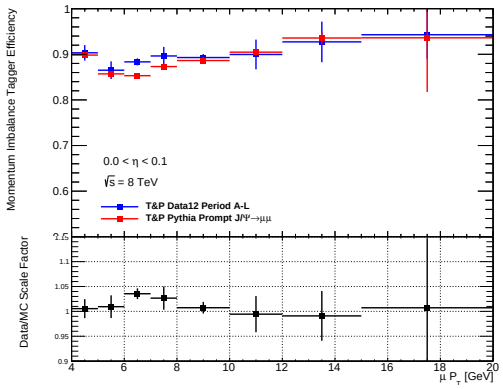

(a) Crack $|\eta|$ region.

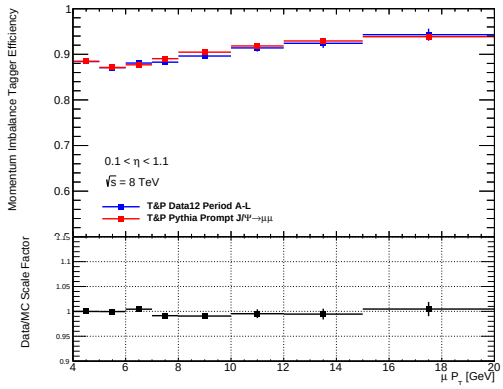

(b) Barrel $|\eta|$ region.

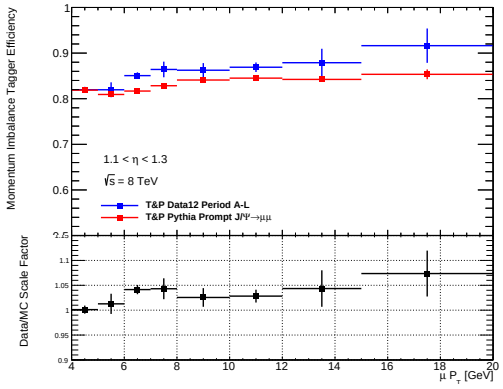

(c) Transition $|\eta|$ region.

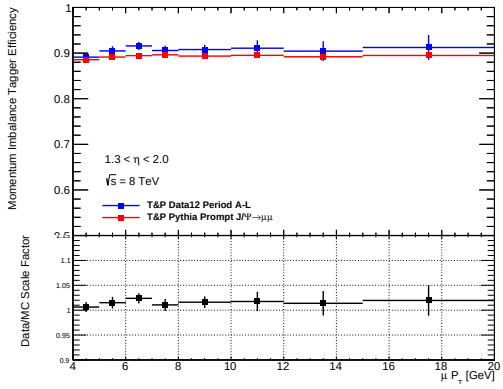

(d) End-cap $|\eta|$ region.

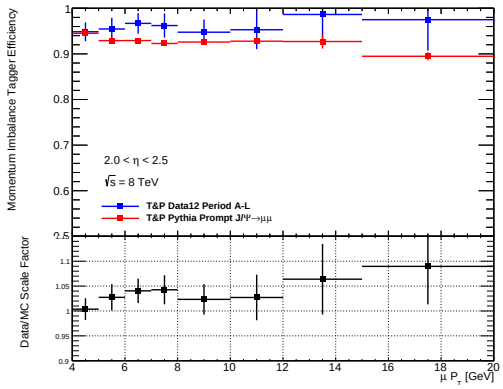

(e) Forward $|\eta|$ region.

Figure 7.9: MI efficiencies with respect to the p_{T} of the negatively charged probe, for the five positive $|\eta|$ regions using all 2012 data.

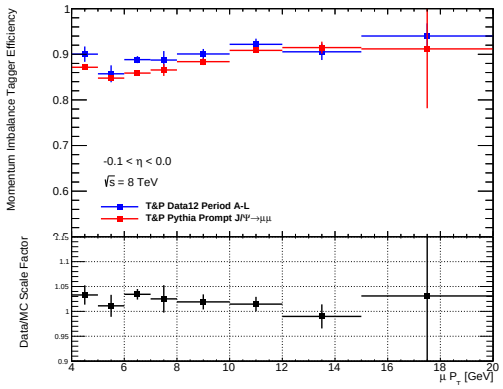

(a) Crack $|\eta|$ region.

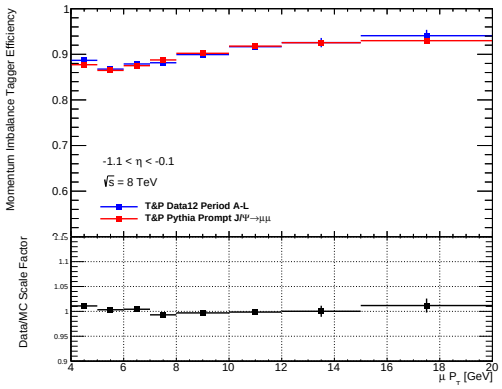

(b) Barrel $|\eta|$ region.

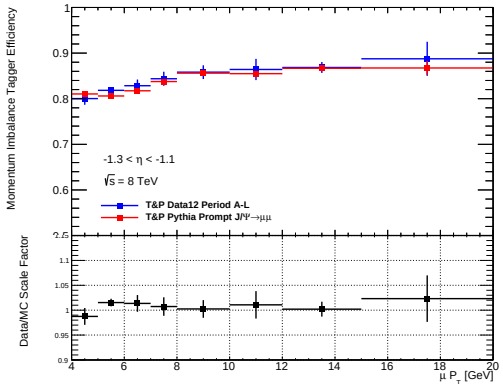

(c) Transition $|\eta|$ region.

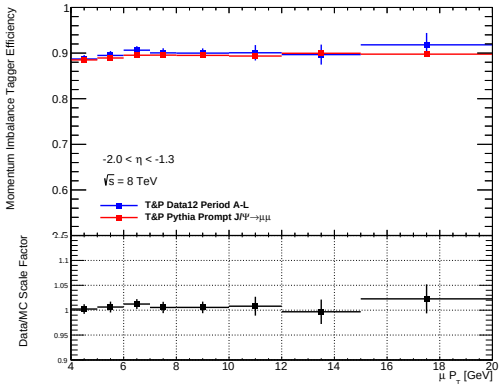

(d) End-cap $|\eta|$ region.

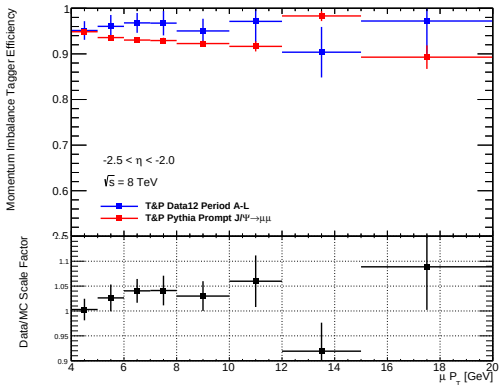

(e) Forward $|\eta|$ region.

Figure 7.10: MI efficiencies with respect to the p_{T} of the positively charged probe, for the five negative $|\eta|$ regions using all 2012 data.

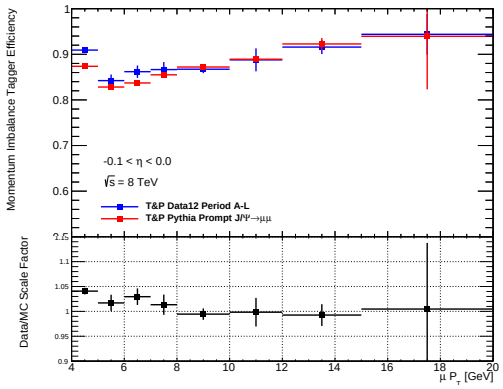

(a) Crack $|\eta|$ region.

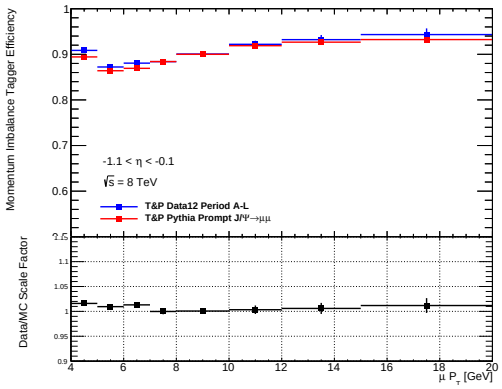

(b) Barrel $|\eta|$ region.

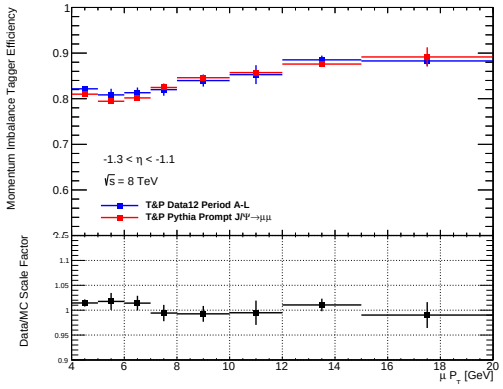

(c) Transition $|\eta|$ region.

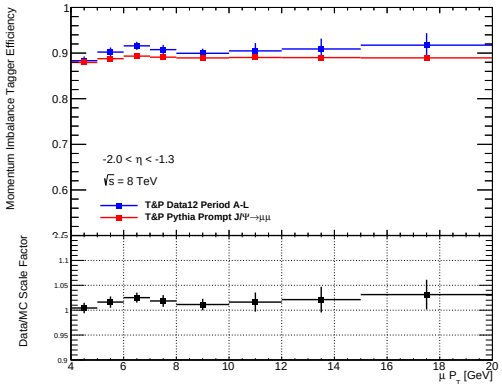

(d) End-cap $|\eta|$ region.

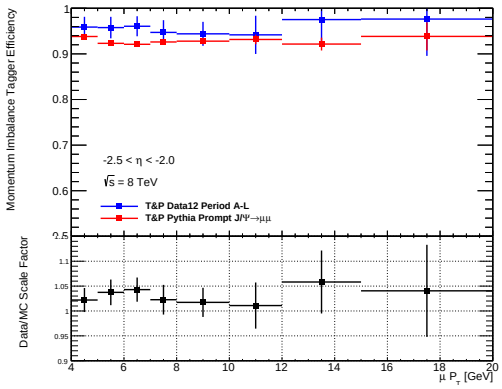

(e) Forward $|\eta|$ region.

Figure 7.11: MI efficiencies with respect to the p_{T} of the negatively charged probe, for the five negative $|\eta|$ regions using all 2012 data.

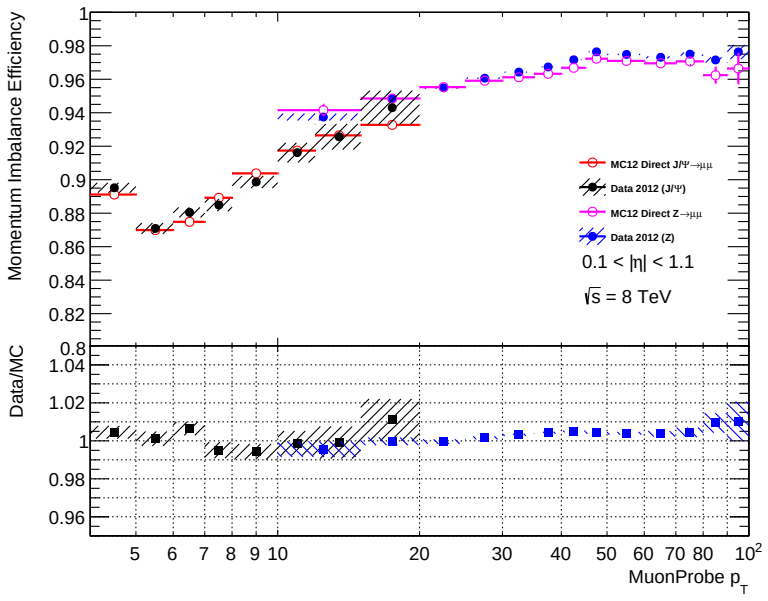

Figure 7.12: The SMT efficiencies with respect to the p_{T} of the Probe, for the barrel region with $J/\psi \to \mu\mu$ and $Z \to \mu\mu$ combined

p_T [GeV]	$\varepsilon_{\mathrm{MC}}$ [$\times 10^{-3}$]	$\varepsilon_{\mathrm{data}}$ [$\times 10^{-3}$]	Scale Factor (Data/MC)
$25-80$	2.24 ± 0.09	1.50 ± 1.12	0.66 ± 0.82
$80-140$	4.16 ± 0.15	1.72 ± 1.08	0.80 ± 0.42
$140-220$	6.60 ± 0.39	4.28 ± 0.85	0.94 ± 0.20
$220-360$	9.81 ± 0.37	5.94 ± 0.31	0.83 ± 0.15
$360-500$	11.63 ± 0.38	9.14 ± 0.25	0.83 ± 0.11
$500-1000$	16.49 ± 0.50	12.82 ± 1.10	0.90 ± 0.11

Table 7.3: Summary of SMT mistag rate and Data/MC scale factors

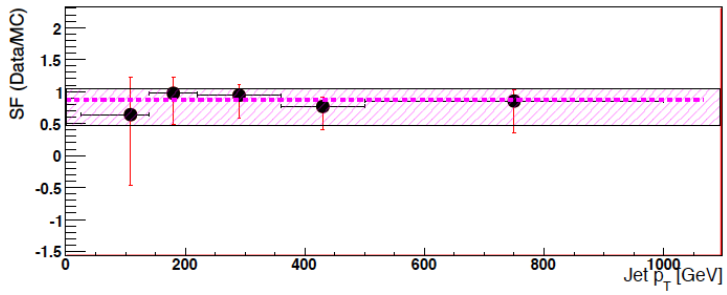

Figure 7.13: Coarsely-binned scale factors for the mistag rate between data and MC simulation. The purple line is an all-data derived SF of $0.87^{+0.18}_{-0.38}$.

I don't believe in no-win scenarios

James Tiberius Kirk

Chapter 8

Event selection

This section describes the MC samples used for the analysis, and the critera applied to MC and to data to identify $t\bar{t}$ ℓ+jets decays and reject the other processes with the highest purity possible. The nominal selection, in Section 8.2.3 is prescribed by the ATLAS top quark group. The background estimations (Section 8.3), for the MC simulated processes, and the data-driven W+jets and multijet processes, are performed by a colleague at QMUL, as well as the derivation of the relevant event weights. The optimisation of the selection to improve the purity for this analysis is performed jointly between myself and a colleague and is described in Section 8.2.4.

8.1 Collision data and simulated samples

The collisions recorded by the ATLAS detector which are used in this analysis amount to 20.3 fb^{-1} of Run 1 data at a centre-of-mass energy of $\sqrt{s} = 8$ TeV. Events needed to satisfy requirements set by the ATLAS *GoodRunList* (GRL) which defines quality thresholds, according to the detector functionality and running conditions. The MC samples, used to simulate the signal and background physics processes, are detailed as follows:

- $t\bar{t}$ (nominal) - POWHEG generator [65] interfaced to PYTHIA6 [68] for parton shower modelling
- $t\bar{t}$ (PDF systematic) - MC@NLO generator [66], interfaced to HERWIG++ [67] for parton shower modelling

- $t\bar{t}$ (ISR/FSR systematic) - POWHEG generator [65] interfaced to PYTHIA6 [68] for parton shower modelling
- $t\bar{t}$ (MC generator systematic) - POWGEG generator [65] and MC@NLO generator [REF], both interfaced to HERWIG++ [67] for parton shower modelling
- $t\bar{t}$ (Parton shower systematic) - POWHEG generator [65] interfaced to PYTHIA6 [68] and HERWIG++ [67] for parton shower modelling
- Single-top (background) - POWHEG generator [65] interfaced to PYTHIA6 [68] for parton shower modelling
  - Four samples are required: t-channel top, t-channel anti-top s-channel and Wt-channel
- W+jets (background) - ALPGEN generator [71] interfaced to PYTHIA6 [68] for parton shower modelling
  - Parton flavour specific samples with additional objects are generated separately. A heavy flavour overlap removal (HFOR) procedure is required to avoid double counting events which satisfy multiple categories in the following:
    - LF partons with 0-5 additional partons
    - $c\bar{c}$ with 0-3 additional partons
    - $b\bar{b}$ with 0-3 additional partons
    - c with 0-4 additional partons
- Z+jets (background) - ALPGEN generator [71] interfaced to PYTHIA6 [68] for parton shower modelling
  - Parton flavour specific samples with additional objects are generated separately
    - LF partons with 0-5 additional partons
    - $c\bar{c}$ with 0-3 additional partons
    - $b\bar{b}$ with 0-3 additional partons
- Diboson (background) - HERWIG++ [67] for both generation and parton shower modelling

The samples used are all standard samples within the ATLAS top quark group. The majority use the full ATLAS detector simulation of GEANT4 [72] however several systematic $t\bar{t}$ samples instead utilise ATLFAST2 [73–75] fast simulation. To simulate pile-up, all samples are overlaid with PYTHIA8 [88] minimum bias events, and all events are reweighted to normalise the average pile-up density $< \mu >$ (the average number of pile-up interactions per bunch crossing) to that which is measured in data, as in Figure 5.4. Finally, it must be noted that the b-hadron production fractions and the $b \to \mu$ decay branching ratios as implemented in the existing versions of PYTHIA6 and HERWIG++ are not in agreement with those specified in the Review of Particle Physics (RPP) [41] and calculated by the Heavy Flavour Averaging Group (HFAG) [89]. It is necessary to apply a re-weighting scheme to correct for this as these branching ratios are crucial to the measurement. An associated systematic uncertainty is introduced as a result of the reweighting procedure. Table 8.1 details the b-hadron production fractions as listed in the RPP and as implemented in PYTHIA6 and HERWIG++. Table 8.2 is an equivalent comparison of the $b \to \mu$ branching ratios.

Hadron	RPP (%)	PYTHIA6 (%)	HERWIG++ (%)
B^0	40.5 ± 0.6	42.2	39.0
$B^{\pm}$	40.5 ± 0.6	42.2	39.2
B_s^0	10.5 ± 0.5	8.2	10.1
b-baryon	8.5 ± 1.1	7.5	11.7

Table 8.1: Production fractions for b-hadrons as observed in the PYTHIA6 and HERWIG++ MC generators, compared to the RPP reference values.

Hadron	RPP (%)	PYTHIA6 (%)	HERWIG++ (%)
$b \to \mu$	$10.95^{+0.29}_{-0.25}$	9.8	8.9
$b \to \tau \to \mu$	0.42 ± 0.04	0.6	0.7
$b \to c \to \mu$	8.02 ± 0.19	8.0	5.2
$b \to c\bar{c} \to \mu$	$1.6^{+0.4}_{-0.5}$	3.0	5.4
$c \to \mu$	8.2 ± 0.5	9.8	8.1

Table 8.2: Branching ratios for $b \to \mu$ decays as observed in the PYTHIA6 and HERWIG++ MC generators, compared to the RPP reference values.

8.2 Object identification and event selection

8.2.1 Trigger selection

The lowest unprescaled single electron trigger (EF_e24vhi_medium1) is used to identify electron objects, which is a trigger chain implemented in stages from the Level 1 trigger (L1) to the event filter (EF). This utilises a $p_T > 24$ GeV criterion and a dead material correction. It is known to produce inefficiencies on selecting very high energy ($E_t > 200$ GeV) electrons and so is combined with a logical *OR* with a second trigger (EF_e60_medium1) which has looser requirements for higher energy objects. The EF_e24vhi_medium1 trigger applies a loose track isolation requirement of $\frac{p_T^{cone20}}{E_T} > 0.1$ to reduce the effects of multijet backgrounds. Single muon triggers (EF_mu24i_tight, EF_mu36_tight) are combined (logical *OR*) to identify muon signals. They utilise p_T thresholds of 24 GeV and 36 GeV respectively and the second trigger has in addition an isolation requirement of $\frac{p_T^{0.2}}{p_{T,\mu}} < 0.12$.

8.2.2 Offline selection

All selection criteria below follow the recommendations of the ATLAS top quark group for a Run 1 $t\bar{t}$ ℓ+jets analysis, unless otherwise specified. Departures from the recommendations beneficial specifically to this analysis include the use of multiple b-tagging algorithms and the omission of missing transverse energy (E_T^{miss}) and W-boson transverse mass (m_T^W) requirements, detailed in the following sections. The offline selection is applied to MC and to data.

Electrons

Electron objects (associated with the decays of W bosons in this analysis) are required to satisfy a *tight*++ offline identification criteria. Detailed descriptions of the *loose, medium, tight* and *tight*++ criterion may be found in [77] and in Appendix C. The overarching electron requirements are as follows:

- $p_T > 25$ GeV
- $|\eta_{\text{cluster}}| > 2.47$ (detector acceptance)

- $1.37 < |\eta_{\text{cluster}}| < 1.52$ excluded, due to poor instrumentation in the barrel and end-cap calorimeter transition regions.
- E_T^{cone20} isolation requirements to reduce the multijet background, tuned as a function of E_t and η_{cluster} to maintain a uniform 90% efficiency.
- p_T^{cone30} isolation requirements to reduce the multijet background, tuned as a function of E_t and η_{cluster} to maintain a uniform 90% efficiency.

where *cluster* refers to the energy deposits in the ECAL reconstructed as electrons. The isolation requirements are functions of E_T and η_{cluster} such as to maintain a uniform 90% electron selection efficiency. In addition, a procedure known as *overlap removal* is used to prevent the double counting of energy clusters as both electrons and jets. Jets within a cone of $\Delta R < 0.2$ of reconstructed electrons are removed, and for surviving jets within a cone of $\Delta R < 0.4$ of electrons, the electrons are instead discarded, to suppress semileptonic $b \to e$ decays.

Muons

Muon objects (associated with the decays of W-bosons in this analysis, as distinct from the soft-muons described in Section 7) are required to satisfy the reconstruction criteria for MUID combined muons (see Section 6.2.3). The overarching muon requirements are as follows:

- $p_T > 25$ GeV
- $|\eta| < 2.5$ (detector acceptance)
- Satisfy MCP requirements as detailed in Section 7.1.2
- $E_T^{cone20} < 4$ GeV isolation requirements in both the ID and ECAL/HCAL
- $p_T^{cone30} < 2.5$ GeV isolation requirements in both the ID and ECAL/HCAL

In addition, overlap removal is again utilised to reduce contamination from punch-through and from heavy flavour parton to muon decays inside of jets. Muons within a cone of $\Delta R < 0.4$ from the nearest jet are discarded.

Jets

The reconstruction of jets is performed using the anti-k_t [83] clustering algorithm (see Section 6.2.4) with a cone radius of $R = 0.4$. Jet reconstructions begins with topological clusters, which are then corrected for pile-up effects and calibrated using a p_T and η dependent scheme for the jet energy scale (JES). The overarching jet requirements are as follows:

- $p_T > 25$ GeV
- $|\eta| < 2.5$ (detector acceptance)
- $|\text{JVF}| > 0.5$ for $p_T < 50$ GeV jets, to reduce the effects of pile-up minimum bias interactions

where JVF is the *jet vertex fraction* which is defined as the fraction of track momenta associated with the jet, to also be associated with the PV

$$\text{JVF} = \frac{\sum p_T \text{ofjettracksfromPV}}{\sum p_T \text{ofjettracks}}. \tag{8.1}$$

b-tagging

b-tagging is a process by which an attempt is made to identify heavy flavour jets which contain *b*-hadron decays as distinct from jets which contain only light-flavour (LF) hadron decays. It is critical for this analysis to identify *b*-jets which contain soft-muons using the SMT algorithm as described in Section 7. A more common tagging algorithm (MV1 [86]), based on a multivariate analysis of the track parameters in jets to identify secondary vertices related to *b*-hadron decays (see Section 6.2.5), is regularly used for *b*-tagging at the ATLAS experiment. The MV1 tagger works on orthogonal variables to the SMT algorithm and has an independent efficiency and fake rate. In Section 8.2.4 the potential to combine the SMT and MV1 taggers in a logical AND to tag *b*-jets is explored. Following the optimisation below, this analysis requires at least one *b*-tagged jet per event, required to satisfy both the SMT (Section 7) and MV1 (Section 6.2.5) tagging criteria.

Missing transverse energy and W transverse mass

For events in which neutrinos escape the detector undetected, the vector sum of transverse momentum in the event will be non-zero and yield a measurement of the missing energy, E_T^{miss}. A related parameter, the transverse mass of the W boson m_T^W, is also considered. The transverse mass is defined as

$$m_T^W = \sqrt{2p_T^l p_T^\nu (1 - \cos(\phi^l - \phi^\nu))}, \tag{8.2}$$

where p_T^ν and ϕ^ν are calculated assuming they are the components of the E_T^{miss} 4-vector. ATLAS top-quark analyses usually utilise the following ('nominal') requirements:

- $|\eta_{E_T^{\text{miss}}}| < 4.9$
- $E_T^{\text{miss}} > 30$ GeV and $m_T^W > 30$ GeV for the e+jets channel
- $E_T^{\text{miss}} > 20$ GeV and $\left(E_T^{\text{miss}} + m_T^W\right) > 60$ GeV for the μ+jets channel

However it will be shown in Section 8.2.4 that for this analysis an improved signal purity may be achieved by neglecting any selection requirements based on these variables.

8.2.3 Event selection

The nominal event selection for this analysis is as follows:

- Only one hard electron OR muon, with a veto on any second hard lepton (to avoid dilepton events)
- ≥ 4 jets
- ≥ 1 b-tagged jet, tagged by both the SMT and MV1@85% algorithms (justified in Section 8.2.4)
- For μ+jets events, the muon identified as originating from the W-boson decay must not be the same object as the muon utilised in the SMT algorithm ($\Delta R(\mu, SMT) > 0.01$)
- No requirements based on E_T^{miss} or m_T^W (justified in Section 8.2.4)

where a 'hard' lepton is defined as one passing the $p_T > 25$ GeV requirement.

8.2.4 Optimisation

The event selection is optimised in order to maximise the signal purity in the final data sample, to reduce the uncertainties on the final results. However, optimisation of selection to maximise the purity should not be permitted to reduce too heavily the efficiency of the selection, as this would lead to a large statistical uncertainty. This analysis is expected to be limited by its statistical uncertainty. The following metrics are considered (where S, B denote the number of signal and background events respectively after a selection is performed):

- Signal significance (maximise): $S/\sqrt{S+B}$
- Background fraction (minimise): $B/(S+B)$
- Proxy for statistical uncertainty (minimise): $1/\sqrt{S}$

The background events include $t\bar{t}$ contributions from fake SMT muons (referred to as $t\bar{t}$ backgrounds), alongside the non-$t\bar{t}$ events documented in Section 8.3. The $t\bar{t}$ background events include dilepton events, and muons from initial or final state radiation, decay-in-flight of LF hadrons, and pile-up. These types of events are abbreviated as $t\bar{t}$ mis-ID from hereon. Although the fake rate for the SMT algorithm is extremely small, the low efficiency due to the 21% $b \to \mu$ branching ratio results in fake SMT muons still contributing a considerable background. The breakdown of the $t\bar{t}$ backgrounds (from fake SMT muons) after the optimised selection is given in Section 10.2.1.

In order to focus on reducing the fake SMT muon contributions specifically, combinations of the SMT tagger with the MV1 tagger are considered. It is found, as detailed in Tables 8.3-8.9 that the combination of taggers results in a more powerful rejection of background events than either tagger individually. In order to retain high statistics multiple working points of the MV1 tagger are considered, where each working point represents the efficiency of the tagger for a specific calibration (the price for higher efficiency being a lower purity). Alternate MV1 algorithms with enhanced c-jet rejection (MV1c [86]) are tested as well, and in addition, for each tagging combination, statistics are recuperated by removal both the nominal E_T^{miss} and m_T^W requirements.

Tables 8.3- 8.9 detail the 12 event selections considered with the resultant event yields and performance. These tables also detail the performance as a function of 'same-top' (ST) and

'different-top' (DT) muons within $t\bar{t}$, as discussed in Section 4. Events labelled '$t\bar{t}$ same- and diff-top' contain two SMT muons from different jets, and enter the event yields twice. In all cases the signal significance is found to improve after removing both the nominal E_T^{miss} and m_T^W requirements, and larger statistics overall, although the price is a slightly larger background fraction. While the SMT-only tagging selection yields a high signal significance, the large background fraction is notable. This is alleviated applying the MV1 tagging algorithm subsequent to the SMT, and the highest signal significance is found for the combination of SMT+MV1@85%. This combination has a larger background fraction than the other combined tagging options, but it is still much lower than the SMT-only background fraction. The MV1c algorithms yield minimal notable difference to the original MV1 results.

Tagger = SMT	Without E_T^{miss}, m_T^W criteria			With E_T^{miss}, m_T^W criteria		
Sample	e+jets	μ+jets	Combined	e+jets	μ+jets	Combined
W+jets	4890	5696	10586	3095	4835	7931
MultiJet	3788	2715	6502	1127	1247	2374
Single-Top	2236	2417	4653	1550	2109	3659
Z+jets	1518	1242	2760	498	727	1225
Diboson	85	87	172	50	68	118
$\sum$ Background	12517	12156	24673	6320	8986	15306
$t\bar{t}$	36506	41445	77951	25148	35937	61085
$t\bar{t}$ same-top	14767	17610	32377	10039	15158	25197
$t\bar{t}$ diff-top	14675	15954	30629	10192	13893	24085
$t\bar{t}$ same- and diff-top	1454	1493	2947	1004	1289	2294
$t\bar{t}$ mis-ID	5611	6387	11998	3913	5596	9509
Signal	30896	35057	65953	21235	30341	51576
Background	18127	18543	36671	10234	14582	24815
$S/\sqrt{S+B}$	140	151	206	120	143	187
$B/(S+B)$	0.37	0.35	0.36	0.33	0.32	0.32
$1/\sqrt{S}$	0.0057	0.0053	0.0039	0.0069	0.0057	0.0044

Table 8.3: Event optimisation table for events in which at least one jet is tagged by the SMT algorithm. Shown with and without E_T^{miss} and m_T^W criteria applied. No uncertainties are shown and no weights are applied to the W+jets. Yields are scaled to an integrated luminosity of 20.3 fb^{-1}.

8.2.5 Fiducial selection

A fiducial volume, required to extract the CP asymmetries measured by this analysis, is defined to be as close as possible to the nominal event selection. The fiducial selection is as follows:

- Only one hard electron OR muon (with $p_T > 25$ GeV), with a veto on any second hard lep-

Tagger = SMT + MV1@70%	Without E_T^{miss}, m_T^W criteria			With E_T^{miss}, m_T^W criteria		
Sample	e+jets	μ+jets	Combined	e+jets	μ+jets	Combined
W+jets	1373	1520	2893	875	1291	2167
MultiJet	1246	970	2215	381	422	803
Single-Top	1460	1601	3061	1021	1389	2410
Z+jets	552	249	802	195	164	358
Diboson	33	26	60	19	22	41
$\sum$ Background	4665	4366	9031	2491	3288	5779
$t\bar{t}$	24407	27774	52181	16791	24039	40830
$t\bar{t}$ same-top	10873	12964	23838	7384	11139	18523
$t\bar{t}$ diff-top	10802	11775	22578	7508	10252	17760
$t\bar{t}$ same- and diff-top	750	763	1513	517	660	1176
$t\bar{t}$ mis-ID	1982	2271	4253	1382	1989	3371
Signal	22425	25503	47928	15409	22050	37459
Background	6647	6637	13284	3873	5277	9150
$S/\sqrt{S+B}$	132	142	194	111	133	174
$B/(S+B)$	0.23	0.21	0.22	0.20	0.19	0.20
$1/\sqrt{S}$	0.0067	0.0063	0.0046	0.0081	0.0067	0.0052

Table 8.4: Event yields in which at least one jet is tagged by the SMT algorithm combined with the MV1@70% algorithm. Shown with and without E_T^{miss} and m_T^W criteria applied. No uncertainties are shown and no weights are applied to the W+jets. Yields are scaled to an integrated luminosity of 20.3 fb^{-1}.

ton. Dressed lepton 4-momenta are used (final-state leptons recombined with surrounding photons ($\Delta R < 0.1$) not produced from hadronic decays, to account for electromagnetic final state radiation).

- Lepton $p_T > 25$ GeV
- Lepton $|\eta| < 2.5$
- ≥ 4 reconstructed jets using the anti-k_t algorithm with a cone radius of $R = 0.4$ built from stable MC particles (after all radiative effects and decays)
- Jet $p_T > 25$ GeV
- Jet $|\eta| < 2.5$
- ≥ 1 b-jet with a semileptonic $b \to \mu$ decay
- No requirements on E_T^{miss} or m_T^W, for consistency with the nominal event selection

Tagger = SMT + MV1@80%	Without E_T^{miss}, m_T^W criteria			With E_T^{miss}, m_T^W criteria		
Sample	e+jets	μ+jets	Combined	e+jets	μ+jets	Combined
W+jets	1975	2199	4174	1236	1875	3112
MultiJet	1761	1323	3084	529	583	1111
Single-Top	1691	1839	3530	1178	1601	2780
Z+jets	698	342	1039	241	220	461
Diboson	44	36	80	26	30	57
$\sum$ Background	6169	5738	11908	3211	4309	7520
$t\bar{t}$	28112	31934	60046	19351	27652	47003
$t\bar{t}$ same-top	12299	14668	26967	8362	12616	20978
$t\bar{t}$ diff-top	12238	13314	25552	8505	11590	20095
$t\bar{t}$ same- and diff-top	976	993	1969	672	860	1532
$t\bar{t}$ mis-ID	2600	2958	5558	1812	2585	4397
Signal	25513	28976	54488	17539	25067	42606
Background	8769	8697	17465	5023	6895	11918
$S/\sqrt{S+B}$	138	149	203	117	140	182
$B/(S+B)$	0.26	0.23	0.24	0.22	0.22	0.22
$1/\sqrt{S}$	0.0063	0.0059	0.0043	0.0076	0.0063	0.0048

Table 8.5: Event yields in which at least one jet is tagged by the SMT algorithm combined with the MV1@80% algorithm. Shown with and without E_T^{miss} and m_T^W criteria applied. No uncertainties are shown and no weights are applied to the W+jets. Yields are scaled to an integrated luminosity of 20.3 fb^{-1}.

The b-jet criterion requires a good SMT muon be found within $\Delta R < 0.5$ of the jet axis. The SMT muon must have a b-hadron with a $p_T > 5$ GeV found in its MC production chain, and this b-hadron must also fall within $\Delta R < 0.5$ of the associated jet, and originate from a top-quark decay.

8.3 Background estimation

The background estimations described in this chapter are performed by a colleague working on the analysis. I have involvement in some initial studies for the W+jets data driven background estimation, but not in the production the code framework or performance of the final estimation.

There are several other physics signatures which either share a final state with the ℓ+jets $t\bar{t}$ decay or have a very similar final state which may satisfy the same selection. Single leptons, multiple jets (with one or more b-tagged jets) and missing momentum are common signatures in a number of decays from pp collisions, referred to hereon as *backgrounds* if they are not from the signal decay mode. The primary backgrounds for this particular signature are: W+jets,

Tagger = SMT + MV1@85%	Without E_T^{miss}, m_T^W criteria			With E_T^{miss}, m_T^W criteria		
Sample	e+jets	μ+jets	Combined	e+jets	μ+jets	Combined
W+jets	2343	2639	4982	1462	2250	3713
MultiJet	2077	1521	3598	620	680	1301
Single-Top	1830	1986	3816	1273	1728	3002
Z+jets	814	424	1239	281	268	550
Diboson	50	43	93	29	35	64
$\sum$ Background	7114	6613	13727	3666	4963	8629
$t\bar{t}$	30131	34188	64319	20738	29612	50350
$t\bar{t}$ same-top	13028	15527	28555	8855	13360	22215
$t\bar{t}$ diff-top	12974	14094	27068	9014	12267	21281
$t\bar{t}$ same- and diff-top	1108	1134	2242	764	982	1746
$t\bar{t}$ mis-ID	3022	3433	6455	2106	3002	5108
Signal	27109	30755	57864	18632	26610	45242
Background	10136	10046	20182	5772	7965	13737
$S/\sqrt{S+B}$	140	152	207	119	143	186
$B/(S+B)$	0.27	0.25	0.26	0.24	0.23	0.23
$1/\sqrt{S}$	0.0061	0.0057	0.0042	0.0073	0.0061	0.0047

Table 8.6: Event yields in which at least one jet is tagged by the SMT algorithm combined with the MV1@85% algorithm. Shown with and without E_T^{miss} and m_T^W criteria applied. No uncertainties are shown and no weights are applied to the W+jets. Yields are scaled to an integrated luminosity of 20.3 fb^{-1}.

Z+jets, diboson, single-top and multijet (QCD). Several of the backgrounds (multijet, Z+jets, diboson) are produced charge symmetrically, and with the charges of the charged-lepton (from the W-boson decay) and the soft-muon uncorrelated, these backgrounds should contribute flat distributions to the charge asymmetries (CA). Other backgrounds (W+jets, single-top) have some elements of charge asymmetric production and correlation between the aforementioned lepton charges, these backgrounds will likely contribute non-flat distributions to the CAs and must be estimated with care. Figure 8.1 shows example Feynman diagrams for each background channel, with labels to identify production charge (a)symmetries and lepton charge correlations in each case.

Each background, other than W+jets and multijets which will be discussed separately, is well-modelled and accounted for using MC simulations. Diboson (WW, WZ, ZZ) events may satisfy the selection as they contain real leptons, missing momentum (from neutrinos or undetected other leptons), and jets (either b-tagged heavy-flavour (HF) or mistagged light-flavour (LF)). Diboson WW and ZZ events are produced charge symmetrically, however WZ events are produced charge asymmetrically, due to the quark anti-quark content of the protons (uud) gen-

Tagger = SMT + MV1c@70%	Without E_T^{miss}, m_T^W criteria			With E_T^{miss}, m_T^W criteria		
Sample	e+jets	μ+jets	Combined	e+jets	μ+jets	Combined
W+jets	1367	1500	2867	862	1266	2127
MultiJet	1290	1003	2293	392	443	835
Single-Top	1481	1610	3091	1036	1397	2433
Z+jets	548	250	798	193	164	356
Diboson	33	27	60	19	22	41
$\sum$ Background	4719	4388	9108	2501	3292	5793
$t\bar{t}$	24652	28021	52672	16959	24251	41210
$t\bar{t}$ same-top	10995	13101	24097	7468	11256	18724
$t\bar{t}$ diff-top	10925	11890	22815	7590	10351	17941
$t\bar{t}$ same- and diff-top	766	779	1545	528	673	1200
$t\bar{t}$ mis-ID	1965	2250	4215	1373	1971	3344
Signal	22687	25770	48457	15586	22279	37865
Background	6684	6639	13323	3874	5263	9137
$S/\sqrt{S+B}$	132	143	195	112	134	175
$B/(S+B)$	0.23	0.20	0.22	0.20	0.19	0.19
$1/\sqrt{S}$	0.0066	0.0062	0.0045	0.0080	0.0067	0.0051

Table 8.7: Event yields in which at least one jet is tagged by the SMT algorithm combined with the MV1c@70% algorithm. Shown with and without E_T^{miss} and m_T^W criteria applied. No uncertainties are shown and no weights are applied to the W+jets. Yields are scaled to an integrated luminosity of 20.3 fb^{-1}.

erating a larger cross-section for W^+-boson production (using two possible u valence quarks and one anti-d sea quark) compared to W^--boson production (using only one possible d valence quark and one anti-u sea quark). The charge of the soft muon and charged lepton are uncorrelated, for WW events either W-boson may decay leptonically or hadronically, and either jet from the hadronic decay may be tagged, for ZZ events either lepton may be reconstructed as the charged lepton, and either jet may be tagged, for WZ events, either boson may decay leptonically or hadronically and in the hadronic case either jet may be tagged.

Single-top events are able to satisfy the event selection requirements as they contain a real charged-lepton, missing momentum and a b-jets from the top-quark decay. This can coincide with other HF or LF jets and provide all of the signatures of a $t\bar{t}$ decay. The production charge for single-top events is asymmetric due to the asymmetric production of W-bosons from the quark content of the protons. In the first diagram of Figure 8.1, assuming the charged lepton and the SMT muon both originate from the decay products of the top quark, the two leptons will be correlated in charge. In the second and third diagram, either b-jet could be tagged and the lepton and soft muon charged become uncorrelated. In the Wt diagram, the charges are again

Tagger = SMT + MV1c@80%	Without E_T^{miss}, m_T^W criteria			With E_T^{miss}, m_T^W criteria		
Sample	e+jets	μ+jets	Combined	e+jets	μ+jets	Combined
W+jets	1950	2175	4125	1218	1857	3075
MultiJet	1738	1318	3056	523	583	1106
Single-Top	1703	1846	3549	1186	1607	2793
Z+jets	698	339	1036	240	218	458
Diboson	44	36	80	26	30	56
$\sum$ Background	6132	5713	11846	3194	4294	7488
$t\bar{t}$	28096	31926	60023	19336	27647	46983
$t\bar{t}$ same-top	12290	14667	26956	8352	12614	20966
$t\bar{t}$ diff-top	12228	13309	25538	8495	11588	20083
$t\bar{t}$ same- and diff-top	977	992	1969	674	859	1532
$t\bar{t}$ mis-ID	2602	2958	5560	1815	2587	4402
Signal	25494	28968	54462	17521	25061	42581
Background	8734	8672	17406	5009	6881	11890
$S/\sqrt{S+B}$	138	149	203	117	140	182
$B/(S+B)$	0.26	0.23	0.24	0.22	0.22	0.22
$1/\sqrt{S}$	0.0063	0.0059	0.0043	0.0076	0.0063	0.0048

Table 8.8: Event yields in which at least one jet is tagged by the SMT algorithm combined with the MV1c@80% algorithm. Shown with and without E_T^{miss} and m_T^W criteria applied. No uncertainties are shown and no weights are applied to the W+jets. Yields are scaled to an integrated luminosity of 20.3 fb^{-1}.

Tagger	Without E_T^{miss}, m_T^W criteria			With E_T^{miss}, m_T^W criteria		
	$S/\sqrt{S+B}$	$B/(S+B)$	$1/\sqrt{S}$	$S/\sqrt{S+B}$	$B/(S+B)$	$1/\sqrt{S}$
SMT	206	0.36	0.0039	187	0.32	0.0044
SMT + MV1@70%	194	0.22	0.0046	174	0.20	0.0052
SMT + MV1@80%	203	0.24	0.0043	182	0.22	0.0048
SMT + MV1@85%	207	0.26	0.0042	186	0.23	0.0047
SMT + MV1c@70%	195	0.22	0.0045	175	0.19	0.0051
SMT + MV1c@80%	203	0.24	0.0043	182	0.22	0.0048

Table 8.9: Event optimisation summary table for all event selections considered. The magnitude of the uncertainty on values of the signal significance in the first column is $\sigma_{\text{signif}} \sim 0.5$, the uncertainty on the values of the background fraction in the second column is $\sigma_{\text{bkgFrac}} \sim 0.002$, the uncertainty on the values of the proxy for the statistical uncertainty in the third column is $\sigma_{\text{statProxy}} \sim 10^{-5}$.

correlated assuming both leptons originate from the decay products of the top quark.

Z+jets decays can result in leptons (charged or neutral) coincident with HF or LF jets. For the case of two charged leptons ($Z \to \ell^+\ell^-$), one lepton may fail to be reconstructed due to detector inefficiencies (such as the crack region or dead pixels) or fall outside of the selection acceptance, this would give the signature of missing momentum. For the case of two neutral

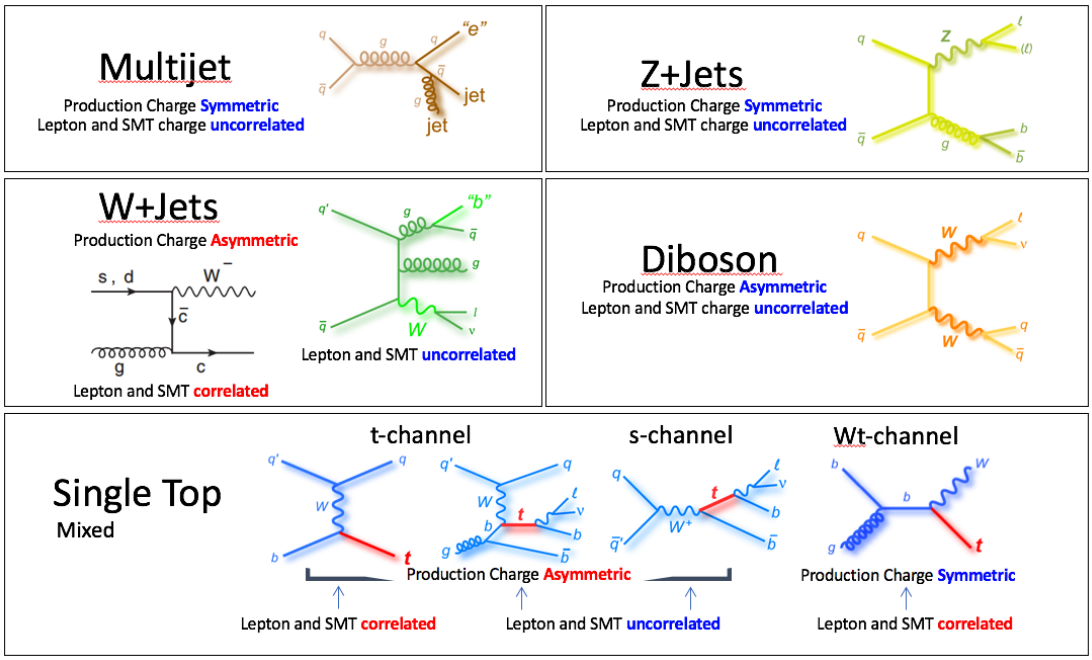

Figure 8.1: Example Feynman diagrams for each of the main backgrounds to a ℓ+jets $t\bar{t}$ signal. Labels indicate the production charge (a)symmetries in terms of the charge of the charged-lepton (from the W-boson decay), and correlations between the charges of the charged-lepton (from the W-boson decay) and the soft-muon.

leptons ($Z \to \nu\bar{\nu}$), one of the additional jets may fake the signature of a real electron in the ECAL, or a real muon (if punch-through occurs beyond the HCAL). Additionally, $Z \to \tau\tau$ decays may result in a real lepton and neutrino from a leptonic τ decay, and jets from the other τ decay. Z+jets events contain multiple charged leptons and jets, either lepton could be reconstructed as the charge lepton and numerous jets could pass the tagging requirements, so the SMT muon and charged lepton are uncorrelated.

Multijet events contain numerous LF and HF jets which may satisfy the b-tagging requirements. It is possible for jets to be misidentified as leptons, or to contain real electrons or muons through photon conversions and semileptonic decays of heavy-flavour quarks which may then be reconstructed and satisfy the lepton selection requirements. Missing momentum is also required, this could be present in multijet events due to misreconstruction. Pile-up, the crack-region, malfunctioning calorimeter cells and object misidentification may all contribute to a missing momentum signature. The cross-section for multijet events is extremely large, and as such constitutes a considerable background even though the probability of object mis-reconstruction is small. Data driven methods are utilised instead of MC simulations to estimate the multijet back-

grounds, this is because our knowledge of QCD processes is not sufficient to accurately predict multijet final states, especially towards lower p_T regions. Numerous jets in a multijet events may fake a lepton (or produce a real charged lepton) or pass the SMT tagging requirements, so the charged lepton and SMT charges are uncorrelated.

W+jets events can produce real charged-lepton and neutrino pairs in association with multiple LF or HF jets. A data-driven method is utilised for estimating this background, described in Section 8.4 below. In $t\bar{t}$ analyses, W+jets is often the most prevalent background due to its large production cross-section and the presence of real charged-leptons, b-jets and missing momentum. The Wc production mode gives correlation to the charged lepton (from the W-boson decay) and soft muon (from $c \to \mu$) which comes directly from the correlation of the initial charges of the W-boson and c-quark. The second diagram in Figure 8.1 provides numerous jets which may pass the b-tagging requirements and the charges become uncorrelated.

8.4 W+jets data-driven estimation

There is significant uncertainty on the overall normalisation of the W+jets background and on the quark-flavour of the jets (knowledge of this is required to accurately predict tagging rates), as such W+jets MC simulations may not be reliable. Data-driven methods are instead utilised to estimate the W+jets background, utilising the ratio of W^+ to W^-, as the ratio of the cross-sections is known better than either cross-section individually. The primary method used is known as W charge asymmetry [90], it relies on pp collisions yielding a non-unitary ratio of positive to negative W-bosons. As stated above, this asymmetry stems from the quark anti-quark content of the protons (uud) generating a larger production cross-section for W^+ bosons (using two possible u valence quarks and one anti-d sea quark) compared to W^- bosons (using only one possible d valence quarks and one anti-u sea quark). The uncertainty on the ratio of cross-sections $\frac{\sigma_{W^+}}{\sigma_{W^-}}$ is smaller than the uncertainty on either individual cross-section [90]. The ratio may be used to attain the correct normalisation for the number of asymmetric events in data, using Equation 8.4,

$$N_{W^+}^{\mathrm{MC}'} + N_{W^-}^{\mathrm{MC}'} = \frac{\left(N_{W^+}^{\mathrm{MC}} + N_{W^-}^{\mathrm{MC}}\right)}{\left(N_{W^+}^{\mathrm{MC}} - N_{W^-}^{\mathrm{MC}}\right)} \left(D^+ - D^-\right), \tag{8.3}$$

$$= \frac{(r_{MC}+1)}{(r_{MC}-1)} \left(D^+ - D^-\right),$$

$$r_{MC} = \frac{N_{W^+}^{MC}}{N_{W^-}^{MC}} = \frac{\sigma(pp \to W^+)}{\sigma(pp \to W^-)}, \tag{8.4}$$

where $N_{W^\pm}^{MC}$ is the number of positive/negative W-boson events in MC, $D^\pm$ is the number of positively/negatively charged lepton in data (without any b-tagging criteria applied to the event), and r_{MC} is the ratio of interest. A scale factor may be defined as

$$f_{CA} = \frac{\frac{(r_{MC}+1)}{(r_{MC}-1)}\left(D^+ - D^-\right)}{N_{W^+}^{MC} + N_{W^-}^{MC}}. \tag{8.5}$$

This method utilises the ratio r_{MC} to correct the W+jets charge asymmetry in MC to that in the data. It uses the same cuts as the primary analysis (in p_T, η, isolation etc) but further subdivides the samples into events containing positively or negative charged leptons and different jet multiplicities. It relies on the only source of asymmetry present in the data being W-boson events. For this assumption to be true it is first necessary to subtract from data the estimations of the diboson and single-top backgrounds. All other backgrounds are found to be charge-symmetric, as shown in Tables 8.10- 8.11.

	2-jet exclusive		4-jet inclusive	
Sample	+ve	-ve	+ve	-ve
$t\bar{t}$	0.50	0.50	0.50	0.50
Single-top Wt-channel	0.50	0.50	0.50	0.50
Z+jets	0.50	0.50	0.50	0.50
Multijet	0.50	0.50	0.50	0.50
Single-top t/s-channel	0.37	0.63	0.35	0.65
Diboson	0.47	0.53	0.46	0.54

Table 8.10: Relative percentage of charged lepton production in MC for each W+jets background following a l+jets selection in the e+jets channel. Separated by N-jet bins.

The secondary method used is required to estimate the heavy-flavour fractions in the jets present in this background. This is necessary to accurately predict the number of W+jet events which will satisfy the tagging requirements used in the analysis. The number of W+jets events

	2-jet exclusive		4-jet inclusive	
Sample	+ve	-ve	+ve	-ve
$t\bar{t}$	0.50	0.50	0.50	0.50
Single-top Wt-channel	0.49	0.51	0.50	0.50
Z+jets	0.50	0.50	0.50	0.50
Multijet	0.50	0.50	0.51	0.40
Single-top t/s-channel	0.37	0.63	0.35	0.65
Diboson	0.47	0.53	0.46	0.54

Table 8.11: Relative percentage of charged lepton production in MC for each W+jets background following a l+jets selection in the μ+jets channel. Separated by N-jet bins.

predicted at the tag level is given by Equation 8.6. Note that $HF = c$ refers to a W-boson event with a c-quark jet, as in Figure 8.1 and is not equivalent to the signal process of $t \to Wb \to Wc$ (where the c comes from the b) or the $t\bar{t}$ fake process of $t \to Wb \to csb$ (where the c comes from the W).

$$W_{\text{tag}}^{n-\text{jets}} = R_{\text{tag},LF}^{n-\text{jets}} \cdot W_{\text{pretag},LF}^{n-\text{jets}} + \sum_{HF}^{HF=c,c\bar{c},b\bar{b}} \left(R_{\text{tag},HF}^{n-\text{jets}} \cdot W_{\text{pretag},HF}^{n-\text{jets}} \right) \tag{8.6}$$

where $R_{\text{tag},LF}^{n-\text{jets}}$ represents the mistag rate on LF jets and $R_{\text{tag},HF}^{n-\text{jets}}$ represents the tag rate on HF jets, for the b-tagging algorithm of interest. A set of scale factors K_i ($i = c, c\bar{c}, b\bar{b}, LF$) are derived to alter the flavour fractions in MC to that determined to be in the data. The constraints are the total number of positive and negative W+jets events in data (after background subtraction), $D_{W^\pm}$, and the requirement for $\sum_i K_i = 1$. The system can be solved if the assumption is made that $K_{b\bar{b}} = K_{c\bar{b}}$ to reduce to three unknown parameters.

The whole system for the b-tagged sample may be described by a matrix relation shown in Equation 8.7.

$$\begin{bmatrix} f_{CA} \cdot \left(N_{MC,W^-}^{b\bar{b}} + N_{MC,W^-}^{c\bar{c}} \right) & f_{CA} \cdot N_{MC,W^-}^{c} & f_{CA} \cdot N_{MC,W^-}^{LF} \\ (f_{b\bar{b}} + f_{c\bar{c}}) & f_c & f_{LF} \\ f_{CA} \cdot \left(N_{MC,W^+}^{b\bar{b}} + N_{MC,W^+}^{c\bar{c}} \right) & f_{CA} \cdot N_{MC,W^+}^{c} & f_{CA} \cdot N_{MC,W^+}^{LF} \end{bmatrix} \cdot \begin{bmatrix} K_{b\bar{b},c\bar{c}} \\ K_c \\ K_{LF} \end{bmatrix} = \begin{bmatrix} D_{W^-} \\ 1.0 \\ D_{W^+} \end{bmatrix} \tag{8.7}$$

The system is then solved using an iterative approach, applying the scaling factors K_i to the pretag yields, recalculating f_{CA}, inverting Equation 8.7 to extract new K_i and repeating until the scale factors are stable.

The combination of these data-driven methods provides the total estimation for the W+jets background. To reduce uncertainties, the estimations are calculated in the high-statistics 1-lepton and 2-jet exclusive bin and then extrapolated to the analysis region of 1-lepton and $\geq$ 4 jets inclusive region using MC. In order to reduce the overall uncertainty further, the data-driven estimate is recalculated for every systematic variation considered in this analysis. This estimation is therefore performed approximately 350 times per channel. Only the statistical component of the W+jets estimate is considered separately, the magnitude of which may been seen in Tables 12.1-12.7 in Section 12.

8.4.1 b-Tagging combinations

Further justification for the combination of the SMT and MV1 b-tagging algorithms may be found by exploring the uncertainties on the W+jets estimations for the MV1, SMT and combined MV1+SMT b-tagging algorithms in turn. The uncertainties on the scale factors are shown in Table 8.12 for each b-tagging option. The combination of the taggers leads to an overall smaller uncertainty on the scale factors $K_{b\bar{b},c\bar{c}}$ and K_{LF}, although there is an increase for K_c. However, the reduction in the uncertainty on $K_{b\bar{b},c\bar{c}}$ is greater than the increase for K_c, this is a secondary motivation (to the selection purity) for combining the taggers.

Channel	Tagger	$K_{b\bar{b},c\bar{c}}$	K_c	K_{LF}
e+jets	MV1@85%	$1.5^{+0.7}_{-0.8}$	$0.8^{+0.3}_{-0.3}$	$1.0^{+0.2}_{-0.1}$
e+jets	SMT%	$1.2^{+0.5}_{-0.4}$	$0.7^{+0.3}_{-0.3}$	$1.04^{+0.09}_{-0.08}$
e+jets	SMT+MV1@85%	$1.7^{+0.6}_{-0.4}$	$0.4^{+0.4}_{-0.6}$	$1.03^{+0.10}_{-0.09}$
μ+jets	MV1@85%	$1.7^{+0.7}_{-0.7}$	$0.9^{+0.1}_{-0.1}$	$0.9^{+0.1}_{-0.1}$
μ+jets	SMT%	$1.8^{+0.3}_{-0.3}$	$0.7^{+0.1}_{-0.2}$	$0.95^{+0.07}_{-0.06}$
μ+jets	SMT+MV1@85%	$1.7^{+0.2}_{-0.2}$	$0.7^{+0.2}_{-0.3}$	$0.96^{+0.06}_{-0.06}$

Table 8.12: Scale factors K_i for each b-tagging option for the 2-jet exclusive region

8.4.2 Extrapolation of flavour fractions to 4-jet inclusive region

Table 8.12 must be utilised to derive the flavour fractions for the 2-jet exclusive bin and then extrapolate these values to the 4-jet inclusive bin. The flavour fractions, f_i, may be attained using the normalisation condition

$$f_i^{\text{2j } excl.,\text{ final}} = f_i^{\text{2j } excl.,\text{ initial}} \cdot K_i, \tag{8.8}$$

$$\sum_i f_i^{\text{2j } excl.,\text{ final}} = 1, \tag{8.9}$$

from which the extrapolation of the flavour fractions to the 4-jet inclusive region is be performed

$$f_i^{\text{4j } incl.,\text{ final}} = f_i^{\text{4j } incl.,\text{ initial}} \cdot \frac{f_i^{\text{2j } excl.,\text{ final}}}{f_i^{\text{2j } excl.,\text{ initial}}}, \tag{8.10}$$

$$\sum_i f_i^{\text{4j } incl.,\text{ final}} = 1, \tag{8.11}$$

where in all cases the initial flavour fractions are taken from MC. The final flavour fractions in the 4-jet inclusive region are given in Table 8.13. There is no explicit uncertainty related to the extrapolation from the 2-jet exclusive to the 4-jet inclusive region, however the 3- and 4-jet exclusive jet multiplicity regions are used as control regions in order to understand and monitor the extrapolation. Other studies [91] have shown that this technique provides the lowest overall uncertainty and is stable against systematic variations.

Channel	Tagger	$f_{b\bar{b}}$	$f_{c\bar{c}}$	f_c	f_{LF}
e+jets	MV1@85%	$0.18^{+0.06}_{-0.07}$	$0.27^{+0.08}_{-0.11}$	$0.14^{+0.04}_{-0.04}$	$0.4^{+0.2}_{-0.1}$
e+jets	SMT	$0.30^{+0.05}_{-0.05}$	$0.29^{+0.05}_{-0.05}$	$0.19^{+0.07}_{-0.08}$	$0.22^{+0.08}_{-0.07}$
e+jets	SMT+MV1@85%	$0.60^{+0.08}_{-0.06}$	$0.27^{+0.04}_{-0.03}$	$0.1^{+0.1}_{-0.1}$	$0.06^{+0.02}_{-0.02}$
μ+jets	MV1@85%	$0.200^{+0.06}_{-0.07}$	$0.29^{+0.08}_{-0.09}$	$0.15^{+0.03}_{-0.03}$	$0.4^{+0.1}_{-0.1}$
μ+jets	SMT	$0.36^{+0.04}_{-0.03}$	$0.34^{+0.02}_{-0.03}$	$0.14^{+0.02}_{-0.03}$	$0.17^{+0.04}_{-0.04}$
μ+jets	SMT+MV1@85%	$0.56^{+0.05}_{-0.03}$	$0.27^{+0.03}_{-0.03}$	$0.12^{+0.04}_{-0.05}$	$0.06^{+0.01}_{-0.01}$

Table 8.13: Flavour fractions f_i for each b-tagging option for the 4-jet inclusive region

8.4.3 Charge asymmetry in the 4-jet inclusive region

Equation 8.5 is responsible for extrapolating the iteratively corrected f_{CA}. In analogy with Table 8.13, the breakdowns of the charge asymmetry factors for different tagging combinations and the associated uncertainties are shown in Table 8.14.

Channel	Tagger	2-jet exclusive f_{CA}	4-jet inclusive f_{CA}
e+jets	MV1@85%	$1.0^{+0.2}_{-0.2}$	$0.9^{+0.1}_{-0.1}$
e+jets	SMT	$0.93^{+0.09}_{-0.09}$	$0.9^{+0.1}_{-0.2}$
e+jets	SMT+MV1@85%	$0.9^{+0.1}_{-0.1}$	$0.8^{+0.1}_{-0.2}$
μ+jets	MV1@85%	$1.1^{+0.1}_{-0.1}$	$0.9^{+0.1}_{-0.1}$
μ+jets	SMT	$1.05^{+0.08}_{-0.08}$	$0.8^{+0.1}_{-0.1}$
μ+jets	SMT+MV1@85%	$1.05^{0.08}_{-0.08}$	$0.8^{+0.1}_{-0.1}$

Table 8.14: Flavour fractions f_i for each b-tagging option for the 4-jet inclusive region

8.4.4 Final combined scale factors

The total corrected scale factors ($\mathrm{SF}_i = f_{CA} \cdot f_i$) are computed as described in the sections above, and re-calculated for every systematic variation in order to fully profile the W+jets systematics. Table 8.15 details the final scale factors (for the nominal sample) with their total uncertainties for comparison.

Channel	Tagger	$\mathrm{SF}_{b\bar{b},c\bar{c}}$	SF_c	SF_{LF}
e+jets	MV1@85%	$1.3^{+0.4}_{-0.6}$	$0.7^{+0.2}_{-0.2}$	$0.8^{+0.3}_{-0.2}$
e+jets	SMT%	$1.1^{+0.2}_{-0.2}$	$0.7^{+0.3}_{-0.3}$	$1.0^{+0.3}_{-0.3}$
e+jets	SMT+MV1@85%	$1.3^{+0.3}_{-0.2}$	$0.3^{+0.4}_{-0.5}$	$0.8^{+0.3}_{-0.3}$
μ+jets	MV1@85%	$1.4^{+0.4}_{-0.5}$	$0.7^{+0.1}_{-0.1}$	$0.8^{+0.2}_{-0.2}$
μ+jets	SMT%	$1.3^{+0.1}_{-0.1}$	$0.5^{+0.1}_{-0.2}$	$0.7^{+0.2}_{-0.2}$
μ+jets	SMT+MV1@85%	$1.2^{+0.2}_{-0.2}$	$0.5^{+0.1}_{-0.2}$	$0.7^{+0.2}_{-0.1}$

Table 8.15: Scale factors K_i for each b-tagging option for the 2-jet exclusive region

8.5 Multijet data-driven estimation

A technique known as the *matrix method* is used to estimate the contribution from the multijet background in both the electron and muon channels, this is also known as the 'fake lepton' background as it requires a jet to fake the signal of a hard lepton (as described earlier) to pass the event selection. In the electron and muons channels, the loose lepton definitions are used (Section 6) without any isolation requirements, and events in data are separated by whether they pass the standard tight++ lepton selections ($N^{tight++}$) or only the loose lepton selections (N^{loose}).

The total number of events will contain contributions from both real leptons and fakes,

$$N^{\text{tight++}} = rN^{\text{loose}}_{\text{real}} + fN^{\text{loose}}_{\text{fake}}, \tag{8.12}$$

$$N^{\text{loose}} = N^{\text{loose}}_{\text{real}} + N^{\text{loose}}_{\text{fake}}, \tag{8.13}$$

where r, f are the fractions of the real and fake events which satisfy the loose criteria to also satisfy the tight++ criteria. With knowledge of r, f the number of events with fake leptons to enter into the data may be calculated as

$$N^{\text{tight++}}_{\text{fake}} = fN^{\text{loose}}_{\text{fake}} = f\frac{N^{\text{tight++}} - rN^{\text{loose}}}{f-r}. \tag{8.14}$$

The relative fraction for real electrons (muons) is measured in an inclusive sample of $Z \to ee$ ($Z \to \mu\mu$) decays. The relative fractions for fake leptons are measured in data samples dominated by non-prompt and fake lepton backgrounds. For fake electrons, f is measured using a sample with the transverse mass of the W-boson, $M_T^W < 20$ GeV and the sum of the missing transverse energy and the transverse mass of the W-boson $E_T^{\text{miss}} + M_T^W < 60$ GeV. For fake muons, f is measured in a sample with the muon impact parameter significance $d_0^{\text{sig}} = d_0/\sigma(d_0) > 5$, therefore giving tracks unlikely to be associated with the primary decay process.A conservative uncertainty of 50% is applied to both of the fraction estimates and propagated through to the pretag multijet uncertainty. Additional uncertainties that derive from the data driven method relate to uncertainty on the number of real leptons subtracted from the data samples used for the f-estimates (a $\pm 10\%$ systematic), and alternate measurements of the real and fake fractions using different samples or control regions.

8.6 Control plots

This section contains control plots to analyse the data-MC agreement in different kinematic distributions. All predictions are found to be in good agreement with the data within uncertainties. There does not appear to be any discrepancies as a function of the variables shown in Figures 8.2-8.9 in either the e+jets or μ+jets channel. In all plots the hashed area represents all experimental systematic uncertainties as well as the b-hadron production and hadron-to-muon branching ratio

uncertainties, all are from [92].

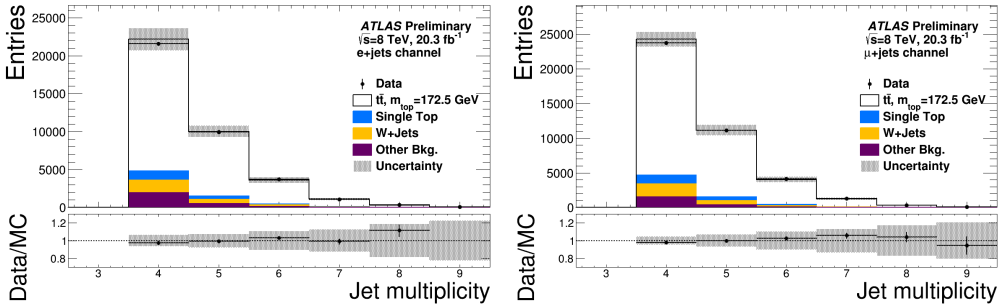

(a) e+jets channel (b) μ+jets channel

Figure 8.2: Jet multiplicity distributions.

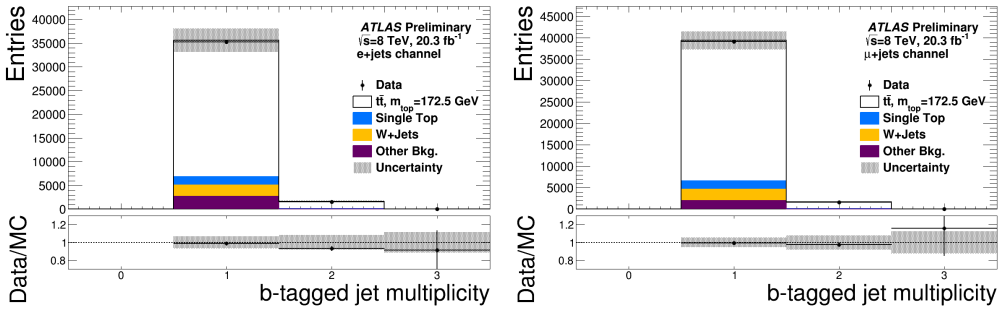

(a) e+jets channel (b) μ+jets channel

Figure 8.3: b-tagged jet multiplicity.

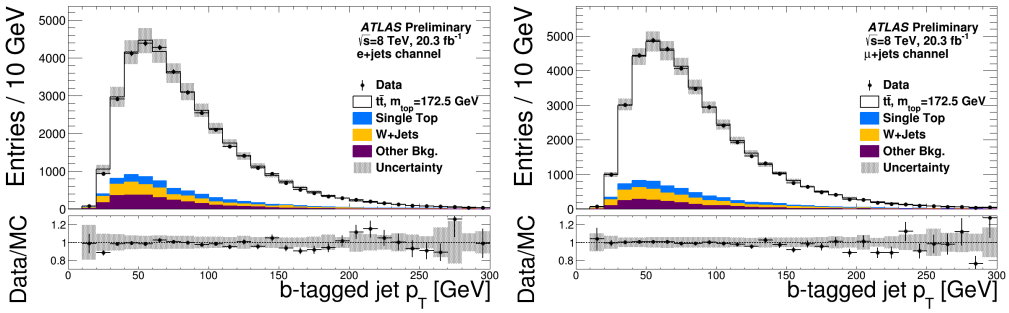

(a) e+jets channel (b) μ+jets channel

Figure 8.4: b-tagged jet p_T distributions.

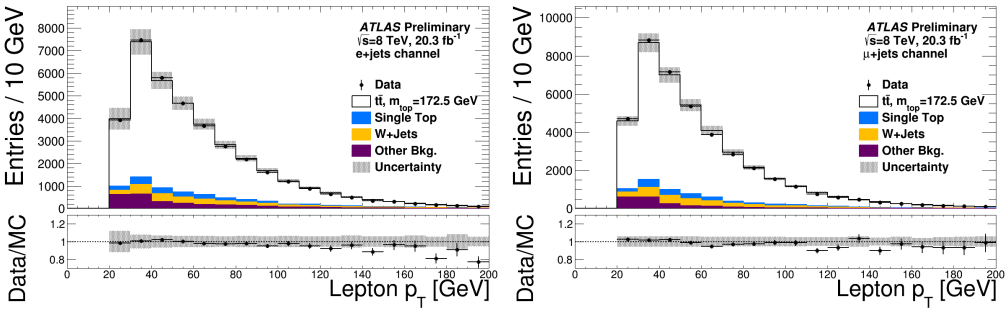

(a) e+jets channel (b) μ+jets channel

Figure 8.5: Lepton p_T distributions.

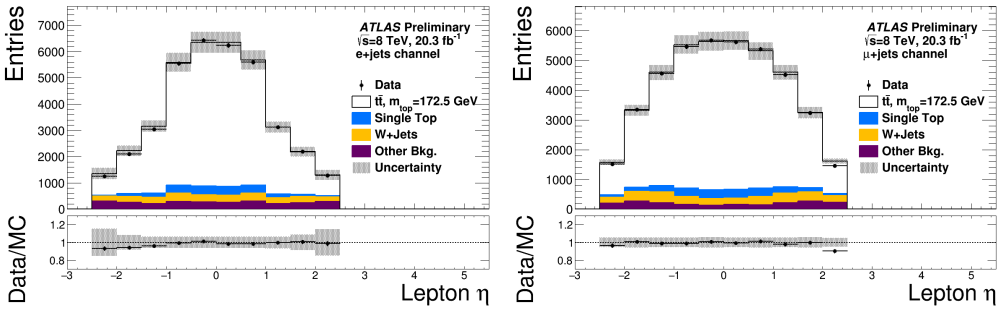

(a) e+jets channel (b) μ+jets channel

Figure 8.6: Lepton η distributions.

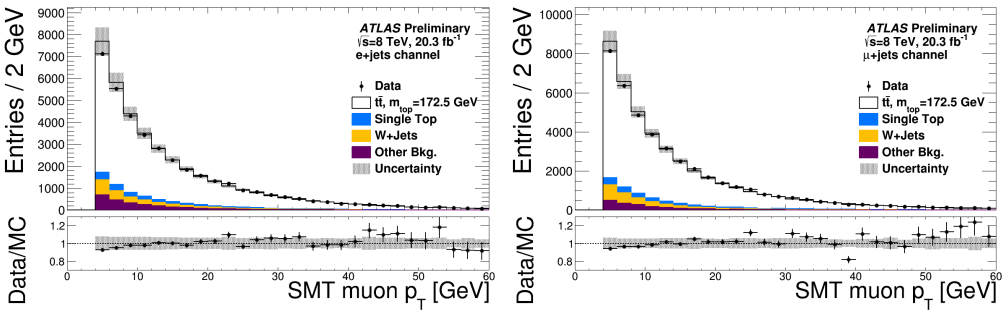

(a) e+jets channel (b) μ+jets channel

Figure 8.7: SMT p_T distributions.

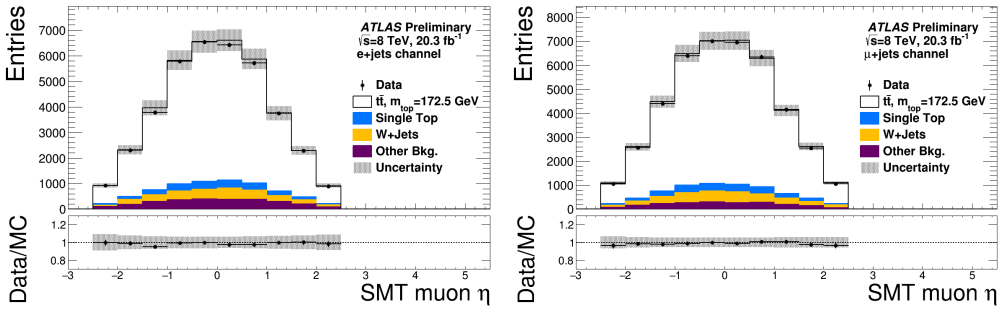

(a) e+jets channel (b) μ+jets channel

Figure 8.8: SMT η distributions.

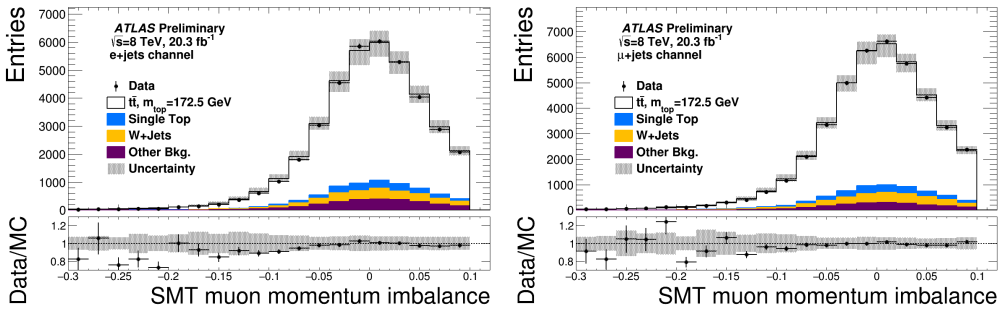

(a) e+jets channel (b) μ+jets channel

Figure 8.9: SMT *MI* distributions.

It's never too late to get back on track

Zach Anner

Chapter 9

Systematic Uncertainties

Systematics describe experimental or theoretical uncertainties which may affect the normalisation or shapes of distributions relevant to the measurement of a particular analysis. The systematics relevant to this analysis are described below. I provide only an overview of each systematic as I have no involvement in the implementation of this part of the analysis. The impact of all systematics decribed here, on the $t\bar{t}$ cross-section and the asymmetry measurements, is discussed in the results in Section 12.

9.1 Experimental uncertainties

Experimental systematic uncertainties describe those which relate to the mismeasurements of the properties of analysis objects. Uncertainties related to the hard lepton, the four jets, the SMT muon and the b-tagging procedure are all considered. In the charge and CP asymmetry (CA, CPA) measurements, many systematic uncertainties will be reduced due to the ratios of events cancelling out these effects to first order. This ratio also, as described in Section 4.1.1, removes the dependency of the analysis on experimental effects which might result in different numbers of reconstructed leptons from W-bosons. The systematics will not be reduced in this way for the cross-section measurement presented in Section 12.1, as will be seen in a quantitative way in the results of Tables 12.1, 12.3 and 12.7.

9.1.1 Lepton reconstruction, identification and trigger

The reconstruction of leptons using the ATLAS detector may differ slightly between simulation and data. Charged-dependent scale factors (SF) are derived using tag-and-probe analysis on Z-boson and J/ψ to charged lepton decays to correct the simulation reconstruction efficiencies. These SFs have uncertainties and the systematic contribution to this analysis is found by repeating the CA and CPA measurements after varying the SFs up and down by their uncertainties. The electron reconstruction efficiency at ATLAS [93] varies from $97-99\%$ depending on the η region and the transverse energy of the electron. The uncertainty on the reconstruction efficiency varies from $0.5-5.0\%$, where the lower value is measured in high-statistics high-energy ($E_T > 35$ GeV) $Z \to e^+e^-$ decays, and the larger value is a conservative uncertainty assigned to the region of electron $E_T < 15$ GeV where MC simulations are used due to the lack of available statistics. The electron identification efficiency, for the *tight* electron definition, is found to be $\sim 65-95\%$ depending on the electron E_T and η. The uncertainty on the electron identification efficiency is of the order 0.5% for central electrons with high E_T, and 10% for electrons with low E_T in the transition regions of the detector. The combined reconstruction and identification efficiencies for electrons, ranging from $65-95\%$, alongside the total statistical and systematic uncertainties and the Data/MC SFs, are shown in Figure 9.1 [93]. For muons the reconstruction efficiency is measured to be above 99% for the region of $|\eta|< 2.7$ and $5 \leq p_T \leq 100$ GeV, with an uncertainty of $\sim 0.1\%$, as shown in Figure 9.2 [93] alongside the Data/MC SFs.

9.1.2 Lepton energy scale and resolution

The resolution of the lepton energy may differ slightly between simulation and data. Z-boson to charged lepton decays are again utilised to provide SFs to correct the simulation distributions to those in the data. The SFs have uncertainties and their systematic contribution to this analysis is found by repeating the CA and CPA measurements after varying the SFs up and down by their uncertainties. For electrons, the energy resolution is E_T dependent but averages around 10%, with an uncertainty of less than 10% for $E_T < 50$ GeV, and 40% for $E_T \sim 500$ GeV [94]. For muons, the momentum resolution varies from 1.7% in the central η region at $p_T \sim 10$ GeV, to 4% in the largest rapidity region at $p_T \sim 100$ GeV [94].

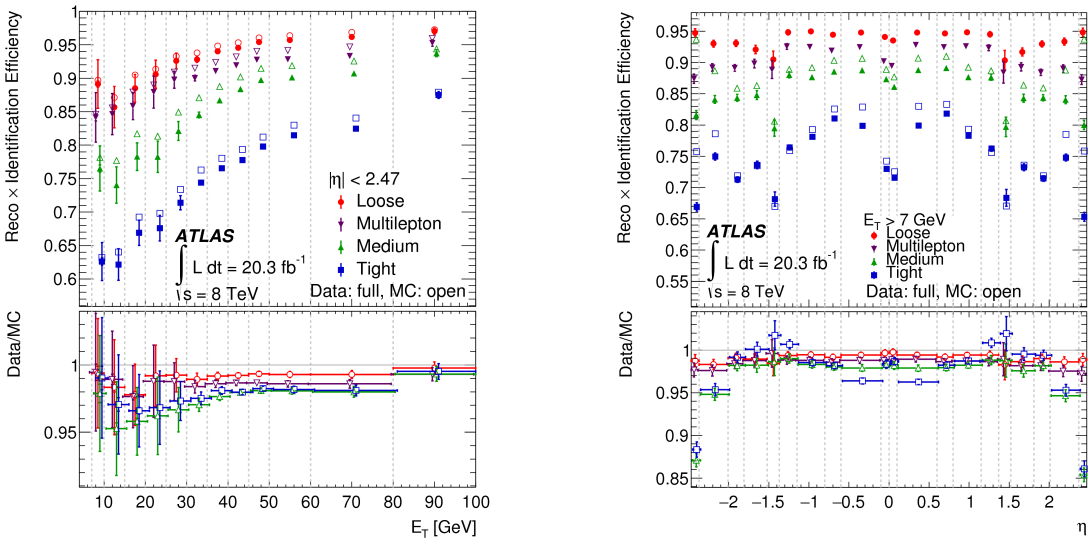

Figure 9.1: Measured combined reconstruction and identification efficiencies as a function of E_T and η for different cut-based selections in data, compared to MC simulations. The lower panel shows the Data/MC SFs.

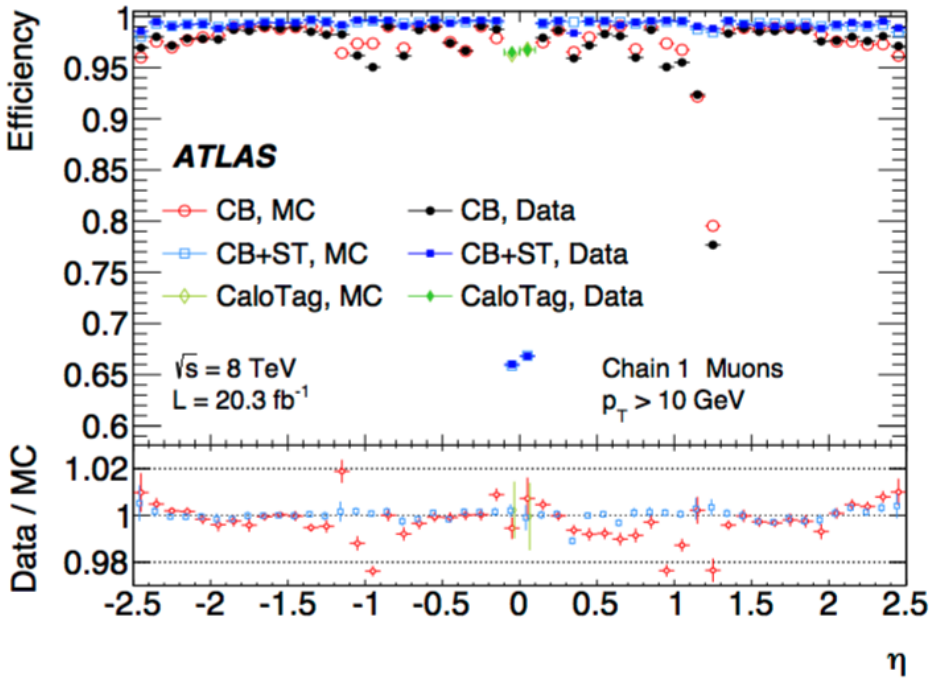

Figure 9.2: Muon reconstruction efficiency as a function of η for different muon reconstruction techniques, CB = Combined, ST = Segment-Tagged. The lower panel shows the Data/MC SFs.

9.1.3 Lepton charge misidentification

Lepton charge misidentification at ATLAS is considered negligible in the muon channel due to the low bremsstrahlung of muons within the detector and the larger number of ID and MS

hits each one creates, increasing the performance of track reconstruction algorithms. Charge misidentification in the electron channel must however be considered as it is non-negligible at ATLAS. Electrons which undergo bremsstrahlung will emit photons which may pair-produce. One of the subsequent positrons may be reconstructed instead of the original electron and this can lead to charge misidentification. This is more likely to occur towards higher values of pseudorapidity as the electrons must traverse a greater number of interaction lengths in the detector material. Moreover, high energy electrons will produce increasingly straight tracks which may be harder to accurately reconstruct than their muon equivalents which benefit from additional MS hits. Figure 9.3 [93] shows the electron charge misidentification probability as a function of pseudorapidity at the ATLAS detector, which varies from $0-10\%$ over the range $0 < |\eta| < 2.5$. Only a small number of electrons selected in this analysis will be in the largest pseudorapidity region where poor performance occurs. SFs are produced to correct the charge misidentification of simulation to that in data, using $Z \to e^+e^-$ tag-and-probe techniques [93]. These SFs have uncertainties and the systematic contribution to this analysis is found by repeating the CA and CPA measurements after varying the SFs up and down by their uncertainties.

9.1.4 Jet energy scale (JES)

The energy measurement of jets is dependent on a number of different experimental issues, for example the definition of jet clusters using the anti-k_T algorithm will alter the number of particles associated with each jet and the overall jet energy and angular properties. Modelling of pile-up, additional radiation and detector response must also be accounted for. Additional sources of JES uncertainty are η-calibration, jet flavour composition and mismodelling due to the measurement of high-p_T single hadrons. Each source of JES uncertainty requires SFs to correct the simulation to measurements in data. These SFs have uncertainties and the systematic contribution to this analysis is found by repeating the CA and CPA measurements after varying the SFs up and down by their uncertainties. As shown in Figure 9.4 the uncertainty in the measured jet energy at ATLAS is 4% in the region of $17 < p_T < 25$ GeV and $1-3\%$ for jets with $35 < p_T < 210$ GeV, for jets at the most central region of $|\eta| = 0.0$. Figure 9.5 shows the uncertainty as a function of η for jets with $p_T = 40$ GeV, where the uncertainty ranges between $4-6\%$.

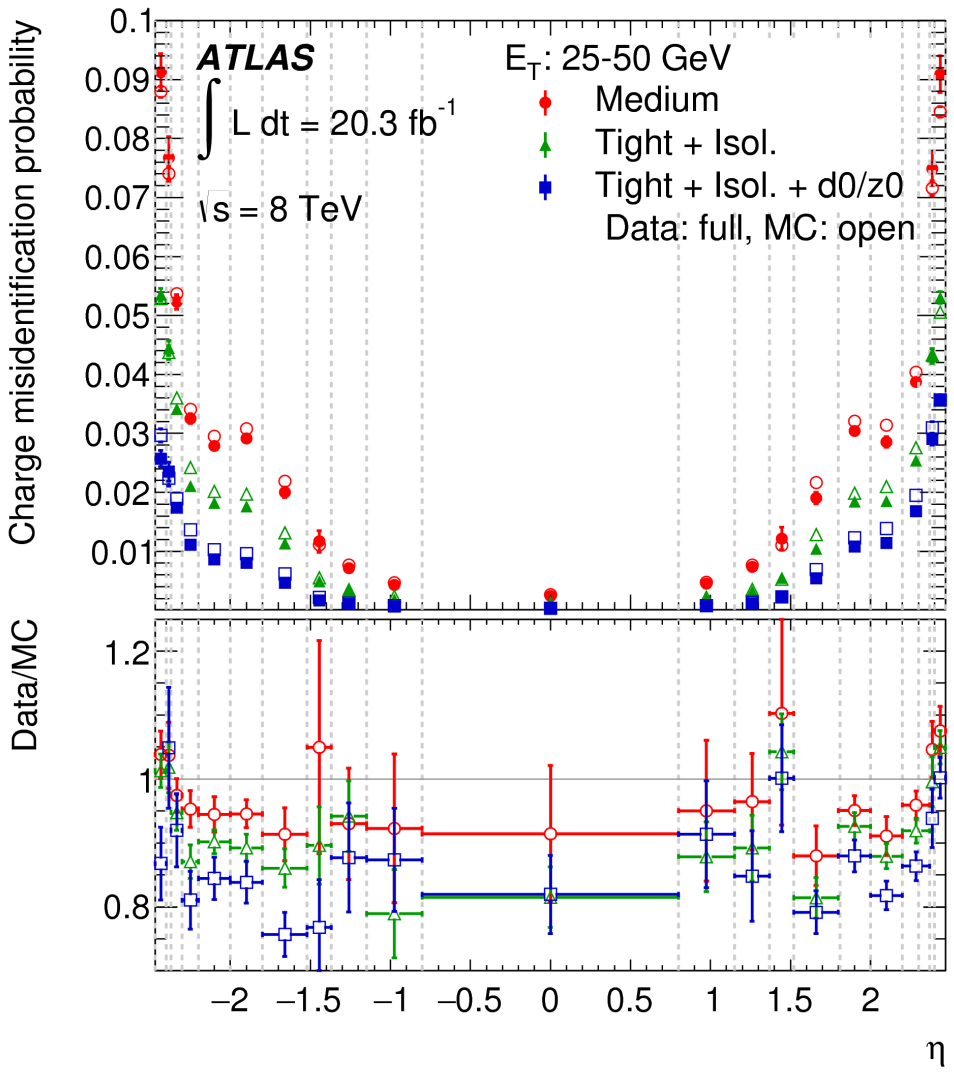

Figure 9.3: Charge misidentification probability in data as a function of η for different reconstruction criteria, compared to MC simulations. The lower panel shows the Data/MC SFs.

9.1.5 Jet energy resolution (JER)

The jet energy resolution may differ slightly between simulation and data. The differences are studied [95] as a function of p_T and η and additional jet smearing is applied to the simulation to account for this. The uncertainty in the jet energy resolution at ATLAS is $\sim 20\%$ in the region of $20 < p_T < 80$ GeV.

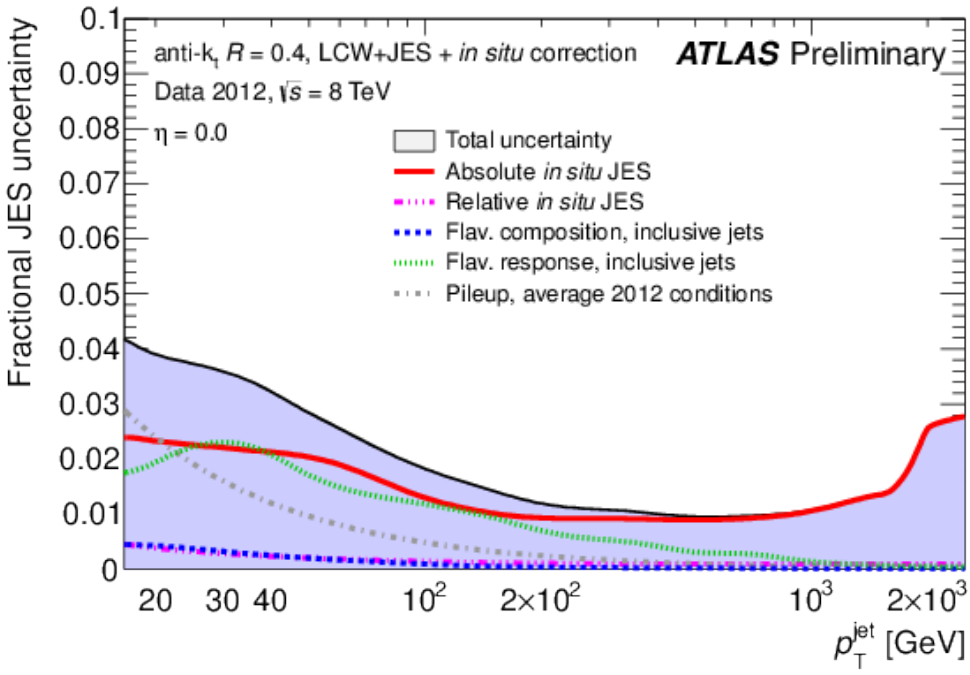

Figure 9.4: The fractional systematic uncertainty components as a function of p_T on the JES for jets with $|\eta|= 0.0$. The total uncertainty (all components summed in quadrature) is shown as a filled blue region topped by a solid black line.

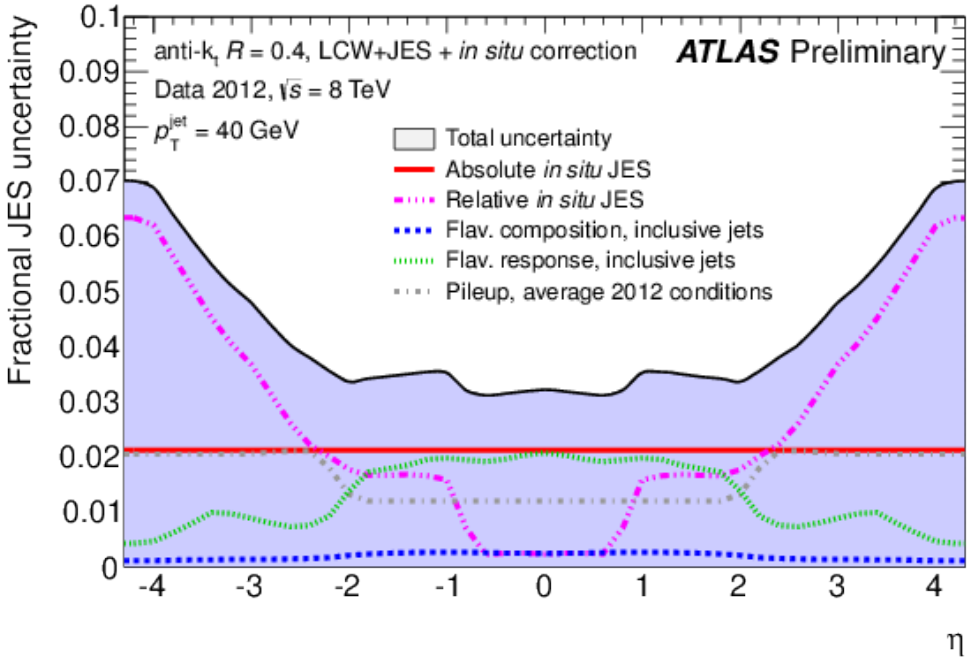

Figure 9.5: The fractional systematic uncertainty components as a function of η on the JES for jets with $p_T = 40$ GeV. The total uncertainty (all components summed in quadrature) is shown as a filled blue region topped by a solid black line.

9.1.6 Jet reconstruction efficiency

Slight differences may exist in the jet reconstruction efficiency between simulation and data. Studies at ATLAS [95] have found the difference to be of the order 0.2% for $p_T^{\text{jet}} < 30$ GeV. To account for this, 0.2% of jets in that transverse momentum region are randomly removed from the nominal sample and the CA and CPA measurements are performed again.

9.1.7 Jet vertex fraction (JVF)

The jet vertex fraction requirements (Section 8.2.2) may be satisfied by a different fraction of jets in simulation than in data. To account for this the in JVF efficiency is studied in simulation and in data using Z+1-jet events enriched in hard-scatter jets or pile-up. The JVF requirement in this analysis is altered by the magnitude of the measured differences between simulation and data to evaluate the systematic uncertainty.

9.1.8 Flavour tagging uncertainty

This systematic uncertainty relates to the usage of the MV1 tagging algorithm for the identification of jets from b-hadron decays. The performance of this algorithm varies for b-jets and c-jets, and the efficiencies for each as well as the mistag rate for light-flavour jets may differ in simulation compared to data. SFs are required to correct the tagging rates, binned by p_T and η. These SFs have uncertainties and the systematic contribution to this analysis is found by repeating the CP and CA measurements after varying the SFs up and down by their uncertainties. The calibration of the MV1 algorithm at ATLAS is performed using a combinatorial likelihood approach using dilepton top-quark pair events [96]. An overview of the technique, built up as described in [96] is as follows. After a kinematic selection to obtain $t\bar{t}$ dilepton events with a high purity, all jets in each event are treated individually and to extract the b-tagging efficiency ε_b the fraction of jets selected by the tagger, f_{tagged} is defined as

$$f_{\text{tagged}} = f_b \varepsilon_b (1 - f_b) \varepsilon_j, \tag{9.1}$$

where f_b is the fraction of b-jets in the sample, ε_b is the b-jet tagging efficiency and ε_j is the light-flavour jet efficiency. With this technique, f_{tagged} is measured in data whilst f_b and ε_j are determined in simulation. Additional information may be utilised for two-jet events, as in $t\bar{t}$

dilepton decays, by expanding to a system of two equations which define the fraction of events with one or two tagged jets, $f_{1\text{ tag}}$ or $f_{2\text{ tags}}$ as

$$f_{1\text{ tag}} = 2f_{bb}\varepsilon_b(1-\varepsilon_b) + f_{bj}[\varepsilon_j(1-\varepsilon_b) + (1-\varepsilon_j)\varepsilon_b] + \left(1-f_{bb}-f_{bj}\right)2\varepsilon_j(1-\varepsilon_j) \tag{9.2}$$

$$f_{2\text{ tags}} = f_{bb}\varepsilon_b^2 + f_{bj}\varepsilon_j\varepsilon_b + \left(1-f_{bb}-f_{bj}\right)\varepsilon_j^2 \tag{9.3}$$

where f_{bb} and f_{bj} are the fractions of events in the sample with true bb and bj jet pairs. With this technique, $f_{1\text{ tag}}$ and $f_{2\text{ tags}}$ may be measured in data, whilst utilising determinations of f_{bb}, f_{bj} and ε_j from simulation to get a higher precision estimate of ε_b. To expand on this approach with two jets, a per-event likelihood function is defined as

$$\begin{aligned}\mathcal{L}(p_{T1}, p_{T2}, \omega_1, \omega_2) = &[f_{bb}\mathcal{P}_{bb}(p_{T1}, p_{T2})\,\mathcal{P}_b(\omega_1|p_{T1})\,\mathcal{P}_b(\omega_2|p_{T2}) \\ &+ f_{bj}\mathcal{P}_{bj}(p_{T1}, p_{T2})\,\mathcal{P}_b(\omega_1|p_{T1})\,\mathcal{P}_j(\omega_2|p_{T2}) \\ &+ f_{jj}\mathcal{P}_{jj}(p_{T1}, p_{T2})\,\mathcal{P}_j(\omega_1|p_{T1})\,\mathcal{P}_j(\omega_2|p_{T2}) \\ &+ 1 \leftrightarrow 2]/2,\end{aligned} \tag{9.4}$$

where f_x are the usual jet flavour fractions, $\mathcal{P}_f(\omega|p_T)$ is the probability density function (PDF) of the b-tagging discriminant ω_i for jet i of flavour f and a given transverse momentum, and $\mathcal{P}_{f_1 f_2}(p_{T1}, p_{T2})$ is the two-dimensional PDF for two jets with flavours $f_{1,2}$ and transverse momenta $p_{T1,2}$. The b-tagging efficiency is then extracted as

$$\varepsilon_b(p_T) = \int_{\omega_{\text{cut}}}^{\infty} d\omega' \mathcal{P}_b\left(\omega', p_T\right). \tag{9.5}$$

This technique, with expansion to events with 3 or more jets, it utilised to calculate the b-tagging efficiency of the MV1 algorithm on MC and on data and provide SFs (with statistical and systematic errors) to apply in analyses, as detailed in [96], and to identify the b-tagging discriminant cuts required to define working points for particular efficiencies.

9.1.9 SMT uncertainty

The efficiencies and fake rates discussed in Section 7 have associated uncertainties. The systematic contribution to this analysis is found by repeating the CA and CPA measurements after varying the SFs up and down by their uncertainties.

9.1.10 Background uncertainties

In addition to the statistical uncertainties, the data-driven multijet background has additional uncertainties deriving from the techniques used in its estimation. The cross-section of each of the background estimates from MC simulations are varied up and down by their total uncertainties and the CA and CPA measurements are re-performed in each case.

9.1.11 Luminosity

The uncertainty on the luminosity affects the measurement of the cross-section $\sigma_{t\bar{t}}$, as the luminosity directly appears in the denominator of the cross-section calculation

$$\sigma_{t\bar{t}} = \frac{N_{\text{data}} - N_{\text{bkg}}}{\int L\mathrm{d}t \times \varepsilon \times BR}. \tag{9.6}$$

The uncertainty related to the integrated luminosity for the 8 TeV data set is 1.9% [97]. The measured luminosity is varied up and down by its uncertainty to account for this effect. A shift in the overall event yield will not affect the measured CA and CPAs.

9.1.12 Beam energy

The uncertainty on the LHC beam energy also affects the measurement of the cross-section $\sigma_{t\bar{t}}$. The uncertainty related to the beam energy at the LHC for the 8 TeV data set is 1.7% [98]. The beam energy is varied up and down by its uncertainty to account for this effect. A shift in the overall event yield will not affect the measured CA and CPAs.

9.2 Modelling uncertainties

Modelling systematic uncertainties describe those which relate to the accuracy of the simulation oh physics processes. Uncertainties related to particle production and decay rates, partons

showering, hadronisation and similar effects are all considered. Many modelling systematic uncertainties will be reduced due to the ratios of events in the CA and CPA calculations cancelling out these effects to first order.

9.2.1 b-hadron production

SFs are required to correct the b-hadron production fractions in simulation to the world average measurements listed in the RPP [41] (and detailed in Section 8) and each SF has an associated uncertainty. The systematic contribution to this analysis is found by repeating the CA and CPA measurements after varying the SFs up and down by their uncertainties.

9.2.2 Hadron-to-muon branching ratios

The scale factors required to correct the $b \to \mu$ branching ratios in simulation to the world average measurements listed in the RPP (and detailed in Section 8) have associated uncertainties. The systematic contribution to this analysis is found by repeating the CP and CA measurements after varying the SFs up and down by their uncertainties.

9.2.3 Asymmetry of single-top production

In pp collisions a charge asymmetry exists in the production of single-top-quarks for the t- and s-channels, due to the available valence quarks in proton-proton collisions. The proton valence quarks are able to produce more W^+-bosons than W^--bosons in each case, resulting in more $W^+ \to tb$ vertices than the charge conjugate. Differences in the asymmetry predicted in theory and implemented in the simulation may exist. For this analysis, a conservative approach is taken to account for any charge-related effects. The theoretical cross-sections for the t-channel and s-channel are varied within their uncertainties, but with the additional consideration that a shift in the total asymmetry may be caused by enhanced or reduced top or anti-top production separately. Four systematics are considered for the t- and s-channels, where for each either the top or anti-top production cross-section is varied individually to generate new CA and CPA measurements. Tables 9.1- 9.3 detail the theoretical production cross-sections, and the systematic variations in the t- and s-channels as described. In these tables, $\uparrow$ and $\downarrow$ represent shifts in the top or anti-top cross section with the other held static.

Process	Total cross section pb	Top cross section pb (%)	Anti-Top cross section (%)
t-channel [99]	$87.76^{+3.44}_{-1.91}$	56.9 (64.8%)	30.9 (35.2%)
s-channel [100]	5.61 ± 0.22	3.83 (68.3%)	1.78 (31.7%)
Wt [101]	22.37 ± 1.52	11.18 (50%)	11.18 (50%)

Table 9.1: Theoretical cross sections for single-top at $\sqrt{s} = 8$ TeV at the LHC. The numbers in parentheses detail the expected relative amount of t and $\bar{t}$ predicted for each single top channel.

Systematic	Total Cross Section	Top XS	AntiTop XS	Top %	AntiTop %	Top SF	AntiTop SF
Nominal	87.76	57.66	30.10	65.7	34.3	1.0	1.0
Top $\uparrow$	91.20	61.10	30.10	67.0	33.0	1.020	0.962
Top $\downarrow$	85.85	55.75	30.10	64.9	35.1	0.988	1.022
AntiTop $\uparrow$	91.20	57.66	33.54	63.2	36.8	0.962	1.072
AntiTop $\downarrow$	85.85	57.66	28.19	67.2	32.8	1.022	0.957

Table 9.2: Single-top t-channel production asymmetry systematic variations, with relative top and anti-top cross-sections determined in MC.

Systematic	Total Cross Section	Top XS	AntiTop XS	Top %	AntiTop %	Top SF	AntiTop SF
Nominal	5.61	3.64	1.97	64.8	35.2	1.0	1.0
Top $\uparrow$	5.83	3.86	1.97	66.1	33.9	1.021	0.962
Top $\downarrow$	5.39	3.42	1.97	63.4	36.6	0.978	1.041
AntiTop $\uparrow$	5.83	3.64	2.19	62.4	37.6	0.962	1.070
AntiTop $\downarrow$	5.39	3.64	1.75	67.4	32.6	1.041	0.925

Table 9.3: Single-top s-channel production asymmetry systematic variations, with relative top and anti-top cross-sections determined in MC.

9.2.4 Next-to-leading order (NLO) generator

The choice of event generator may produce a number of differences in the distributions considered in simulation and used for generation of response matrices during unfolding. To account for this, an uncertainty is evaluated as the difference between two different generators (MC@NLO and POWHEG, both interfaced with HERWIG++) in calculating the CA and CP asymmetries.

9.2.5 Parton shower and hadronisation

Analogously, the choice of model to describe the parton shower and hadronisation in the simulated samples will also generate different results. To account for this, an uncertainty is evaluated as the difference between two different samples (POWHEG, interfaced with PYTHIA6 and HERWIG++ separately) in calculating the CA and CP asymmetries.

9.2.6 Additional radiation

Mismodelling of the magnitude of initial- and final-state radiation in pp collisions produce the largest variation in results for this analysis due to the presence of additional jets which affect the performance of kinematic likelihood fitting (Section 10). Samples are generated using POWHEG with additional and reduced radiation and the largest difference in measurements of CA and CP asymmetries with respect to the nominal sample is taken as the total systematic uncertainty.

9.2.7 Parton distribution function

The parton distribution function describes the fraction of energy carried by each parton inside of the protons used in the LHC collisions. Following the prescription of PDF4LHC [102], three different PDF sets (CT10, MSTW2008, NNPDF2.3) are considered (using MC@NLO interfaced with HERWIG++). The differences in the measured CA and CP asymmetries due to the choice of PDF set are taken as systematic uncertainties on the final results.

I'm not trapped in here with you, you're trapped in here with me!

Rorschach

Chapter 10

Kinematic Fitting

To determine accurately the correct charge-pairings of soft muons and charged leptons from W-boson decays, it is required to separate events into two categories; same-top (ST) and different-top (DT). Events in which the two leptons both originate from the decay products of an individual top quark are labelled ST, and event in which the two leptons originate from the decay products of two different top quarks are labelled as DT. Any event classified as DT must have its charge information altered before inclusion into the charge and CP asymmetry measurements, for example an event with a positive charged lepton from the W-boson, l^+, and a negative soft muon from the b-quark, μ^-, would (with no ST/DT separation) enter into the bin yield N^{+-}. However, once identified as a DT event, the first charge must be flipped to correctly reflect the charge of the W-boson originating from the same-top decay as the soft-muon, $N^{+-} \Rightarrow N^{--}$, as this is required in the definition of the charge asymmetries. To achieve the ST/DT separation in this analysis, kinematic fitting is employed as described in the sections below. The task is not to perfectly rebuild the entire $t\bar{t}$ decay from the available analysis objects as is most commonly required of kinematic fitters, but only to correctly assign the SMT-tagged jet to the correct top-quark decay in the event.

10.1 Kinematic Likelihood Fitter

The Kinematic Likelihood Fitter (KLF) [103] is a standard ATLAS package using ROOT [104] and MINUIT [105] from a Bayesian Analysis Toolkit (BAT). It uses a maximum likelihood method, as described below, to produce estimates of unknown parameters when presented with

data and a model decay channel. The goal of the fitter is two-fold; to find both the pairings (*matchings*) between measured objects and those in the model, and to fit the measured properties of those objects to reflect more realistic values with the knowledge of the expected true decay. In many analyses the fitted parameters are used to perform further calculations (reconstruction of top-quark mass for example), however the fitted parameters are not utilised for the CA and CPA measurements.

10.1.1 Kinematic fitting

In the context of this analysis the goal is to ascertain the most likely pairings between reconstructed objects and model particles for the decay. Given a single lepton and four jets, the task is to find the most likely orientation of the jets to match to the known partons. It is possible to build a likelihood function using the measured jet and lepton properties and constraints from theory and from detector resolution.

Constraints

For the $t\bar{t}\ell$+jets decays channel it is expected to measure four jets (two b-jets from the top-quark decays, and two light-jets from a W-boson decay) and a charged lepton, and to expect missing momentum due to a neutrino. This provides multiple opportunities to place constraints on the system, such as on the invariant mass of the reconstructed parent particles. The first constraint is provided by the probability to measure the value of the invariant mass of the two light jets given a Breit-Wigner (BW) distribution for the known W-boson mass $M_W = 80.4$ GeV of width $\Gamma_W = 2.1$ GeV. A second similar requirement is put on the invariant mass $m_{l\nu}$ built from the lepton and missing energy. Other constraints may be created by reconstructing the invariant masses of the top quarks on either side of the decay, via m_{jjj} and $m_{l\nu j}$, given a BW of the top-quark mass $M_t = 172.5$ GeV with a width of $\Gamma_W = 1.5$ GeV (from MC). This describes four constraints for a likelihood calculation, which may provide some power in identifying the most likely combination of jets for the decay topology. The BW distribution for measurements of a mass m around an expected central mass M and width Γ is

$$BW(m|M) = \frac{2}{\pi}\frac{\Gamma M^2}{(m^2 - M^2)^2 + \Gamma^2 M^2}. \tag{10.1}$$

Transfer functions

The energies and angular properties of each the charged lepton and the jets will not be perfectly measured, which may also be accounted for in the likelihood, for example a poorly measured η_{jet} distribution could affect the likelihood to assign any particular jet to any particular parton. This is considered by the use of a 'transfer function' (TF). The TFs relate the input and the output of the detector system. They utilise detector resolution information, binned in energy (E) and η-regions, to estimate potential shifts in measurements due to the detector response. TFs are used to map the detector response (for example for jets) onto single particles from hard-scattering processes. This is relevant for both the model quarks and leptons. It is possible to build transfer functions (resolution functions) for a measured value in the ATLAS detector when given some true value, according to the resolution of the detector, designed to account for imperfect measurements of the energies $\tilde{E}$ and angular properties $\tilde{\Omega}_i$ of the jets and leptons. The KLFitter toolkit comes with transfer functions for E and η bins; $W(\hat{E}_i|E_i)$ and $W(\hat{\Omega}_i|\Omega_i)$. These are derived using MC to calculate the relative deviations between truth particles and reconstructed objects, including the effects of physical detector issues such as dead pixels, and also of reconstruction algorithms. The TFs are asymmetric, as often the true energy of a particle is more than is measured by the detector ($E_{\text{truth}} > E_{\text{measured}}$) and therefore the resolution ($\frac{E_{\text{truth}} - E_{\text{measured}}}{E_{\text{truth}}}$) is not symmetric. The TFs are therefore built using double Gaussian functions of the form

$$W(\delta E) = \frac{1}{\sqrt{2\pi}(p_2 + p_3 p_5)} \left[\exp\left(-\frac{(\delta E - p_1)^2}{2p_2^2} \right) + p_3 \exp\left(-\frac{(\delta E - p_4)^2}{2p_5^2} \right) \right] \tag{10.2}$$

with $\delta E = \frac{E_{\text{truth}} - E_{\text{measured}}}{E_{\text{truth}}}$ and $p_{1,\ldots,5}$ parameters of the detector and reconstruction performance and E_{truth} which are fit, as described in [103]. The TFs are binned in η due to variations in the detector resolution and efficiency, specifically related to the calorimeter crack region.

Input parameters

In order to build a likelihood using the constraints and TFs as described above, it is required to provide 18 measured input parameters, as follows:

- the energies $\tilde{E}_i$ of four jets

- the angular information of four jets, $\tilde{\Omega}_i = \left(\tilde{\eta}_i, \tilde{\phi}_i\right)$
- the energy $\tilde{E}_l$ of the lepton
- the angular information of the lepton, $\tilde{\Omega}_l = \left(\tilde{\eta}_l, \tilde{\phi}_l\right)$
- the missing momentum x-, y- and z-components. The z-component is calculated using a constraint on the W-boson mass, $M_W^2 = (p_\nu + p_\ell)^2$. In general two solutions exist, and the one which results in the larger likelihood is selected. If no solution exists (or if both fall outside of a ± 1 TeV bound) then the longitudinal momentum is set to 0 GeV. Additionally the transverse momentum components $p_{x,y}^\nu$ are permitted to float during the fit alongside the other parameters.

The lepton information is used in the invariant mass constraints, however it is assumed that there is no uncertainty on the measured direction of the lepton and as such this angular information does not float during the fit.

10.1.2 The likelihood function

The likelihood takes a form which accounts for all of the above constraints and TFs, using all leptonic, jet and missing energy information. The nominal likelihood as prescribed in the nominal usage of the KLFitter is

$$L = \left(\prod_{i=1}^{4} W(\tilde{E}_i|E_i)\right) \cdot W(\tilde{E}_l|E_l) \cdot W(E_x^{miss}|p_x^\nu) \cdot W(E_y^{miss}|p_y^\nu) \cdot \left(\prod_{i=1}^{4} W(\tilde{\Omega}_i|\Omega_i)\right) \cdot$$
$$BW(m_{jj}|M_W) \cdot BW(m_{l\nu}|M_W) \cdot BW(m_{jjj}|M_t) \cdot BW(m_{l\nu j}|M_t). \quad (10.3)$$

The KLFitter makes use of the Minuit minimisation algorithm in order to find the global minimum of the negative log likelihood $-\ln L$, to test each of the four reconstructed jets as placed in each of the possible parton positions within the event topology. Using four reconstructed jets in four positions results in 24 possible permutations, however as the likelihood is insensitive to a swapping two jets in the place of the hadronic W-bosons decay, the fit is simplified to only 12 permutations. There is further possibility to reduce (or increase) this complexity as discussed in sections below.

Angular Likelihood

The $V-A$ structure of the electroweak interaction in the top-quark decay provides predictions for the angular distribution of the charged lepton. There is the option to use an extra angular term in the likelihood fit taking into account helicity corrections in the decays of the W-bosons. These corrections take the form

$$\frac{1}{\Gamma_W}\frac{d\Gamma_W}{d\cos\theta^*_{l\,b_{lep}}} = \frac{3}{4}F_0\left(1-\cos\theta^*_{l\,b_{lep}}{}^2\right)+\frac{3}{8}F_L\left(1-\cos\theta^*_{l\,b_{lep}}\right)^2+\frac{3}{8}F_R\left(1+\cos\theta^*_{l\,b_{lep}}\right)^2, \tag{10.4}$$

$$\frac{1}{\Gamma_W}\frac{d\Gamma_W}{d\cos\theta^*_{q\,b_{had}}} = \frac{3}{4}F_0\left(1-\cos\theta^*_{q\,b_{had}}{}^2\right)+\frac{3}{8}\left(F_L+F_R\right)\left(1-\cos\theta^*_{q\,b_{had}}{}^2\right), \tag{10.5}$$

where $F_{0,L,R}$ represent the W-helicity fractions for longitudinal, left- and right-handed W-bosons respectively. These are set to $F_0 = 0.687$, $F_L = 0.311$ and $F_R = 0.002$ in the KLFitter following the theoretical predictions [106].

Fit parameters

Within each permutation, the KLFitter has the freedom to fit the measurement of each parameter. The fit simultaneously finds the most optimal distribution of jets whilst correcting the event kinematics. The KLFitter is designed, for every jet permutation, to scan over 16 parameters defined below as part of the likelihood minimisation process:

- energy of the four quarks, $E_i \in [min(0,\tilde{E}_i - 7\cdot\sqrt{\tilde{E}_i}),\tilde{E}_i + 7\cdot\sqrt{\tilde{E}_i}]$ GeV
- energy of the lepton, $E_l \in [min(0,\tilde{E}_l - 2\cdot\sqrt{\tilde{E}_l}),\tilde{E}_l + 2\cdot\sqrt{\tilde{E}_l}]$ GeV
- missing energy x- and y-components, $p^{\nu}_{x,y} \in [E^{miss}_{x,y} - 100, E^{miss}_{x,y} + 100]$ GeV
- missing energy z-component, $p^{\nu}_z \in [-1000, +1000]$ GeV
- pseudorapidity of the four quarks, $\eta_i \in [\tilde{\eta}_i - 0.2, \tilde{\eta}_i + 0.2]$
- azimuthal angle of the four quarks, $\phi_i \in [\tilde{\phi}_i - 0.1, \tilde{\phi}_i + 0.1]$

The parameter ranges are intended to be conservative with respect to the resolution of the detector, to prevent the fit on each from reaching the edge of the parameter space [107]. Optionally, it is possible to include a 17th free parameter in the form of the top-quark mass, however such a wide mass window is unlikely to produce an increase in performance and this is tested further later. The default use for permitting a free top-quark mass is to provide functionality for analyses using the KLFitter which wish to measure the top-quark mass and avoid bias, for all other analyses the default top-quark mass constraint is expected to provide better performance.

- Top-quark mass, $M_t \in [100, 1000]$ GeV

10.2 KLFitter optimisation

The KLFitter may be configured in many ways in order to increase the performance of the likelihood fit. It is important to find the best configuration, unique to each analysis, to maximise the performance of the tool; here defined as the purity of the final selection. The use case for this analysis is to identify specifically the correct placement of any SMT-tagged jet considered by the analysis, in order to classify the jet as either a 'same-top' (ST) or 'different-top' (DT) jet (events in which the the charged lepton from the W-boson and the soft muon from the b-quark both originate from the decay products of an individual top quark are labelled ST, and event in which the two leptons originate from the decay products of two different top quarks are labelled as DT). The KLFitter does not know about the soft muon itself, and bases its decisions on the kinematics of the reconstructed jets.

10.2.1 Truth matching and performance

Before it is possible to measure the performance of the KLFitter in classifying tagged jets as either ST or DT, it must be known in simulation what the tagged jet represents. The MC contains information required to track the full history of every soft muon contained in the simulation record for each event. Each soft muon is classified as either ST, DT signal, or as one of several backgrounds; dilepton (DIL), pileup ($g \to b\bar{b} \to \mu X$), additional radiation ($g(q) \to b\bar{b} \to \mu X$), $c \to \mu$ ($t \to Wb \to csb \to \mu bX$) and light flavour (LF, such as $\pi^+ \left(u\bar{d}\right) \to \mu^+\nu$). The breakdown of the nominal $t\bar{t}$ MC into signal and backgrounds (anything which is not ST or DT is referred to as a $t\bar{t}$ background) is shown in Tables 10.1- 10.4. Figure 10.1 and Figure 10.2 include

the non-$t\bar{t}$ backgrounds also. The yields are separated by reconstructed charge-pair bin after a KLFitter ST/DT decision, for these tables in particular the KLFitter decision has been made using the optimised configuration as described at the end of this chapter, as opposed to the nominal configuration initially described below.

The signal $t\bar{t}$ processes is dominated by direct $b \to \mu$ (see Table 10.9 below) which in ST events will populate the opposite-sign (OS) bins, and in DT events will populate the same-sign (SS) bins (until flipping the charge of the first lepton to account for this, and therefore populating the OS bins as seen below).

For the background $c \to \mu$, where the muon originates from a W-boson hadronic decay, the pairing of the soft muon and the charged lepton from the other W-boson is by definition a DT-type event, with the expected charge pairing to be of opposite sign (OS). If the KLFitter mistakenly classifies this type of event as ST, then it will populate the ST OS bins, as shown in Table 10.1. If the KLFitter correctly identifies this type of event as DT (which it does correctly for most occurrences), then it will flip the charge of the first lepton, and populate the DT same-sign (SS) bins, as shown in Table 10.2. This is the reason for the difference in shapes between the ST and DT plots shown in Figure 10.1 and Figure 10.2.

The light flavour background is seen to have a slight asymmetry between SS and OS, and also between ST and DT, however the magnitude of the differences in each bin fall within one standard deviation of the systematic uncertainties, which are of the order of ± 20 events for each LF bin.

The dilepton background is extremely asymmetric, this is because the tagged muon is not a real SMT muon but is instead the second charged lepton from a W-boson in the event. The two leptons are then by definition perfectly anti-correlated in charge and also constructed as a DT-type event. If the KLFitter mistakenly classifies this type of event as ST, then it will populate the ST OS bins, as shown in Table 10.1. If the KLFitter correctly identifies this type of event as DT (which it does for most occurrences), then it will flip the charge of the first lepton, and populate the DT SS bins, as shown in Table 10.2.

The additional radiation background is found to be fairly symmetric across all ST, DT, SS and OS bins, any deviations are well within the systematic uncertainty on each bin which is of the order ± 30 events.

The pileup background, originating from interactions within a $t\bar{t}$ event but not from the

hard scatter, is the second smallest contribution to the $t\bar{t}$ backgrounds. It is shown to have a slight asymmetry in favour of positive SMT muon fakes, larger than the magnitude of the systematic uncertainty on each bin which is of the order ± 4 events. This is considered to be a real effect, although given the very small number of events (pileup fakes $\leq 1\%$ total yield, largest bin deviation $\sim 0.03\%$ of true $t\bar{t}$ signal yield) it is considered to have a negligible effect within the uncertainties of the CA and CPA measurements. A possible hypothesis for the slight asymmetry could result from the presence of kaons in the underlying event, as the interaction cross-section of a negative kaon in the detector is greater than that for a positive kaon. This means a positive kaon is more likely to decay and produce a soft muon before it is absorbed in the detector material. As the SMT tagger fake rate is calibrated in data it is expected that the contribution of these types of fakes is well understood, and as the acceptance is extremely small kaons do not constitute the same magnitude of difficulty as for the inclusive muon measurement at D0 [46].

e+jets same-top	N^{++}	N^{--}	N^{+-}	N^{-+}
Total $t\bar{t}$ simulation	3237 (0.4)	3389 (0.4)	4629 (0.3)	4640 (0.3)
$t\bar{t}$ Backgrounds				
Total	241 (2)	231 (2)	506 (1)	516 (1)
Dilepton	0 (95)	0 (57)	53 (3)	53 (3)
Pileup	43 (4)	32 (4)	37 (4)	53 (3)
Additional radiation	53 (3)	55 (3)	56 (3)	53 (3)
$c \to \mu$	32 (4)	34 (4)	239 (2)	235 (3)
Light flavor	113 (3)	110 (3)	122 (2)	122 (3)

Table 10.1: $t\bar{t}$ background composition of e+jets same-top like events, rounded to the nearest integer. The percentage MC statistical uncertainty is given in parentheses. Where a percentage of zero appears in the dilepton channel, this is due to a very small number of weighted events which round to zero for one significant digit.

e+jets different-top	N^{++}	N^{--}	N^{+-}	N^{-+}
Total $t\bar{t}$ simulation	3708 (0.4)	3676 (0.4)	4157 (0.4)	4229 (0.4)
$t\bar{t}$ Backgrounds				
Total	725 (0.9)	717 (0.9)	277 (1)	301 (1)
Dilepton	75 (3)	79 (3)	0 (100)	0 (99)
Pileup	49 (3)	34 (4)	38 (4)	58 (3)
Additional radiation	62 (3)	62 (3)	64 (3)	64 (3)
$c \to \mu$	412 (1)	422 (1)	40 (4)	42 (4)
Light flavor	127 (2)	121 (2)	134 (2)	137 (2)

Table 10.2: $t\bar{t}$ background composition of e+jets different-top like events, rounded to the nearest integer. The percentage MC statistical uncertainty is given in parentheses.

μ+jets same-top	N^{++}	N^{--}	N^{+-}	N^{-+}
Total $t\bar{t}$ simulation	3945 (0.4)	3913 (0.4)	5415 (0.3)	5832 (0.3)
$t\bar{t}$ Backgrounds				
Total	278 (1)	262 (1)	576 (1)	598 (1)
Dilepton	0 (60)	0 (84)	56 (3)	53 (3)
Pileup	48 (3)	38 (4)	43 (4)	64 (3)
Additional radiation	63 (3)	59 (3)	59 (3)	63 (3)
$c \to \mu$	36 (4)	34 (4)	268 (1)	267 (1)
Light flavor	132 (2)	132 (2)	149 (2)	151 (2)

Table 10.3: $t\bar{t}$ background composition of μ+jets same-top like events, rounded to the nearest integer. The percentage MC statistical uncertainty is given in parentheses. Where a percentage of zero appears in the dilepton channel, this is due to a very small number of weighted events which round to zero for one significant digit.

μ+jets different-top	N^{++}	N^{--}	N^{+-}	N^{-+}
Total $t\bar{t}$ simulation	4101 (0.4)	4084 (0.4)	4520 (0.4)	4550 (0.4)
$t\bar{t}$ Backgrounds				
Total	802 (0.8)	774 (0.9)	314 (1)	328 (1)
Dilepton	80 (3)	79 (3)	0 (100)	0 (52)
Pileup	51 (3)	39 (4)	45 (4)	63 (3)
Additional radiation	70 (3)	72 (3)	73 (3)	73 (3)
$c \to \mu$	453 (1)	451 (1)	46 (3)	43 (4)
Light flavor	149 (2)	133 (2)	151 (2)	149 (2)

Table 10.4: $t\bar{t}$ background composition of μ+jets different-top like events, rounded to the nearest integer. The percentage MC statistical uncertainty is given in parentheses. Where a percentage of zero appears in the dilepton channel, this is due to a very small number of weighted events which round to zero for one significant digit

The performance of the KLFitter can be measured by looking at the *purity* of its decisions, here described for the ST case but relevant for DT also,

$$\text{KLFitter Purity: } \rho_{\text{KL}} = \frac{N^{\text{ST}}_{\text{truth}} \text{ and } N^{\text{ST}}_{\text{KL}}}{N^{\text{ST}}_{\text{KL}}} = \text{P}(\text{T}_{\text{ST}}|\text{KL}_{\text{ST}}) \tag{10.6}$$

where $N^{\text{ST}}_{\text{truth}}$ is the number of truth ST events, $N^{\text{ST}}_{\text{KL}}$ is the number of events classified as ST by the KLF, and $\text{P}(\text{T}_{\text{ST}}|\text{KL}_{\text{ST}})$ is the probability of an event being a truth ST event T_{ST} given a ST KLFitter decision KL_{ST}.

The performance may only be measured for SMT muons which are classified in the truth record as ST or DT, all $t\bar{t}$ background muons in MC are removed. A high purity is required to maximise the diagonality of the response matrix for unfolding, and minimise the uncertainties propagated through the matrix inversion.

10.2.2 Nominal setup

The nominal setup for the KLFitter is based on the prescription described in [103]. The initial configuration, all of which may be altered and is optimised in the following sections, is given in Table 10.5.

Configuration option	Nominal setting
b-tagging	SMT+MV1@85%
Number of b-tags	≥ 1
Jet multiplicity	Four jets permuted per event only
Jet selection priority	Highest p_T jets selected for permutations
b-tagged jet positions	No permutations with tagged jets in light flavour positions
Top-quark mass treatment	Fixed at 172.5 GeV
Likelihood	Basic (not angular)
Permutation selection	Permutation with maximum likelihood
Likelihood cuts	No cuts

Table 10.5: Overview of the nominal KLFitter configuration.

Using this configuration, the nominal performance of the KLFitter is presented in Tables 10.6 and 10.7, where each entry represents the probability for an event of true charge pairing $\alpha\beta$ to be reconstructed with charge pairing ab. The magnitude of the MC statistical uncertainty on all performance figures for the tables in this section is of the order of ~ 0.001. It has not been added onto every table to prevent repetition. In all cases the muon channel has the same performance as the electron channel, and is not shown.

The results of the KLFitter are used to produce a response matrix required for the unfolding of the measurement and described in detail in Section 11. For the nominal setup, the response matrices (as separated by ST and DT) appear as below. There is a clear difference in performance between SS and OS bins, which is discussed and resolved in Section 10.2.3 below. Also present is a difference in performance between ST and DT type events, similar to that observed in [103]. Prior to unfolding, the electron and muon channels, and ST and DT classifications are combined, with the total performance shown in Table 10.7.

10.2.3 Semileptonic corrections

The KLFitter performances deviates significantly between the SS and OS bins. OS leptons appear in all decay chains of truth $t\bar{t}$ events. There is no correlation between the drop in per-

e+jets	Same-top				Different-top			
	N^{++}_{Reco}	N^{--}_{Reco}	N^{+-}_{Reco}	N^{-+}_{Reco}	N^{++}_{Reco}	N^{--}_{Reco}	N^{+-}_{Reco}	N^{-+}_{Reco}
N^{++}_{truth}	0.699	0.000	0.000	0.301	0.772	0.000	0.000	0.228
N^{--}_{truth}	0.000	0.697	0.303	0.000	0.000	0.772	0.228	0.000
N^{+-}_{truth}	0.000	0.350	0.650	0.000	0.000	0.256	0.744	0.000
N^{-+}_{truth}	0.355	0.000	0.000	0.645	0.254	0.000	0.000	0.746

Table 10.6: Performance of the KLFitter using the nominal configuration, in the e+jets channel. The MC statistical uncertainty is ~ 0.002.

	N^{++}_{reco}	N^{--}_{reco}	N^{+-}_{reco}	N^{-+}_{reco}
N^{++}_{truth}	0.734	0.000	0.000	0.266
N^{--}_{truth}	0.000	0.733	0.267	0.000
N^{+-}_{truth}	0.000	0.303	0.697	0.000
N^{-+}_{truth}	0.304	0.000	0.000	0.696

Table 10.7: Performance of the KLFitter using the nominal configuration, with the combined e+jets and μ+jets channels, with ST and DT also combined. The MC statistical uncertainty is ~ 0.001

formance as a function of charge when the events are separated by ST or DT, or in terms of the charge of either of either lepton individually. The only identifiable difference between well reconstructed and poorly reconstructed events is the SS/OS classification of the two leptons. In order to find the root cause, the SS and OS decays are studied individually to search for discrepancies. Equations 2-7 in [50] show the possible $b \to \mu$ decay channels, labelled as PRL2 to PRL7 to easily compare with the equations from that paper:

- Same sign decays:
  - PRL2: $t \to l^{\pm}\nu(b \to \bar{b}) \to l^{\pm}l^{\pm}X$
  - PRL3: $t \to l^{\pm}\nu(b \to c) \to l^{\pm}l^{\pm}X$
  - PRL4: $t \to l^{\pm}\nu(b \to \bar{b} \to c\bar{c}) \to l^{\pm}l^{\pm}X$
- Opposite sign decays:
  - PRL5: $t \to l^{\pm}\nu b \to l^{\pm}l^{\mp}X$
  - PRL6: $t \to l^{\pm}\nu(b \to \bar{b} \to \bar{c}) \to l^{\pm}l^{\mp}X$
  - PRL7: $t \to l^{\pm}\nu(b \to c\bar{c}) \to l^{\pm}l^{\mp}X$

where in each case it is the second lepton which is identified as the soft muon in the event.

The purity ρ_{KL} may be measured as broken down by decay chains PRL2 - PRL7. Table 10.8 shows the KLFitter performance for each PRL equation, within their primary SS/OS category only (PRL2-4 performance is for SS, PRL5-7 performance is for OS, as indicated by the event yields shown in Table 10.9.)

PRL	ρ_{KL}
2	69.2
3	74.4
4	76.0
5	68.9
6	74.2
7	76.0

Table 10.8: Purity of the KLFitter selection broken down by true decay chain in the *e*+jets channel

PRL	*e*+jets					
	N^{++}_{Truth}	N^{--}_{Truth}	N^{+-}_{Truth}	N^{-+}_{Truth}	% of total SS	% of OS
2	760.1	741.1	1.3	1.9	20.6	0.0
3	2566.4	2531.3	4.8	4.8	70.1	0.1
4	323.4	330.7	0.9	1.3	9.0	0.0
5	7.7	8.1	5385.1	5414.7	0.2	88.1
6	0.8	0.2	416.7	406.7	0.0	6.7
7	0.7	0.8	307.8	309.2	0.0	5.0

Table 10.9: Yields broken down by true decay chain, in the *e*+jets channel

Similar performance is seen for PRL3-4 and PRL6-7, whilst the performance for PRL2 and PRL5 is significantly worse. This means that whilst a decay chain with poor ρ_{KL} is present for both the SS and OS decays, the relative yields show why the drop in performance is only apparent for the full sample in the OS case. PRL2 only makes up about 20% of the SS decays and therefore the stronger performance from PRL3 dominates the total. PRL5 however makes up about 89% of the OS decays and it is the performance of the KLFitter on this decay which is seen primarily.

The explanation for this lies in the intermediate *D*-meson for the better performing decays. The KLFitter TFs are designed to map a measured jet's energy and angular variables back to that of its parent quark. Performance degrades if the jet's reconstruction is significantly different than expected by the TFs. As the jets in consideration are *b*-jets with semileptonic decays, the

measurement of the jet will never be exact as there will always be energy removed by the soft muon and its associated neutrino. The greater the energy of the $\nu_\mu\mu$ pair, the more unlike the initial quark the b-jet will appear and the more the TFs will struggle to produce a good likelihood for positioning that jet correctly within the $t\bar{t}$ topology. When an intermediate D-meson exists, the total energy given to the soft muon and the neutrino is smaller than for a more direct $b \to \mu$ transition and the TFs perform well. However without the D-meson the soft muon comes directly from the B-meson and has a larger energy on average with a larger neutrino energy alongside, in those cases the KLFitter has worse performance. Without measurement of the neutrino, other than its contribution to the total missing momentum, tests may be made using only the soft muon as an approximation. The soft muon and the neutrino will be highly correlated in terms of energy. Figure 10.3 shows the SMT p_T distribution for each PRL decay, and Figure 10.4 shows the difference in energy between the reconstructed b-jet and its true MC b-quark, $\Delta p_T^{b_q j}$.

It is clear that there are two distinct shapes in the SMT p_T distribution according to the presence of a D-meson. It is possible to plot the performance of the KLFitter as a function of difference between reconstructed jet p_T and the matched MC parton b-quark p_T in order to gauge the direct dependence, as in Figure 10.5.

The KLFitter dependency on $\Delta p_T^{b_q j}$ shows that it is the missing energy from the semileptonic decay which is causing the drop in performance. It is possible to alleviate this issue by correcting every tagged SMT jet with the expected energy loss from the soft muon and neutrino. An ATLAS internal tool performs this correction using scale factors calibrated in double b-tagged dijet events. The correction is applied as follows:

1. Identify reconstructed muons within the radius of the jet cone (the SMT muon).
2. Subtract the expected muon ionisation E_μ^{loss} (energy left in the detector) from the reconstructed jet.
3. Identify the characteristic scale factor, f_{SLC}, required to correct a jet of measured energy E_j with muon(s) of energy E_μ, to the correct value when neutrinos are accounted for.
4. Reconstruct the corrected jet energy as: $E_j^{\text{SLC}} = f_{\text{SLC}} \left(E_j + E_\mu + E_\mu^{\text{loss}}\right)$

Apply the soft-lepton corrections (SLC) significantly reduces the difference between the KLFitter performance for the SS and the OS events and also improves the performance of the

KLFitter overall. The purity of the KLFitter per decay chain with this SLC correction and the updated response matrices are shown in the tables below.

PRL	ρ_{KL} e+jets (%)
2	77.0
3	78.1
4	79.1
5	76.8
6	77.9
7	78.6

Table 10.10: Purity of the KLFitter selection broken down by decay chain in the e+jets channel, after applying semileptonic corrections to the SMT tagged jets

e+jets	Same-top				Different-top			
	N^{++}_{Reco}	N^{--}_{Reco}	N^{+-}_{Reco}	N^{-+}_{Reco}	N^{++}_{Reco}	N^{--}_{Reco}	N^{+-}_{Reco}	N^{-+}_{Reco}
N^{++}_{truth}	0.758	0.000	0.000	0.242	0.804	0.000	0.000	0.196
N^{--}_{truth}	0.000	0.757	0.243	0.000	0.000	0.801	0.199	0.000
N^{+-}_{truth}	0.000	0.256	0.744	0.000	0.000	0.205	0.795	0.000
N^{-+}_{truth}	0.258	0.000	0.000	0.742	0.202	0.000	0.000	0.798

Table 10.11: Performance of the KLFitter using the nominal configuration with semileptonic jet corrections in the e+jets channel. The MC statistical uncertainty is ~ 0.002

	N^{++}_{reco}	N^{--}_{reco}	N^{+-}_{reco}	N^{-+}_{reco}
N^{++}_{truth}	0.777	0.000	0.000	0.223
N^{--}_{truth}	0.000	0.777	0.223	0.000
N^{+-}_{truth}	0.000	0.232	0.768	0.000
N^{-+}_{truth}	0.232	0.000	0.000	0.768

Table 10.12: Performance of the KLFitter using the nominal configuration with semileptonic jet corrections, with the combined e+jets and μ+jets channels, with ST and DT also combined. The MC statistical uncertainty is ~ 0.001

The effect of the SLC corrections on the above distributions is clear, with in all cases the larger improvement occuring in the direct $b \to \mu$ decay channels (PRL2, PRL5) as expected. In all cases the difference between the reconstructed b-jet p_T and the matched b-quark p_T is reduced, as in Figure 10.6. The improvement in the KLFitter performance is produced by providing the fitter with reconstructed b-jets closer in properties to the b-quarks into which the

KLFitter tries to transform them, in search of the correct jet-parton pairings in the event topology. The KLFitter TFs are required to alter the reconstructed jet p_T by a lesser amount during the fit in order to reconstruct the top-quark and W-boson masses as part of the likelihood constraints. This reduction of the 'strain' on the TFs results in a higher likelihood for the correct jet permutations. This may be seen in Figures 10.7 and 10.8.

10.2.4 Configuration optimisation

The follow sections, with reference to the nominal settings given in Table 10.5, explore alterations to the configuration of the KLFitter to optimise the performance. Each alteration is performed individually, and the performance tables below are to each be compared directly to Tables 10.6 and 10.7 (unless otherwise stated), and each is performed without the semileptonic corrections applied. A summary table giving the average performance over all bins for each alteration, as well as the optimised performance for the final configuration, is provided at the end of this section.

Tagging selection

In this analysis, it is a requirement to use the SMT tagger in order to identify the soft muon utilised for the charge asymmetry. However it is interesting to study the performance of the KLFitter as a function of different MV1 tagger working points (combined with the SMT). Performance of the KLFitter using MV1 tagging alone would be higher, as the fraction of double-tagged events would increase. The KLFitter is known to have much stronger performance on events with two tagged jets, where there are only two possible permutations to consider [103]. Tables 10.13- 10.22 show the performance of the KLFitter with the SMT tagger only, and the combination of the SMT tagger with the MV1 tagger at various working points. The MV1 working points are selected from the available ATLAS calibrations, with 70%, 80%, and 85% (nominal) b-jet tagging efficiency. In addition, two working points (70%, 80%) are tests for the modified MV1c tagger [86] which provides additional charm jet rejection. It is seen that providing the KLFitter with MV1 information in addition to SMT tagging does not affect the performance of the KLFitter and ρ_{KL} is stable. The power of the tagging combination is utilised in the reduction of fakes as described in Section 8.

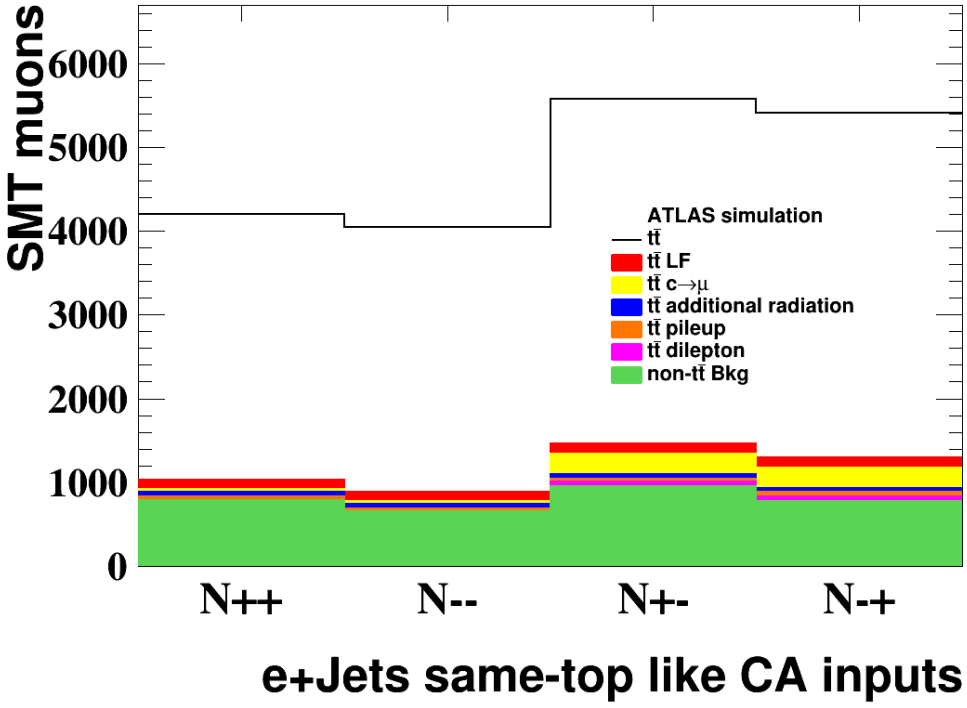

(a) Same-top SMT Muons.

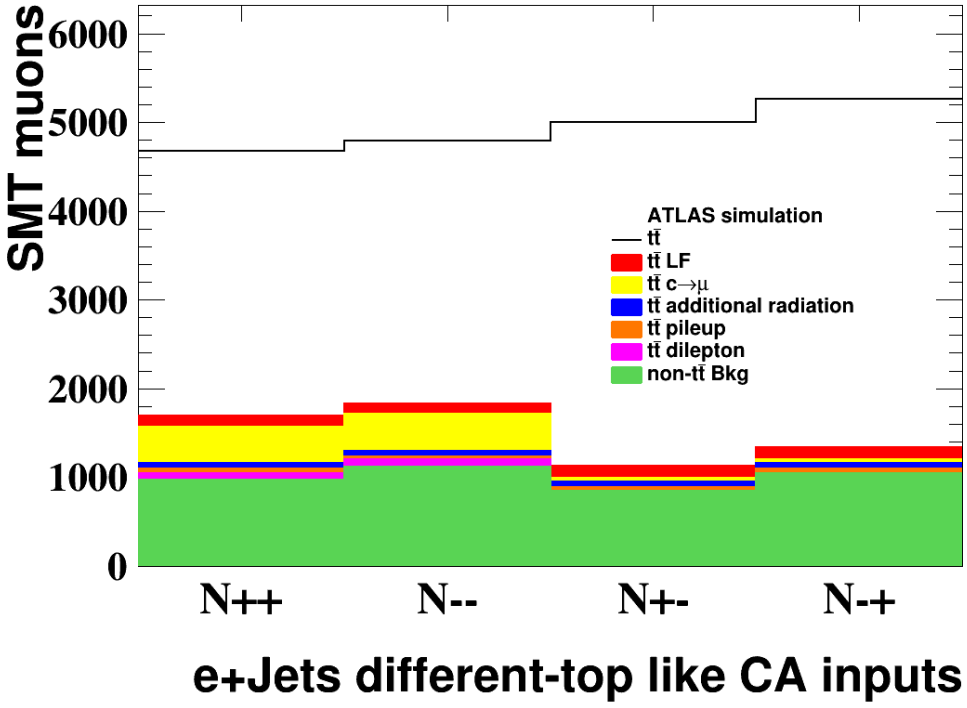

(b) Different-top SMT Muons.

Figure 10.1: e+jets background composition. This is a stacked histogram showing the relative contributions in simulation to the total event yield from the signal $t\bar{t}$, the $t\bar{t}$ backgrounds which consist of fake SMT muons within $t\bar{t}$ events, and the non-$t\bar{t}$ backgrounds (in green) which consist of the other channels such as W+jets and single top decays.

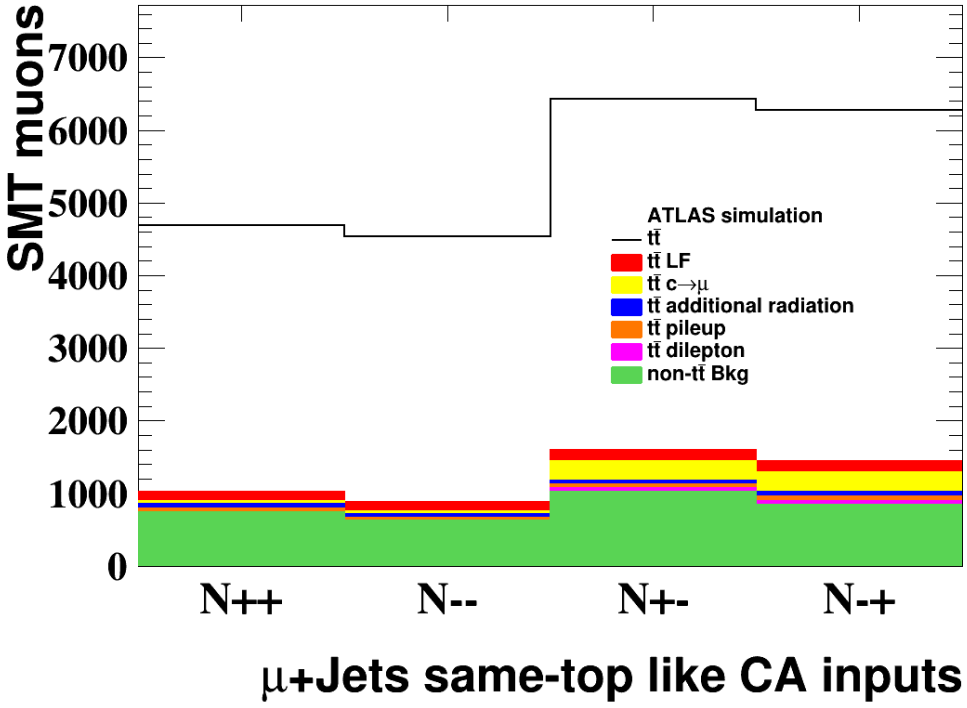

(a) Same-top SMT Muons.

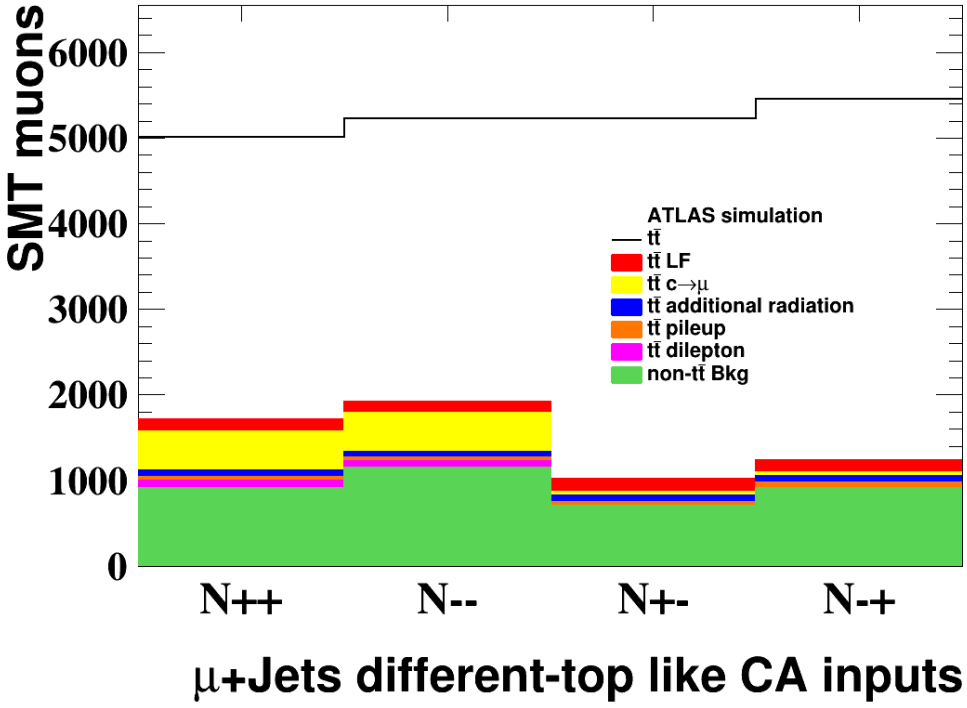

(b) Different-top SMT Muons.

Figure 10.2: μ+jets background composition. This is a stacked histogram showing the relative contributions in simulation to the total event yield from the signal $t\bar{t}$, the $t\bar{t}$ backgroundswhich consist of fake SMT muonswithin $t\bar{t}$ events, and the non-$t\bar{t}$ backgrounds (in green) which consist of the other channels such as W+jets and single top decays.

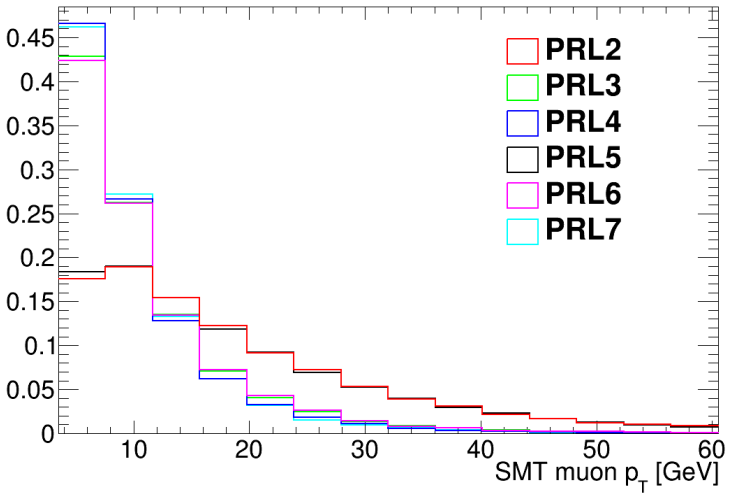

Figure 10.3: SMT p_T distributions broken down by b-quark decay chain in the e+jets channel. The μ+jets distribution is analogous

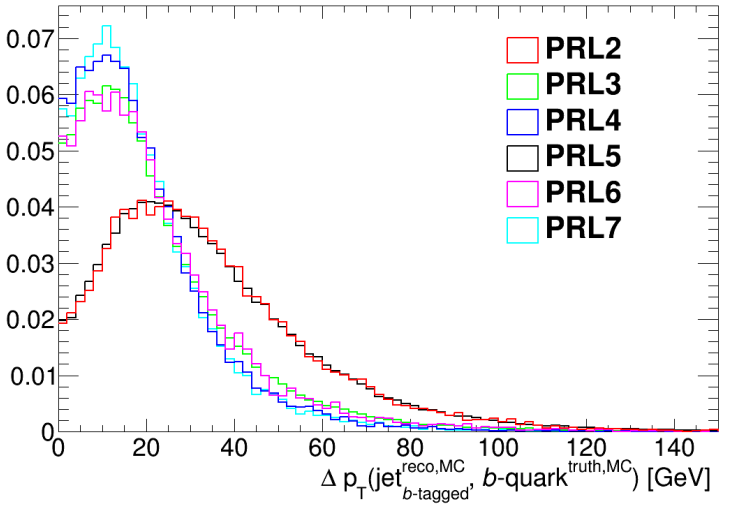

Figure 10.4: Magnitude of the difference between reconstructed jet p_T and the matching MC parton b-quark p_T in the e+jets channel. The μ+jets distribution is analogous

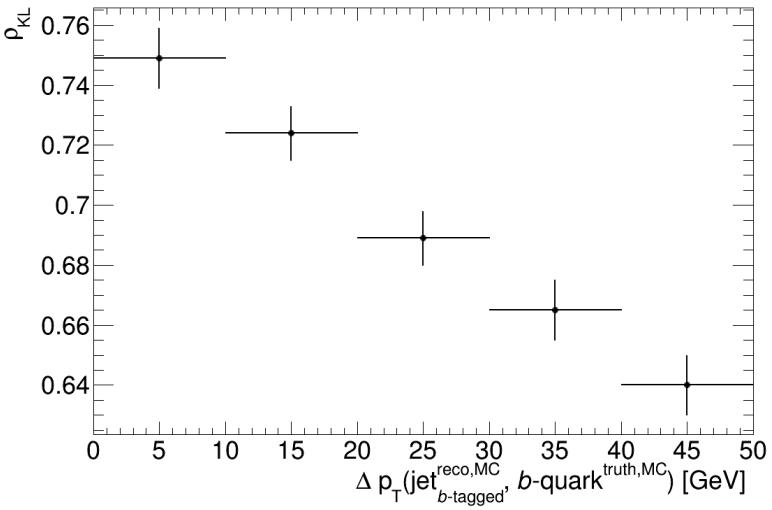

Figure 10.5: KLFitter performance as a function of the magnitude of the difference between reconstructed jet p_T and the matching MC parton b-quark p_T. Shown in in the e+jets channel. the μ+jets distribution is analogous

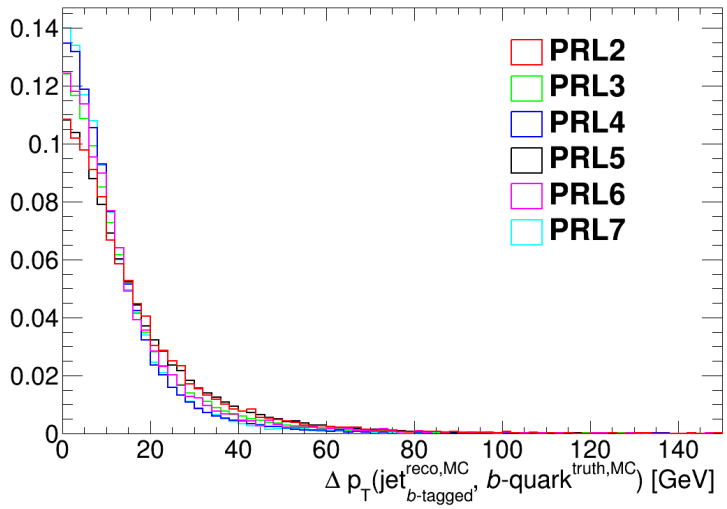

Figure 10.6: Magnitude of the difference between reconstructed jet p_T (with SLC correction) and the matching MC parton b-quark p_T in the e+jets channel. The μ+jets distribution is analogous

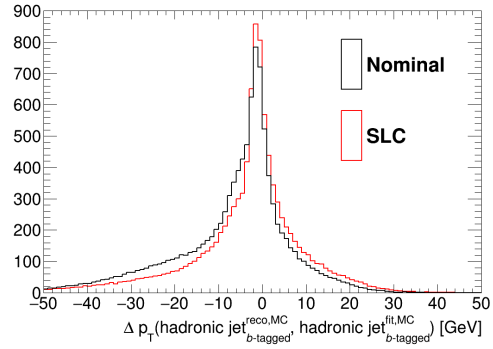

(a) e+jets channel, DT

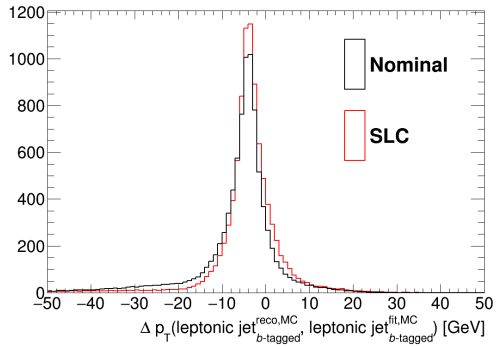

(b) e+jets channel, ST

Figure 10.7: Difference between reconstructed jet p_T (with and without SLC correction) and fitted jet p_T returned by the KLFitter. The shift of the mean towards zero in the SLC corrections indicates a less strenuous fit performed, and leads to a higher permutation likelihood. Shown in the e+jets channel, the μ+jets distribution is analogous

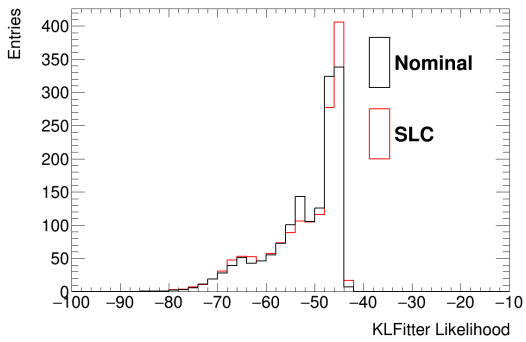

(a) e+jets channel, PRL2

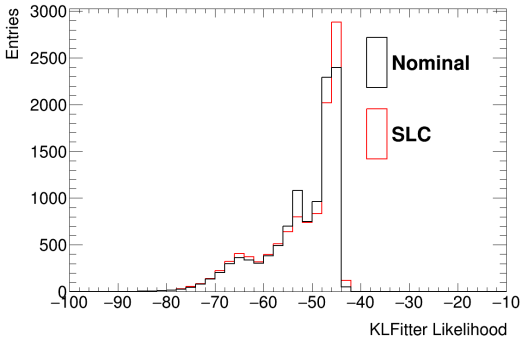

(b) e+jets channel, PRL5

Figure 10.8: Log likelihood distributions for the best permutation in each event as decided by the KLFitter, overlayed for events before and after the jet SLC corrections, for the PRL2 and PRL5 decay channels. The improvement in likelihood leads to a better performance of the KLFitter. Shown in the e+jets channel, the μ+jets distribution is analogous

e+jets	Same-top				Different-top			
	N^{++}_{Reco}	N^{--}_{Reco}	N^{+-}_{Reco}	N^{-+}_{Reco}	N^{++}_{Reco}	N^{--}_{Reco}	N^{+-}_{Reco}	N^{-+}_{Reco}
N^{++}_{truth}	0.700	0.000	0.000	0.300	0.768	0.000	0.000	0.232
N^{--}_{truth}	0.000	0.699	0.301	0.000	0.000	0.767	0.233	0.000
N^{+-}_{truth}	0.000	0.348	0.652	0.000	0.000	0.260	0.740	0.000
N^{-+}_{truth}	0.353	0.000	0.000	0.647	0.257	0.000	0.000	0.743

Table 10.13: Performance of the KLFitter using the nominal configuration with SMT tagging only, in the e+jets channel. The MC statistical uncertainty is ~ 0.002

	N^{++}_{reco}	N^{--}_{reco}	N^{+-}_{reco}	N^{-+}_{reco}
N^{++}_{truth}	0.732	0.000	0.000	0.268
N^{--}_{truth}	0.000	0.732	0.268	0.000
N^{+-}_{truth}	0.000	0.304	0.696	0.000
N^{-+}_{truth}	0.305	0.000	0.000	0.695

Table 10.14: Performance of the KLFitter using the nominal configuration with SMT tagging only, with the combined e+jets and μ+jets channels, with ST and DT also combined. The MC statistical uncertainty is ~ 0.001

e+jets	Same-top				Different-top			
	N^{++}_{Reco}	N^{--}_{Reco}	N^{+-}_{Reco}	N^{-+}_{Reco}	N^{++}_{Reco}	N^{--}_{Reco}	N^{+-}_{Reco}	N^{-+}_{Reco}
N^{++}_{truth}	0.700	0.000	0.000	0.300	0.773	0.000	0.000	0.227
N^{--}_{truth}	0.000	0.699	0.301	0.000	0.000	0.770	0.230	0.000
N^{+-}_{truth}	0.000	0.350	0.650	0.000	0.000	0.254	0.746	0.000
N^{-+}_{truth}	0.352	0.000	0.000	0.648	0.253	0.000	0.000	0.747

Table 10.15: Performance of the KLFitter using the nominal configuration with SMT and MV1@70% tagging, in the e+jets channel. The MC statistical uncertainty is ~ 0.002

Jet multiplicity

The event selection for this analysis requires at least four jets to satisfy quality and momentum requirements. By default in events with more than four jets, only the four with the highest p_T are provided to the KLFitter for consideration. There are events however where the inclusion of the 5^{th} or 6^{th} reconstructed jets may be beneficial. It is possible for ISR/FSR jets from quarks in the event to be measured with larger p_T than other primary jets, and in such a scenario the

	N^{++}_{reco}	N^{--}_{reco}	N^{+-}_{reco}	N^{-+}_{reco}
N^{++}_{truth}	0.735	0.000	0.000	0.265
N^{--}_{truth}	0.000	0.733	0.267	0.000
N^{+-}_{truth}	0.000	0.302	0.698	0.000
N^{-+}_{truth}	0.303	0.000	0.000	0.697

Table 10.16: Performance of the KLFitter using the nominal configuration with SMT and MV1@70% tagging, with the combined *e*+jets and μ+jets channels, with ST and DT also combined. The MC statistical uncertainty is ~ 0.001

e+jets	Same-top				Different-top			
	N^{++}_{Reco}	N^{--}_{Reco}	N^{+-}_{Reco}	N^{-+}_{Reco}	N^{++}_{Reco}	N^{--}_{Reco}	N^{+-}_{Reco}	N^{-+}_{Reco}
N^{++}_{truth}	0.699	0.000	0.000	0.301	0.772	0.000	0.000	0.228
N^{--}_{truth}	0.000	0.698	0.302	0.000	0.000	0.771	0.229	0.000
N^{+-}_{truth}	0.000	0.349	0.651	0.000	0.000	0.255	0.745	0.000
N^{-+}_{truth}	0.354	0.000	0.000	0.646	0.253	0.000	0.000	0.747

Table 10.17: Performance of the KLFitter using the nominal configuration with SMT and MV1@80% tagging, in the *e*+jets channel. The MC statistical uncertainty is ~ 0.002

	N^{++}_{reco}	N^{--}_{reco}	N^{+-}_{reco}	N^{-+}_{reco}
N^{++}_{truth}	0.734	0.000	0.000	0.266
N^{--}_{truth}	0.000	0.733	0.267	0.000
N^{+-}_{truth}	0.000	0.302	0.698	0.000
N^{-+}_{truth}	0.303	0.000	0.000	0.697

Table 10.18: Performance of the KLFitter using the nominal configuration with SMT and MV1@80% tagging, with the combined *e*+jets and μ+jets channels, with ST and DT also combined. The MC statistical uncertainty is ~ 0.001

e+jets	Same-top				Different-top			
	N^{++}_{Reco}	N^{--}_{Reco}	N^{+-}_{Reco}	N^{-+}_{Reco}	N^{++}_{Reco}	N^{--}_{Reco}	N^{+-}_{Reco}	N^{-+}_{Reco}
N^{++}_{truth}	0.698	0.000	0.000	0.302	0.771	0.000	0.000	0.229
N^{--}_{truth}	0.000	0.697	0.303	0.000	0.000	0.771	0.229	0.000
N^{+-}_{truth}	0.000	0.350	0.650	0.000	0.000	0.255	0.745	0.000
N^{-+}_{truth}	0.354	0.000	0.000	0.646	0.253	0.000	0.000	0.747

Table 10.19: Performance of the KLFitter using the nominal configuration with SMT and MV1c@70% tagging, in the *e*+jets channel. The MC statistical uncertainty is ~ 0.002

	N_{reco}^{++}	N_{reco}^{--}	N_{reco}^{+-}	N_{reco}^{-+}
N_{truth}^{++}	0.734	0.000	0.000	0.266
N_{truth}^{--}	0.000	0.732	0.268	0.000
N_{truth}^{+-}	0.000	0.303	0.697	0.000
N_{truth}^{-+}	0.304	0.000	0.000	0.696

Table 10.20: Performance of the KLFitter using the nominal configuration with SMT and MV1c@70% tagging, with the combined *e*+jets and μ+jets channels, with ST and DT also combined. The MC statistical uncertainty is ~ 0.001

e+jets	Same-top				Different-top			
	N_{Reco}^{++}	N_{Reco}^{--}	N_{Reco}^{+-}	N_{Reco}^{-+}	N_{Reco}^{++}	N_{Reco}^{--}	N_{Reco}^{+-}	N_{Reco}^{-+}
N_{truth}^{++}	0.700	0.000	0.000	0.300	0.772	0.000	0.000	0.228
N_{truth}^{--}	0.000	0.698	0.302	0.000	0.000	0.772	0.228	0.000
N_{truth}^{+-}	0.000	0.349	0.651	0.000	0.000	0.255	0.745	0.000
N_{truth}^{-+}	0.353	0.000	0.000	0.647	0.253	0.000	0.000	0.747

Table 10.21: Performance of the KLFitter using the nominal configuration with SMT and MV1c@80% tagging, in the *e*+jets channel. The MC statistical uncertainty is ~ 0.002

	N_{reco}^{++}	N_{reco}^{--}	N_{reco}^{+-}	N_{reco}^{-+}
N_{truth}^{++}	0.734	0.000	0.000	0.266
N_{truth}^{--}	0.000	0.733	0.267	0.000
N_{truth}^{+-}	0.000	0.302	0.698	0.000
N_{truth}^{-+}	0.303	0.000	0.000	0.697

Table 10.22: Performance of the KLFitter using the nominal configuration with SMT and MV1c@80% tagging, with the combined *e*+jets and μ+jets channels, with ST and DT also combined. The MC statistical uncertainty is ~ 0.001

Tagging	Average ρ_{KL}
SMT+MV1@85%	0.715
SMT	0.714
SMT+MV1@70%	0.716
SMT+MV1@80%	0.716
SMT+MV1c@70%	0.715
SMT+MV1c@80%	0.716

Table 10.23: Summary of performance of the KLFitter for different *b*-tagging combinations

KLFitter is unlikely to perform well in reconstructing the correct event topology as it is working with the wrong objects. It is also however possible for SMT-tagged jets to be excluded by

extending the jet multiplicity inclusion, for example if by chance the additional jet combines to produce a higher likelihood than with the primary SMT jet. This section should be considered in context with the following study on jet priority (Section 10.2.4). The results of this study are in Tables 10.24 and 10.31. It can be seen that inclusion of the 5^{th} highest p_T jet (in events for which one exists) provides a similar performance of the KLFitter as the four jet case. However, inclusion of six or more jets begins to show a small decrease in performance in the OS bins - the possibility of creating a reasonable likelihood from a random jet combinatoric increases as more jets are added. It must also be noted from a practical viewpoint that the inclusion of more jets greatly increases the number of permutations per event for which a likelihood must be calculated, and therefore the processing time and computational power required quickly grows. If all jets in every event are included this would become a very limiting factor. The optimal selection is to use five jets in each event, when combined with the study in the following Section 10.2.4.

e+jets	Same-top				Different-top			
	N^{++}_{Reco}	N^{--}_{Reco}	N^{+-}_{Reco}	N^{-+}_{Reco}	N^{++}_{Reco}	N^{--}_{Reco}	N^{+-}_{Reco}	N^{-+}_{Reco}
N^{++}_{truth}	0.710	0.000	0.000	0.290	0.766	0.000	0.000	0.234
N^{--}_{truth}	0.000	0.707	0.293	0.000	0.000	0.767	0.233	0.000
N^{+-}_{truth}	0.000	0.344	0.656	0.000	0.000	0.269	0.731	0.000
N^{-+}_{truth}	0.346	0.000	0.000	0.654	0.267	0.000	0.000	0.733

Table 10.24: Performance of the KLFitter using the nominal configuration permutations of the five highest p_T jets, in the e+jets channel. The MC statistical uncertainty is ~ 0.002

	N^{++}_{reco}	N^{--}_{reco}	N^{+-}_{reco}	N^{-+}_{reco}
N^{++}_{truth}	0.735	0.000	0.000	0.265
N^{--}_{truth}	0.000	0.735	0.265	0.000
N^{+-}_{truth}	0.000	0.308	0.692	0.000
N^{-+}_{truth}	0.307	0.000	0.000	0.693

Table 10.25: Performance of the KLFitter using the nominal configuration with permutations of the five highest p_T jets, with the combined e+jets and μ+jets channels, with ST and DT also combined. The MC statistical uncertainty is ~ 0.001

e+jets	Same-top				Different-top			
	N^{++}_{Reco}	N^{--}_{Reco}	N^{+-}_{Reco}	N^{-+}_{Reco}	N^{++}_{Reco}	N^{--}_{Reco}	N^{+-}_{Reco}	N^{-+}_{Reco}
N^{++}_{truth}	0.710	0.000	0.000	0.290	0.761	0.000	0.000	0.239
N^{--}_{truth}	0.000	0.709	0.291	0.000	0.000	0.764	0.236	0.000
N^{+-}_{truth}	0.000	0.343	0.657	0.000	0.000	0.275	0.725	0.000
N^{-+}_{truth}	0.346	0.000	0.000	0.654	0.273	0.000	0.000	0.727

Table 10.26: Performance of the KLFitter using the nominal configuration with permutations of the six highest p_T jets, in the e+jets channel. The MC statistical uncertainty is ~ 0.002

	N^{++}_{reco}	N^{--}_{reco}	N^{+-}_{reco}	N^{-+}_{reco}
N^{++}_{truth}	0.733	0.000	0.000	0.267
N^{--}_{truth}	0.000	0.734	0.266	0.000
N^{+-}_{truth}	0.000	0.310	0.690	0.000
N^{-+}_{truth}	0.309	0.000	0.000	0.691

Table 10.27: Performance of the KLFitter using the nominal configuration with permutations of the six highest p_T jets, with the combined e+jets and μ+jets channels, with ST and DT also combined. The MC statistical uncertainty is ~ 0.001

e+jets	Same-top				Different-top			
	N^{++}_{Reco}	N^{--}_{Reco}	N^{+-}_{Reco}	N^{-+}_{Reco}	N^{++}_{Reco}	N^{--}_{Reco}	N^{+-}_{Reco}	N^{-+}_{Reco}
N^{++}_{truth}	0.710	0.000	0.000	0.290	0.762	0.000	0.000	0.238
N^{--}_{truth}	0.000	0.708	0.292	0.000	0.000	0.764	0.236	0.000
N^{+-}_{truth}	0.000	0.344	0.656	0.000	0.000	0.276	0.724	0.000
N^{-+}_{truth}	0.346	0.000	0.000	0.654	0.275	0.000	0.000	0.725

Table 10.28: Performance of the KLFitter using the nominal configuration with permutations of the seven highest p_T jets, in the e+jets channel. The MC statistical uncertainty is ~ 0.002

	N^{++}_{reco}	N^{--}_{reco}	N^{+-}_{reco}	N^{-+}_{reco}
N^{++}_{truth}	0.733	0.000	0.000	0.267
N^{--}_{truth}	0.000	0.733	0.267	0.000
N^{+-}_{truth}	0.000	0.311	0.689	0.000
N^{-+}_{truth}	0.310	0.000	0.000	0.690

Table 10.29: Performance of the KLFitter using the nominal configuration with permutations of the seven highest p_T jets, with the combined e+jets and μ+jets channels, with ST and DT also combined. The MC statistical uncertainty is ~ 0.001

e+jets	Same-top				Different-top			
	N^{++}_{Reco}	N^{--}_{Reco}	N^{+-}_{Reco}	N^{-+}_{Reco}	N^{++}_{Reco}	N^{--}_{Reco}	N^{+-}_{Reco}	N^{-+}_{Reco}
N^{++}_{truth}	0.710	0.000	0.000	0.290	0.762	0.000	0.000	0.238
N^{--}_{truth}	0.000	0.708	0.292	0.000	0.000	0.764	0.236	0.000
N^{+-}_{truth}	0.000	0.345	0.655	0.000	0.000	0.276	0.724	0.000
N^{-+}_{truth}	0.346	0.000	0.000	0.654	0.275	0.000	0.000	0.725

Table 10.30: Performance of the KLFitter using the nominal configuration with permutations of the eight highest p_T jets, in the e+jets channel. The MC statistical uncertainty is ~ 0.002

	N^{++}_{reco}	N^{--}_{reco}	N^{+-}_{reco}	N^{-+}_{reco}
N^{++}_{truth}	0.733	0.000	0.000	0.267
N^{--}_{truth}	0.000	0.733	0.267	0.000
N^{+-}_{truth}	0.000	0.311	0.689	0.000
N^{-+}_{truth}	0.310	0.000	0.000	0.690

Table 10.31: Performance of the KLFitter using the nominal configuration with permutations of the eight highest p_T jets, with the combined e+jets and μ+jets channels, with ST and DT also combined. The MC statistical uncertainty is ~ 0.001

Maximum jet multiplicity	Average ρ_{KL}
4	0.715
5	0.714
6	0.712
7	0.711
8	0.711

Table 10.32: Summary of performance of the KLFitter for different jet multiplicity permutations

Jet priority

By default in an event with more jets than the permitted multiplicity described above, the jets provided to the KLFitter to work with are selected based on p_T (hereon labelled as the 'p_T-priority' technique). An event with eight jets but a jet multiplicity allowance of five will have its five highest p_T jets considered only, the remaining three jets will be ignored. This means it is possible to lose events with correctly tagged SMT jets which happen to be at low p_T. To resolve this, it is possible to give priority to SMT tagged jets for use in the KLFitter permutations. If an event has eight jets and the SMT does not qualify as being one of the hardest, it can be given to the KLFitter first regardless, before the remaining spaces in each permutation are filled in p_T or-

der from the remaining jets. This avoids any situation regarding the exclusion of tagged jets and therefore in some events will allow correct permutations to be found when otherwise this may have been impossible. This technique is labelled '*b*-tag priority'. In the tables below, extended versions of the '*b*-tag priority' technique are also applied. The KLFitter may be informed of additional *b*-tagging information on jets which are not tagged by both the SMT and MV1 algorithms (*doubly-tagged*), to improve the reconstruction performance. The KLFitter may be told about additional MV1 or SMT-tagged jets (*singly-tagged*) in the event, to reduce the number of possible permutations (however any additional singly-tagged SMT jets will not be used as input for the charge asymmetry measurement). The fitter then benefits from the inclusion of events with two MV1 tags (as stated previously the KLFitter is known to have stronger performance on events with two tagged jets, where there are only two possible permutations to consider [103]), whilst continuing to ensure that a doubly-tagged SMT+MV1 jet is present in all events. In conjunction with the previous section, this study is performed with a jet multiplicity of four jets (the nominal) and also of five jets. For Tables 10.33- 10.38 the following definitions are used:

- **PtP**: The nominal condition, the hardest jets are given to the KLFitter only. No single-tagged jet information is utilised.
- **PtAdv**: The hardest jets are given to the KLFitter only. Singly-tagged jets are utilised for additional information.
- *b***TagP**: *b*-tagged jets are added to the KLFitter first, followed by the subsequent hardest jets. No singly-tagged jet information is utilised.
- *b***TagPAdv**: *b*-tagged jets are added to the KLFitter first, followed by the subsequent hardest jets. Singly-tagged jets are utilised for additional information.

In the four jet multiplicity study, the best performance comes from prioritising jets by p_T and including information about singly-tagged MV1 and SMT jets. In the five jet multiplicity study, the best performance comes from prioritising the addition to the KLFitter of firstly doubly-tagged jets (SMT+MV1), and then secondary singly-tagged MV1-only and SMT-only jets. In both cases this is because although we only use the doubly-tagged jets for the analysis, the individual efficiencies of the taggers (primarily the MV1 tagger) are high enough that there is a good chance the additional tagged jets are also real *b*-jets. Using the results from Table 6.3, it is

e+jets	Same-top				Different-top			
	N^{++}_{Reco}	N^{--}_{Reco}	N^{+-}_{Reco}	N^{-+}_{Reco}	N^{++}_{Reco}	N^{--}_{Reco}	N^{+-}_{Reco}	N^{-+}_{Reco}
N^{++}_{truth}	0.750	0.000	0.000	0.250	0.732	0.000	0.000	0.268
N^{--}_{truth}	0.000	0.751	0.249	0.000	0.000	0.736	0.264	0.000
N^{+-}_{truth}	0.000	0.289	0.711	0.000	0.000	0.291	0.709	0.000
N^{-+}_{truth}	0.291	0.000	0.000	0.709	0.291	0.000	0.000	0.709

Table 10.33: Performance of the KLFitter using the nominal configuration with jet priority set to PtPAdv, in the e+jets channel. The MC statistical uncertainty is ~ 0.002

	N^{++}_{reco}	N^{--}_{reco}	N^{+-}_{reco}	N^{-+}_{reco}
N^{++}_{truth}	0.742	0.000	0.000	0.258
N^{--}_{truth}	0.000	0.742	0.258	0.000
N^{+-}_{truth}	0.000	0.288	0.712	0.000
N^{-+}_{truth}	0.289	0.000	0.000	0.711

Table 10.34: Performance of the KLFitter using the nominal configuration with jet priority set to PtPAdv, with the combined e+jets and μ+jets channels, with ST and DT also combined. The MC statistical uncertainty is ~ 0.001

e+jets	Same-top				Different-top			
	N^{++}_{Reco}	N^{--}_{Reco}	N^{+-}_{Reco}	N^{-+}_{Reco}	N^{++}_{Reco}	N^{--}_{Reco}	N^{+-}_{Reco}	N^{-+}_{Reco}
N^{++}_{truth}	0.688	0.000	0.000	0.312	0.770	0.000	0.000	0.230
N^{--}_{truth}	0.000	0.685	0.315	0.000	0.000	0.769	0.231	0.000
N^{+-}_{truth}	0.000	0.366	0.634	0.000	0.000	0.258	0.742	0.000
N^{-+}_{truth}	0.370	0.000	0.000	0.630	0.255	0.000	0.000	0.745

Table 10.35: Performance of the KLFitter using the nominal configuration with jet priority set to bTagP, in the e+jets channel. The MC statistical uncertainty is ~ 0.002

	N^{++}_{reco}	N^{--}_{reco}	N^{+-}_{reco}	N^{-+}_{reco}
N^{++}_{truth}	0.727	0.000	0.000	0.273
N^{--}_{truth}	0.000	0.725	0.275	0.000
N^{+-}_{truth}	0.000	0.312	0.688	0.000
N^{-+}_{truth}	0.312	0.000	0.000	0.688

Table 10.36: Performance of the KLFitter using the nominal configuration with jet priority set to bTagP, with the combined e+jets and μ+jets channels, with ST and DT also combined. The MC statistical uncertainty is ~ 0.001

e+jets	Same-top				Different-top			
	N^{++}_{Reco}	N^{--}_{Reco}	N^{+-}_{Reco}	N^{-+}_{Reco}	N^{++}_{Reco}	N^{--}_{Reco}	N^{+-}_{Reco}	N^{-+}_{Reco}
N^{++}_{truth}	0.749	0.000	0.000	0.251	0.726	0.000	0.000	0.274
N^{--}_{truth}	0.000	0.749	0.251	0.000	0.000	0.728	0.272	0.000
N^{+-}_{truth}	0.000	0.295	0.705	0.000	0.000	0.297	0.703	0.000
N^{-+}_{truth}	0.297	0.000	0.000	0.703	0.296	0.000	0.000	0.704

Table 10.37: Performance of the KLFitter using the nominal configuration with jet priority set to bTagPAdv, in the e+jets channel. The MC statistical uncertainty is ~ 0.002

	N^{++}_{reco}	N^{--}_{reco}	N^{+-}_{reco}	N^{-+}_{reco}
N^{++}_{truth}	0.737	0.000	0.000	0.263
N^{--}_{truth}	0.000	0.737	0.263	0.000
N^{+-}_{truth}	0.000	0.294	0.706	0.000
N^{-+}_{truth}	0.295	0.000	0.000	0.705

Table 10.38: Performance of the KLFitter using the nominal configuration with jet priority set to bTagPAdv, with the combined e+jets and μ+jets channels, with ST and DT also combined. The MC statistical uncertainty is ~ 0.001

e+jets	Same-top				Different-top			
	N^{++}_{Reco}	N^{--}_{Reco}	N^{+-}_{Reco}	N^{-+}_{Reco}	N^{++}_{Reco}	N^{--}_{Reco}	N^{+-}_{Reco}	N^{-+}_{Reco}
N^{++}_{truth}	0.757	0.000	0.000	0.243	0.734	0.000	0.000	0.266
N^{--}_{truth}	0.000	0.759	0.241	0.000	0.000	0.736	0.264	0.000
N^{+-}_{truth}	0.000	0.282	0.718	0.000	0.000	0.297	0.703	0.000
N^{-+}_{truth}	0.287	0.000	0.000	0.713	0.296	0.000	0.000	0.704

Table 10.39: Performance of the KLFitter using the nominal configuration with permutations of up to five jets and jet priority set to PtPAdv, in the e+jets channel. The MC statistical uncertainty is ~ 0.002

	N^{++}_{reco}	N^{--}_{reco}	N^{+-}_{reco}	N^{-+}_{reco}
N^{++}_{truth}	0.745	0.000	0.000	0.255
N^{--}_{truth}	0.000	0.745	0.255	0.000
N^{+-}_{truth}	0.000	0.288	0.712	0.000
N^{-+}_{truth}	0.289	0.000	0.000	0.711

Table 10.40: Performance of the KLFitter using the nominal configuration with permutations of up to five jets and jet priority set to PtPAdv, with the combined e+jets and μ+jets channels, with ST and DT also combined. The MC statistical uncertainty is ~ 0.001

e+jets	Same-top				Different-top			
	N^{++}_{Reco}	N^{--}_{Reco}	N^{+-}_{Reco}	N^{-+}_{Reco}	N^{++}_{Reco}	N^{--}_{Reco}	N^{+-}_{Reco}	N^{-+}_{Reco}
N^{++}_{truth}	0.708	0.000	0.000	0.292	0.765	0.000	0.000	0.235
N^{--}_{truth}	0.000	0.704	0.296	0.000	0.000	0.766	0.234	0.000
N^{+-}_{truth}	0.000	0.349	0.651	0.000	0.000	0.271	0.729	0.000
N^{-+}_{truth}	0.350	0.000	0.000	0.650	0.268	0.000	0.000	0.732

Table 10.41: Performance of the KLFitter using the nominal configuration with permutations of up to five jets and jet priority set to bTagP, in the e+jets channel. The MC statistical uncertainty is ~ 0.002

	N^{++}_{reco}	N^{--}_{reco}	N^{+-}_{reco}	N^{-+}_{reco}
N^{++}_{truth}	0.734	0.000	0.000	0.266
N^{--}_{truth}	0.000	0.733	0.267	0.000
N^{+-}_{truth}	0.000	0.310	0.690	0.000
N^{-+}_{truth}	0.309	0.000	0.000	0.691

Table 10.42: Performance of the KLFitter using the nominal configuration with permutations of up to five jets and jet priority set to bTagP, with the combined e+jets and μ+jets channels, with ST and DT also combined. The MC statistical uncertainty is ~ 0.001

e+jets	Same-top				Different-top			
	N^{++}_{Reco}	N^{--}_{Reco}	N^{+-}_{Reco}	N^{-+}_{Reco}	N^{++}_{Reco}	N^{--}_{Reco}	N^{+-}_{Reco}	N^{-+}_{Reco}
N^{++}_{truth}	0.757	0.000	0.000	0.243	0.733	0.000	0.000	0.267
N^{--}_{truth}	0.000	0.758	0.242	0.000	0.000	0.734	0.266	0.000
N^{+-}_{truth}	0.000	0.284	0.716	0.000	0.000	0.300	0.700	0.000
N^{-+}_{truth}	0.287	0.000	0.000	0.713	0.298	0.000	0.000	0.702

Table 10.43: Performance of the KLFitter using the nominal configuration with permutations of up to five jets and jet priority set to bTagPAdv, in the e+jets channel. The MC statistical uncertainty is ~ 0.002

	N^{++}_{reco}	N^{--}_{reco}	N^{+-}_{reco}	N^{-+}_{reco}
N^{++}_{truth}	0.744	0.000	0.000	0.256
N^{--}_{truth}	0.000	0.743	0.257	0.000
N^{+-}_{truth}	0.000	0.290	0.710	0.000
N^{-+}_{truth}	0.291	0.000	0.000	0.709

Table 10.44: Performance of the KLFitter using the nominal configuration with permutations of up to five jets and jet priority set to bTagPAdv, with the combined e+jets and μ+jets channels, with ST and DT also combined. The MC statistical uncertainty is ~ 0.001

possible to estimate that the fraction of events with two SMT+MV1 tagged jets is only $\sim 0.8\%$, the fraction of events with two SMT tagged jets is $\sim 1\%$, whilst the fraction of events with two MV1 tagged jets is $\sim 73\%$.

Prioritising doubly-tagged jets slightly lowers the performance in both cases. Without this configuration, events with the lowest p_T doubly-tagged jets are discarded as the KLFitter is not given an opportunity to make a ST or DT decision. With this configuration, approximately 3000 events are recovered, however as the KLFitter performance improves with jet p_T, the performance on the recovered events is poor. In all cases, providing additional information to the fitter about singly-tagged jets is beneficial as it reduces the fit to only two permutations (per four jets) and the KLFitter performs extremely well. Using the five jet multiplicity, the improvement in performance on events with additional singly-tagged jets outweighs the drop in performance from the low p_T doubly-tagged jets, whilst retaining the gain in statistics, potentially from the opportunity to throw out surviving high p_T IFSR jets.

b-tagged jet positions

In the nominal setup the KLFitter interprets a jet which is tagged as being the absolute truth. A tagged jet is considered to be a *b*-jet without question, and therefore when permuting the jets within the event topology any tagged jets are only placed in *b*-quark positions. Placing a *b*-jet into a light-quark position is vetoed and the likelihood is not calculated to save time, this configuration within the KLFitter is known as 'kVetoNoFit'. The KLFitter is able to include an extra term in the likelihood which takes into account the efficiency and mistag rate of the *b*-tagger in use. This is designed to reduce problems caused by a tagger with a high mistag rate in data, and therefore having numerous events with chance of finding correct jet permutation. This alternative setup is known as the 'kWorkingPoint' configuration. In this analysis however usage of kWorkingPoint is non-trivial. It is not clear whether to quote the SMT efficiency as inclusive of the low $b \to \mu$ branching ratio for the likelihood calculation. The tagger's real efficiency is much higher (see Section 7), however with the inclusion of the 21% $b \to \mu$ branching ratio the KLFitter may assume that the majority of tagged jets are mistags. Such a low effective efficiency would cause the KLFitter to give a low weight to *b*-tagged jets and to effectively ignore the tagger. Secondly as it has already been decided to combine the SMT+MV1 taggers, the situation is complicated further by trying to provide a single efficiency and mistag rate for

the combined tags. Lastly, as it is already known that the inclusion of MV1 tagging removes many of the mistagged SMT jets (see Section 8.2.4), it is unlikely that the kWorkingPoint mode would provide much additional power against mistagged jets still in the events.

Top-quark mass constraints

As part of the nominal likelihood calculation the KLFitter reconstructs the event topology using as a constraint top-quark mass 'target' of 172.5 GeV, for each side of the decay. This provides strong limits for how far the fitter can modify the reconstructed jet and lepton energies and angular variables within their resolutions. However it could be argued that, in the interest of separating signal events from non $t\bar{t}$ backgrounds, a reconstruction of the top-quark mass for a real $t\bar{t}$ event would tend to produce a mass much closer to the real top-quark mass than a selection of jets from a background event such a W+jets. In a fixed-mass scenario (nominal) this constraint should decrease the average likelihood of all background event permutations as the objects need to be smeared further from their true properties to reconstruct a target top-quark mass (which could then be separated by a cut on the likelihood, as is explored in Section 10.2.6 below). For the signal $t\bar{t}$ events, in general, placing more limits on the system will result in a better result. However, it is interesting to study the option of permitting a free top-quark mass as this allows for plotting of the reconstructed top-quark mass for the best permutation in each event, to see if there is a signal to background separation. It is seen in the Figure 10.9 that the distinction is unclear, as the yield of true $t\bar{t}$ events selected is already so much greater than that of background events, any cuts would be detrimental to the overall selection purity. Tables 10.45- 10.46 of the KLFitter performance indicate working with a free top-quark mass is not beneficial.

e+jets	Same-top				Different-top			
	N^{++}_{Reco}	N^{--}_{Reco}	N^{+-}_{Reco}	N^{-+}_{Reco}	N^{++}_{Reco}	N^{--}_{Reco}	N^{+-}_{Reco}	N^{-+}_{Reco}
N^{++}_{truth}	0.572	0.000	0.000	0.428	0.728	0.000	0.000	0.272
N^{--}_{truth}	0.000	0.566	0.434	0.000	0.000	0.724	0.276	0.000
N^{+-}_{truth}	0.000	0.452	0.548	0.000	0.000	0.282	0.718	0.000
N^{-+}_{truth}	0.453	0.000	0.000	0.547	0.278	0.000	0.000	0.722

Table 10.45: Performance of the KLFitter using the nominal configuration with removal of the fixed top-quark mass constraint, in the e+jets channel. The MC statistical uncertainty is ~ 0.002

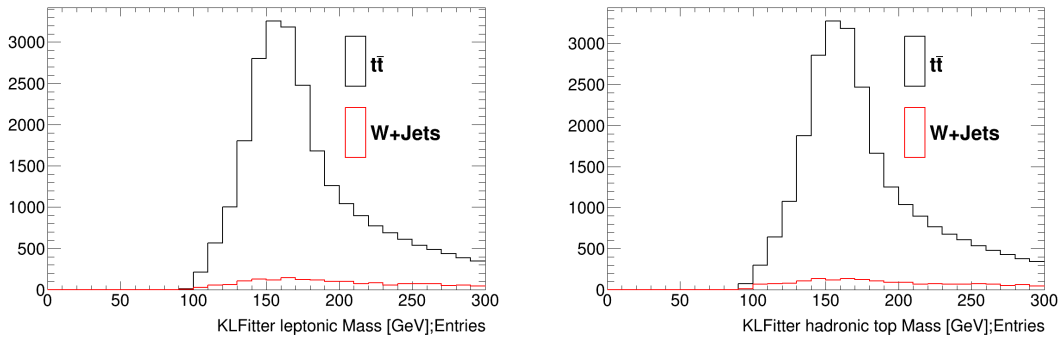

(a) Top-quark parent of leptonically decaying W-boson (b) Top-quark parent of hadronically decaying W-boson

Figure 10.9: KLFitter top-quark mass reconstruction with removal of fixed top-quark mass constraint, for $t\bar{t}$ MC with $t\bar{t}$ backgrounds removed, and W+jets background estimation, in the e+jets channel

	N^{++}_{reco}	N^{--}_{reco}	N^{+-}_{reco}	N^{-+}_{reco}
N^{++}_{truth}	0.647	0.000	0.000	0.353
N^{--}_{truth}	0.000	0.643	0.357	0.000
N^{+-}_{truth}	0.000	0.370	0.630	0.000
N^{-+}_{truth}	0.368	0.000	0.000	0.632

Table 10.46: Performance of the KLFitter using the nominal configuration with removal of the fixed top-quark mass constraint, with the combined e+jets and μ+jets channels, with ST and DT also combined. The MC statistical uncertainty is ~ 0.001

Angular likelihood

As mentioned in Section 10.1.2, there is a choice in the likelihood calculation used for the event between the nominal, and the angular form with W-boson helicity corrections. Tables 10.47 and 10.48 show the purity of the KLFitter selection as a function of the choice of likelihood. The performance of the KLFitter is seen to improve with the angular likelihood.

e+jets	Same-top				Different-top			
	N^{++}_{Reco}	N^{--}_{Reco}	N^{+-}_{Reco}	N^{-+}_{Reco}	N^{++}_{Reco}	N^{--}_{Reco}	N^{+-}_{Reco}	N^{-+}_{Reco}
N^{++}_{truth}	0.715	0.000	0.000	0.285	0.779	0.000	0.000	0.221
N^{--}_{truth}	0.000	0.712	0.288	0.000	0.000	0.781	0.219	0.000
N^{+-}_{truth}	0.000	0.332	0.668	0.000	0.000	0.251	0.749	0.000
N^{-+}_{truth}	0.339	0.000	0.000	0.661	0.247	0.000	0.000	0.753

Table 10.47: Performance of the KLFitter using the nominal configuration with the angular likelihood in the e+jets channel. The MC statistical uncertainty is ~ 0.002

	N_{reco}^{++}	N_{reco}^{--}	N_{reco}^{+-}	N_{reco}^{-+}
N_{truth}^{++}	0.745	0.000	0.000	0.255
N_{truth}^{--}	0.000	0.744	0.256	0.000
N_{truth}^{+-}	0.000	0.291	0.709	0.000
N_{truth}^{-+}	0.293	0.000	0.000	0.707

Table 10.48: Performance of the KLFitter using the nominal configuration with the angular likelihood, with the combined e+jets and μ+jets channels, with ST and DT also combined. The MC statistical uncertainty is ~ 0.001

It is shown that better performance is achieved by adding terms to the likelihood using W-boson helicity fractions, and therefore it is this option which is used in the analysis.

10.2.5 Likelihood interpretation

Having optimised the input to the KLFitter in the previous section, it is important to continue to look for improvement which can be made once the output of the fitter has been determined. Studies in this section onward are performed on the 'optimised' KLFitter configuration as defined in Table 10.55, comparisons in performance should be made directly with Tables 10.56 and Tables 10.57.

Studying the output of the fitter may allow for the possibility to identify further discrepancies between the behaviour of true ST, DT and background events.

It is possible to study the distribution of likelihoods calculated from each permutation, per event. The default technique is to select the permutation with the best likelihood as the correct one. However alternative options exist as described in the sections below which may represent more sophisticated ways to interpret the likelihood output.

Highest likelihood

The default option is to pick the permutation in each event which produces the highest likelihood. The full performance, with all of the optimisations from the previous section, is given in Tables 10.56 and Tables 10.57.

Highest average likelihood

For events with a single tagged and four jets in total to permute (the majority of events), the KLFitter will calculate six permutations falling into only two categories; ST or DT, depending on the position of the tagged jet. In many permutations all of the calculated likelihoods are extremely similar, comparable likelihoods for all permutations may lead to selections of jet combinatorics by chance. A technique for avoiding potential combinatoric contamination could be to consider the results not as six separate permutations, but as two sets of three; defined by the placement of the SMT+MV1 jet. Taking the average likelihood of the ST permutations compared with the DT permutations may provide a slight increase in performance. The performance with this configuration is given in Tables 10.49 and Tables 10.50, it is not found to provide an increase in purity of the KLFitter decision, the performance is equivalent to the highest likelihood option.

e+jets	Same-top				Different-top			
	N^{++}_{Reco}	N^{--}_{Reco}	N^{+-}_{Reco}	N^{-+}_{Reco}	N^{++}_{Reco}	N^{--}_{Reco}	N^{+-}_{Reco}	N^{-+}_{Reco}
N^{++}_{truth}	0.814	0.000	0.000	0.186	0.781	0.000	0.000	0.219
N^{--}_{truth}	0.000	0.817	0.183	0.000	0.000	0.776	0.224	0.000
N^{+-}_{truth}	0.000	0.198	0.802	0.000	0.000	0.229	0.771	0.000
N^{-+}_{truth}	0.195	0.000	0.000	0.805	0.229	0.000	0.000	0.771

Table 10.49: Performance of the KLFitter using the optimised configuration, with averaged likelihood calculations, in the e+jets channel. The MC statistical uncertainty is ~ 0.002

	N^{++}_{reco}	N^{--}_{reco}	N^{+-}_{reco}	N^{-+}_{reco}
N^{++}_{truth}	0.796	0.000	0.000	0.204
N^{--}_{truth}	0.000	0.794	0.206	0.000
N^{+-}_{truth}	0.000	0.214	0.786	0.000
N^{-+}_{truth}	0.214	0.000	0.000	0.786

Table 10.50: Performance of the KLFitter using the optimised configuration, with averaged likelihood calculations, with the combined e+jets and μ+jets channels, with ST and DT also combined. The MC statistical uncertainty is ~ 0.001

Dominant likelihood

Another method for many-permutation events, is to pick the category (ST or DT) which appears most of the top 50% of all permutations, once ordered by likelihood. In a six permutation event, this would select the modal ST or DT decision in the top three permutations. This technique could remove any 'fluke' high likelihoods from an incorrect reconstructions. The performance with this configuration is given in Tables 10.51 and Tables 10.52, it is not found to increase the purity purity of the KLFitter decision.

e+jets	Same-top				Different-top			
	N^{++}_{Reco}	N^{--}_{Reco}	N^{+-}_{Reco}	N^{-+}_{Reco}	N^{++}_{Reco}	N^{--}_{Reco}	N^{+-}_{Reco}	N^{-+}_{Reco}
N^{++}_{truth}	0.815	0.000	0.000	0.185	0.742	0.000	0.000	0.258
N^{--}_{truth}	0.000	0.814	0.186	0.000	0.000	0.736	0.264	0.000
N^{+-}_{truth}	0.000	0.199	0.801	0.000	0.000	0.270	0.730	0.000
N^{-+}_{truth}	0.195	0.000	0.000	0.805	0.266	0.000	0.000	0.734

Table 10.51: Performance of the KLFitter using the optimised configuration, with dominant likelihood selection, in the e+jets channel. The MC statistical uncertainty is ~ 0.002

	N^{++}_{reco}	N^{--}_{reco}	N^{+-}_{reco}	N^{-+}_{reco}
N^{++}_{truth}	0.777	0.000	0.000	0.223
N^{--}_{truth}	0.000	0.774	0.226	0.000
N^{+-}_{truth}	0.000	0.233	0.767	0.000
N^{-+}_{truth}	0.233	0.000	0.000	0.767

Table 10.52: Performance of the KLFitter using the optimised configuration, with dominant likelihood selection, with the combined e+jets and μ+jets channels, with ST and DT also combined. The MC statistical uncertainty is ~ 0.001

Lowest likelihood rejection

Similar to selecting the highest likelihood permutation as being correct, it is possible to use the alternative of rejecting the ST or DT decision given by the lowest likelihood permutation. If the tagged jet is in the correct position, the calculated likelihood for each permutation is expected to be better than permutations where the tagged jet is not correctly placed, although this is very sensitive to the positions of the other jets. Focusing on the lowest likelihood permutation in each event and selecting as correct the category the opposite decision may yield an improvement in

performance. The performance with this configuration is given in Tables 10.53 and Tables 10.54, it is not found to increase the purity of the KLFitter decision.

e+jets	Same-top				Different-top			
	N^{++}_{Reco}	N^{--}_{Reco}	N^{+-}_{Reco}	N^{-+}_{Reco}	N^{++}_{Reco}	N^{--}_{Reco}	N^{+-}_{Reco}	N^{-+}_{Reco}
N^{++}_{truth}	0.830	0.000	0.000	0.170	0.717	0.000	0.000	0.283
N^{--}_{truth}	0.000	0.827	0.173	0.000	0.000	0.711	0.289	0.000
N^{+-}_{truth}	0.000	0.182	0.818	0.000	0.000	0.296	0.704	0.000
N^{-+}_{truth}	0.179	0.000	0.000	0.821	0.294	0.000	0.000	0.706

Table 10.53: Performance of the KLFitter using the optimised configuration, with rejection of the lowest likelihood decision, in the e+jets channel. The MC statistical uncertainty is ~ 0.002

	N^{++}_{reco}	N^{--}_{reco}	N^{+-}_{reco}	N^{-+}_{reco}
N^{++}_{truth}	0.773	0.000	0.000	0.227
N^{--}_{truth}	0.000	0.768	0.232	0.000
N^{+-}_{truth}	0.000	0.238	0.762	0.000
N^{-+}_{truth}	0.237	0.000	0.000	0.763

Table 10.54: Performance of the KLFitter using the optimised configuration, with rejection of the lowest likelihood decision, with the combined e+jets and μ+jets channels, with ST and DT also combined. The MC statistical uncertainty is ~ 0.001

10.2.6 Likelihood manipulation

Further to considering potential combinations or reinterpretations of likelihoods within a single event, it is possible to study the distribution of the selected permutation likelihoods for the sample as a whole. It is possible to compare the distributions of likelihoods for truth ST and DT separately, for signal versus background events, and within signal events it is possible to compare the distributions according to whether the KLFitter decision is correct or incorrect. Further to the total likelihood distribution, it is possible to break the likelihood down into its constituent parts and also compare each of those distributions in the aforementioned categories. It may be possible to find separation in the distributions to improve the overall performance on signal events, or reject additional background events, using cuts on the final likelihood.

Cut for $t\bar{t}$ signal enhancement

Figure 10.10 shows the likelihood distributions for the selected permutations in signal and background events. Background events may have distributions shifted further to the low-negative (worst-performance) side than signal events, as the KLFitter is attempting to fit non-$t\bar{t}$ reconstructed objects to a $t\bar{t}$ topology, which would provide the possibility of cutting on the likelihood distribution to increase the signal purity. However as the figure shows, it is difficult to differentiate between signal and background using the likelihood, as any difference in shape is hidden underneath the large difference in yields of signal to background events over the full distribution.

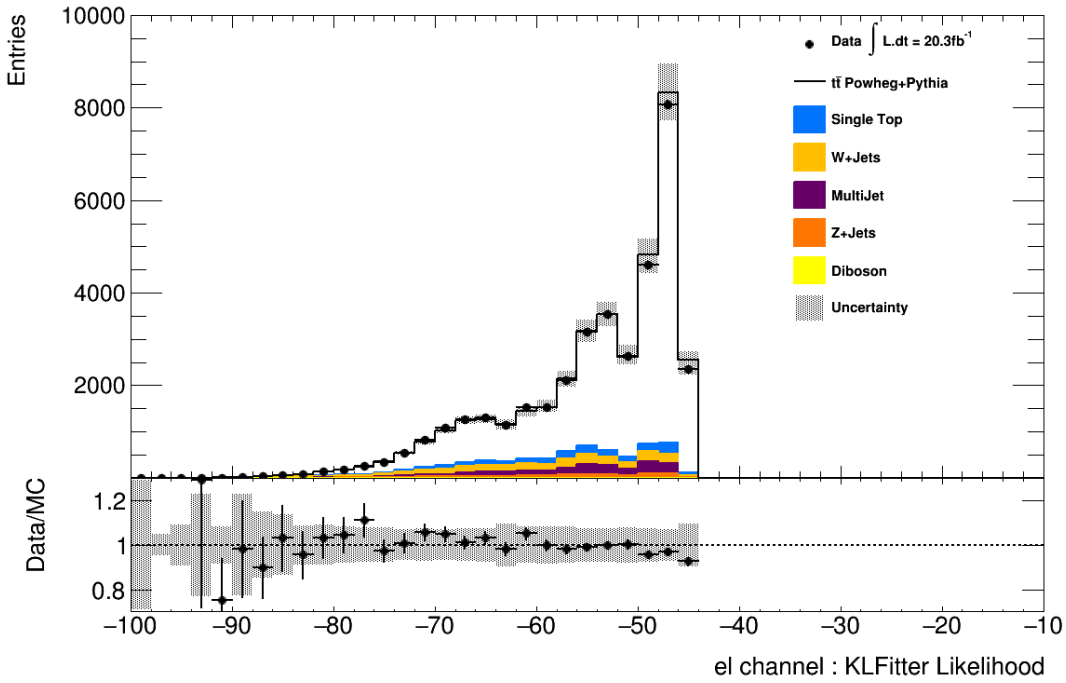

Figure 10.10: KLFitter likelihood distributions for signal and background events in the e+jets channel. The μ+jets distribution is analogous

Cuts for KLFitter purity enhancement

Figure 10.11 shows the likelihood distributions for the highest likelihood permutations in signal events only, separated by whether or not the KLFitter decision is correct. Any difference in shape is hidden underneath the large difference in yields of correct to incorrect decisions over the full distribution. Applying any cut would remove more correctly identified events than incorrectly identified events.

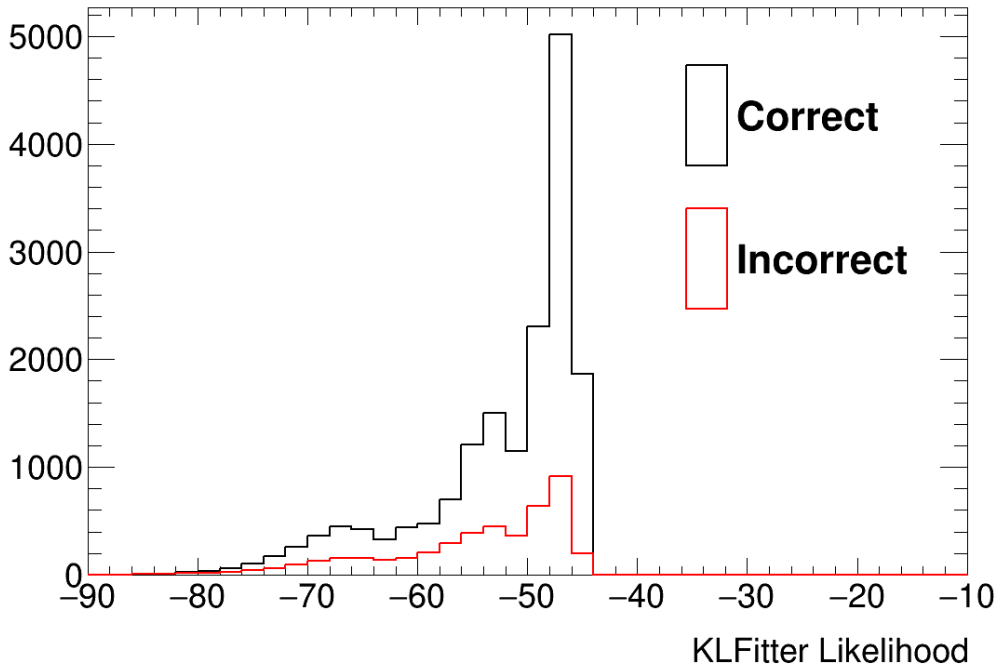

Figure 10.11: KLFitter likelihood distributions for $t\bar{t}$ MC signal (with $t\bar{t}$ backgrounds removed) separated by correct or incorrect KLFitter decision, in the e+jets channel. The μ+jets distribution is analogous

10.2.7 KLFitter performance

The optimised configuration is given in Table 10.55 described by the studies in this chapter. The performance for the optimised KLFitter is given in Tables 10.56 and 10.57. However there remains a small difference in the performance between the true ST and true DT events. A potential hypothesis relates to the semileptonic jet corrections. The missing momentum correction has been applied to the tagged jets, however it has not been corrected for in the total MET for the event. Considering the event topology, the missing momentum from the semileptonic decay will tend to be more aligned with the MET in the ST events and less aligned with the MET in the DT events. Whilst in both cases the angular information and the total amplitude for the MET will be mismeasured (with respect to the removal of the neutrino in the semileptonic b-quark decay), the measurement will be worse in DT as the difference in angle is greater. The MET-x and MET-y components provided to the fitter will vary by a larger degree from the truth in the DT case than the ST case, leading to a worse reconstruction. However, differences in performance between ST and DT events are quoted in KLFitter implementation papers [103], and the magnitude of the difference in performce and not deemed to be an issue. All events, ST or DT, are combined be-

fore the response matrix used for unfolding is constructed. A future improvement to the analysis would be to apply diagnose this difference fully and apply a correction to increase the combined performance of the fitter.

Configuration option	Optimal setting
b-tagging	SMT+MV1@85%
Number of b-tags	≥ 1
Corrections	Semileptonic jets
Jet multiplicity	Five jets permuted per event only
Jet selection priority	b-tagged jets are added to the KLFitter first followed by the subsequent hardest jets. Singly-tagged MV1 or SMT jets are utilised for additional information
b-tagged jet positions	No permutations with tagged jets in light flavour positions
Top-quark mass treatment	Fixed at 172.5 GeV
Likelihood	Angular
Permutation selection	Permutation with maximum likelihood
Likelihood cuts	No cuts

Table 10.55: Overview of the optimised KLFitter configuration

e+jets	Same-top				Different-top			
	N^{++}_{Reco}	N^{--}_{Reco}	N^{+-}_{Reco}	N^{-+}_{Reco}	N^{++}_{Reco}	N^{--}_{Reco}	N^{+-}_{Reco}	N^{-+}_{Reco}
N^{++}_{truth}	0.812	0.000	0.000	0.188	0.782	0.000	0.000	0.218
N^{--}_{truth}	0.000	0.815	0.185	0.000	0.000	0.778	0.222	0.000
N^{+-}_{truth}	0.000	0.200	0.800	0.000	0.000	0.229	0.771	0.000
N^{-+}_{truth}	0.197	0.000	0.000	0.803	0.229	0.000	0.000	0.771

Table 10.56: Performance of the KLFitter using the optimised configuration, in the e+jets channel. The MC statistical uncertainty is ~ 0.002

	N^{++}_{reco}	N^{--}_{reco}	N^{+-}_{reco}	N^{-+}_{reco}
N^{++}_{truth}	0.795	0.000	0.000	0.205
N^{--}_{truth}	0.000	0.793	0.207	0.000
N^{+-}_{truth}	0.000	0.214	0.786	0.000
N^{-+}_{truth}	0.214	0.000	0.000	0.786

Table 10.57: Performance of the KLFitter using the optimised configuration, with the combined e+jets and μ+jets channels, with ST and DT also combined. The MC statistical uncertainty is ~ 0.001

You're all probably too tired to even stand up after all the fighting. But . . . we still have a chance to win

Squall Leonhart

Chapter 11

Unfolding techniques

Unfolding is the process by which all detector, algorithmic or other effects which may cause a measurement to differ from a true value in nature are removed. Measurement only have meaning within the context of the experiment in which they are made, equivalent measurements performed under different experimental conditions cannot be compared directly until all of the experimental effects are removed. This include the experimental phase space, measurement resolutions, efficiencies, acceptances and bias. In order to make a measurement globally accessible, each analysis must 'undo' all of these factors. The method for unfolding will differ from experiment to experiment and analysis to analysis as necessary; the intended method for this analysis is reported in this section. From a mathematical perspective, the goal of unfolding is to construct estimators for the contents of a 'true' histogram y given a reconstructed histogram x, where the probability density functions (PDF) are unknown, but related in the form of Equation 11.1 [108].

$$f_{\text{meas}}(x) = \int R(x|y)\, f_{\text{true}} dy, \tag{11.1}$$

where $R(x|y)$ is known as the response function and defines the transformation between the true and measured PDFs. In some analyses events are counted and filled into histograms as approximations for PDFs, in this scenario the relation takes the form

$$\nu_i = \sum_{j=1}^{M} M_{ij}\mu_j, \tag{11.2}$$

where ν_i is the expectation value for the number of observed events in bin i of variable x, and μ_j is the expectation value for bin j from the true histogram y. In this formulation, M_{ij} is a *response*

matrix which defines the probability of migration for a true event in any bin j to be reconstructed and observed in any bin i, as in

$$M_{ij} = P\left(\text{observed in bin } i | \text{true value in bin } j\right). \tag{11.3}$$

In reality however the presence of background events β must also be considered, and so Equation 11.2 is modified into

$$\nu_i = \sum_{j=1}^{M} M_{ij}\mu_j + \beta_i. \tag{11.4}$$

Unfolding describes the process reversal this equation to solve for μ_j and rebuild an estimation for true histogram y. This requires the inversion of the response matrix, to produce Equation 11.5, where for N bins $\mu = (\mu_1, ..., \mu_N)$, $\nu = (\nu_1, ..., \nu_N)$, and each has been replaced by their estimators $\hat{\mu}$ and n (assuming independent Poisson-distributed events in the observed data set).

$$\hat{\mu} = M^{-1}\left(n - \beta\right) \tag{11.5}$$

However the application of this inversion is not always trivial, and is explored further in Section 11.7.

11.1 Unfolding formulation

In order to unfold an experimental measurement several additional steps are required. The complete function for the analysis presented here is

$$N^i = \frac{1}{\varepsilon^i} \cdot \sum_j \mathcal{M}_{ij}^{-1} \cdot f_{\text{acc}}^j \cdot (N_{\text{data}}^j - N_{\text{bkg}}^j), \tag{11.6}$$

where $i, j = \{\text{N}^{++}, \text{N}^{--}, \text{N}^{+-}, \text{N}^{-+}\}$ and index i runs over the particle-level (MC truth) while index j runs over the reconstruction-level. N_{data}^j and N_{bkg}^j are the number of events observed in data and the estimated background, respectively. An acceptance term, f_{acc}^j, and an efficiency term, ε^i, are applied bin-by-bin and are discussed in the sections below.

The response matrix, $\mathcal{M}_{ij}$, is a discrete 4×4 matrix, shown in Table 10.57, where non-zero off-diagonal terms can only occur via charge misidentification or via the misassignment of the

same- or different-top SMT muon classification.

11.2 Combination of e+jets and μ+jets channels

The physics of interest should not depend on the flavor of the lepton from the W-boson should also not depend the ST or DT classification of the soft muon. Prior to measurement of the CA and CP asymmetries, and prior to the construction of the response matrix and the acceptance and efficiency factors used for unfolding, the observed ST and DT events in both the e+jets and μ+jets data must be combined. The background composition and total yield varies for each $N^{\alpha\beta}$ bin, and as such all backgrounds are subtracted from the data prior to combination. ST and DT distributions are combined via direct addition, and for the data the e+jets and μ+jets are also combined via addition. For MC, the e+jets channel reweighted such that the Monte Carlo ratio of e/μ events, matches that of the data ($\varepsilon_{e/\mu}$) according to $N_{\text{cb}} = \left(\varepsilon_{e/\mu} \cdot N_e\right) + N_\mu$, where N_e is the binned e+jets yield, N_μ is the binned μ+jets yield and N_{cb} is the combined yield for any particular bin. A factor of $\varepsilon_{e/\mu} = 0.993^{+0.039}_{-0.038}$ is observed, with the systematic uncertainty break down given in Table 11.1. The dominant uncertainty comes from additional radiation. A separate epsilon emu data / MC ratio is calculated and used for each systematic uncertainty individually.

11.3 Fiducial volume

A fiducial volume describes the region of phase space in which an analysis is performed after removing all experimental effects. An ideal analysis would have an unconstrained fiducial volume, representing a fully inclusive result and yielding an estimation for the value of interest as it exists in nature. However the extrapolation of any measurement to an unconstrained fiducial volume is impractical, as for example modelling uncertainties on low-energy QCD processes are prohibitively large. Attempting to extrapolate a measurement to include a low energy regime would increase modelling systematics such as those from additional radiation and parton distribution functions by several orders of magnitude. Instead a fiducial volume within which physics processes are well understood is defined. Comparisons to theoretical models may still be made as predictions for each model may be constrained to the same fiducial volume of interest.

In the case of this analysis, as presented in Equations 4.20- 4.24, the charge and CP asymmetries are related by decay-chain fractions (DCFs) which describe the relative contributions

Nominal	0.99
Sources of experimental uncertainty in %	
Lepton charge misidentification	+0.00 -0.01
Lepton energy resolution	+0.28 -0.17
Lepton trigger, reco, identification	+2.01 -1.96
Jet energy scale	+0.27 -0.46
Jet energy resolution	+0.18 -0.18
Jet reco efficiency	+0.00 -0.00
Jet vertex fraction	+0.04 -0.04
Fake lepton estimate	+3.06 -2.99
Background normalisation	+0.02 -0.02
W+jets estimate (statistical)	+0.01 -0.01
Single-top production asymmetry	+0.00 -0.04
b-tagging efficiency	+0.03 -0.03
c-jet mistag rate	+0.02 -0.02
Light-jet mistag rate	+0.01 -0.01
SMT reco identification	+0.01 -0.01
SMT momentum imbalance	+0.02 -0.02
SMT light-jet mistag rate	+0.02 -0.02
Sources of modelling uncertainty in %	
Hadron-to-muon branching ratio	+0.06 -0.07
b-hadron production fractions	+0.00 -0.04
Additional radiation	$\pm$1.19
MC generator	$\pm$0.09
Parton shower	$\pm$0.34
Parton distribution function	$\pm$0.39
Total experimental uncertainty	+3.69 -3.62
Total modelling uncertainty	+1.30 -1.30
Total systematic uncertainty	+3.91 -3.84

Table 11.1: Data / MC scale factor for the e/μ ratio, $\varepsilon_{e/\mu}$

of each decay channel to the measurement asymmetries. The DCFs are dependent on the event selection and fiducial volume, and are determined using MC simulation.

11.4 Acceptance

The acceptance, f^{j}_{acc}, is a bin-by-bin correction factor to account for events which satisfy reconstruction requirements, but fail to satisfy particle-level requirements. This can occur due to resolution effects from the detector, a jet with true p_T near (but outside of) the selection phase space may be mismeasured (p_T smearing) and therefore allow the event to be erroneously included

at reconstruction-level. The acceptance factor is designed to scale down from all events which satisfy reconstruction-level requirements, to only those events which satisfy both reconstruction-level and particle-level requirements. The acceptance term also includes backgrounds within the $t\bar{t}$ sample itself, such as muons originating from light-flavour, pile-up, $c \to \mu$, initial- and final-state radiation and dilepton $t\bar{t}$ events. This choice (as opposed to subtracting the $t\bar{t}$ background events with the non-$t\bar{t}$ backgrounds) removes dependency of the acceptance terms on the $t\bar{t}$ production cross section. If the $t\bar{t}$ backgrounds are subtracted with the non-$t\bar{t}$ backgrounds, an iterative process is required, as the measured production cross section $\sigma_{t\bar{t}}^{\text{meas}}$ would differ slightly from the cross section used to scale the $t\bar{t}$ MC sample (inclusive of those backgrounds) initially. The measurement would have to be repeated several times until the two values agreed. Allowing the $t\bar{t}$ backgrounds to factor into the acceptance terms directly avoids this issue. The acceptance terms take the form of $f_{acc}^{j} = \left(\frac{N_{\text{reco}\wedge\text{fid}}}{N_{\text{reco}}}\right)^{j}$, where N_{reco} is the number of MC reconstructed events after background subtraction, and $N_{\text{reco}\wedge\text{fid}}$ is the number of MC reconstructed events after background subtraction for which the MC truth is also inside the fiducial volume.

The result of performing the acceptance correction is to create a distribution of events which satisfy both reconstruction- and particle-levels requirements, and which exist within a well-defined phase space (the fiducial volume). The acceptance factors, for the combined ST and DT distributions, with both electron and muon channels, are as follows:

$$f_{acc}^{++} = 0.642^{+0.021}_{-0.021}\,(\text{Expt.})^{+0.015}_{-0.015}\,(\text{Model}) \tag{11.7}$$

$$f_{acc}^{--} = 0.644^{+0.019}_{-0.020}\,(\text{Expt.})^{+0.016}_{-0.016}\,(\text{Model}) \tag{11.8}$$

$$f_{acc}^{+-} = 0.694^{+0.021}_{-0.021}\,(\text{Expt.})^{+0.018}_{-0.018}\,(\text{Model}) \tag{11.9}$$

$$f_{acc}^{-+} = 0.692^{+0.020}_{-0.021}\,(\text{Expt.})^{+0.017}_{-0.017}\,(\text{Model}) \tag{11.10}$$

where the experimental (Expt.) and modelling (Model) systematic uncertainties are broken down in Table 11.2. The opposite-sign (OS) acceptances are larger as (from Tables 10.1- 10.4) the OS events suffer from a smaller $t\bar{t}$ background fraction, primarily due to the distribution of the $c \to \mu$ background events.

Nominal	0.64	0.64	0.69	0.69
Sources of experimental uncertainty in %				
Lepton charge misidentification	+0.00 -0.00	+0.00 -0.00	+0.00 -0.00	+0.00 -0.00
Lepton energy resolution	+0.10 -0.02	+0.08 -0.09	+0.06 -0.06	+0.08 -0.12
Lepton trigger, reco, identification	+0.00 -0.00	+0.01 -0.01	+0.01 -0.01	+0.00 -0.00
Jet energy scale	+2.05 -1.93	+1.81 -2.04	+1.86 -1.80	+1.80 -1.95
Jet energy resolution	+2.52 -2.52	+2.38 -2.38	+2.32 -2.32	+2.23 -2.23
Jet reco efficiency	+0.02 -0.02	+0.02 -0.02	+0.01 -0.01	+0.01 -0.01
Jet vertex fraction	+0.34 -0.34	+0.33 -0.33	+0.30 -0.30	+0.30 -0.30
Fake lepton estimate	+0.00 -0.00	+0.00 -0.00	+0.00 -0.00	+0.00 -0.00
Background normalisation	+0.00 -0.00	+0.00 -0.00	+0.00 -0.00	+0.00 -0.00
W+jets estimate (statistical)	+0.00 -0.00	+0.00 -0.00	+0.00 -0.00	+0.00 -0.00
Single-top production asymmetry	+0.00 -0.00	+0.00 -0.00	+0.00 -0.00	+0.00 -0.00
b-tagging efficiency	+0.16 -0.16	+0.16 -0.16	+0.12 -0.11	+0.12 -0.12
c-jet mistag rate	+0.27 -0.27	+0.27 -0.27	+0.15 -0.15	+0.14 -0.14
Light-jet mistag rate	+0.08 -0.08	+0.08 -0.08	+0.08 -0.07	+0.08 -0.08
SMT reco identification	+0.08 -0.08	+0.07 -0.07	+0.09 -0.09	+0.10 -0.09
SMT momentum imbalance	+0.00 -0.00	+0.00 -0.00	+0.01 -0.01	+0.01 -0.01
SMT light-jet mistag rate	+0.15 -0.16	+0.13 -0.15	+0.11 -0.12	+0.12 -0.13
Sources of modelling uncertainty in %				
Hadron-to-muon branching ratio	+0.48 -0.52	+0.48 -0.53	+0.28 -0.28	+0.28 -0.28
b-hadron production	+0.07 -0.07	+0.06 -0.06	+0.03 -0.03	+0.03 -0.03
Additional radiation	$\pm$2.02	$\pm$2.12	$\pm$1.93	$\pm$1.68
MC generator	$\pm$0.73	$\pm$0.80	$\pm$0.23	$\pm$0.72
Parton shower	$\pm$0.77	$\pm$0.85	$\pm$1.76	$\pm$1.67
Parton distribution Function	$\pm$0.24	$\pm$0.29	$\pm$0.13	$\pm$0.12
Total experimental uncertainty	+3.29 -3.21	+3.03 -3.17	+3.01 -2.96	+2.90 -3.00
Total modelling uncertainty	+2.35 -2.35	+2.48 -2.49	+2.64 -2.64	+2.50 -2.50
Total systematic uncertainty	+4.04 -3.98	+3.92 -4.03	+4.00 -3.97	+3.82 -3.90

Table 11.2: Acceptance for the combination of the e+jets and μ+jets channels, with ST and DT combined also. Uncertainties are given as a percentage of the nominal value.

11.5 Response matrix

A response matrix (or migration matrix) is designed to correct for events which drift between CA bins due to misidentification. Traditionally, migration matrices account for effects of measurement resolution; in a distribution of jet p_T event reconstruction with a given detector 'smears' the shape of the histogram due imperfect resolution. In this analysis the causes of migrations between bins are much simpler; a mistake in the KLFitter decision, or a charge mis-ID on the triggered lepton or soft muon. With the ATLAS detector charge mis-ID is extremely small (see

Section 9.1.3), as such the response matrix will be entirely dominated by the purity of the KLFitter decision. There is a correlation between the diagonality of the response matrix and the statistical uncertainty associated with the measurement (see Section 11.8.3 below); so ensuring the best performance from the KLFitter is important. Any response matrix, whether a 50% diagonal or 95% diagonal, should unfold the data to the correct measurement, however the 95% purity matrix will do so with a much smaller uncertainty. The response matrix, $\mathcal{M}_{ij}$, is populated exclusively by SMT muons which are matched between the reconstruction and particle level (no $t\bar{t}$ background events). A response matrix must be inverted in order to undo the effects of misidentification, this process requires some optimisation and is discussed in Section 11.7. The response matrix produced for this analysis, for the combined ST and DT distributions, with both electron and muon channels, is shown in Table 11.3 (as shown also in Table 10.57 in the previous chapter).

	N^{++}_{reco}	N^{--}_{reco}	N^{+-}_{reco}	N^{-+}_{reco}
N^{++}_{truth}	0.795	0.000	0.000	0.205
N^{--}_{truth}	0.000	0.793	0.207	0.000
N^{+-}_{truth}	0.000	0.214	0.786	0.000
N^{-+}_{truth}	0.214	0.000	0.000	0.786

Table 11.3: Response matrix for the combined e+Jets and μ+Jets channels, with ST and DT also combined. The MC statistical uncertainty is ~ 0.001

11.6 Particle-level corrections

The efficiency ε_i in unfolding is to account for events which have not yet been included in the analysis as they failed to satisfy the reconstruction-level requirements. The analysis must scale up from the sample which now satisfies all reconstruction- and particle-level requirements, to a sample weighted to include events which satisfy particle-level requirements but are not successfully reconstructed. An efficiency term, ε_i, is applied bin-by-bin to the unfolded data to correct for these non-reconstructed SMT muons. The efficiency terms take the form of Equation 11.11, where N_{fid} is the number of MC truth events which are inside the fiducial volume, and $N_{\text{reco}\wedge\text{fid}}$ is the number of MC reconstructed events after background subtraction for which the MC truth is inside the fiducial volume.

$$\varepsilon^i = \left(\frac{N_{\text{reco}\wedge\text{fid}}}{N_{\text{fid}}} \right)^i \tag{11.11}$$

The efficiency factors,for the combined ST and DT distributions, with both electron and muon channels,are as follows:

$$\varepsilon_{eff}^{++} = 0.273^{+0.013}_{-0.013}\,(\text{Expt.})^{+0.021}_{-0.020}\,(\text{Model}) \tag{11.12}$$

$$\varepsilon_{eff}^{--} = 0.272^{+0.013}_{-0.013}\,(\text{Expt.})^{+0.021}_{-0.021}\,(\text{Model}) \tag{11.13}$$

$$\varepsilon_{eff}^{+-} = 0.279^{+0.014}_{-0.014}\,(\text{Expt.})^{+0.022}_{-0.022}\,(\text{Model}) \tag{11.14}$$

$$\varepsilon_{eff}^{-+} = 0.279^{+0.014}_{-0.014}\,(\text{Expt.})^{+0.022}_{-0.022}\,(\text{Model}) \tag{11.15}$$

where the experimental (Expt.) and modelling (Model) systematic uncertainties are broken down in Table 11.4.

11.7 Matrix inversion and regularisation

The inversion of a response matrix must be performed carefully. Matrices which are considered to be very ‘off-diagonal’ (a relative phrase dependent on the bin sizing and measurement resolution) may produce highly oscillatory results from minor fluctuations and increase the overall uncertainty on analysis results. This is primarily caused by statistical fluctuations. For a PDF with fine structure, the details of that structure and the random fluctations become indistinguishable. This is generally a greater problem for distributions with too many bins and as such a compromise is required between the desired resolution of the measurement for the variable of interest and the extent of the systematic error resulting from the matrix inversion. Response matrices are often regularised in order to decrease the variance on the inverted result by enforcing some constraints on the ’smoothness’ of the resulting distribution. The more regularised a matrix is however the greater the bias it will also produce, as regularisation introduces correlations between bins in the unfolded distribution. Following the examples in [108] for a log-likelihood method, for a regularised matrix inversion it might be chosen to maximise

$$\Phi(\mu) = \alpha \ln L(\mu) + S(\mu), \tag{11.16}$$

Nominal	0.27	0.27	0.28	0.28
Sources of experimental uncertainty in %				
Lepton charge misidentification	+0.00 -0.00	+0.00 -0.00	+0.00 -0.00	+0.00 -0.00
Lepton energy resolution	+1.00 -1.06	+0.89 -0.93	+0.62 -0.66	+0.72 -0.76
Lepton trigger, reco, identification	+1.88 -1.89	+1.88 -1.89	+1.88 -1.89	+1.88 -1.89
Jet energy scale	+2.35 -2.36	+2.37 -2.45	+2.79 -2.93	+2.75 -2.90
Jet energy resolution	+2.25 -2.25	+2.39 -2.39	+2.44 -2.44	+2.52 -2.52
Jet reco efficiency	+0.04 -0.04	+0.03 -0.03	+0.05 -0.05	+0.05 -0.05
Jet vertex fraction	+0.57 -0.57	+0.59 -0.59	+0.60 -0.60	+0.65 -0.65
Fake lepton estimate	+0.10 -0.10	+0.11 -0.10	+0.09 -0.08	+0.09 -0.09
Background normalisation	+0.00 -0.00	+0.00 -0.00	+0.00 -0.00	+0.00 -0.00
W+jets estimate (statistical)	+0.00 -0.00	+0.00 -0.00	+0.00 -0.00	+0.00 -0.00
Single-top production asymmetry	+0.00 -0.00	+0.00 -0.00	+0.00 -0.00	+0.00 -0.00
b-tagging efficiency	+2.04 -2.06	+2.04 -2.06	+2.17 -2.19	+2.19 -2.21
c-jet mistag rate	+0.01 -0.01	+0.01 -0.01	+0.01 -0.01	+0.01 -0.01
Light-jet mistag rate	+0.16 -0.19	+0.17 -0.19	+0.14 -0.16	+0.14 -0.16
SMT reco identification	+1.45 -1.45	+1.45 -1.45	+1.13 -1.13	+1.13 -1.13
SMT momentum imbalance	+0.91 -0.91	+1.00 -0.99	+0.91 -0.91	+0.83 -0.83
SMT light-jet mistag rate	+0.15 -0.14	+0.16 -0.15	+0.18 -0.17	+0.18 -0.17
Sources of modelling uncertainty in %				
SMT Branching ratio	+0.20 -0.22	+0.20 -0.21	+0.24 -0.24	+0.24 -0.24
B Hadron production	+0.96 -0.07	+0.95 -0.06	+0.10 -0.12	+0.13 -0.12
Additional radiation	$\pm$2.38	$\pm$2.52	$\pm$1.57	$\pm$1.67
MC generator	$\pm$0.34	$\pm$0.31	$\pm$0.75	$\pm$0.95
Parton shower	$\pm$0.50	$\pm$0.86	$\pm$3.19	$\pm$3.34
Parton distribution function	$\pm$7.07	$\pm$7.06	$\pm$6.95	$\pm$6.90
Total experimental uncertainty	+4.76 -4.79	+4.83 -4.89	+4.98 -5.08	+5.02 -5.12
Total modelling uncertainty	+7.55 -7.49	+7.61 -7.55	+7.85 -7.85	+7.91 -7.91
Total systematic uncertainty	+8.92 -8.89	+9.02 -9.00	+9.30 -9.35	+9.37 -9.42

Table 11.4: Efficiency for the combination of the e+jets and μ+jets channels, with ST and DT combined also. Uncertainties are given as a percentage of the nominal value.

where $S(\mu)$ is a *regularisation function* and α is a *regularisation parameter*. These represent the 'smoothness' and may be chosen freely. Often $S(\mu)$ is chosen to be related to the second derivative of μ in each bin, a technique known as *Tikhonov* regularisation [109, 110].

This analysis has the advantage of only using four bins, due to this minor fluctuations between the bins will not produce significant effects. This suggests that unfolding may be achieved by Unregularised Matrix Inversion (UMI). In the following sections, studies are performed to compare the performance of UMI, against Iterative Bayesian (IB) matrix inversion [111], with four (IB4) and eight (IB8) iterations respectively.

11.7.1 Unregularised matrix inversion

Unregularised matrix inversion is a very simple algorithm which directly inverts the response matrix without any smoothing or regularisation. It is considered to be the most vulnerable to statistical fluctuations, however it is also known to produce the smallest possible variance for an unbiased estimator. In the sections below, unfolding performed using unregularised matrix inversion is labelled as UMI.

11.7.2 Iterative Bayesian matrix inversion

Iterative Bayesian matrix inversion was first proposed in 1995 [111]. This approach uses a freely defined prior probability p_i for finding each true event in each reconstructed bin, along with Bayes' theorem [112] to update estimators for the true bin contents as

$$\hat{\mu}_i = \frac{1}{\varepsilon_i} \sum_{j=1}^{N} P(\text{true value in bin } i | \text{found in bin } j)\, n_j = \frac{1}{\varepsilon_i} \sum_{j=1}^{N} \left(\frac{M_{ij} p_i}{\sum_k M_{jk} p_k} \right) n_j, \tag{11.17}$$

where $\hat{\mu}_i$ is the estimator for the number of events in true bin i, n_j is the number of events in reconstructed bin j, and $\varepsilon_i = \sum_{i=1}^{N} M_{ij} = P(\text{observed anywhere} | \text{true value in bin } j)$ is the probability to observed each event at all. Equation 11.17 is applied iteratively (using $\frac{\hat{\mu}_i}{\sum_i \mu_i}$ as the value for the next p_i) until an accepted balance between the variance on the estimated μ_i and the introduced bias is reached. In the sections below, unfolding performed using iterative bayesian matrix inversion is labelled as IB4 or IB8 for inversion using four or eight iterations respectively.

11.8 Statistical uncertainty and bias

11.8.1 Closure test

To ensure the correct functioning of the unfolding code, a software *closure test* must be performed. The acceptance and efficiency factors and the response matrix are all built from MC. If the same MC at the reconstruction-level is unfolded using these factors and matrix, it should reproduce exactly the MC at the fiducial truth-level. This test is performed on the nominal MC in this analyses and the system is found to close fully.

11.8.2 Stress tests

Stress tests are designed to ensure that the method is robust against mistakes in modelling such as the simulation of the expected charge asymmetries (CA). Unfolding should be able to recover the truth parameters, regardless of what the true parameters are. An unfolding method which is not robust against modelling mistakes would return erroneous results when applied to data. The unfolding technique must be unbiased with respect to the CA modelled in the MC from which it is built is the , and the CA in the sample it is applied to. The steps below are taken to test the capability of the response matrix and efficiency terms to unfold a distribution built from the same MC but with different CAs. The acceptance terms are not included in this stress test, as the technique involves reweighting the nominal sample at the fiducial truth-level to produce a sample with a new inbuilt charge asymmetry. This reweighting is only applicable to events which are true $t\bar{t}$ signal events and fall within the fiducial volume, reconstructed events which are true $t\bar{t}$ but fall outside of the fiducial volume, or which are part of the $t\bar{t}$ backgrounds, cannot be subject to the same reweighting procedure as there is no fiducial-truth level event to link their reweighting to. This means that a sample of reconstructed-level events including those $t\bar{t}$ events which are not fiducial is poorly defined, and applying acceptance factors to such a sample is also poorly defined. As such, the following technique is used to stress test the unfolding procedure from the point of the response matrix inversion only, and the potential effects of the acceptance factors are assumed to be similar to that of the efficiency factors, which are stressed:

1. Create nominal CA bins and efficiency factors from $t\bar{t}$ MC

2. Calculate scale factors to alter each bin yield in order to artificially produce a sample at the fiducial truth-level with a different desired CA (SS or OS in turn, as they are anti-correlated and therefore not uniquely controlled)

3. Reweight every event in order to produce new CA bins with the desired CA at the reconstruction level, for the subset of events which are also present at the fiducial truth level (after the point of an acceptance scale factor in the nominal unfolding process). The modelling of these events is identical in every way to the nominal sample except the CA has been altered to stress test the unfolding. This reweighting method provides an effectively new sample for which both reconstructed and truth events already exist

4. Use the nominal response matrix (and efficiency terms) to unfold the CA-altered reconstructed samples and compare the unfolded outputs to the CA-altered true fiducial values.

The analysis bias is defined as the raw difference between the unfolded CAs (CA_{UF}) and their true fiducial values (CA_{fid}). This is measured in MC as bias $b = CA^{MC}_{fid} - CA^{MC}_{UF}$. This may be measured at the point directly subsequent to the matrix inversion, as in Tables 11.5 and 11.6, or following the application of the efficiency factors, as in Tables 11.7 and 11.8.

Tables 11.5 and 11.6 show that the UMI method is unbiased against changes in the CA of the test sample. The IB4 method shows minimal bias, whilst the IB8 method falls inbetween. Tables 11.7 and 11.8 show that the affect of the efficiency factors is similar, the UMI method has a bias which falls between $0-10\%$ of the central value (which is negligible with respect to the overall uncertainties on the measurement), IB4 has a bias between $3-10\%$ and on average higher than UMI, and IB8 again falls inbetween.

Fiducial A^{ss}	UMI Bias		IB4 Bias		IB8 Bias	
0.000	2×10^{-5}	(1.1)	7×10^{-5}	(3.5)	3×10^{-5}	(1.6)
0.002	2×10^{-5}	(0.6)	1×10^{-4}	(2.5)	4×10^{-5}	(1.0)
0.004	2×10^{-5}	(0.4)	1×10^{-4}	(2.2)	5×10^{-5}	(0.8)
0.006	2×10^{-5}	(0.3)	2×10^{-4}	(2.0)	5×10^{-5}	(0.6)
0.008	2×10^{-5}	(0.2)	2×10^{-4}	(1.9)	5×10^{-5}	(0.6)
0.01	2×10^{-5}	(0.2)	3×10^{-4}	(1.8)	6×10^{-5}	(0.5)
0.02	2×10^{-5}	(0.1)	3×10^{-4}	(1.6)	9×10^{-5}	(0.4)
0.04	3×10^{-5}	(0.07)	6×10^{-4}	(1.5)	1×10^{-4}	(0.4)
0.06	3×10^{-5}	(0.05)	8×10^{-4}	(1.5)	2×10^{-4}	(0.4)
0.08	3×10^{-5}	(0.04)	1×10^{-3}	(1.5)	3×10^{-4}	(0.4)
0.1	4×10^{-5}	(0.04)	1×10^{-3}	(1.5)	3×10^{-4}	(0.4)

Table 11.5: Bias of the response matrix on the truth-level charge asymmetry A^{ss} (prior to efficiency factors), for the unregularised matrix inversion (UMI) and interative bayes algorithms (IB4, IB8 with four and eight iterations respectively) for MC samples reweighted to have different fiducial truth-level same-sign charge asymmetries A^{ss}. The first value in each column is the raw bias, the value in parentheses is the bias as a percentage of the truth-level A^{ss}. Note, the leftmost column gives the fiducial charge asymmetries for the whole sample, without the reduction of events by the efficiency factors, which will change the observed asymmetry. The percentages in parentheses are percentages of the observed charge asymmetry when the efficiency factors are applied to the whole sample (not shown).

Fiducial A^{os}	UMI Bias		IB4 Bias		IB8 Bias	
0.000	1×10^{-5}	(1.1)	4×10^{-5}	(3.6)	2×10^{-5}	(1.6)
0.002	1×10^{-5}	(2.0)	2×10^{-5}	(2.3)	1×10^{-5}	(2.1)
0.004	1×10^{-5}	(0.5)	1×10^{-5}	(0.5)	7×10^{-6}	(0.3)
0.006	1×10^{-5}	(0.3)	4×10^{-5}	(0.8)	3×10^{-6}	(0.1)
0.008	1×10^{-5}	(0.2)	6×10^{-5}	(1.0)	5×10^{-6}	(0.1)
0.01	1×10^{-5}	(0.1)	9×10^{-5}	(1.1)	1×10^{-5}	(0.1)
0.02	1×10^{-5}	(0.06)	2×10^{-4}	(1.3)	4×10^{-5}	(0.2)
0.04	1×10^{-5}	(0.03)	5×10^{-4}	(1.3)	1×10^{-4}	(0.3)
0.06	1×10^{-5}	(0.02)	7×10^{-4}	(1.4)	2×10^{-4}	(0.3)
0.08	7×10^{-6}	(0.01)	1×10^{-3}	(1.4)	2×10^{-4}	(0.3)
0.1	7×10^{-6}	(0.01)	1×10^{-3}	(1.3)	3×10^{-4}	(0.3)

Table 11.6: Bias of the response matrix on the truth-level charge asymmetry A^{os} (prior to efficiency factors), for the unregularised matrix inversion (UMI) and interative bayes algorithms (IB4, IB8 with four and eight iterations respectively) for MC samples reweighted to have different fiducial truth-level opposite-sign charge asymmetries A^{os}. The first value in each column is the raw bias, the value in parenthesesis the bias as a percentage of the truth-level A^{os}. Note, the leftmost column gives the fiducial charge asymmetries for the whole sample, without the reduction of events by the efficiency factors, which will change the observed asymmetry. The percentages in parentheses are percentages of the observed charge asymmetry when the efficiency factors are applied to the whole sample (not shown).

Fiducial A^{ss}	UMI Bias		IB4 Bias		IB8 Bias	
0.000	1×10^{-4}		9×10^{-5}		1×10^{-4}	
0.002	9×10^{-6}	(0.4)	7×10^{-5}	(3.3)	8×10^{-6}	(0.4)
0.004	1×10^{-4}	(3.3)	2×10^{-4}	(5.8)	2×10^{-4}	(3.8)
0.006	3×10^{-4}	(4.3)	4×10^{-4}	(6.5)	3×10^{-4}	(4.8)
0.008	4×10^{-4}	(4.9)	5×10^{-4}	(6.8)	4×10^{-4}	(5.3)
0.01	5×10^{-4}	(5.1)	7×10^{-4}	(7.0)	6×10^{-4}	(5.5)
0.02	1×10^{-3}	(5.8)	1×10^{-3}	(7.4)	1×10^{-3}	(6.1)
0.04	2×10^{-3}	(6.1)	3×10^{-3}	(7.6)	3×10^{-3}	(6.5)
0.06	4×10^{-3}	(6.3)	5×10^{-3}	(7.7)	4×10^{-3}	(6.6)
0.08	5×10^{-3}	(6.3)	6×10^{-3}	(7.7)	5×10^{-3}	(6.6)
0.1	6×10^{-3}	(6.3)	8×10^{-3}	(7.8)	7×10^{-3}	(6.7)

Table 11.7: Bias of the response matrix on the fiducial truth-level charge asymmetry A^{ss} (after efficiency factors), for the unregularised matrix inversion (UMI) and interative bayes algorithms (IB4, IB8 with four and eight iterations respectively) for MC samples reweighted to have different fiducial truth-level same-sign charge asymmetries A^{ss}. The first value in each column is the raw bias, the value in parenthesesis the bias as a percentage of the fiducial truth-level A^{ss}.

11.8.3 Statistical Uncertainty

Monte Carlo pseudo-experiments (*toys*, described below) are used to predict the statistical uncertainty on the results of the analysis. The same technique is used to calculate the actual statistical

Fiducial A^{os}	UMI Bias		IB4 Bias		IB8 Bias	
0.000	8×10^{-5}		6×10^{-5}		8×10^{-5}	
0.002	2×10^{-4}	(11.1)	2×10^{-4}	(11.0)	2×10^{-4}	(11.1)
0.004	4×10^{-4}	(8.8)	4×10^{-4}	(9.5)	4×10^{-4}	(9.0)
0.006	5×10^{-4}	(8.0)	5×10^{-4}	(8.9)	5×10^{-4}	(8.2)
0.008	6×10^{-4}	(7.6)	7×10^{-4}	(8.6)	6×10^{-4}	(7.8)
0.01	7×10^{-4}	(7.2)	8×10^{-4}	(8.3)	8×10^{-4}	(7.5)
0.02	1×10^{-3}	(6.9)	2×10^{-3}	(8.1)	1×10^{-3}	(7.1)
0.04	3×10^{-3}	(6.7)	3×10^{-3}	(7.9)	3×10^{-3}	(7.0)
0.06	4×10^{-3}	(6.6)	5×10^{-3}	(7.9)	4×10^{-3}	(6.9)
0.08	5×10^{-3}	(6.6)	6×10^{-3}	(7.8)	5×10^{-3}	(6.9)
0.1	7×10^{-3}	(6.6)	8×10^{-3}	(7.8)	7×10^{-3}	(6.8)

Table 11.8: Bias of the response matrix on the fiducial truth-level charge asymmetry A^{os} (after efficiency factors), for the unregularised matrix inversion (UMI) and interative bayes algorithms (IB4, IB8 with four and eight iterations respectively) for MC samples reweighted to have different fiducial truth-level opposite-sign charge asymmetries A^{os}. The first value in each column is the raw bias, the value in parenthesesis the bias as a percentage of the fiducial truth-level A^{ss}.

uncertainty on data. The study described in this section is also used to justify the optimisation of the KLFitter. It will be shown that the statistical uncertainty on the unfolded results has a dependency on KLFitter performance. In order to estimate the statistical uncertainty on the charge asymmetries using the optimised KLFitter:

1. Construct the acceptances, efficiencies and response matrix using the nominal MC signal.

2. Run tests with varying numbers of toys. For every toy, smear the contents of each CA bin by a Poisson function, then use the nominal unfolding components to unfold the smeared sample back to a fiducial truth-level.

3. For each toy, calculate the unfolded CAs and CPs. Plotting these asymmetries into histograms results in Gaussian distributions around the true CA and CP values. The width of these distributions gives an estimate of the statistical uncertainty on the asymmetry measurements.

Figures 11.1 and 11.2 are used to determine that the statistical uncertainty may be reasonable predicted using 5000 toys, the central values the errors on the uncertainties are stable. The pull of the distributions after 5000 toys, used to ensure that the statistical uncertainties are correctly estimated, is defined in Equation 11.18, where x is a measured value, μ is the mean of all

measured values, and σ is the estimated statistical uncertainty. The measured pulls are given in Table 11.9, all are in good agreement with unity, showing that the statistical uncertainties are well estimated.

$$\text{pull} \quad p = \frac{x-\mu}{\sigma} \tag{11.18}$$

Method	Pull	
	A^{ss}	A^{os}
UMI	1.00 ± 0.01	1.00 ± 0.01
IB4	1.00 ± 0.01	1.00 ± 0.01
IB8	1.00 ± 0.01	1.00 ± 0.01

Table 11.9: Pulls on the charge asymmetrys calculated after 5000 MC toys, for three different matrix inversion techniques.

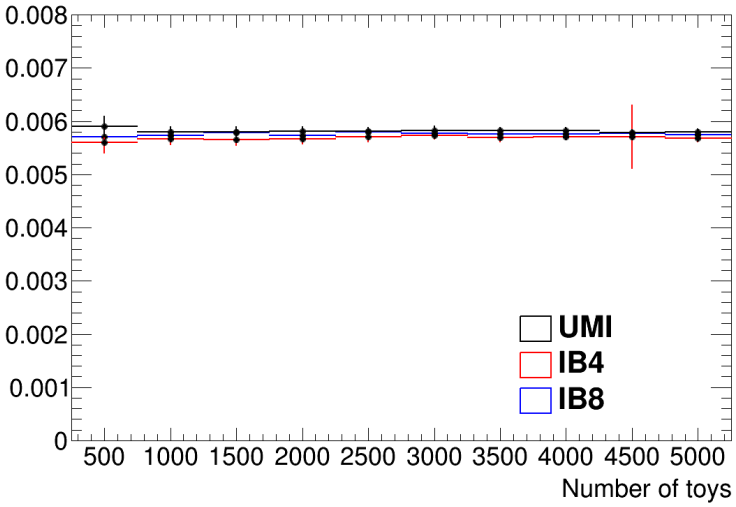

Figure 11.1: The statistical uncertainty on A^{ss} as measured in the nominal $t\bar{t}$ MC scaled to an integrated luminosity of 20.3 fb^{-1}, when using the UMI, IB4 and IB8 unfolding techniques. The uncertainty is found to be stable and similar for each.

Figures 11.3 and 11.4 show the statistical uncertainty predictions made after 5000 toys, generated using an artificial KLFitter decisions with predefined purity ρ_{KL}. The decisions are based on a random number generator, using truth information to provide a specific probability of correctly identifying each SMT jet as ST or DT. For UMI, IB4 and IB8 it is apparent that the statistical uncertainty is dependent on ρ_{KL}, however all three converge at $\rho_{\text{KL}} = 80\%$. Therefore it is determined that for KLFitter purity of 80%, UMI is the optimal choice of matrix inversion.

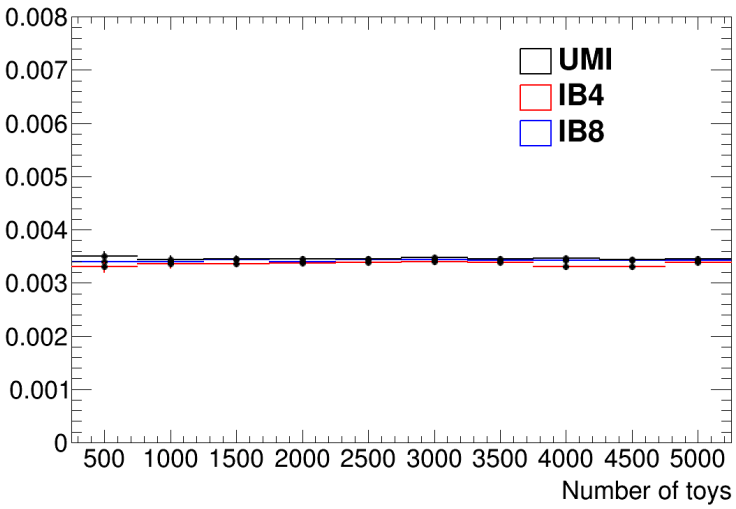

Figure 11.2: The statistical uncertainty on A^{os} as measuredin the nominal $t\bar{t}$ MC scaled to an integrated luminosityof 20.3 fb^{-1}, when using the UMI, IB4 and IB8 unfolding techniques. The uncertainty is found to be stable and similar for each.

At $\rho_{KL} = 80\%$, UMI provides an equally small statistical uncertainty as the iterative bayesian methods, with the most negligible bias contribution.

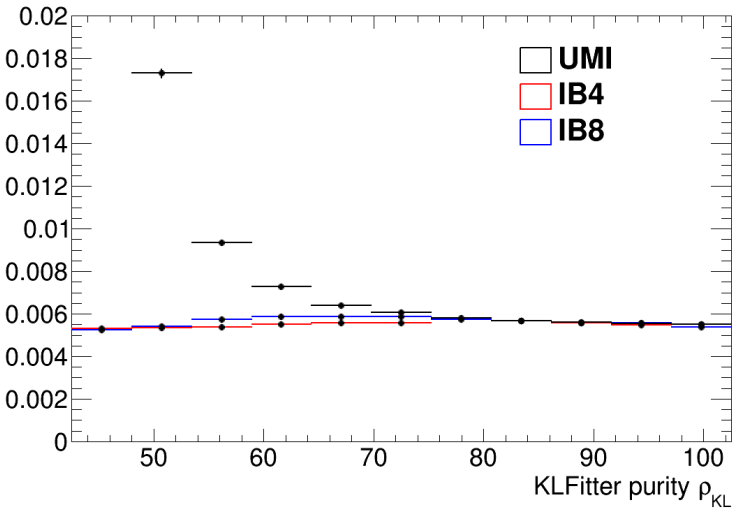

Figure 11.3: The statistical uncertainty on A^{ss} as measured in the nominal $t\bar{t}$ MC scaled to an integrated luminosity of 20.3 fb^{-1}, when using the UMI, IB4 and IB8 unfolding techniques. The uncertainty is found as a function of the KLFitter purity ρ_{KL}. All three unfolding techniques converge in statistical uncertainty around $\rho_{KL} = 80\%$.

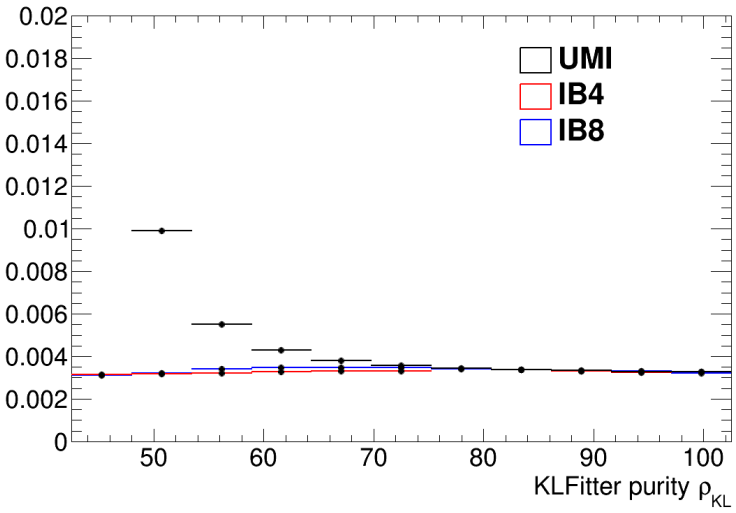

Figure 11.4: The statistical uncertainty on A^{os} as measured in the nominal $t\bar{t}$ MC scaled to an integrated luminosity of 20.3 fb^{-1}, when using the UMI, IB4 and IB8 unfolding techniques. The uncertainty is found as a function of the KLFitter purityρ_{KL}. All three unfolding techniques converge in statistical uncertainty around $\rho_{KL} = 80\%$.

I'm so proud of you

Mum

Chapter 12

Results

Following from the definition and optimisation of the analysis in the previous sections, the results of this measurement are presented in this section.

12.1 Measurement of $t\bar{t}$ cross-section

To demonstrate good understanding of the signal process and relevant backgrounds it is informative to report the $t\bar{t}$ cross-section determined using the events in this analysis. This is an inclusive cross-section as measured using the b-tagged event selection and built from Equation 12.1,

$$\sigma_{t\bar{t}} = \frac{N_{\text{data}} - N_{\text{bkg}}}{\int L\mathrm{d}t \times \varepsilon \times BR}, \tag{12.1}$$

where N_{data} is the measured data yield, N_{bkg} is the predicted background yield, $BR = 0.543$ is the branching ratio for the single-lepton and dilepton channels derived using the $W \to \ell\nu$ branching ratio $BR(W \to \ell\nu) = 0.108$ per flavour (e, μ, τ) [41]. The signal efficiency ε also relates only to the single-lepton and dilepton channels as the acceptance for the $t\bar{t}$ fully hadronic channel is negligible. The signal efficiencies are observed to be

$$\varepsilon_{t\bar{t}}^{e+\text{jets}} = 0.0109 \pm 0.0011, \tag{12.2}$$

$$\varepsilon_{t\bar{t}}^{\mu+\text{jets}} = 0.0124 \pm 0.0010, \tag{12.3}$$

$$\varepsilon_{t\bar{t}} = 0.0232 \pm 0.0020. \tag{12.4}$$

where the uncertainties include both statistical and systematic components. The cross-section is measured in the e+jets and μ+jets channels separately as well as in the combined selection. The results are shown in Equations 12.5- 12.7 and the full breakdown of uncertainties is shown in Table 12.1 [92].

$$\sigma_{t\bar{t}}^{e+Jets} = 247.6 \pm 1.6\,(\text{Stat.})^{+26.9}_{-26.6}\,(\text{Syst.}) \pm 4.6\,(\text{Lumi.}) \pm 4.3\,(\text{Beam})\,\text{pb} \tag{12.5}$$

$$\sigma_{t\bar{t}}^{\mu+Jets} = 251.4 \pm 1.5\,(\text{Stat.})^{+21.6}_{-21.1}\,(\text{Syst.}) \pm 4.7\,(\text{Lumi.}) \pm 4.3\,(\text{Beam})\,\text{pb} \tag{12.6}$$

$$\sigma_{t\bar{t}} = 249.6 \pm 1.1\,(\text{Stat.})^{+23.5}_{-23.1}\,(\text{Syst.}) \pm 4.7\,(\text{Lumi.}) \pm 4.3\,(\text{Beam})\,\text{pb} \tag{12.7}$$

The uncertainty related to the beam energy at the LHC is 1.7% [98], and the uncertainty related to the integrated luminosity is 1.9% [97].

The cross-sections are found to be in good agreement with both the 8 TeV theoretical prediction and the most recent results from the ATLAS and CMS experiments, as shown in Table 12.2. The result agrees within one standard deviation with the existing ATLAS ℓ+jets channel measurement, and benefits from an improved luminosity estimation (due to time spent by ATLAS improving the understanding of the luminosity between the measurements), the events used for the two analyses are highly correlated, although updates to detector calibrations and MC simulations may have occurred in between. However this measurement is not competitive with the ATLAS and CMS dilepton results. The dilepton channel has much smaller statistics, and therefore an overall increase in the statistical uncertainty, however it also has minimal background contamination and less jet modelling required, so the overall systematic uncertainties are reduced. The exception to this is the dilepton channel with τ-leptons, where the τs may decay leptonically or hadronically. The dominant systematics on the cross-section are found to be the jet energy scale (JES), the MV1 b-tagging fake rate, the hadron-to-muon branching ratio uncertainties and the MC modelling.

	e+jets	μ+jets	ℓ+jets
$\sigma_{t\bar{t}}$ [pb]	248.0	251.4	249.6
Statistical uncertainty in %	$\pm$0.6	$\pm$0.6	$\pm$0.4
Sources of experimental uncertainty in %			
Lepton charge misidentification	+0.0 −0.0	+0.0 −0.0	+0.0 −0.0
Lepton energy resolution	+1.1 −1.0	+1.0 −1.0	+1.0 −1.0
Lepton trigger, reco, identification	+2.8 −2.6	+2.1 −2.0	+2.1 −2.0
Jet energy scale	+5.2 −5.2	+4.7 −4.6	+5.0 −4.8
Jet energy resolution	+0.1 −0.1	+0.3 −0.3	+0.1 −0.1
Jet reco efficiency	+0.1 −0.1	+0.1 −0.1	+0.1 −0.1
Jet vertex fraction	+1.0 −1.0	+1.0 −1.0	+1.0 −1.0
Fake lepton estimate	+4.7 −4.7	+1.0 −1.0	+2.7 −2.7
Background normalisation	+0.2 −0.2	+0.1 −0.1	+0.2 −0.2
W+jets estimate (statistical)	+0.0 −0.0	+0.0 −0.0	+0.0 −0.0
Single-top production asymmetry	+0.1 −0.0	+0.1 −0.0	+0.1 −0.0
b-tagging efficiency	+2.2 −2.1	+2.2 −2.1	+2.2 −2.1
c-jet mistag rate	+0.4 −0.4	+0.4 −0.4	+0.4 −0.4
Light-jet mistag rate	+0.1 −0.1	+0.1 −0.1	+0.1 −0.1
SMT reco identification	+1.6 −1.5	+1.5 −1.5	+1.5 −1.5
SMT momentum imbalance	+1.0 −1.0	+1.0 −1.0	+1.0 −1.0
SMT light-jet mistag rate	+0.4 −0.5	+0.4 −0.5	+0.4 −0.5
Sources of modelling uncertainty in %			
Hadron-to-muon branching ratio	+2.8 −2.6	+2.8 −2.5	+2.8 −2.6
b-hadron production fractions	+0.4 −0.3	+0.4 −0.4	+0.4 −0.4
Additional radiation	$\pm$5.3	$\pm$3.9	$\pm$4.5
MC generator	$\pm$3.0	$\pm$3.1	$\pm$3.0
Parton shower	$\pm$2.1	$\pm$1.7	$\pm$1.9
Parton distribution function	$\pm$1.1	$\pm$0.8	$\pm$0.9
Total experimental uncertainty	+8.3 −8.1	+6.2 −6.0	+6.9 −6.7
Total modelling uncertainty	+7.1 −7.0	+6.0 −5.9	+6.5 −6.4
Total systematic uncertainty	+11 −11	+8.6 −8.4	+9.4 −9.3
Luminosity uncertainty	$\pm$1.9	$\pm$1.9	$\pm$1.9
LHC beam energy	$\pm$1.7	$\pm$1.7	$\pm$1.7

Table 12.1: Measurements of $\sigma_{t\bar{t}}$ for the e+jets, μ+jets and combined ℓ+jets channels, with systematic uncertainties in percentage.

12.2 Measurement of charge asymmetries

The measurement of the charge asymmetries (CA) is performed as described in the previous sections. The observed charge asymmetries are found to be compatible with zero, and with good MC to data agreement. The results are given in Equations 12.8 and 12.9 with the full breakdown of uncertainties shown in Table 12.3. Figure 12.1 and 12.2 show the same-top-like (ST) and

This measurement	$\sigma_{t\bar{t}} = 249.6 \pm 1.1\,(\text{Stat.})^{+23.5}_{-23.1}\,(\text{Syst.}) \pm 4.7\,(\text{Lumi.}) \pm 4.3\,(\text{Beam})\,\text{pb}$
Theoretical prediction [39]	$\sigma_{t\bar{t}} = 252.0 \pm 11.7^{+6.4}_{-8.6}\text{pb}$
ATLAS di-lepton $e\mu$ [113]	$\sigma_{t\bar{t}} = 242.4 \pm 1.7\,(\text{Stat.}) \pm 5.5\,(\text{Syst.}) \pm 7.5\,(\text{Lumi.}) \pm 4.2\,(\text{Beam})\,\text{pb}$
ATLAS ℓ+Jets [114]	$\sigma_{t\bar{t}} = 260 \pm 1\,(\text{Stat.})^{+22}_{-23}\,(\text{Syst.}) \pm 8\,(\text{Lumi.}) \pm 4\,(\text{Beam})\,\text{pb}$
CMS di-lepton ee, $\mu\mu$, $e\mu$ [115]	$\sigma_{t\bar{t}} = 239 \pm 2\,(\text{Stat.}) \pm 11\,(\text{Syst.}) \pm 6\,(\text{Lumi.})\,\text{pb}$
CMS di-lepton $e\tau$, $\mu\tau$ [116]	$\sigma_{t\bar{t}} = 257 \pm 3\,(\text{Stat.}) \pm 24\,(\text{Syst.}) \pm 7\,(\text{Lumi.})\,\text{pb}$
CMS all hadronic [117]	$\sigma_{t\bar{t}} = 275.6 \pm 6.1\,(\text{Stat.}) \pm 37.8\,(\text{Syst.}) \pm 7.2\,(\text{Lumi.})\,\text{pb}$

Table 12.2: Summary of all $\sqrt{s} = 8$ TeV $\sigma_{t\bar{t}}$ measurements and the theoretical prediction.

different-top-like (DT) CA distributions, as determined by the KLFitter, prior to background subtraction and unfolding. The uncertainties shown represent the quadratic combination of the statistical and systematic components.

$$A^{\text{ss}} = -0.007 \;\; \pm 0.006 \;\; (\text{stat.})\, ^{+0.002}_{-0.002}\; (\text{expt.}) \pm 0.005 \;\; (\text{model})\,, \tag{12.8}$$

$$A^{\text{os}} = \quad 0.0041 \pm 0.0035\,(\text{stat.})\, ^{+0.0013}_{-0.0011}\,(\text{expt.}) \pm 0.0027\,(\text{model})\,. \tag{12.9}$$

where the total statistical and systematic correlations between A^{ss} and A^{os} are estimated to be $\rho_{\text{ss,os}} = -1.0$. This estimation was derived using poisson smearing of the MC sample to produce MC toys as discussed in Section 11.8.3, and calculating the correlation via the normal equations,

$$\rho_{\text{ss,os}} = \frac{\Sigma_i \left(A_i^{ss} - A^{\bar{ss}}\right)\left(A_i^{os} - A^{\bar{os}}\right)}{\sigma_{ss}\sigma_{os}}, \tag{12.10}$$

where $A_i^{ss,os}$ are the MC toy measurements, $A^{s\bar{s},os}$ are the means of the toy distributions, and $\sigma_{ss,os}$ are the uncertainties. A strong correlation between A^{ss} and A^{os} is expected, as shown in Equations 4.9, they are both built from the same four numbers, N^{++}, N^{--}, N^{+-}, N^{-+}.

The majority of systematic shifts are small as they alter the yields in the four charge bins in similar ways, such that their effects are cancelled out when applied to the ratio structure in the CA calculations. The largest systematic uncertainties are those which adversely affect the structure of the response matrix. The additional radiation is found to be the dominant systematic uncertainty. An increase in the number of additional radiation jets (IFSR) results in poorer performance of the KLFitter, moreso than any other systematic uncertainty (equivalently, a decrease in the number of additional radiation jets results in a better performance of the KLFitter).

	$A^{ss}\,(10^{-2})$		$A^{os}\,(10^{-2})$	
Measured value	-0.7		0.41	
Statistical uncertainty	± 0.6		± 0.35	
Sources of experimental uncertainty				
Lepton charge misidentification	+0.002	−0.002	+0.001	−0.001
Lepton energy resolution	+0.09	−0.11	+0.07	−0.06
Lepton trigger, reco, identification	+0.004	−0.004	+0.002	−0.002
Jet energy scale	+0.10	−0.14	+0.08	−0.06
Jet energy resolution	+0.019	−0.019	+0.009	−0.009
Jet reco efficiency	+0.010	−0.010	+0.006	−0.006
Jet vertex fraction	+0.09	−0.09	+0.05	−0.05
Fake lepton estimate	+0.05	−0.05	+0.025	−0.025
Background normalisation	+0.002	−0.002	+0.001	−0.001
W+jets estimate (statistical)	+0.003	−0.002	+0.001	−0.002
Single-top production asymmetry	+0.016	−0.002	+0.001	−0.009
b-tagging efficiency	+0.008	−0.008	+0.004	−0.004
c-jet mistag rate	+0.020	−0.020	+0.013	−0.013
Light-jet mistag rate	+0.022	−0.023	+0.013	−0.012
SMT reco identification	+0.004	−0.004	+0.004	−0.004
SMT momentum imbalance	+0.06	−0.06	+0.04	−0.035
SMT light-jet mistag rate	+0.010	−0.009	+0.005	−0.005
Sources of modelling uncertainty				
Hadron-to-muon branching ratio	+0.04	−0.05	+0.026	−0.022
b-hadron production	+0.013	−0.008	+0.003	−0.008
Additional radiation	± 0.4		± 0.23	
MC generator	± 0.05		± 0.025	
Parton shower	± 0.04		± 0.017	
Parton distribution function	± 0.22		± 0.13	
Total experimental uncertainty	+0.19	−0.22	+0.13	−0.11
Total modelling uncertainty	+0.5	−0.5	+0.27	−0.27
Total systematic uncertainty	+0.5	−0.5	+0.30	−0.29

Table 12.3: Measurements A^{ss} and A^{os}, in units of 10^{-2}, and breakdown of absolute uncertainties.

This generates a response matrices which vary from the nominal by a greater degree than other systematics. Additionally, due to the random nature of IFSR, the performance on each true charge-pair bin varies in a non-uniform way which generates additional variations in the charge asymmetries. Table 12.4 shows the diagonal components of the response matrices generated by the nominal MC, the increased IFSR MC, the decreased IFSR MC, two JES systematic MC samples, and MC samples with the SMT momentum imbalance scale factor shifted up and down by its uncertainty. In brackets are the raw differences between the nominal values and the shifted values in each bin. The largest shift in each bin, which is a measure of the KLFitter performance,

is caused by the changes in the IFSR. For comparison with the results in Table 12.3, the values in Table 12.5 shows the total systematic uncertainties as converted into an uncertainty on the response matrix (shown to three decimal places). The first row shows the central values of the diagonal with a full combination of the systematic uncertainties from all sources, each subsequent row shows the individual contributions of the systematic uncertainties from the IFSR, JES and SMT systematics. The relative magnitude of these uncertainties is coherent with the relative systematics in Table 12.3. The MC statistical uncertainty on the central values is ~ 0.001.

Sample	$++$	$--$	$+-$	$-+$
Nominal	0.795	0.793	0.786	0.786
Additional radiation 'up'	0.787 (0.008)	0.786 (0.007)	0.777 (0.009)	0.778 (0.008)
Additional radiation 'down'	0.803 (0.008)	0.800 (0.007)	0.789 (0.003)	0.788 (0.002)
JesEffectiveDet1˙Up	0.796 ($\sim 10^{-3}$)	0.793 ($\sim 10^{-4}$)	0.786 ($\sim 10^{-4}$)	0.787 ($\sim 10^{-3}$)
JesEffectiveDet1˙Down	0.795 ($\sim 10^{-4}$)	0.792 ($\sim 10^{-3}$)	0.786 ($\sim 10^{-4}$)	0.787 ($\sim 10^{-3}$)
SMT 'up'	0.795 ($\sim 10^{-5}$)	0.793 ($\sim 10^{-5}$)	0.786 ($\sim 10^{-5}$)	0.786 ($\sim 10^{-5}$)
SMT 'down'	0.795 ($\sim 10^{-5}$)	0.793 ($\sim 10^{-5}$)	0.786 ($\sim 10^{-5}$)	0.786 ($\sim 10^{-5}$)

Table 12.4: The diagonal components of response matrices generated by the nominal and systematically altered MC samples. The numbers in brackets are the raw differences between the nominal values and the systematic values in each bin.

Sample	$++$	$--$	$+-$	$-+$
Nominal	$0.795^{0.013}_{0.013}$	$0.793^{0.010}_{0.011}$	$0.786^{0.010}_{0.011}$	$0.786^{0.008}_{0.008}$
Additional radiation	± 0.008	± 0.007	± 0.008	± 0.006
JES	± 0.004	± 0.003	± 0.002	± 0.003
SMT	± 0.000	± 0.000	± 0.000	± 0.000

Table 12.5: The diagonal components of the nominal response matrix with a measure of the total systematic uncertainty. The subsequent rows show the contributions (to be added in quadrature across all systematics) of individual systematic uncertainties. The largest uncertainties on the response matrix (the largest modifiers to the KLFitter performance) align with the largest uncertainties on the measured charge and CP asymmetries.

This measurement is therefore currently statistically limited. Future analyses with larger statistics would focus on the reduction of the systematic uncertainties, this is discussed further in Section 13.1.

For comparison, the CA are also calculated using the nominal MC sample using the same procedure as applied to the data. This gives a measure of the CAs as they are implemented in the nominal MC model with a small uncertainty owing to the large MC statistics. The MC results are found to be compatible with zero and in good agreement with the data and are shown in Equations 12.11 and 12.12, with the MC statistical uncertainty.

$$A_{\text{sim}}^{\text{ss}} = \quad 0.0005 \pm 0.0016\,(\text{MCstat.}) \tag{12.11}$$

$$A_{\text{sim}}^{\text{os}} = -0.0003 \pm 0.0009\,(\text{MCstat.}) \tag{12.12}$$

12.3 Measurement of CP asymmetries

As described in Section 4, the charge asymmetries are linear combinations of CP asymmetries (CPA) shown in Equations 12.13 and 12.14.

$$A^{\text{ss}} = r_b A_{\text{mix}}^{b\ell} + r_c \left(A_{\text{dir}}^{bc} - A_{\text{dir}}^{c\ell} \right) + r_{c\bar{c}} \left(A_{\text{mix}}^{bc} - A_{\text{dir}}^{c\ell} \right) \tag{12.13}$$

$$A^{\text{os}} = \widetilde{r}_b A_{\text{dir}}^{b\ell} + \widetilde{r}_c \left(A_{\text{mix}}^{bc} + A_{\text{dir}}^{c\ell} \right) + \widetilde{r}_{c\bar{c}} A_{\text{dir}}^{c\ell} \tag{12.14}$$

where the decay chain fractions represent the relative contributions from each decay channel in Equations 4.1-4.6.

12.3.1 Decay chain fractions

The decay chain fractions (DCF) are measured in MC at the particle level, with definitions given in Equations 12.15-12.17, where each N refers to the number of events to follow the decay chains previousyl described in Equations 4.1-4.6. The DCFs obtained are shown with their modelling systematic uncertainties in Table 12.6. In all cases the systematics are dominated by the parton shower and hadron-to-muon branching ratio uncertainties. The parton shower modelling controls the probability for any particular decay to propagate via a $b \to c$ transition or to include b-meson mixing, and the hadron-to-muon branching ratio uncertainty controls the probability for each b- or c-quark to produce a soft muon. Variations of each will alter the

relative fractions of each decay chain of interest.

$$r_b = \frac{N_{r_b}}{N_{r_b}+N_{r_c}+N_{r_{c\bar{c}}}}, \qquad \widetilde{r}_b = \frac{N_{\widetilde{r}_b}}{N_{\widetilde{r}_b}+N_{\widetilde{r}_c}+N_{\widetilde{r}_{c\bar{c}}}}, \tag{12.15}$$

$$r_c = \frac{N_{r_c}}{N_{r_b}+N_{r_c}+N_{r_{c\bar{c}}}}, \qquad \widetilde{r}_c = \frac{N_{\widetilde{r}_c}}{N_{\widetilde{r}_b}+N_{\widetilde{r}_c}+N_{\widetilde{r}_{c\bar{c}}}}, \tag{12.16}$$

$$r_{c\bar{c}} = \frac{N_{r_{c\bar{c}}}}{N_{r_b}+N_{r_c}+N_{r_{c\bar{c}}}}, \qquad \widetilde{r}_{c\bar{c}} = \frac{N_{\widetilde{r}_{c\bar{c}}}}{N_{\widetilde{r}_b}+N_{\widetilde{r}_c}+N_{\widetilde{r}_{c\bar{c}}}}. \tag{12.17}$$

	r_b	r_c	$r_{c\bar{c}}$	$\widetilde{r}_b$	$\widetilde{r}_c$	$\widetilde{r}_{c\bar{c}}$
Nominal	0.200	0.715	0.085	0.882	0.069	0.048
Relative uncertainty in %						
Hadron-to-muon branching ratio	+3.8 −3.2	+2.9 −2.3	+23 −30	+1.6 −1.3	+3.3 −3.3	+25 −31
b-hadron production	+1.8 −1.8	+0.5 −0.5	+0.3 −0.3	+0.2 −0.2	+1.9 −1.9	+0.2 −0.2
Additional radiation	±2.4	±0.6	±0.4	±0.1	±0.9	±1.1
MC generator	±0.2	±0.1	±0.1	±0.1	±0.5	±0.7
Parton shower	±6.8	±2.2	±2.6	±0.6	±12	±6.1
Parton distribution function	±0.1	±0.1	±0.9	±0.0	±0.3	±0.2
Total uncertainty	+8.4 −8.1	+3.7 −3.3	+23 −30	+1.7 −1.4	+13 −13	+25 −31

Table 12.6: Decay-chain fractions obtained from MC simulation at the particle level. Uncertainties are in percent.

12.3.2 CP asymmetry extraction

Attempting to extract four CPAs from two CA measurements is non-trivial, the system is under-constrained and this results in extremely large uncertainties on all parameters as many combinations of CPAs may recreate the same CA values. Since a linear combination of CPAs may cancel each other out, each can potentially vary from -100% to $+100\%$ and still produce CAs near to 0%. In order to tighten the uncertainties on the measured CPAs it is necessary to implement further constraints. The SM predictions (see Table 12.8) for each CA and CP parameter are small and compatible with zero. It is therefore justified to produce an upper limit on each CPA individually by considering each one to be solely responsible for the measured CAs in turn, and setting all other CPAs to zero. This technique [50] leads to a fully constrained system, and removes the requirement to perform a fit, as it is now possible to produce a one-to-one relationship between the CAs and CPAs (including the DCFs) as shown in Equations 12.18-12.21 (for parameters which appear in both A^{ss} and A^{os}, the result with the smallest uncertainty is taken). Furthermore

as suggested in [50, 118, 119], in the case of no direct CP violation, $A^{b\ell}_{mix} = A^{bc}_{mix}$ (comparing Equations 4.15-4.19, if direct CP violation in $b \to \mu$ and $b \to c$ decays is disallowed, $A^{b\ell}_{mix}$ and A^{bc}_{mix} are only sensitive to $b \to \bar{b}$ mixing). The mixing asymmetry from hereon is referred to as simply A^{b}_{mix}. The full breakdown of uncertainties is shown in Table 12.7.

$$A^{b}_{\text{mix}} = \frac{A^{\text{ss}}}{r_b + r_{c\bar{c}}} = -0.025 \pm 0.021\,(\text{stat.}) \pm 0.008\,(\text{expt.}) \pm 0.017\,(\text{model}) \tag{12.18}$$

$$A^{b\ell}_{\text{dir}} = \frac{A^{\text{os}}}{\widetilde{r_b}} = 0.005 \pm 0.004\,(\text{stat.}) \pm 0.001\,(\text{expt.}) \pm 0.003\,(\text{model}) \tag{12.19}$$

$$A^{c\ell}_{\text{dir}} = \frac{-A^{\text{ss}}}{r_c + r_{c\bar{c}}} = 0.009 \pm 0.007\,(\text{stat.}) \pm 0.003\,(\text{expt.}) \pm 0.006\,(\text{model}) \tag{12.20}$$

$$A^{bc}_{\text{dir}} = \frac{A^{\text{ss}}}{r_c} = -0.010 \pm 0.008\,(\text{stat.}) \pm 0.003\,(\text{expt.}) \pm 0.007\,(\text{model}) \tag{12.21}$$

This measurement is therefore currently statistically limited. Future analyses with larger statistics would focus on the reduction of the systematic uncertainties, this is discussed further in Section 13.1.

For comparison, the CPAs are also calculated using the nominal MC sample using the same procedure as applied to the data. This gives a measure of the CPAs as they are implemented in the nominal MC model with a small uncertainty owing to the large MC statistics. The MC results are found to be compatible with zero and in good agreement with the data and are shown in Equations 12.22 and 12.25, with the MC statistical uncertainty shown.

$$A^{b}_{\text{mix,sim}} = 0.002 \pm 0.005\,(\text{MCstat.}) \tag{12.22}$$

$$A^{b\ell}_{\text{dir,sim}} = 0.000 \pm 0.001\,(\text{MCstat.}) \tag{12.23}$$

$$A^{c\ell}_{\text{dir,sim}} = -0.0006 \pm 0.0019\,(\text{MCstat.}) \tag{12.24}$$

$$A^{bc}_{\text{dir,sim}} = 0.0007 \pm 0.0022\,(\text{MCstat.}) \tag{12.25}$$

12.4 Interpretation of results

Table 12.8 shows all of the results from this analysis, in the context of the existing limits from other experiments and the expectations of the SM. The latter two columns represent upper limits

Measured value	$A^b_{\rm mix}\,(10^{-2})$ -2.5		$A^{b\ell}_{\rm dir}\,(10^{-2})$ 0.5		$A^{c\ell}_{\rm dir}\,(10^{-2})$ 0.9		$A^{bc}_{\rm dir}\,(10^{-2})$ -1.0	
Statistical uncertainty	$\pm$ 2.1		$\pm$ 0.4		$\pm$ 0.7		$\pm$ 0.8	
Sources of experimental uncertainty								
Lepton charge misidentification	+0.008	−0.007	+0.001	−0.002	+0.002	−0.003	+0.003	−0.003
Lepton energy resolution	+0.33	−0.39	+0.07	−0.06	+0.14	−0.12	+0.13	−0.15
Lepton trigger, reco, identification	+0.016	−0.015	+0.003	−0.003	+0.005	−0.006	+0.006	−0.006
Jet energy scale	+0.4	−0.5	+0.09	−0.07	+0.17	−0.13	+0.15	−0.19
Jet energy resolution	+0.07	−0.07	+0.011	−0.011	+0.024	−0.024	+0.027	−0.027
Jet reco efficiency	+0.034	−0.034	+0.006	−0.006	+0.012	−0.012	+0.014	−0.014
Jet vertex fraction	+0.33	−0.33	+0.06	−0.06	+0.12	−0.12	+0.13	−0.13
Fake lepton estimate	+0.18	−0.19	+0.029	−0.029	+0.07	−0.07	+0.07	−0.08
Background normalisation	+0.008	−0.009	+0.001	−0.001	+0.003	−0.003	+0.003	−0.003
W+jets estimate (statistical)	+0.009	−0.008	+0.002	−0.002	+0.003	−0.003	+0.004	−0.003
Single-top production asymmetry	+0.06	−0.01	+0.002	−0.011	+0.002	−0.020	+0.022	−0.003
b-tagging efficiency	+0.028	−0.028	+0.005	−0.005	+0.010	−0.010	+0.011	−0.011
c-jet mistag rate	+0.07	−0.07	+0.015	−0.015	+0.025	−0.026	+0.029	−0.027
Light-jet mistag rate	+0.08	−0.08	+0.014	−0.014	+0.028	−0.028	+0.031	−0.032
SMT reco identification	+0.013	−0.012	+0.004	−0.004	+0.004	−0.005	+0.005	−0.005
SMT momentum imbalance	+0.21	−0.22	+0.04	−0.04	+0.08	−0.08	+0.09	−0.09
SMT light-jet mistag rate	+0.035	−0.031	+0.005	−0.006	+0.011	−0.012	+0.014	−0.012
Sources of modelling uncertainty								
Hadron-to-muon branching ratio	+0.25	−0.36	+0.023	−0.020	+0.06	−0.05	+0.04	−0.04
b-hadron production fractions	+0.031	−0.021	+0.004	−0.010	+0.013	−0.020	+0.022	−0.015
Additional radiation	$\pm$1.4		$\pm$0.26		$\pm$0.6		$\pm$0.6	
MC generator	$\pm$0.17		$\pm$0.029		$\pm$0.07		$\pm$0.08	
Parton shower	$\pm$0.08		$\pm$0.021		$\pm$0.06		$\pm$0.07	
Parton distribution function	$\pm$0.8		$\pm$0.15		$\pm$0.29		$\pm$0.32	
Total experimental uncertainty	+0.7	−0.8	+0.14	−0.12	+0.27	−0.24	+0.27	−0.31
Total modelling uncertainty	+1.6	−1.7	+0.30	−0.30	+0.6	−0.6	+0.7	−0.7
Total systematic uncertainty	+1.8	−1.8	+0.34	−0.33	+0.7	−0.6	+0.7	−0.7

Table 12.7: Measurements of $A^b_{\rm mix}$, $A^{b\ell}_{\rm dir}$, $A^{c\ell}_{\rm dir}$ and $A^{bc}_{\rm dir}$, in units of 10^{-2}, and breakdown of absolute uncertainties.

on the absolute values $|A|$. The existing experimental limits are derived from measurements in exclusive channels which are extrapolated to inclusive estimations by considering uncertainties on relevant branching ratios (each CPA prediction makes no assumption on the value of any other CPA). For $A^b_{\rm mix}$ the last two columns are determined using the prescription from [50], with inputs from the HFAG world average high-energy $f_{d,s}$ [89] and either the world average [89] or the SM predictions [120] for $a^d_{\rm sl}$ and $a^s_{\rm sl}$ respectively (where $a^{d,s}_{\rm sl}$ are the flavour-specific CP asymmetries, and $f_{d,s}$ are the fragmentation functions of $B^0_{d,s}$, as discussed in Section 4.2). The observations are compatible with the SM. This analysis is found to provide an equivalent limit to the existing limit on $A^{b\ell}_{dir}$, a stronger limit on $A^{c\ell}_{dir}$, and the first limits on A^{bc}_{dir}, A^{ss} and A^{os}.

	Data (10^{-2})		MC (10^{-2})		Existing limits (2σ) (10^{-2})		SM prediction (10^{-2})	
$A^{\rm ss}$	-0.7	$\pm\,0.8$	0.05	$\pm\,0.23$	-		$< 10^{-2}$	[50]
$A^{\rm os}$	0.4	$\pm\,0.5$	-0.03	$\pm\,0.13$	-		$< 10^{-2}$	[50]
$A^{b}_{\rm mix}$	-2.5	$\pm\,2.8$	0.2	$\pm\,0.7$	< 0.1	[89]	$< 10^{-3}$	[89] [120]
$A^{b\ell}_{\rm dir}$	0.5	$\pm\,0.5$	-0.03	$\pm\,0.14$	< 1.2	[121]	$< 10^{-5}$	[50] [121]
$A^{c\ell}_{\rm dir}$	1.0	$\pm\,1.0$	-0.06	$\pm\,0.25$	< 6.0	[121]	$< 10^{-9}$	[50] [121]
$A^{bc}_{\rm dir}$	-1.0	$\pm\,1.1$	0.07	$\pm\,0.29$	-		$< 10^{-7}$	[122]

Table 12.8: Comparison of measurements of charge asymmetries and constraints on CP asymmetries, with MC simulation (detailed in the text), existing experimental limits and SM predictions.

12.4.1 The D0 anomalous dimuon asymmetry

As discussed in Section 4, an inclusive like-sign dimuon charged asymmetry measurement was reported by the D0 experiment [46], which observed an excess of approximately 3σ from the SM. The asymmetry may be interpreted as the result of either mixing or direct CP asymmetries. It is calculated that to account for the D0 result in terms of mixing CP violation it would be required that $A^{b}_{\rm mix} \approx -0.008 \pm 0.003$ [46]. To account for the D0 result in terms of direct CP violation it would be required that $A^{b\ell}_{\rm dir} \approx (0.003 \pm 0.001)$ or $A^{c\ell}_{\rm dir} \approx (0.009 \pm 0.003)$ [52] (no equivalent calculation has been performed for $A^{bc}_{\rm dir}$). The observed CPAs are compatible with both the SM and with the D0 results within 1σ.

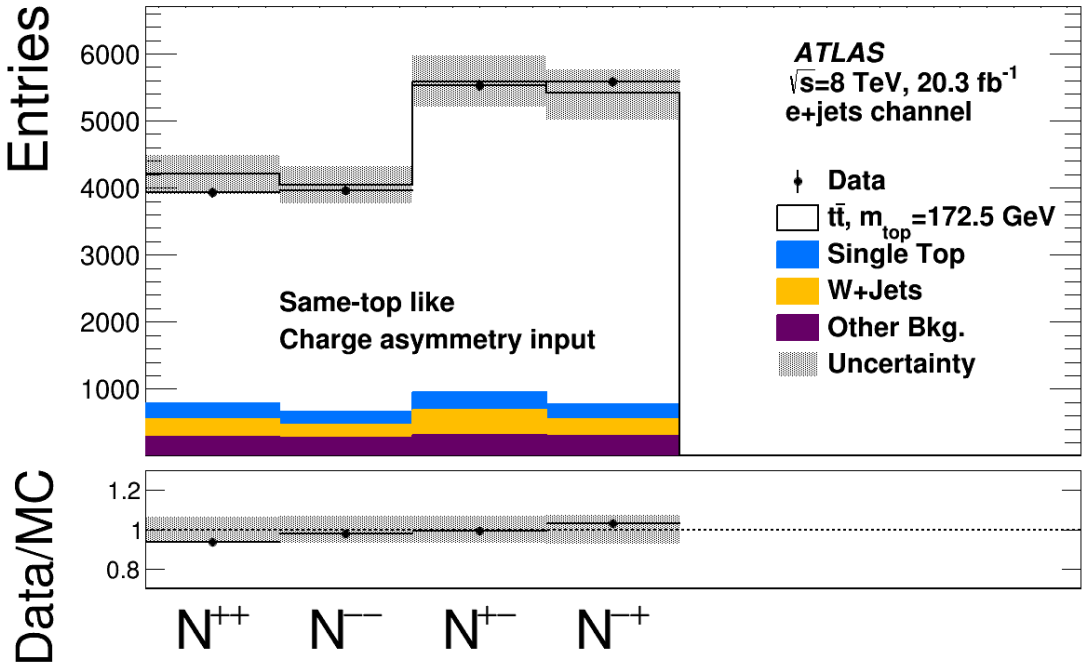

(a) *e*+jets channel.

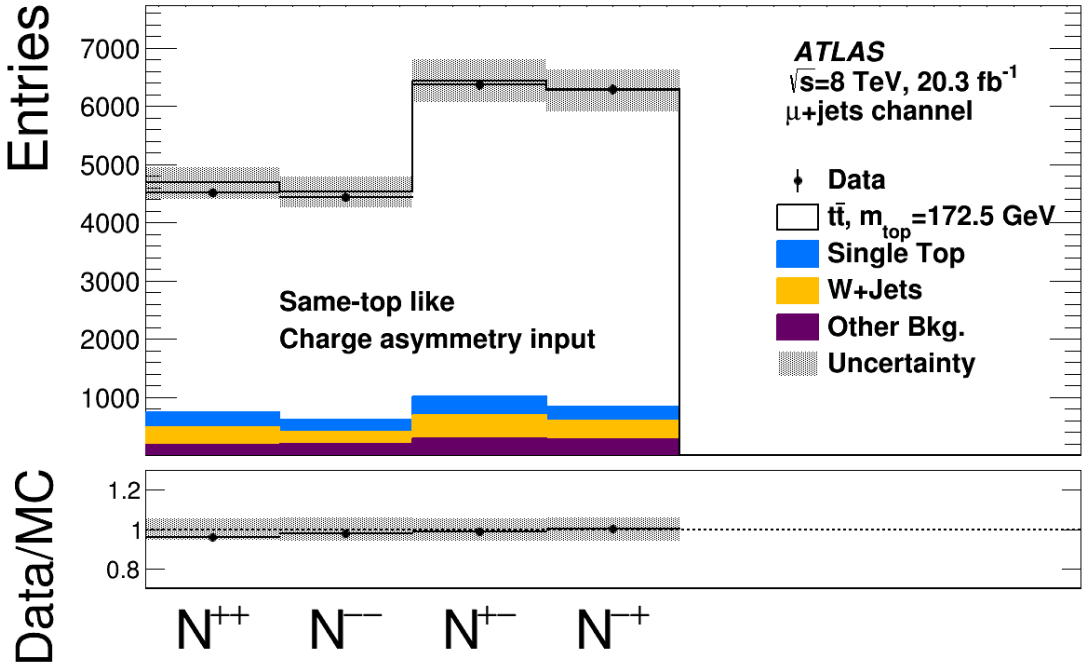

(b) μ+jets channel.

Figure 12.1: Same-top-like charge-pairings distributions. The hashed area represents all experimental systematic uncertainties as well as the *b*-hadron production and hadron-to-muon branching ratio uncertainties. The lower panel of the distributions show the ratio of the data divided by the simulation. (a) shows the *e*+jets channel while (b) shows the μ+ jets channel.

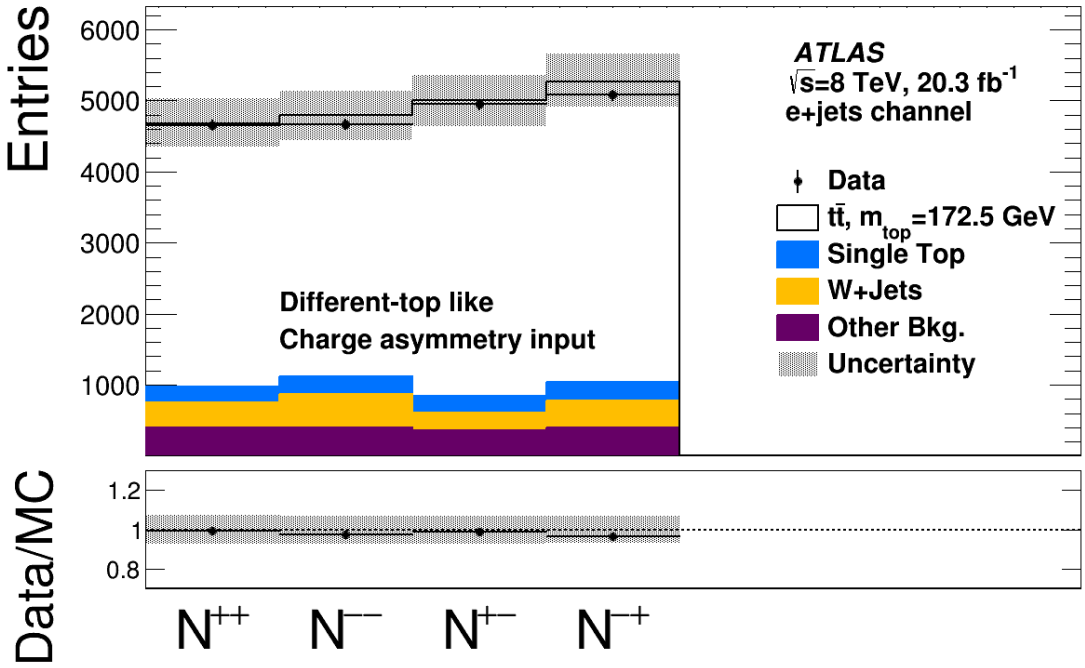

(a) *e*+jets channel.

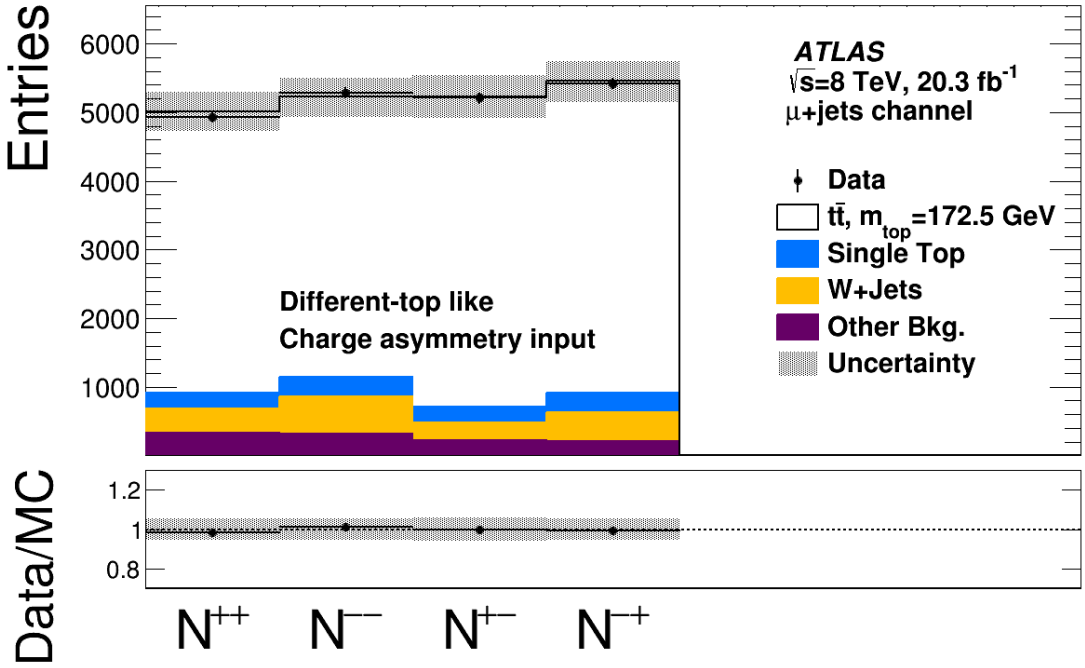

(b) μ+jets channel.

Figure 12.2: Different-top-like charge-pairings distributions. The hashed area represents all experimental systematic uncertainties as well as the *b*-hadron production and hadron-to-muon branching ratio uncertainties. The lower panel of the distributions show the ratio of the data divided by the simulation. (a) shows the *e*+jets channel while (b) shows the μ+jets channel.

You're my best friend

Dad

Chapter 13

Conclusions

A study of CP violation in inclusive b- and c-hadron is performed in the $t\bar{t}$ ℓ+jets decay channel using collisions recorded by the ATLAS detector at the LHC, amounting to 20.3 fb^{-1} of Run 1 data at a centre-of-mass energy of $\sqrt{s} = 8$ TeV. Same- and opposite-sign charge asymmetries are measured, each built from the pairing of a lepton from the W-boson in the top-quark decay and a soft muon from the semileptonic decay of a b- or c-hadron.

Soft muons are identified by the ATLAS Soft Muon Tagger (SMT), which is calibrated using $J/\psi \to \mu\mu$ and $Z \to \mu\mu$ events. The SMT tagger uses the fractional difference in absolute momentum, the Momentum Imbalance (MI), between a track measured in the Inner Detector (ID) and Muon Spectrometer (MS) (extrapolated back to the primary vertex) in order to differentiate between true soft muons from heavy-flavour decays and fakes. The calibration takes the form of a tag and probe analysis, and the efficiency is measured as a function of muon transverse momentum and angular position. It is also studied as a function of the isolation of the muon, to determine that the calibration performed on isolated muons from J/ψ and Z decays may be utilised in a jet environment for $t\bar{t}$ decays.

Background estimates are taken from MC for the Z+jets, diboson and single-top backgrounds, whilst data-driven methods ware utilised to estimate the multijet and W+jets backgrounds. Contributions from $t\bar{t}$ fakes (such as soft muons from $c \to \mu$ decays and pile-up) are reduced and the signal purity is maximised by combining the SMT tagger with a multivariate (MV1) tagger at the 80% efficiency working point. A measurement of the $t\bar{t}$ ℓ+jets cross-section is performed and found to be in agreement with other experimental results and the Standard Model expectation.

A kinematic likelihood fitting algorithm is optimised and used to resolve the ambiguity related to the source of the leptons from the W-boson and the soft muon (whether they are the result of the same- or different-top-quark decays) with a purity of $\rho_{\mathrm{KL}} = 79 \pm 1\%$. The Kinematic Likelihood Fitter (KLFitter) performance is studied when altering many parameters, the final optimisation for which may be found in Table 10.55.

Unfolding to correct for the KLFitter event misidentification is performed using an unregularised matrix inversion to determine the charge asymmetries in a well-defined fiducial volume. Unregularised matrix inversion is chosen to avoid the introduction of bias from regularised methods. At the $\rho_{\mathrm{KL}} = 79 \pm 1\%$ working point, the statistical uncertainty on the final results yielded by the regularised and unregularised methods are comparable.

Decay chain fractions are taken from MC, and used to extract four CP asymmetries (CPAs). Each CPA is extracted from the CAs individually, using the assumption that all other CPAs are negligible in turn. This is justified using the SM expectations for each CPA shown in Table 12.8.

This is the first measurement of the inclusive charge asymmetries presented, and the results reported are compatible with zero and with the Standard Model. The analysis also sets the first limits on A_{dir}^{bc}, and reports an equivalent value to the existing limit on $A_{dir}^{b\ell}$, a stronger limit on $A_{dir}^{c\ell}$, and the first limits on A_{dir}^{bc}. All results reported are also compatible with the anomalous D0 dimuon asymmetry [46].

13.1 Future improvements

A repeat of this experiment using the Run 2 data set has the potential to yield significantly improved results. Assuming (naively) that the statistical uncertainty on each CA and CPA will decrease as a direct function of the cross-section and integrated luminosity, the predictions for a 13 TeV analysis using 100 fb^{-1} are shown in Table 13.1. The numbers in this table are derived using the theory values for the $t\bar{t}$ production cross-section of $\sigma_{8\ \mathrm{TeV}} = 252$ pb [39] and $\sigma_{13\ \mathrm{TeV}} = 832$ pb [39, 123], assuming the same reconstruction efficiencies apply. For the calculation of the total uncertainty, it is assumed that the systematics will not decrease.

An analysis under these conditions would find negligible statistical uncertainty, and focus would be put onto reduction of the dominant systematic uncertainties. The largest individual systematic uncertainty is the additional radiation (the modelling of the initial- and final-state

Uncertainties	Observed at 8 TeV, 20.3 fb^{-1}, (10^{-2})			Predicted at 13 TeV, 100 fb^{-1}, (10^{-2})		
	Statistical	Systematic	Total	Statistical	Systematic	Total
A^{ss}	0.6	0.5	0.8	0.2	0.5	0.5
A^{os}	0.5	0.4	0.5	0.1	0.3	0.3
A^{b}_{mix}	2.1	1.8	2.8	0.5	1.8	1.9
$A^{b\ell}_{\text{dir}}$	0.4	0.3	0.5	0.1	0.3	0.4
$A^{c\ell}_{\text{dir}}$	0.7	0.7	1.0	0.2	0.7	0.7
A^{bc}_{dir}	0.8	0.7	1.1	0.2	0.7	0.7

Table 13.1: Predictions for the uncertainties on a repeated analysis using 100 fb^{-1} of Run 2 LHC data at a collision energy of $\sqrt{s} = 13$ TeV.

radiation in pp collisions resulting in the formation of additional jets). Reduction of the additional radiation systematic could be achieved by focusing on the exclusion of IFSR jets. In this analysis the KLFitter is optimised to include up to five jets. Reverting the selection to only the hardest four jets would allow for less contamination from IFSR, although it would also produce a small decrease of the KLFitter performance. The most promising potential change would be to increase the cut on the jet transverse momentum. At 8 TeV the peak in the jet p_T spectrum is around 50 GeV, for existing 13 TeV analyses the peak is seen to be around 70 GeV. The large gain in statistics might allow for increasing the p_T cut to 50 GeV to remove contributions from softer IFSR jets without suffering from a significant increase in statistical uncertainty. The reduce number of IFSR jets would decrease the additional radiation systematic, and potentially also reduce the second and third largest systematics of the jet energy scale and jet vertex fraction also. Increasing the jet p_T cut would also provide the additional benefit of improving the KLFitter performance. The KLFitter purity is known to increase as a function of transverse momentum, as higher p_T jets tend to be more collimated and better separated than low p_T jets. At 13 TeV this performance increase combined with the decrease of the additional radiation systematic might provide considerable improvement to the resolution on the measured asymmetries.

Another alternative is to replace usage of the KLFitter with a multivariate approach. A multivariate discriminant trained on angular variables such as $\Delta R(\mu_{\text{SMT}}, \ell^{\pm})$ has the potential to yield similar performance. If the chosen input variables could be designed as independent from additional radiation, this could produce a reduction in the systematic uncertainties.

The current analysis is reported to be competitive in measuring the direct CP asymmetries, however to be competitive with existing limits on the mixing CP asymmetries (which are dominated by B-factory measurements and LHCb) would require a reduction on the total uncertainty

on A^b_{mix} to 0.1%. Using the same technique as utilised to build Table 13.1, it would require at least 3000 fb^{-1} of 13 TeV data (the expected yield of the high-luminosity LHC by 2035) and a significant reduction of systematic uncertainties (a factor of 20) to achieve this level of precision. To refute the central value of the D0 result in mixing to a level of 3σ however, a total uncertainty on the order of 0.25% would be required. This could be achieved with 500 fb^{-1} assuming again a similar reduction of systematic uncertainties.

One final technique which could be utilised to reduce the uncertainties on specific CP asymmetries could be to modify the definition of the fiducial volume to include more phase space (and therefore more statistics) for a particular decay chain, or to have a variety of fiducial volume definitions to optimise the extraction of each one. A study is performed to monitor the change in central values of the decay chain fractions as a function of the fiducial volume requirement applied to the soft muon p_T and jet p_T. Table 13.2 shows the variation in decay chain fractions observed, however it is unlikely that alterations of this magnitude would be significant for the uncertainties on the final results. Taking the fifth row as an example (Soft muon $p_T > 8$ GeV, jet $p_T > 25$ GeV), the increase of r_b would only reduce the statistical uncertainty component of A^b_{mix} down to 0.020 from 0.021, a much larger alteration of the fiducial volume would be required to enhance the contribution of $b \to \bar{b} \to \ell$ decays to have a significant effect.

	r_b	r_c	$r_{c\bar{c}}$	$\widetilde{r}_b$	$\widetilde{r}_c$	$\widetilde{r}_{c\bar{c}}$
Nominal Muon $p_T > 4$ GeV, jet $p_T > 25$ GeV	0.199	0.714	0.087	0.882	0.069	0.049
Soft muon $p_T > 5$ GeV, jet $p_T > 25$ GeV	0.207	0.708	0.085	0.886	0.067	0.047
Soft muon $p_T > 6$ GeV, jet $p_T > 25$ GeV	0.213	0.703	0.084	0.890	0.065	0.045
Soft muon $p_T > 7$ GeV, jet $p_T > 25$ GeV	0.219	0.698	0.083	0.893	0.063	0.044
Soft muon $p_T > 8$ GeV, jet $p_T > 25$ GeV	0.223	0.695	0.083	0.896	0.062	0.042
Soft muon $p_T > 4$ GeV, jet $p_T > 30$ GeV	0.197	0.716	0.087	0.880	0.070	0.050
Soft muon $p_T > 4$ GeV, jet $p_T > 35$ GeV	0.194	0.718	0.088	0.878	0.071	0.051
Soft muon $p_T > 4$ GeV, jet $p_T > 40$ GeV	0.191	0.721	0.088	0.886	0.072	0.052

Table 13.2: Decay chain fractions as determined using the nominal $t\bar{t}$ MC for different fiducial volumes, varied by selection on transverse momenta of the soft muon and of the jets.

Additionally, the increase in statistics might permit for an analysis binned by b-hadron lifetime. In analogy to the technique utilised in [46], the difference in the impact parameters (IP) between the charged lepton track and the soft muon track gives an indication of travel distance of the B before decay. The CP asymmetry for CP violation in neutral B-meson mixing is actually

a linear combination of flavour-specific asymmetries

$$A^b_{\rm mix} = C_d A^d_{\rm mix} + C_s A^s_{\rm mix} \tag{13.1}$$

which are the CP asymmetries for mixing in B^0_d and B^0_s mesons respectively. C_q are functions of the mean mixing probabilities (χ_q) and production fractions of B^0_d and B^0_s mesons. The mixing probabilities of neutral B mesons follow the form of 1 - $\cos(\Delta m_q t)$ and the proper decay time t. Samples with large IP tend to have larger t and as a result larger χ_q. Although $A^s_{\rm mix}$ are independent of the proper decay time, their extraction using this technique requires this information. Binning by b-hadron lifetime also opens sensitivity to CP violation in the interference between mixing and decay, in the form of an asymmetry $A^{\rm int}$, from decay chains with similar identical final states (such as $t \to \ell^+\nu\,(b \to c\bar{c}) \to \ell^+\ell^- X$ decays including charge conjugation).

Appendix A

Charge and CP asymmetry relations

This appendix justifies the relations between the charge asymmetries (CA) in Equations A.1 and A.2, and the CP asymmetries (CPA) in Equations A.3-A.7, via the decay chain fractions (DCF) in Equations A.8-A.16.

For A^{ss}, it is expected for events to contain two leptons in the final state with the same charge. Each term is justified here, where decay chains starting with a b-quark (as opposed to a $\bar{b}$-quark) will always contain an ℓ^+ from the W-boson, and therefore to qualify as same-sign, require an ℓ^+ in the final state from the b-quark decay chain. Charge conjugation is assumed for the $\ell^-\ell^-$ pairings.

- $\mathbf{r_b A^{b\ell}_{mix}}$
  - $A^{b\ell}_{\text{mix}}$ requires a $b \to \bar{b} \to \ell^+$ decay chain, this exactly lines up with the chain given in Equation A.11 to which r_b relates.
- $\mathbf{r_c A^{bc}_{dir}}$
  - A^{bc}_{dir} requires a $b \to c$ decay chain, and r_c provides $b \to c \to \ell^+$.
- $-\mathbf{r_c A^{c\ell}_{dir}}$
  - $A^{c\ell}_{\text{dir}}$ is defined in 'reverse' to the other asymmetries as the anti-quark appears on the left of the asymmetries in Equation A.6. Nonetheless, it requires a $c \to \ell^+$ decay, which is provided by r_c. The negative contribution to the same-sign events is a result of the 'reversed' asymmetry definition.

- $\mathbf{r_{c\bar{c}} A^{bc}_{mix}}$
  - A^{bc}_{mix} requires a $b \to \bar{b} \to \bar{c}$ decay, this is provided by $r_{c\bar{c}}$, however to reconstruct this as a same-sign event the lepton must come from the c decay, not the $\bar{c}$ decay.
- $\mathbf{r_{c\bar{c}} A^{c\ell}_{dir}}$
  - $A^{c\ell}_{\text{dir}}$ as described above has the 'reverse' definition. In this case, as in the previous $r_{c\bar{c}}$ case, the lepton must come fromthe c decay, not the $\bar{c}$ decay. The negative contribution to the same-sign events is a result of the 'reversed' asymmetry definition.

For A^{os}, it is expected for events to contain two leptons in the final state with opposite charge. Each term is justified here, where decay chains starting with a b-quark (as opposed to a$\bar{b}$-quark) will always contain an ℓ^+ from the W-boson, and therefore to qualify as opposite-sign, require an ℓ^- in the final state from the b-quark decay chain. Charge conjugation is assumed for the $\ell^-\ell^+$ pairings.

- $\mathbf{\widetilde{r}_b A^{b\ell}_{dir}}$
  - $A^{b\ell}_{\text{dir}}$ requires a $b \to \ell^-$ decay, this exactly lines up with the chain given in Equation A.14 to which $\widetilde{r}_b$ relates.
- $\mathbf{\widetilde{r}_c A^{bc}_{mix}}$
  - A^{bc}_{mix} requires a $b \to \bar{b} \to \bar{c}$ decay, which agrees with Equation A.15 where the final lepton comes from the $\bar{c}$ as expected.
- $\mathbf{\widetilde{r}_c A^{c\ell}_{dir}}$
  - $A^{c\ell}_{\text{dir}}$ is defined in 'reverse' to the other asymmetries as the anti-quark appears on the left of the asymmetries in Equation A.6. The $\widetilde{r}_c$ however provides this correctly as part of the longer $b \to \bar{b} \to \bar{c}$ decay, so $A^{c\ell}_{\text{dir}}$ may appear with a positive contribution in the opposite-sign asymmetry, as opposed to in the same-sign asymmetry.
- $\mathbf{\widetilde{r}_{c\bar{c}} A^{c\ell}_{dir}}$
  - $A^{c\ell}_{\text{dir}}$ as described above has a 'reverse' definition. In the $\widetilde{r}_{c\bar{c}}$ decays the $b \to c\bar{c}$ satisfies the opposite-sign requirements assuming the lepton comes from the $\bar{c}$ decay, so $A^{c\ell}_{\text{dir}}$ may again appear with a positive contribution in the opposite-sign asymmetry.

$$A^{\rm ss} = r_b A^{b\ell}_{\rm mix} + r_c \left(A^{bc}_{\rm dir} - A^{c\ell}_{\rm dir} \right) + r_{c\bar{c}} \left(A^{bc}_{\rm mix} - A^{c\ell}_{\rm dir} \right), \tag{A.1}$$

$$A^{\rm os} = \widetilde{r}_b A^{b\ell}_{\rm dir} + \widetilde{r}_c \left(A^{bc}_{\rm mix} + A^{c\ell}_{\rm dir} \right) + \widetilde{r}_{c\bar{c}} A^{c\ell}_{\rm dir}. \tag{A.2}$$

$$A^{b\ell}_{\rm mix} = \frac{\Gamma\left(b \to \overline{b} \to \ell^+ X\right) - \Gamma\left(\overline{b} \to b \to \ell^- X\right)}{\Gamma\left(b \to \overline{b} \to \ell^+ X\right) + \Gamma\left(\overline{b} \to b \to \ell^- X\right)}, \tag{A.3}$$

$$A^{bc}_{\rm mix} = \frac{\Gamma\left(b \to \overline{b} \to \overline{c} X\right) - \Gamma\left(\overline{b} \to b \to c X\right)}{\Gamma\left(b \to \overline{b} \to \overline{c} X\right) + \Gamma\left(\overline{b} \to b \to c X\right)}, \tag{A.4}$$

$$A^{b\ell}_{\rm dir} = \frac{\Gamma\left(b \to \ell^- X\right) - \Gamma\left(\overline{b} \to \ell^+ X\right)}{\Gamma\left(b \to \ell^- X\right) + \Gamma\left(\overline{b} \to \ell^+ X\right)}, \tag{A.5}$$

$$A^{c\ell}_{\rm dir} = \frac{\Gamma\left(\overline{c} \to \ell^- X_L\right) - \Gamma\left(c \to \ell^+ X_L\right)}{\Gamma\left(\overline{c} \to \ell^- X_L\right) + \Gamma\left(c \to \ell^+ X_L\right)}, \tag{A.6}$$

$$A^{bc}_{\rm dir} = \frac{\Gamma\left(b \to c X_L\right) - \Gamma\left(\overline{b} \to \overline{c} X_L\right)}{\Gamma\left(b \to c X_L\right) + \Gamma\left(\overline{b} \to \overline{c} X_L\right)}, \tag{A.7}$$

$$r_b = \frac{N_{r_b}}{N_{r_b} + N_{r_c} + N_{r_{c\bar{c}}}}, \qquad \widetilde{r}_b = \frac{N_{\widetilde{r}_b}}{N_{\widetilde{r}_b} + N_{\widetilde{r}_c} + N_{\widetilde{r}_{c\bar{c}}}}, \tag{A.8}$$

$$r_c = \frac{N_{r_c}}{N_{r_b} + N_{r_c} + N_{r_{c\bar{c}}}}, \qquad \widetilde{r}_c = \frac{N_{\widetilde{r}_c}}{N_{\widetilde{r}_b} + N_{\widetilde{r}_c} + N_{\widetilde{r}_{c\bar{c}}}}, \tag{A.9}$$

$$r_{c\bar{c}} = \frac{N_{r_{c\bar{c}}}}{N_{r_b} + N_{r_c} + N_{r_{c\bar{c}}}}, \qquad \widetilde{r}_{c\bar{c}} = \frac{N_{\widetilde{r}_{c\bar{c}}}}{N_{\widetilde{r}_b} + N_{\widetilde{r}_c} + N_{\widetilde{r}_{c\bar{c}}}}. \tag{A.10}$$

$$N_{r_b} = N\left[t \to \ell^+\nu\left(b \to \overline{b}\right) \to \ell^+\ell^+X\right], \tag{A.11}$$

$$N_{r_c} = N\left[t \to \ell^+\nu\left(b \to c\right) \to \ell^+\ell^+X\right], \tag{A.12}$$

$$N_{r_{c\overline{c}}} = N\left[t \to \ell^+\nu\left(b \to \overline{b} \to c\overline{c}\right) \to \ell^+\ell^+X\right], \tag{A.13}$$

$$N_{\widetilde{r}_b} = N\left[t \to \ell^+\nu b \to \ell^+\ell^-X\right], \tag{A.14}$$

$$N_{\widetilde{r}_c} = N\left[t \to \ell^+\nu\left(b \to \overline{b} \to \overline{c}\right) \to \ell^+\ell^-X\right], \tag{A.15}$$

$$N_{\widetilde{r}_{c\overline{c}}} = N\left[t \to \ell^+\nu\left(b \to c\overline{c}\right) \to \ell^+\ell^-X\right], \tag{A.16}$$

Appendix B

Decay chain fractions and CP asymmetries with normalisations

This appendix justifies the of the decay chain fractions (DCF) discussed in Section 4.1.2 following the substitution of $N^{\alpha\beta} \to \dfrac{N^{\alpha\beta}}{N^{\alpha}}$.

B.1 Performing the substitution

Applying the same substitution ($N^{\alpha\beta} \to \dfrac{N^{\alpha\beta}}{N^{\alpha}}$) to each decay chain fraction leads to

$$r_b = \frac{\frac{N^{++}_{r_b}}{N^+} + \frac{N^{--}_{r_b}}{N^-}}{\frac{N^{++}}{N^+} + \frac{N^{--}}{N^-}}, \qquad \widetilde{r}_b = \frac{\frac{N^{+-}_{\widetilde{r}_b}}{N^+} + \frac{N^{-+}_{\widetilde{r}_b}}{N^-}}{\frac{N^{+-}}{N^+} + \frac{N^{-+}}{N^-}}, \tag{B.1}$$

$$r_c = \frac{\frac{N^{++}_{r_c}}{N^+} + \frac{N^{--}_{r_c}}{N^-}}{\frac{N^{++}}{N^+} + \frac{N^{--}}{N^-}}, \qquad \widetilde{r}_c = \frac{\frac{N^{+-}_{\widetilde{r}_c}}{N^+} + \frac{N^{-+}_{\widetilde{r}_c}}{N^-}}{\frac{N^{+-}}{N^+} + \frac{N^{-+}}{N^-}}, \tag{B.2}$$

$$r_{c\bar{c}} = \frac{\frac{N^{++}_{r_{c\bar{c}}}}{N^+} + \frac{N^{--}_{r_{c\bar{c}}}}{N^-}}{\frac{N^{++}}{N^+} + \frac{N^{--}}{N^-}}, \qquad \widetilde{r}_{c\bar{c}} = \frac{\frac{N^{+-}_{\widetilde{r}_{c\bar{c}}}}{N^+} + \frac{N^{-+}_{\widetilde{r}_{c\bar{c}}}}{N^-}}{\frac{N^{+-}}{N^+} + \frac{N^{-+}}{N^-}}. \tag{B.3}$$

and adjustments to the CPAs (as $N \propto \Gamma$):

$$A^{b\ell}_{\text{mix}} = \frac{\frac{\Gamma\left(b\to\bar{b}\to\ell^+X\right)}{\Gamma(b)} - \frac{\Gamma\left(\bar{b}\to b\to\ell^-X\right)}{\Gamma\left(\bar{b}\right)}}{\frac{\Gamma\left(b\to\bar{b}\to\ell^+X\right)}{\Gamma(b)} + \frac{\Gamma\left(\bar{b}\to b\to\ell^-X\right)}{\Gamma\left(\bar{b}\right)}}, \tag{B.4}$$

$$A^{bc}_{\text{mix}} = \frac{\frac{\Gamma\left(b\to\bar{b}\to\bar{c}X\right)}{\Gamma(b)} - \frac{\Gamma\left(\bar{b}\to b\to cX\right)}{\Gamma\left(\bar{b}\right)}}{\frac{\Gamma\left(b\to\bar{b}\to\bar{c}X\right)}{\Gamma(b)} + \frac{\Gamma\left(\bar{b}\to b\to cX\right)}{\Gamma\left(\bar{b}\right)}}, \tag{B.5}$$

$$A^{b\ell}_{\text{dir}} = \frac{\frac{\Gamma(b\to\ell^-X)}{\Gamma(b)} - \frac{\Gamma\left(\bar{b}\to\ell^+X\right)}{\Gamma\left(\bar{b}\right)}}{\frac{\Gamma(b\to\ell^-X)}{\Gamma(b)} + \frac{\Gamma\left(\bar{b}\to\ell^+X\right)}{\Gamma\left(\bar{b}\right)}}, \tag{B.6}$$

$$A^{c\ell}_{\text{dir}} = \frac{\frac{\Gamma(\bar{c}\to\ell^-X_L)}{\Gamma(\bar{c})} - \frac{\Gamma(c\to\ell^+X_L)}{\Gamma(c)}}{\frac{\Gamma(\bar{c}\to\ell^-X_L)}{\Gamma(\bar{c})} + \frac{\Gamma(c\to\ell^+X_L)}{\Gamma(c)}}, \tag{B.7}$$

$$A^{bc}_{\text{dir}} = \frac{\frac{\Gamma(b\to cX_L)}{\Gamma(b)} - \frac{\Gamma\left(\bar{b}\to\bar{c}X_L\right)}{\Gamma\left(\bar{b}\right)}}{\frac{\Gamma(b\to cX_L)}{\Gamma(b)} + \frac{\Gamma\left(\bar{b}\to\bar{c}X_L\right)}{\Gamma\left(\bar{b}\right)}}. \tag{B.8}$$

The CPT theorem permits the cancellation of all new denominators and these collapse back to their original form, leading to

$$A^{\text{ss}} = \left(\frac{1}{\frac{N^{++}}{N^+} + \frac{N^{--}}{N^-}}\right)\left(\left(\frac{N^{++}_{r_b}}{N^+} + \frac{N^{--}_{r_b}}{N^-}\right)A^{b\ell}_{\text{mix}} + \left(\frac{N^{++}_{r_c}}{N^+} + \frac{N^{--}_{r_c}}{N^-}\right)\left(A^{bc}_{\text{dir}} - A^{c\ell}_{\text{dir}}\right) + \left(\frac{N^{++}_{r_{c\bar{c}}}}{N^+} + \frac{N^{--}_{r_{c\bar{c}}}}{N^-}\right)\left(A^{bc}_{\text{mix}} - A^{c\ell}_{\text{dir}}\right)\right), \tag{B.9}$$

$$A^{\text{os}} = \left(\frac{1}{\frac{N^{+-}}{N^+} + \frac{N^{-+}}{N^-}}\right)\left(\left(\frac{N^{+-}_{\widetilde{r}_b}}{N^+} + \frac{N^{-+}_{\widetilde{r}_b}}{N^-}\right)A^{b\ell}_{\text{dir}} + \left(\frac{N^{+-}_{\widetilde{r}_c}}{N^+} + \frac{N^{-+}_{\widetilde{r}_c}}{N^-}\right)\left(A^{bc}_{\text{mix}} + A^{c\ell}_{\text{dir}}\right) + \left(\frac{N^{+-}_{\widetilde{r}_{c\bar{c}}}}{N^+} + \frac{N^{-+}_{\widetilde{r}_{c\bar{c}}}}{N^-}\right)A^{c\ell}_{\text{dir}}\right). \tag{B.10}$$

The DCFs are determined in MC which does not include the most asymmetric effects such as $t\bar{t}$ charge asymmetry. In the fiducial volume $N^+ = N^-$ within statistical uncertainties and changes to r_i are negligible. This permits Equations 4.9, 4.15-4.19, and 4.23-4.24, to be used.

Appendix C

Electron identification criteria

The appendix is entirely based on [77]. Three cut-based selections, *loose*, *medium* and *tight* are optimised in 10 bins of $|\eta|$ and 11 bins of E_T. *tight* is a subset of *medium*, and *medium* is a subset of *loose*. Table C.1 defines the discriminating variables available for use. Figure C.1 summarises which variables are used to perform each selection.

	Cut-based				Likelihood		
Name	*loose*	*medium*	*tight*	*multilepton*	LOOSE	MEDIUM	VERY TIGHT
$R_{\text{Had(1)}}$	✓	✓	✓	✓	✓	✓	✓
f_3		✓	✓	✓	✓	✓	✓
$W_{\eta 2}$	✓	✓	✓	✓	✓	✓	✓
R_η	✓	✓	✓	✓	✓	✓	✓
R_ϕ					✓	✓	✓
w_{stot}	✓	✓	✓	✓	✓	✓	✓
E_{ratio}	✓	✓	✓	✓	✓	✓	✓
f_1					✓	✓	✓
n_{Blayer}		✓	✓	✓	✓	✓	✓
n_{Pixel}	✓	✓	✓	✓	✓	✓	✓
n_{Si}	✓	✓	✓	✓	✓	✓	✓
d_0		✓	✓			✓	✓
σ_{d_0}						✓	✓
$\Delta p/p$				✓	✓	✓	✓
n_{TRT}		✓	✓	✓			
F_{HT}		✓	✓	✓	✓	✓	✓
$\Delta\eta_1$	✓	✓	✓	✓	✓	✓	✓
$\Delta\phi_2$			✓				
$\Delta\phi_{\text{res}}$				✓	✓	✓	✓
E/p			✓				
isConv			✓				✓

Figure C.1: The variables used in the different selections of the electron identification menu

Type	Description	Name
Hadronic leakage	Ratio of E_T in the first layer of the hadronic calorimeter to E_T of the EM cluster (used over the range $\|\eta\|< 0.8$ or $\|\eta\|> 1.37$)	R_{Had1}
	Ratio of E_T in the hadronic calorimeter to E_T of the EM cluster (used over the range $\|\eta\|< 0.8$ or $\|\eta\|> 1.37$)	R_{Had}
Back layer of EM calorimeter	Ratio of the energy in the back layer to the total energy in the EM accordion calorimeter	f_3
Middle layer of EM calorimeter	Lateral shower width, $\sqrt{\left(\Sigma E_i \eta_i^2\right)/(\Sigma E_i) - \left((\Sigma E_i \eta_i)/(\Sigma E_i)\right)^2}$, where E_i is the energy and η_i is the pseudorapidity of cell i and the sum is calculated within a window of 3×5 cells	W_{η^2}
	Ratio of the energy in 3×3 cells over the energy in 3×7 cells centered at the electron cluster position	R_ϕ
	Ratio of the energy in 3×7 cells over the energy in 7×7 cells centered at the electron cluster position	R_η
Strip layer of EM calorimeter	Shower width, $\sqrt{\left(\Sigma E_i \left(i - i_{\max}\right)^2\right)/(\Sigma E_i)}$, where i runs over all strips in a window of $\Delta\eta \times \Delta\phi \sim 0.0625 \times 0.2$, corresponding typically to 20 strips in η, and $i_{\max}$ is the index of the highest-energy strip	ω_{stot}
	Ratio of the energy dierence between the largest and second largest energy deposits in the cluster over the sum of these energies	E_{ratio}
	Ratio of the energy in the strip layer to the total energy in the EM accordion calorimeter	f_1
Track quality	Number of hits in the B-layer (discriminates against photon conversions)	$n_{B-\text{layer}}$
	Number of hits in the pixel detector	n_{Pixel}
	Number of total hits in the pixel and SCT detectors	n_{Si}
	Transverse impact parameter	d_0
	Significance of transverse impact parameter defined as the ratio of d_0 and its uncertainty	σ_{d_0}
	Momentum lost by the track between the perigee and the last measurement point divided by the original momentum	$\Delta p/p$
TRT	Total number of hits in the TRT	n_{TRT}
	Ratio of the number of high-threshold hits to the total number of hits in the TRT	F_{HT}
Track-cluster matching	$\Delta\eta$ between the cluster position in the strip layer and the extrapolated track	$\Delta\eta_1$
	$\Delta\phi$ between the cluster position in the middle layer and the extrapolated track	$\Delta\phi_2$
	Defined as $\Delta\phi_2$, but the track momentum is rescaled to the cluster energy before extrapolating the track to the middle layer of the calorimeter $\Delta\phi_{\text{res}}$	
	Ratio of the cluster energy to the track momentum	E/p
Conversions	Veto electron candidates matched to reconstructed photon conversions	isConv

Table C.1: Definitions of the electron discriminating variables

Bibliography

[1] ATLAS Collaboration, The ATLAS Experiment at the CERN Large Hadron Collider, JINST 3 (2008) S08003. doi:10.1088/1748-0221/3/08/S08003.

[2] L. Evans, P. Bryant, LHC Machine, Journal of Instrumentation 3 (08) (2008) S08001.
URL http://stacks.iop.org/1748-0221/3/i=08/a=S08001

[3] J. Haffner, The CERN accelerator complex. Complexe des accélérateurs du CERN, General Photo.
URL https://cds.cern.ch/record/1621894

[4] B. R. Martin, G. Shaw, Particle Physics, 2008.
URL http://eu.wiley.com/WileyCDA/WileyTitle/productCd-0470032944.html

[5] A. D. Sakharov, Violation of CP Invariance, c Asymmetry, and Baryon Asymmetry of the Universe, Pisma Zh. Eksp. Teor. Fiz. 5 (1967) 32–35, [Usp. Fiz. Nauk161,61(1991)]. doi:10.1070/PU1991v034n05ABEH002497.

[6] BaBar Collaboration, B. Aubert et al., Observation of CP violation in the B^0 meson system, Phys. Rev. Lett. 87 (2001) 091801. arXiv:hep-ex/0107013, doi:10.1103/PhysRevLett.87.091801.

[7] Belle Collaboration, K. Abe et al., Observation of large CP violation in the neutral B meson system, Phys. Rev. Lett. 87 (2001) 091802. arXiv:hep-ex/0107061, doi:10.1103/PhysRevLett.87.091802.

[8] LHCb Collaboration, R. Aaij et al., First observation of CP violation in the decays of B_s^0 mesons, Phys. Rev. Lett. 110 (22) (2013) 221601. arXiv:1304.6173, doi:10.1103/PhysRevLett.110.221601.

[9] NA31 Collaboration, J. Burkhardt et al., First Evidence for Direct CP Violation, Phys. Lett. B206 (1988) 169–176. doi:10.1016/0370-2693(88)91282-8.

[10] NA48 Collaboration, V. Fanti et al., A New measurement of direct CP violation in two pion decays of the neutral kaon, Phys. Lett. B465 (1999) 335–348. arXiv:hep-ex/9909022, doi:10.1016/S0370-2693(99)01030-8.

[11] KTeV Collaboration, A. Alavi-Harati et al., Observation of direct CP violation in $K_{S,L} \to \pi\pi$ decays, Phys. Rev. Lett. 83 (1999) 22–27. arXiv:hep-ex/9905060, doi:10.1103/PhysRevLett.83.22.

[12] BaBar Collaboration, B. Aubert et al., Observation of direct CP violation in $B^0 \to K^+\pi^-$ decays, Phys. Rev. Lett. 93 (2004) 131801. arXiv:hep-ex/0407057, doi:10.1103/PhysRevLett.93.131801.

[13] Belle Collaboration, Y. Chao et al., Evidence for direct CP violation in $B^0 \to K^+\pi^-$ decays, Phys. Rev. Lett. 93 (2004) 191802. arXiv:hep-ex/0408100, doi:10.1103/PhysRevLett.93.191802.

[14] Belle Collaboration, A. Poluektov et al., Evidence for direct CP violation in the decay $B \to D^{(*)}K, D \to K^0_S\pi^+\pi^-$ and measurement of the CKM phase ϕ_3, Phys. Rev. D81 (2010) 112002. arXiv:1003.3360, doi:10.1103/PhysRevD.81.112002.

[15] BaBar Collaboration, P. del Amo Sanchez et al., Measurement of CP observables in $B^\pm \to D_{CP}K^\pm$ decays and constraints on the CKM angle γ, Phys. Rev. D82 (2010) 072004. arXiv:1007.0504, doi:10.1103/PhysRevD.82.072004.

[16] LHCb Collaboration, R. Aaij et al., Observation of CP violation in $B^\pm \to DK^\pm$ decays, Phys. Lett. B712 (2012) 203–212, [Erratum: Phys. Lett.B713,351(2012)]. arXiv:1203.3662, doi:10.1016/j.physletb.2012.04.060, 10.1016/j.physletb.2012.05.060.

[17] M. Thomson, Modern Particle Physics, Cambridge University Press, New York, 2013.
URL http://www-spires.fnal.gov/spires/find/books/www?cl=QC793.2.T46::2013

[18] D. Boutigny, et al., The BABAR physics book: Physics at an asymmetric B factory, in: Workshop on Physics at an Asymmetric B Factory (BaBar Collaboration Meeting) Pasadena, California, September 22-24, 1997.

[19] J. E. Blanco, Top quark measurements and calibration of the Soft Muon Tagger using the ATLAS detector at the Large Hadron Collider, Royal Holloway, University of London, PhD Thesis, 2013.

[20] Belle Collaboration, K. Abe et al., Observation of a new narrow charmonium state in exclusive $B^+ \to K^\pm\pi^+\pi^- J/\psi$ decays, in: Proceedings, 21st International Symposium on Lepton and Photon Interactions at High Energies (LP 03): Batavia, ILL, August 11-16, 2003, 2003. arXiv:hep-ex/0308029.

[21] LHCb Collaboration, R. Aaij et al., Observation of $J/\psi p$ Resonances Consistent with Pentaquark States in $\Lambda^0_b \to J/\psi K^- p$ Decays, Phys. Rev. Lett. 115 (2015) 072001. arXiv:1507.03414, doi:10.1103/PhysRevLett.115.072001.

[22] J. Christenson, et al., Evidence for the 2 π decay of the K^0_2 meson, Phys.Rev.Lett. 13 (1964) 138–140. doi:10.1103/PhysRevLett.13.138.

[23] G. Anzivino, CP Violation results from the NA48 experiments, Journal of Physics: Conference Series 335 (1) (2011) 012015.
URL http://stacks.iop.org/1742-6596/335/i=1/a=012015

[24] B. Grinstein, Lectures on Flavor Physics and CP Violation, in: Proceedings, 8th CERN–Latin-American School of High-Energy Physics (CLASHEP2015): Ibarra,

Ecuador, March 05-17, 2015, 2016, pp. 43–84. arXiv:1701.06916, doi:10.5170/CERN-2016-005.43.
URL https://inspirehep.net/record/1510457/files/arXiv:1701.06916.pdf

[25] J. Charles, et al., CP violation and the CKM matrix: Assessing the impact of the asymmetric *B* factories, Eur. Phys. J. C41 (1) (2005) 1–131, updated results and plots available at: http://ckmfitter.in2p3.fr. arXiv:hep-ph/0406184, doi:10.1140/epjc/s2005-02169-1.

[26] A. Arbey, et al., Constraints on the CP-Violating MSSM, in: 6th Workshop on Theory, Phenomenology and Experiments in Flavour Physics: Interplay of Flavour Physics with electroweak symmetry breaking (Capri 2016) Anacapri, Capri, Italy, June 11, 2016, 2016. arXiv:1611.05061.
URL https://inspirehep.net/record/1498324/files/arXiv:1611.05061.pdf

[27] D. Chang, et al., Neutrino mixing and large CP violation in B physics, Phys. Rev. D67 (2003) 075013. arXiv:hep-ph/0205111, doi:10.1103/PhysRevD.67.075013.

[28] Y. Grossman, et al., CP asymmetries in B decays with new physics in decay amplitudes, Phys. Lett. B395 (1997) 241–249. arXiv:hep-ph/9612269, doi:10.1016/S0370-2693(97)00068-3.

[29] M. Ciuchini, et al., The Chromomagnetic dipole operator and the B semileptonic branching ratio, Phys. Lett. B388 (1996) 353–365, [Erratum: Phys. Lett.B393,489(1997)]. arXiv:hep-ph/9604438, doi:10.1016/S0370-2693(96)01168-9, 10.1016/S0370-2693(96)01631-0.

[30] F. del Aguila, et al., CP violation from new quarks in the chiral limit, Nucl. Phys. B510 (1998) 39–60. arXiv:hep-ph/9703410, doi:10.1016/S0550-3213(97)00708-6, 10.1016/S0550-3213(98)81003-1.

[31] I. A. Connelly, A search for the Higgs boson decaying to two *b*-quarks in association with a dileptonically decaying top-quark pair with the ATLAS detector.

[32] M. Baak, et al., The global electroweak fit at NNLO and prospects for the LHC and ILC, Eur. Phys. J. C74 (2014) 3046. arXiv:1407.3792, doi:10.1140/epjc/s10052-014-3046-5.

[33] C. Campagnari, et al., The Discovery of the top quark, Rev. Mod. Phys. 69 (1997) 137–212. arXiv:hep-ex/9608003, doi:10.1103/RevModPhys.69.137.

[34] S. W. Herb, et al., Observation of a Dimuon Resonance at 9.5-GeV in 400-GeV Proton-Nucleus Collisions, Phys. Rev. Lett. 39 (1977) 252–255. doi:10.1103/PhysRevLett.39.252.

[35] G. Montagna, et al., The Top quark and the Higgs boson mass from LEP SLC and CDF data, Phys. Lett. B335 (1994) 484–489. arXiv:hep-ph/9407246, doi:10.1016/0370-2693(94)90381-6.

[36] A. Heinson, Top pair production and decay diagrams, reproduced from: Useful Diagrams of Top Signals and Backgrounds, accessed: 09-04-2017 (2011).

[37] M. Gallinaro, Top quark physics: A tool for discoveries, Journal of Physics: Conference Series 447 (1) (2013) 012012.
URL http://stacks.iop.org/1742-6596/447/i=1/a=012012

[38] A. D. Martin, et al., Parton distributions for the LHC, Eur. Phys. J. C63 (2009) 189–285. arXiv:0901.0002, doi:10.1140/epjc/s10052-009-1072-5.

[39] M. Czakon, et al., Top++: A Program for the Calculation of the Top-Pair Cross-Section at Hadron Colliders, Comput. Phys. Commun. 185 (2014) 2930. arXiv:1112.5675, doi:10.1016/j.cpc.2014.06.021.

[40] N. Kidonakis, NNLL threshold resummation for top-pair and single-top production, Phys. Part. Nucl. 45 (4) (2014) 714–722. arXiv:1210.7813, doi:10.1134/S1063779614040091.

[41] C. Patrignani, et al., Review of Particle Physics, Chin. Phys. C40 (10) (2016) 100001. doi:10.1088/1674-1137/40/10/100001.

[42] V. Branchina, et al., Top mass determination, Higgs inflation, and vacuum stability, JHEP 09 (2014) 182. arXiv:1407.4112, doi:10.1007/JHEP09(2014)182.

[43] G. Belanger, et al., Top Polarization in Sbottom Decays at the LHCarXiv:1304.2987.

[44] J. A. Aguilar-Saavedra, et al., Asymmetries in top quark pair production at hadron colliders, Rev. Mod. Phys. 87 (2015) 421–455. arXiv:1406.1798, doi:10.1103/RevModPhys.87.421.

[45] G. Rodrigo, The $t\bar{t}$ asymmetry in the Standard Model and beyond, in: 2012 Electroweak Interactions and Unified Theories: Proceedings of the 47th Rencontres de Moriond on Electroweak Interactions and Unified Theories, La Thuile, March 3-10, 2012, 2012, pp. 295–303. arXiv:1207.0331.
URL http://inspirehep.net/record/1120742/files/arXiv:1207.0331.pdf

[46] D0 Collaboration, V. M. Abazov et al., Study of *CP*-violating charge asymmetries of single muons and like-sign dimuons in $p\bar{p}$ collisions, Phys. Rev. D89 (1) (2014) 012002. arXiv:1310.0447, doi:10.1103/PhysRevD.89.012002.

[47] LHCb Collaboration, R. Aaij et al., Measurement of the semileptonic *CP* asymmetry in $B^0 - \overline{B}^0$ mixing, Phys. Rev. Lett. 114 (2015) 041601. arXiv:1409.8586, doi:10.1103/PhysRevLett.114.041601.

[48] LHCb Collaboration, R. Aaij et al., Measurement of the *CP* asymmetry in $B_s^0 - \overline{B}_s^0$ mixing, Phys. Rev. Lett. 117 (6) (2016) 061803, [Addendum: Phys. Rev. Lett.118,no.12,129903(2017)]. arXiv:1605.09768, doi:10.1103/PhysRevLett.118.129903, 10.1103/PhysRevLett.117.061803.

[49] BaBar Collaboration, J. P. Lees et al., Study of *CP* Asymmetry in $B^0 - \bar{B}^0$ Mixing with Inclusive Dilepton Events, Phys. Rev. Lett. 114 (8) (2015) 081801. arXiv:1411.1842, doi:10.1103/PhysRevLett.114.081801.

[50] O. Gedalia, et al., Top B Physics at the LHC, Phys. Rev. Lett. 110 (23) (2013) 232002. arXiv:1212.4611, doi:10.1103/PhysRevLett.110.232002.

[51] ATLAS Collaboration, Measurement of the charge asymmetry in top-quark pair production in the lepton-plus-jets final state in pp collision data at $\sqrt{s} = 8\,\mathrm{T}eV$ with the ATLAS detector, Eur. Phys. J. C76 (2) (2016) 87. arXiv:1509.02358, doi:10.1140/epjc/s10052-016-3910-6.

[52] S. Descotes-Genon, et al., A possible explanation of the d0 like-sign dimuon charge asymmetry, Phys. Rev. D 87 (2013) 074036. doi:10.1103/PhysRevD.87.074036.
URL https://link.aps.org/doi/10.1103/PhysRevD.87.074036

[53] CMS Collaboration, The CMS Experiment at the CERN LHC, JINST 3 (2008) S08004. doi:10.1088/1748-0221/3/08/S08004.

[54] LHCb Collaboration, A. A. Alves et al., The LHCb Detector at the LHC, JINST 3 (2008) S08005. doi:10.1088/1748-0221/3/08/S08005.

[55] TOTEM Collaboration, G. Anelli et al., The TOTEM experiment at the CERN Large Hadron Collider, JINST 3 (2008) S08007. doi:10.1088/1748-0221/3/08/S08007.

[56] LHCf Collaboration, O. Adriani et al., The LHCf detector at the CERN Large Hadron Collider, JINST 3 (2008) S08006. doi:10.1088/1748-0221/3/08/S08006.

[57] NA62 Collaboration, E. Cortina Gil et al., The Beam and detector of the NA62 experiment at CERNarXiv:1703.08501.

[58] ISOLDE Collaboration, B. Hedin et al., THE ISOLDE BEAM.

[59] LHC machine outreach, provided by LHC Machine Outreach, accessed: 09-04-2017.

[60] M. Lamont, Status of the lhc, Journal of Physics: Conference Series 455 (1) (2013) 012001.
URL http://stacks.iop.org/1742-6596/455/i=1/a=012001

[61] ATLAS Luminosity Public Result, provided by Luminosity Public Results, accessed: 09-04-2017.

[62] A. Schaelicke, et al., Event generator for particle production in high-energy collisions, Prog. Part. Nucl. Phys. 53 (2004) 329–338. arXiv:hep-ph/0311270, doi:10.1016/j.ppnp.2004.02.031.

[63] A. Buckley, et al., General-purpose event generators for LHC physics, Phys. Rept. 504 (2011) 145–233. arXiv:1101.2599, doi:10.1016/j.physrep.2011.03.005.

[64] B. Cooper, J. Katzy, M. L. Mangano, A. Messina, L. Mijovic, P. Skands, Importance of a consistent choice of alpha(s) in the matching of AlpGen and Pythia, Eur. Phys. J. C72 (2012) 2078. arXiv:1109.5295, doi:10.1140/epjc/s10052-012-2078-y.

[65] P. Nason, A New method for combining NLO QCD with shower Monte Carlo algorithms, JHEP 11 (2004) 040. arXiv:hep-ph/0409146, doi:10.1088/1126-6708/2004/11/040.

[66] S. Frixione, B. R. Webber, Matching NLO QCD computations and parton shower simulations, JHEP 06 (2002) 029. arXiv:hep-ph/0204244, doi:10.1088/1126-6708/2002/06/029.

[67] G. Corcella, et al., HERWIG 6: An Event generator for hadron emission reactions with interfering gluons (including supersymmetric processes), JHEP 01 (2001) 010. arXiv:hep-ph/0011363, doi:10.1088/1126-6708/2001/01/010.

[68] T. Sjostrand, et al., PYTHIA 6.4 Physics and Manual, JHEP 05 (2006) 026. arXiv:hep-ph/0603175, doi:10.1088/1126-6708/2006/05/026.

[69] T. Sjostrand, Some Comments on Jet Fragmentation Models and α_s Determinations, Z. Phys. C26 (1984) 93. doi:10.1007/BF01572546.

[70] B. Andersson, et al., Parton Fragmentation and String Dynamics, Phys. Rept. 97 (1983) 31–145. doi:10.1016/0370-1573(83)90080-7.

[71] M. L. Mangano, et al., ALPGEN, a generator for hard multiparton processes in hadronic collisions, JHEP 07 (2003) 001. arXiv:hep-ph/0206293, doi:10.1088/1126-6708/2003/07/001.

[72] S. Agostinelli, et al., GEANT4: A Simulation toolkit, Nucl. Instrum. Meth. A506 (2003) 250–303. doi:10.1016/S0168-9002(03)01368-8.

[73] ATLAS Collaboration, The ATLAS Simulation Infrastructure, Eur. Phys. J. C70 (2010) 823–874. arXiv:1005.4568, doi:10.1140/epjc/s10052-010-1429-9.

[74] W. Lukas, Fast Simulation for ATLAS: Atlfast-II and ISF, 2012.
URL http://cdsweb.cern.ch/record/1458503/files/ATL-SOFT-PROC-2012-065.pdf

[75] Performance of the Fast ATLAS Tracking Simulation (FATRAS) and the ATLAS Fast Calorimeter Simulation (FastCaloSim) with single particles, Tech. Rep. ATL-SOFT-PUB-2014-001, CERN, Geneva (Mar 2014).
URL https://cds.cern.ch/record/1669341

[76] ATLAS Collaboration, Electron reconstruction and identification efficiency measurements with the ATLAS detector using the 2011 LHC proton-proton collision data, Eur. Phys. J. C74 (7) (2014) 2941. arXiv:1404.2240, doi:10.1140/epjc/s10052-014-2941-0.

[77] ATLAS Collaboration, Electron efficiency measurements with the ATLAS detector using the 2012 LHC proton-proton collision data.

[78] B. Resende, Muon identification algorithms in ATLAS, Tech. Rep. ATL-PHYS-PROC-2009-113, CERN, Geneva (Sep 2009).
URL https://cds.cern.ch/record/1209632

[79] T. Lagouri, et al., A Muon Identification and Combined Reconstruction Procedure for the ATLAS Detector at the LHC at CERN, IEEE Trans. Nucl. Sci. 51 (2004) 3030–3033. doi:10.1109/TNS.2004.839102.

[80] S. Hassani, et al., A muon identification and combined reconstruction procedure for the ATLAS detector at the LHC using the (MUONBOY, STACO, MuTag) reconstruction packages, Nucl. Instrum. Meth. A572 (2007) 77–79. doi:10.1016/j.nima.2006.10.340.

[81] ATLAS Collaboration, Preliminary results on the muon reconstruction efficiency, momentum resolution, and momentum scale in ATLAS 2012 pp collision data.

[82] G. P. Salam, Towards Jetography, Eur. Phys. J. C67 (2010) 637–686. arXiv:0906.1833, doi:10.1140/epjc/s10052-010-1314-6.

[83] M. Cacciari, et al., The Anti-k(t) jet clustering algorithm, JHEP 04 (2008) 063. arXiv:0802.1189, doi:10.1088/1126-6708/2008/04/063.

[84] G. P. Salam, et al., A Practical Seedless Infrared-Safe Cone jet algorithm, JHEP 05 (2007) 086. arXiv:0704.0292, doi:10.1088/1126-6708/2007/05/086.

[85] ATLAS Collaboration, Calibration of the performance of *b*-tagging for *c* and light-flavour jets in the 2012 ATLAS data.

[86] ATLAS Collaboration, Performance of *b*-Jet Identification in the ATLAS Experiment, JINST 11 (04) (2016) P04008. arXiv:1512.01094, doi:10.1088/1748-0221/11/04/P04008.

[87] ATLAS Collaboration, Performance of Missing Transverse Momentum Reconstruction in Proton-Proton Collisions at 7 TeV with ATLAS, Eur. Phys. J. C72 (2012) 1844. arXiv:1108.5602, doi:10.1140/epjc/s10052-011-1844-6.

[88] T. Sjostrand, et al., A Brief Introduction to PYTHIA 8.1, Comput. Phys. Commun. 178 (2008) 852–867. arXiv:0710.3820, doi:10.1016/j.cpc.2008.01.036.

[89] Y. Amhis, et al., Averages of *b*-hadron, *c*-hadron, and τ-lepton properties as of summer 2016arXiv:1612.07233.

[90] C.-H. Kom, et al., Charge asymmetry in W+jets production at the LHC, Eur. Phys. J. C69 (2010) 67–73. arXiv:1004.3404, doi:10.1140/epjc/s10052-010-1353-z.

[91] B. Acharya, J. Adelman, S. Adomeit, M. Aoki, B. Alvarez, F. Balli, W. Bell, K. Becker, K. Behr, D. Benjamin, E. Bergeaas Kuutmann, C. Bernard, K. Black, S. Calvet, R. Camacho, Y. Coadou, G. Cortiana, N. Cooper-Smith, T. Cornelissen, M. Cristinziani, V. Dao, U. De Sanctis, C. Doglioni, F. Derue, K. Finelli, K. Grahn, J. Groth-Jensen, S. Head, A. Henrichs, D. Hirschbuehl, V. Kaushik, O. Kind, H. Khandanyan, A. Krasznahorkay, T. Kuhl, E. Le Menedeu, H. Lee, A. Lister, K. Loureiro, L. Miljovic, J. Morris, R. Moles Valls, O. Nackenhorst, D. Pelikan, M. Owen, M. Pinamonti, K. Rao, K. Rosbach, M. Rudolph, G. Salamanna, J. Schwindling, J. Searcy, E. Shabalina, K. Shaw, J. Sjolin, R. Soualah, S. Stamm, D. Ta, T. Theveneaux-Pelzer, E. Thompson, K. Uchida, L. Valery, M. Vreeswijk, C. Wasicki, I. Watson, K. Yau, J. Zhong, H. Zhu, M. zur Nedden, Object selection and calibration, background estimations and MC samples for the Winter 2013 Top Quark analyses with 2012 data, Tech. Rep. ATL-COM-PHYS-2013-088, CERN, Geneva (Jan 2013).
URL `https://cds.cern.ch/record/1509562`

[92] ATLAS Collaboration, Measurements of charge and CP asymmetries in *b*-hadron decays using top-quark events collected by the ATLAS detector in pp collisions at $\sqrt{s} = 8$ TeV, JHEP 02 (2017) 071. arXiv:1610.07869, doi:10.1007/JHEP02(2017)071.

[93] ATLAS Collaboration, Electron efficiency measurements with the ATLAS detector using 2012 LHC proton-proton collision data, Eur. Phys. J. C77 (3) (2017) 195. arXiv:1612.01456, doi:10.1140/epjc/s10052-017-4756-2.

[94] ATLAS Collaboration, Electron and photon energy calibration with the ATLAS detector using LHC Run 1 data, Eur. Phys. J. C74 (10) (2014) 3071. arXiv:1407.5063, doi:10.1140/epjc/s10052-014-3071-4.

[95] ATLAS Collaboration, Jet energy resolution in proton-proton collisions at $\sqrt{s} = 7$ TeV recorded in 2010 with the ATLAS detector, Eur. Phys. J. C73 (3) (2013) 2306. arXiv:1210.6210, doi:10.1140/epjc/s10052-013-2306-0.

[96] ATLAS Collaboration, Calibration of *b*-tagging using dileptonic top pair events in a combinatorial likelihood approach with the ATLAS experiment.

[97] ATLAS Collaboration, Luminosity determination in pp collisions at $\sqrt{s}$ = 8 TeV using the ATLAS detector at the LHC, Eur. Phys. J. C76 (12) (2016) 653. arXiv:1608.03953, doi:10.1140/epjc/s10052-016-4466-1.

[98] J. Wenninger, Machine Protection and Operation for LHC, in: Proceedings, 2014 Joint International Accelerator School: Beam Loss and Accelerator Protection: Newport Beach, CA, USA, November 5-14, 2014, 2016, pp. 377–401. arXiv:1608.03113, doi:10.5170/CERN-2016-002.377.
URL http://inspirehep.net/record/1480415/files/arXiv:1608.03113.pdf

[99] N. Kidonakis, Next-to-next-to-leading-order collinear and soft gluon corrections for t-channel single top quark production, Phys. Rev. D83 (2011) 091503. arXiv:1103.2792, doi:10.1103/PhysRevD.83.091503.

[100] N. Kidonakis, NNLL resummation for s-channel single top quark production, Phys. Rev. D81 (2010) 054028. arXiv:1001.5034, doi:10.1103/PhysRevD.81.054028.

[101] N. Kidonakis, Two-loop soft anomalous dimensions for single top quark associated production with a W- or H-, Phys. Rev. D82 (2010) 054018. arXiv:1005.4451, doi:10.1103/PhysRevD.82.054018.

[102] R. Placakyte, Recommendations for PDF usage in LHC predictions, PoS DIS2016 (2016) 019. arXiv:1609.07037.

[103] J. Erdmann, et al., A likelihood-based reconstruction algorithm for top-quark pairs and the KLFitter framework, Nucl. Instrum. Meth. A748 (2014) 18–25. arXiv:1312.5595, doi:10.1016/j.nima.2014.02.029.

[104] R. Brun, et al., ROOT: An object oriented data analysis framework, Nucl. Instrum. Meth. A389 (1997) 81–86. doi:10.1016/S0168-9002(97)00048-X.

[105] F. James, et al., Minuit: A System for Function Minimization and Analysis of the Parameter Errors and Correlations, Comput. Phys. Commun. 10 (1975) 343–367. doi:10.1016/0010-4655(75)90039-9.

[106] A. Czarnecki, et al., Helicity fractions of W bosons from top quark decays at NNLO in QCD, Phys. Rev. D81 (2010) 111503. arXiv:1005.2625, doi:10.1103/PhysRevD.81.111503.

[107] O. Nackenhorst, Top quark pair reconstruction in the electron+jets channel with a Kinematic Likelihood Fitter in the ATLAS Experiment.

[108] G. Cowan, A survey of unfolding methods for particle physics, Conf. Proc. C0203181 (2002) 248–257, [,248(2002)].

[109] A. N. Tikhonov, On the solution of improperly posed problems and the method of regularization, Sov. Math. 5 (1963) 1035.

[110] D. L. Phillips, A technique for the numerical solution of certain integral equations of the first kind, J. ACM. 9 (1962) 84.

[111] G. D'Agostini, A Multidimensional unfolding method based on Bayes' theorem, Nucl. Instrum. Meth. A362 (1995) 487–498. doi:10.1016/0168-9002(95)00274-X.

[112] G. Cowan, Statistical data analysis, 1998.

[113] ATLAS Collaboration, Measurement of the $t\bar{t}$ production cross-section using $e\mu$ events with b-tagged jets in pp collisions at $\sqrt{s}$ = 7 and 8 TeV with the ATLAS detector, Eur. Phys. J. C74 (10) (2014) 3109, [Addendum: Eur. Phys. J.C76,no.11,642(2016)]. arXiv:1406.5375, doi:10.1140/epjc/s10052-016-4501-2, 10.1140/epjc/s10052-014-3109-7.

[114] ATLAS Collaboration, Measurement of the top pair production cross section in 8 TeV proton-proton collisions using kinematic information in the lepton+jets final state with ATLAS, Phys. Rev. D91 (11) (2015) 112013. arXiv:1504.04251, doi:10.1103/PhysRevD.91.112013.

[115] CMS Collaboration, Measurement of the $t\bar{t}$ production cross section in the dilepton channel in pp collisions at $\sqrt{s}$ = 8 TeV, JHEP 02 (2014) 024, [Erratum: JHEP02,102(2014)]. arXiv:1312.7582, doi:10.1007/JHEP02(2014)024, 10.1007/JHEP02(2014)102.

[116] CMS Collaboration, Measurement of the $t\bar{t}$ production cross section in pp collisions at $\sqrt{s} = 8$ TeV in dilepton final states containing one τ lepton, Phys. Lett. B739 (2014) 23–43. arXiv:1407.6643, doi:10.1016/j.physletb.2014.10.032.

[117] CMS Collaboration, Measurement of the $\mathrm{t\bar{t}}$ production cross section in the all-jets final state in pp collisions at $\sqrt{s} = 8$ TeV, Eur. Phys. J. C76 (3) (2016) 128. arXiv:1509.06076, doi:10.1140/epjc/s10052-016-3956-5.

[118] Y. Grossman, et al., Testing New Indirect CP Violation, Phys. Rev. Lett. 103 (2009) 071602. arXiv:0904.0305, doi:10.1103/PhysRevLett.103.071602.

[119] A. L. Kagan, et al., On Indirect CP Violation and Implications for $D^0 - \bar{D}^0$ and $B_s^0 - \bar{B}_s^0$ mixing, Phys. Rev. D80 (2009) 076008. arXiv:0907.3917, doi:10.1103/PhysRevD.80.076008.

[120] M. Artuso, et al., CP violation in the B_s^0 system, Rev. Mod. Phys. 88 (4) (2016) 045002. arXiv:1511.09466, doi:10.1103/RevModPhys.88.045002.

[121] S. Descotes-Genon, et al., A possible explanation of the D0 like-sign dimuon charge asymmetry, Phys. Rev. D87 (2013) 074036, [Erratum: Phys. Rev.D92,no.7,079903(2015)]. arXiv:1207.4483, doi:10.1103/PhysRevD.92.079903, 10.1103/PhysRevD.87.074036.

[122] S. Bar-Shalom, et al., Second order direct CP asymmetry in $B_s \to X\ell\nu$, Phys. Lett. B694 (2011) 374–379. arXiv:1008.4354, doi:10.1016/j.physletb.2010.10.025.

[123] ATLAS Collaboration, Measurement of the $t\bar{t}$ production cross-section using $e\mu$ events with b-tagged jets in pp collisions at $\sqrt{s}$=13 TeV with the ATLAS detector, Phys. Lett. B761 (2016) 136–157. arXiv:1606.02699, doi:10.1016/j.physletb.2016.08.019.